

https://dspace.org/

Optimization of gallium oxide (ga2o3) nanomaterials for gas sensing applications

Gatsi, Nyepudzai Charsline

2024

University of the Witwatersrand, Johannesburg

https://hdl.handle.net/10539/42072

Gatsi, Nyepudzai Charsline. (2024). Optimization of gallium oxide (ga2o3) nanomaterials for gas sensing applications [PHD, University of the Witwatersrand, Johannesburg]. WireDSpace.https://hdl.handle.net/10539/42072

Downloaded from a DSpace repository. https://dspace.org/

OPTIMIZATION OF GALLIUM OXIDE (Ga_2O_3) NANOMATERIALS FOR GAS SENSING APPLICATIONS

by

Nyepudzai Charsline Gatsi

A thesis submitted to the Faculty of Science, University of the Witwatersrand, Johannesburg, in fulfilment of the requirements for the degree of

Doctor of Philosophy

in

Physics



Supervisor: Prof. O.M. Ntwaeaborwa

Co-Supervisors: Prof. G.H. Mhlongo, Prof. N. Moloto, Prof. R.M. Erasmus

03 June 2024

DECLARATION

I, Nyepudzai Charsline Gatsi, hereby declare that the work contained in this thesis is my own original work and that has not previously in its entirety or in part been submitted at any other institution of higher education for a degree.

Signature: 

Date: 03 June 2024

DEDICATION

For our son, Ethan Kapesi

ACKNOWLEDGEMENTS

- ✓ I am grateful to God for His steadfast love throughout this journey. He made this POSSIBLE!
- ✓ My utmost gratitude to my supervisors; Professors O.M. Ntwaeaborwa, G.H. Mhlongo, N. Moloto, and R.M. Erasmus for their academic guidance throughout the journey. I was fortunate to benefit from your expertise. To Prof. Martin Ntwaeaborwa, I am grateful for your supervision, your patience and moral support. Prof. Gugu. H. Mhlongo, my sincere gratitude to you for encouraging me when this journey seemed impossible.
- ✓ I owe my sincere gratitude to Dr. Murendeni Nemufulwi, Dr. Mosima Kgomo and Dr. Katekani Shingange. Thank you for your patience in teaching me how to maneuver in the sensing laboratory and to get a grip on the data analysis.
- ✓ Thank you to my family and friends for your encouragement, and moral and spiritual support.
- ✓ To my husband, Liberty Kapesi, thank you for allowing me to pursue this dream.
- ✓ To our son, Ethan Kapesi, you kept me going. Thanks for keeping me sane, my boy!
- ✓ To Aunty Agnella Ngundu, thank you for your support. This journey became much easier because of your help.
- ✓ My sincere gratitude to the Organization for Women in Science for the Developing World (OWSD) and Sida (Swedish International Development Cooperation Agency) and the National Research Fund (NRF, South Africa) for the financial support.

- ✓ My sincere appreciation to everyone who assisted me academically from the WITS NANOWEBS and CATMAT groups, MMU characterization facilities, School Physics WITS University, and CSIR. Thank you!
- ✓ Lastly, I want to thank myself for not giving up. It wasn't easy being a wife, a mother, and a PhD student. But, through the ups and downs, I remained determined to complete the journey.

CONFERENCES, PUBLICATIONS AND HONOURS

Conferences:

1. N. C. Gatsi, G. H. Mhlongo, N. Moloto, R. M. Erasmus, O. M. Ntwaeaborwa. "Serendipitous *p*- to *n*-type response switching in $\beta - Ga_2O_3$ needles: A potential application to selective CO and CH_4 gas sensors". 66 Annual conference of South African Institute of Physics, Nelson Mandela University, South Africa. 1-8 July 2022 (**Oral presentation**).

2. N.C. Gatsi, G.H. Mhlongo, N. Moloto, R.M. Erasmus, O.M. Ntwaeaborwa. "Effects of defects on gas sensor performance of $\beta - Ga_2O_3$. 67 Annual conference of South African Institute of Physics, University of Zululand, South Africa. 3-7 July 2023 (**Poster presentation**), **1st prize best presentation**.

3. N.C. Gatsi, G.H. Mhlongo, N. Moloto, R.M. Erasmus, O.M. Ntwaeaborwa. "Ga_2O_3 nanostructure-based gas sensors for application in environment and food safety: effects of controlled intrinsic and extrinsic defects". 67 Annual conference of South African Institute of Physics, University of Zululand, South Africa. 3-7 July 2023 (**Oral presentation**).

4. N.C. Gatsi, G.H. Mhlongo, N. Moloto, R.M. Erasmus, O.M. Ntwaeaborwa. Ga_2O_3 nanostructure-based gas sensors for application in environment and food safety: effects of controlled intrinsic and extrinsic defects". 2023 IEEE 13th International Conference "Nanomaterials: Applications & Properties", The Crowne Plaza Hotel, Bratislava, Slovakia. 10-15 September 2023 (**Oral presentation**).

Publications:

1. Gatsi, N. C., et al. "Hierarchically-ordered nanorods of Ga_2O_3 derived from microwave-assisted hydrothermal approach: Investigation of calcination-induced structural evolution and optical behavior." *Materials Today Communications* 33 (2022): 104808. https://doi.org/10.1016/j.mtcomm.2022.104808. *This work has been discussed in Chapter 4 of the thesis.*
2. Gatsi, N. C., et al. "Synthesis, characterization, and gas-sensing performance of rhombohedral (α) and monoclinic (β)$-Ga_2O_3$ nanorods/nanowires." Journal of Surfaces and Interfaces: under review. *This work is discussed as Chapter 5 in the thesis.*
3. Gatsi, N. C., et al. "Effects of reaction pH on regular nanorods and hierarchically structured $\beta - Ga_2O_3$ and their isopropanol sensing capabilities." *Materialia* 34 (2024): 102101. https://doi.org/10.1016/j.mtla.2024.102101. *This work is discussed in chapter 6 of the thesis*.
4. Gatsi, N. C., et al. "A highly ethylene responsive $\beta - Ga_2O_3$ nanorods chemiresistive sensor: Effects of sensitization induced by Ag nanocrystals. Journal of Colloid and Interface Science. Submitted for publication. *This work is discussed in chapter 7 of the thesis.*

Honors

1. Organization for Women in Science for the Developing World (OWSD) PhD Fellowship award.
2. National Research Fund (NRF, South Africa) PhD scholarship.
3. IEEE NAP-2023 Conference “East Meets West” Grant.
4. IEEE Sensors Council Diversity and Inclusion Travel Grant.

ABSTRACT

Gas sensors are needed for monitoring different gases in indoor and outdoor environments, food quality assessment, and health diagnostics. Among materials studied for these applications, semiconducting metal oxides (SMOs) have generated a lot of interest due to their excellent sensitivity, simple circuit, and low cost. One-dimensional ($1D$) Ga_2O_3 nanomaterials are part of the promising candidates explored for the sensing of different gases due to their excellent electrical conductivity, high catalytic behavior, and chemical and thermal stability. This study reports the optimization of crystal structure, morphology, and surface chemistry of Ga_2O_3 nanostructures for use in the detection of various gases. A set of unmodified and noble metal modified $1D$ Ga_2O_3 nanomaterials were synthesized by microwave-assisted hydrothermal method followed by heat-treatment at different temperatures and their gas sensing performances were systematically studied. The samples were characterized by thermogravimetric analysis (TGA), X-ray diffraction (XRD), Raman analysis, scanning electron microscope (SEM), transmission electron microscope (TEM), Brunauer-Emmett-Teller (BET), photoluminescence (PL), diffuse reflectance spectroscopy (DRS), and X-ray photoelectron spectroscopy (XPS) methods. The effects of heat-treatment temperatures on phase transformations and gas sensing performances of various Ga_2O_3 polymorphs were investigated. The $\alpha - Ga_2O_3$, $\beta - Ga_2O_3$ and $\alpha/\beta - Ga_2O_3$ crystal structures were synthesized and evaluated for gas sensing. The $\beta - Ga_2O_3$ sensing layers presented selective response coupled with fast response/recovery times towards carbon monoxide (CO) compared to the $\alpha - Ga_2O_3$ and $\alpha/\beta - Ga_2O_3$ crystal structures. The observed variations in the gas sensing performances of these three crystal structures were attributed to controlled properties of different Ga_2O_3 polymorphs. Furthermore, the $\beta - Ga_2O_3$

polymorph was prepared in the form of regular and hierarchical nanorod-based morphological features which demonstrated different gas sensing behaviors. The $\beta - Ga_2O_3$ regular nanorods showed better capabilities of detecting isopropanol than the nanobundle-like and nanodandelion-like features, and these differences were attributed to changes in textural, porosity, and compositional properties related to different morphologies. The effects of incorporating Ag and Au noble metal nanocrystals on regular $\beta - Ga_2O_3$ nanorods surfaces on their gas sensing behaviour were also investigated. The results revealed that surface modification of $\beta - Ga_2O_3$ nanorods with 0.5 and 1.0 $mol\%$ Ag and Au noble metals significantly lowered the sensor operating temperature compared to that of unmodified $\beta - Ga_2O_3$ nanorods towards the detection of ethylene. In addition, surface incorporation of 1.0 $mol\%$ Ag dramatically increased the sensor sensitivity and selectivity and reduced the response/recovery times towards ethylene gas, and these positive changes were attributed to the electronic and chemical sensitization effects stimulated by the catalytic activity of Ag nanocrystals incorporated on the surface of $\beta - Ga_2O_3$ nanorods. This study unambiguously optimized the crystal structure, morphology, and surface chemistry of Ga_2O_3 nanostructures for the detection of carbon monoxide, ethylene and isopropanol gases. These sensors may potentially be used in real-time detection of carbon monoxide and isopropanol for indoor air quality monitoring to improve human health. In additional they have also demonstrated capabilities for the precise and economical detection of ethylene around plants and fruits, which could be beneficial to the horticultural and agricultural industries.

TABLE OF CONTENTS

DECLARATION i

DEDICATION ii

ACKNOWLEDGEMENTS iii

CONFERENCES, PUBLICATIONS AND HONOURS v

ABSTRACT viii

TABLE OF CONTENTS x

LIST OF FIGURES xviii

CHAPTER 1 1

Introduction 1

1.1 Synopsis 1

1.2 Problem statement 4

1.3 Study aims and objectives 6

1.4 Thesis chapter outline 6

CHAPTER 2 8

Literature review 8

2.1 Introduction 8

2.2 Gas sensors in general 8

2.3 SMO based gas sensors 9

2.3.1 Operating gas sensing phenomenon of SMO gas sensors 10

2.4 Gas sensor characteristics 12

2.4.1 Gas sensor operating temperature 12

2.4.2 Gas sensor response 13

2.4.3 Gas sensor response and recovery times 13

2.4.4 Gas sensor selectivity 14

2.4.5 Gas sensor limit of detection (LoD) 14

2.4.6 Gas sensor sensitivity 15

2.4.7 Gas sensor stability 15

2.5 Applications of SMO-based gas sensors 15

2.6 Fundamental properties of gallium oxide (Ga_2O_3) 16

2.6.1 Polymorphism and lattice parameters of Ga_2O_3 17

2.6.2 Preparation of Ga_2O_3 20

2.6.3 Reaction involved during synthesis of Ga_2O_3 materials through hydrothermal approaches 21

2.6.4 Factors leading to morphological evolution of Ga_2O_3 22

2.6.4.1 Effects of pH 22

2.6.4.2 Effects of reaction aging time 23

2.6.4.3 Effects of growth reaction temperature 24

2.6.4.4 Effects of thermal-treatment temperature 25

2.7 Ga_2O_3 as an active sensing material 25

2.7.1 Adopted strategies for enhancement of Ga_2O_3 based gas sensor performance 28

2.7.1.1 Surface decoration/modification of Ga_2O_3 through addition of noble metal nanoparticles 28

2.7.1.2 Ga_2O_3 heterostructure formation 30

2.7.1.3 Modulation of Ga_2O_3 morphology and properties 32

CHAPTER 3 34

Materials synthesis and characterization 34

3.1 Introduction 34

3.2 Materials synthesis 34

3.2.1 Hydrothermal synthesis method 35

3.2.2 Microwave-assisted hydrothermal method 36

3.2.2.1 Reagents 37

3.2.2.2 Hydrothermal synthesis parameters 38

3.2.3 Post-preparation heat-treatment 39

3.3 Characterization techniques 41

3.3.1 Thermogravimetric Analysis (TGA) 41

3.3.2 X-ray diffraction (XRD) 42

3.3.3 Raman Spectroscopy 45

3.3.4 Scanning electron microscopy (SEM) 47

3.3.5 Transmission electron microscopy (TEM) 48

3.3.6 Brunauer-Emmet-Teller (BET) 50

3.3.7 X-ray Photoelectron Spectroscopy (XPS) 51

3.3.8 Diffuse reflectance spectroscopy (DRS) 54

3.3.9 Photoluminescence (PL) spectroscopy 55

3.3.10 Gas sensor preparation and characterization 57

CHAPTER 4 59

Hierarchically ordered nanorods of Ga_2O_3 derived from microwave-assisted hydrothermal approach: investigation of calcination-induced structural evolution and optical behavior 59

4.1 Introduction 59

4.2 Materials and methods 61

4.2.1 Materials 61

4.2.2 Samples preparation 61

4.2.3 Samples characterization 61

4.3 Results and discussion 62

4.3.1 Thermal stability and structural behavior analysis 62

4.3.2 Particle morphology 66

4.3.2.1 Microwave-assisted hydrothermal method 68

4.3.2.2 Solution pH (=11) 68

4.3.3 Optical absorption and emission properties 70

4.3.4 Compositional analysis 73

4.4 Conclusion 75

CHAPTER 5 76

Synthesis, characterization, and gas-sensing performance of rhombohedral (α) and monoclinic (β) $-Ga_2O_3$ nanorods/nanowires 76

5.1 Introduction 76

5.2 Materials and methods 78

5.2.1 Preparation of Ga_2O_3 78

5.2.2 Characterization 79

5.2.3 Ga_2O_3 based-gas sensors fabrication and testing 79

5.3 Results and discussion 80

5.3.1 Crystal structure 80

5.3.2 Morphology and texture analysis 81

5.3.3 Surface chemistry of Ga_2O_3 nanorods/nanowires 83

5.3.4 Gas-sensing characteristics of Ga_2O_3 nanorod/nanowire-based gas sensors 88

5.3.5 Gas sensing mechanism of Ga_2O_3 nanorods/nanowires-based sensors 97

5.4 Conclusion 99

CHAPTER 6 100

Effects of reaction pH control on regular nanorods and hierarchically structured $\beta - Ga_2O_3$ and their isopropanol sensing capabilities 100

6.1 Introduction 100

6.2 Experimental section 103

6.2.1 Preparation of $\beta - Ga_2O_3$ nanorod-based nanostructures 103

6.3 Sample characterization 104

6.4 Fabrication and testing of $\beta - Ga_2O_3$ nanorods-, nanobundles- and nanodandelions-based gas sensor films 104

6.5 Results and discussion 105

6.5.1 Crystal structure analysis of $\beta - Ga_2O_3$ powders 105

6.5.2 Morphology characterization of $\beta - Ga_2O_3$ nanostructures 106

6.5.3 Texture analysis of $\beta - Ga_2O_3$ nanorods, nanobundles and nanodandelions 108

6.5.4 Chemical composition of $\beta - Ga_2O_3$ nanorods, nanobundles and nanodandelions 109

6.5.5 Gas sensor performances of $\beta - Ga_2O_3$ nanorods-, nanobundles- and nanodandelions-based gas sensors 110

6.5.6 Gas sensing mechanism of $\beta - Ga_2O_3$ sensors produced at pH levels of 7, 11, 14116

6.6 Conclusion 119

CHAPTER 7 120

A highly ethylene responsive $\beta - Ga_2O_3$ nanorods chemiresistive sensor: effects of electronic and chemical sensitization induced by incorporation of noble metal nanocrystals 120

7.1 Introduction 120

7.2 Experimental Section 122

7.2.1 Materials 122

7.2.2 Preparation of unmodified $\beta - Ga_2O_3$ nanorods 122

7.2.3 Preparation of Ag- or Au-modified $\beta - Ga_2O_3$ nanorods 123

7.2.4 Sample characterization 123

7.2.5 Fabrication and gas sensor testing of unmodified and Ag- and Au- modified $\beta - Ga_2O_3$ nanorods 124

7.3 Results and discussion 125

7.3.1 Crystal structure of unmodified and Ag- and Au-modified $\beta - Ga_2O_3$ nanorods. 125

7.3.2 Morphological and structural analysis 127

7.3.3 Chemical state analysis 129

7.3.4 Gas sensing 132

7.3.5 Gas sensing mechanism of unmodified and $1.0 mol\%$ Ag-modified $\beta - Ga_2O_3$ nanorods 138

7.4 Conclusion 141

CHAPTER 8 143

Conclusion and future prospects 143

8.1 Conclusion 143

8.2 Prospects 145

8.3 Further applications of gallium oxide and gallium oxyghydroxide materials 146

REFERENCES 150

LIST OF FIGURES

Fig. 2.1. Sensing mechanism of *n*- and *p*-type semiconductor metal oxides in (a, d) air, (b, e) reducing gas and (c, f) oxidizing gas. O^{x-} represents the charged oxygen species (O^{2-}, O^{-}, and O^{2-}) and x is 1 or 2. 11

Fig. 2.2. Schematic representation of (a-f) crystal structures of the six polymorphs of Ga_2O_3 [23] and (g) preparation temperatures of the different Ga_2O_3 phases [33,81]. 18

Fig. 2.3. Number of research articles published between 1992 and 2023 on Ga_2O_3-based gas sensors. Data obtained from the Web of Science with search words "gallium oxide" OR "Ga_2O_3" and filter words "gas sensor". 27

Fig. 3.1. Schematic representation of the (a) hydrothermal process and (b) set-up used to synthesize Ga_2O_3-based nanostructures using microwave-assisted hydrothermal method and calcination. 36

Fig. 3.2. Schematic depiction of a thermogravimetric analyser [135]..... 42

Fig. 3.3. Schematic diagram of (a) powder X-ray diffractometer with a θ-2θ geometry and (b) X-ray diffraction by a crystalline powder. 43

Fig. 3.4. Schematic diagram of a Raman measurement system [140]..... 46

Fig. 3.5. Schematic representation of a scanning electron microscope and (b) sample-electron beam interaction [142]. 48

Fig. 3.6. Schematic diagram of a transmission electron microscope [143]..... 49

Fig. 3.7. Schematic representation of a Brunauer-Emmet-Teller surface analyser [146]..... 51

Fig. 3.8. Schematic depiction of (a) the photoelectric effect and (b) X-ray Photoelectron Spectroscopy analysis system edited from reference [148]. 52

Fig. 3.9. A schematic representation of a dual-beam UV-Vis spectrophotometer [152]. 55

Fig. 3.10. Schematic representation of a photoluminescence measurement set up [154]. 57

Fig. 3.11. Schematic view of the gas sensing system. 58

Fig. 4.1. Thermogravimetric analysis and derivative thermogravimetric analysis curves obtained by heating the uncalcined sample from room temperature to 880 ℃. 63

Fig. 4.2. (a) X-ray diffraction patterns and (b) Raman spectra show structural evolution as functions of calcination temperature of Ga_2O_3 powders. 65

Fig. 4.3. (a) Scanning electron microscopy micrographs of the as-synthesized $GaOOH$ powder products, (b, c) high-resolution images to show the rod arrangement and appearance in the bunches and urchin-like hierarchical structures present in the $GaOOH$ powders. (d-f) micrographs from powders calcined at 406 ℃ (R-406), 597 ℃ (R-597), and 750 ℃ (R-750). (g) proposed rod-formation mechanism for the hydrothermally synthesized nanostructures. (h) average length of each bunch of rods versus calcination temperature in the various Ga_2O_3 powders in (a-f). 67

Fig. 4.4. (a) UV-Vis diffusive reflectance spectra of the synthesized powder products. The inset shows the Kubelka-Munk plots with determined band energy values, (b) room-temperature photoluminescence of the synthesized powder products, (c) the deconvoluted emission from R-750 powder and the inset shows the blue-emission decay curve. (d) proposed PL mechanism involved in the observed emission. R-Uncal, R-406, R-597, and R-750 represent uncalcined $GaOOH$ powders and Ga_2O_3 powders calcined at 406, 597 and 750 ℃, respectively. 71

Fig. 4.5. X-ray photoelectron (a) survey and ((b)-(e)) high-resolution spectra measured from Ga_2O_3 powders calcined at 750 ℃. 74

Fig. 5.1. Schematic diagrams showing (a) Ga_2O_3 synthesis process and (b) gas sensor characterization system. 79

Fig. 5.2. X-ray diffraction patterns of hydrothermally synthesized Ga_2O_3 powders. S550, S650, S750, S850, and S950 represent Ga_2O_3 powders heat treated at 550, 650, 750, 850, and 950 ℃, respectively. 81

Fig. 5.3. (a-f) Scanning electron microscopy images, (g) Brunauer-Emmett-Teller surface area and Barrett-Joyner-Halenda pore volume, and (h) Nitrogen adsorption-desorption isotherms measured at 77 K of heat treated Ga_2O_3 powders. S550, S650, S750, S850, and S950 represent Ga_2O_3 powders heat treated at 550, 650, 750, 850, and 950 ℃, respectively. 82

Fig. 5.4. (a) X-ray photoelectron spectroscopy survey spectra and (b-d) high resolution spectra of $Ga\ 2p$, $O\ 1s$, and $Cr\ 2p$ core-levels of heat-treated Ga_2O_3 nanorods/nanowires. (e) STEM images of the Ga_2O_3 samples heat treated as indicated. S550, S650, S750, S850, and S950 represent Ga_2O_3 powders heat treated at 550, 650, 750, 850, and 950 ℃, respectively..... 84

Fig. 5.5. (a) As-measured and (b-f) deconvoluted room-temperature photoluminescence emission spectra of heat treated Ga_2O_3 nanorods/nanowires. S550, S650, S750, S850, and S950 represent Ga_2O_3 powders heat treated at 550, 650, 750, 850, and 950 ℃, respectively. 87

Fig. 5.6. (a) Electrical resistance in air (R_a) and 90 $ppm\ CO$ (R_g) versus operating temperature of the Ga_2O_3 sensors. (b) Sensor response towards 90 $ppm\ CO$ at the various operating temperatures. S550, S650, S750, S850, and S950 represent Ga_2O_3 powders heat treated at 550, 650, 750, 850, and 950 ℃, respectively. 89

Fig. 5.7. (a) Dynamic resistance transient curves and (b, c) response against CO concentrations at 165 ℃ of Ga_2O_3 nanorods/nanowires heat treated at 550 ℃ (S550), 650 ℃ (S650), 750 ℃ (S750), 850 ℃ (S850), and 950 ℃ (S950). 90

Fig. 5.8. (a) Responses of Ga_2O_3 sensors at 165 ℃ towards 90 ppm of different gases. (b) responses of S550 and S650 sensors towards 90 ppm of SO_2, CH_4 and NH_3 gases at various operating temperatures. (c) reproducibility and (d) stability curves of the sensors. S550, S650, S750, S850, and S950 represent Ga_2O_3 powders heat treated at 550, 650, 750, 850, and 950 ℃, respectively. 92

Fig. 5.9. Response of the Ga_2O_3 nanorod/nanowire-based sensors under (a) dry (0%RH), (b) 60%RH, and (c) 90%RH. (d) response/recovery curves of the sensors. S550, S650, S750, S850, and S950 represent Ga_2O_3 powders heat treated at 550, 650, 750, 850, and 950 ℃, respectively. 94

Fig. 5.10. (a) Scanning electron microscopy image of the synthesized Ga_2O_3 nanorods/nanowires; the gas sensing mechanism of *n*-type Ga_2O_3 nanorods/nanowires in (b) air and toward (c) CO, (d) NH_3 and (e) SO_2 gases..... 98

Fig. 6.1. (a) Full-range X-ray diffraction patterns of $\beta - Ga_2O_3$ powders prepared using a microwave-assisted hydrothermal method at different reaction pH levels. (b) plot of the (111) X-ray diffraction peaks from the samples. 106

Fig. 6.2. Field emission scanning electron microscopy images of $\beta - Ga_2O_3$ (a) nanorods, (b) nanobundles, and (c) nanodandelions prepared at the pH levels of 7, 11, and 14, respectively. (d) N_2 adsorption-desorption isotherms and pore size distribution of the nanorods, nanobundles and dandelions. 107

Fig. 6.3. High-resolution X-ray photoelectron spectroscopy of the (a) $Ga\ 2p$ and (b-d) $O\ 1s$ core-levels for $\beta - Ga_2O_3$ nanorods, nanobundles and nanodandelions prepared under reaction pH levels of 7, 11 and 14, respectively. 110

Fig. 6.4. Responses of $\beta - Ga_2O_3$ based sensors to 90 ppm isopropanol at different operating temperatures. (b) transient response curves and (c) corresponding double-log plots of $\beta - Ga_2O_3$ sensors exposed to 5 to 90 ppm isopropanol at 150 ℃. (d) Sensor response towards 90 ppm of various gas analytes tested with sensors operating at 150 ℃. pH7, pH11, and pH14 indicate pH conditions at which the samples where synthesized. 112

Fig. 6.5. (a) Response times (t_{res}) and recovery times (t_{rec}) of the $\beta - Ga_2O_3$ sensors, (b) response reproducibility, and (c) response stability curves of the $\beta - Ga_2O_3$ sensors at 150 ℃ exposed to 90 ppm isopropanol. pH7, pH11, and pH14 indicate pH conditions at which the samples where synthesized. 114

Fig. 6.6. Schematic representations and band diagrams of $\beta - Ga_2O_3$ (a, b) nanorods (pH7), (c, d) nanobundles (pH11) and (e, f) nanodandelions (pH14)-based gas sensors in air and towards isopropanol vapour. 118

Fig. 7.1. Schematic presentation of the gas sensing station and process. 125

Fig. 7.2. X-ray diffraction patterns of the samples. 0%, 0.5%Ag, 1.0%Ag, 0.5%Au, and 1.0%Au represent $\beta - Ga_2O_3$ nanorods unmodified and modified with indicated concentration of Ag and Au. 126

Fig. 7.3. Low-resolution transmission electron microscopy images (a, c, e) and high-resolution transmission electron microscopy images and selected area electron diffraction patterns (b, d, f) of unmodified and 1.0$mol\%Ag$- and 1.0$mol\%Au$-modified $\beta - Ga_2O_3$ nanorods. 128

Fig. 7.4. High-resolution X-ray photoelectron spectroscopy core-level spectra of (a) $Ga\ 2p$, (b) $O\ 1s$, (c, d) $Ag\ 3d$, and (e, f) $Au\ 4f$ of the samples. 0%, 0.5%Ag, 1.0%Ag, 0.5%Au, and 1.0%Au represent $\beta - Ga_2O_3$ nanorods unmodified and modified with indicated concentration of Ag and Au. 130

Fig. 7.5. (a) Responses of the sensors towards 90 ppm ethylene at various operating temperatures. (b) dependence of Ra on the sensor operating temperature. (c) transient response curves and (d) corresponding double-log plots sensors exposed to various ethylene concentrations at 165 ℃ for the unmodified sample and at 140 ℃ for the modified samples. (e) response times (t_{res}) and (f) recovery times (t_{rec}) of the unmodified and modified sensors operating at 140 ℃ and 165 ℃, respectively, subjected to 90 ppm ethylene. 0%, 0.5%Ag, 1.0%Ag, 0.5%Au, and 1.0%Au represent $\beta - Ga_2O_3$ nanorods unmodified and modified with indicated concentration of Ag and Au. 133

Fig. 7.6. Sensor performances measured at operating temperatures of 165 ℃ and 140 ℃ for the unmodified and surface modified $\beta - Ga_2O_3$ nanorod-based sensors, respectively. (a) Sensor response towards 90 ppm of various gas analytes. (b) response reproducibility curve, (c) response stability curves, and (d) response (t_{res})-recovery (t_{rec}) curves towards 90 ppm

ethylene of the 1.0%Ag sensor at 0%RH, 30%RH, 60%RH, and 90%RH. 0%, 0.5%Ag, 1.0%Ag, 0.5%Au, and 1.0%Au represent $\beta - Ga_2O_3$ nanorods unmodified and modified with indicated concentration of Ag and Au. 136

Fig. 7.7. Schematic representations and band diagrams of (a, b) unmodified and (c-e) Ag-modified $\beta - Ga_2O_3$ nanorod-based sensors in air and in ethylene gas. (c, d) Electronic sensitization and (e) chemical sensitization of $\beta - Ga_2O_3$ nanorods by the Ag/Ag_2O nanocrystals..... 140

CHAPTER 1

Introduction

1.1 Synopsis

In general, gas sensors are important in various facets of daily life such that they have enabled reliable detection of various gases at low concentration levels for environmental monitoring and control in various sectors such as medical facilities, product quality assurance, occupational sites as well as industrial plants [1]. The evolution of nanoscience technology has led to major breakthroughs in achieving this goal, through the development of nanomaterials that are robust and exhibit commendable selectivity, sensitivity, and promptness of response [2,3]. Nanoscience involves the manipulation of physical and chemical properties of nano-sized (1 – 100 nm) materials to achieve desired capabilities. For this reason, this field has enabled several opportunities for advancement of new generation of multianalyte gas sensors to fulfil the demand of highly selectivity and responsive gas sensors utilizing different functional nanostructured materials [2]. A gas sensor is a device that is used to detect the presence of a gas or change in the gas concentrations by converting a chemical signal into a readable electrical signal [4,5]. To date, there has been a high number of published research articles documenting huge strides of achievements made in terms of the preparation of nanomaterials and their optimization for gas sensing applications [6–10]. However, it still is a research priority to improve the gas sensing capabilities of the existing materials or to fabricate new functional material for gas sensing applications [9].

A variety of materials at a nanoscale such as conducting polymers [11], carbon nanotubes [12], as well as semiconductor metal oxides (SMOs) [13] have been developed for use in gas detectors. Among these materials, chemiresistive gas sensors produced from SMOs have generated a lot of interest due to advantages like ease of processing, low-cost and high sensitivities [14–16]. In addition, chemiresistive gas based on SMOs are sensitive to both oxidizing and reducing gases. However, low selectivity, high operating temperatures and high-power consumption are regarded as their main drawbacks [16–18]. Nevertheless, different types of SMOs have been widely explored for gas sensing applications and their gas sensing behavior have been strongly correlated with the materials' fundamental properties such as surface area, chemical and thermal stability, as well as electrical conductivity [14,18].

Examples of SMOs that have been utilized for the sensing of different gases under various conditions are *n*-type ZnO [19], TiO_2 [20], WO_3 [21], SnO_2 [22], and Ga_2O_3 [23], and *p*-type NiO [24], CuO [25], and $LaFeO_3$ [26]. The *p*-type SMO-based sensors are less studied due to lower response towards both oxidizing and reducing gases, compared to the *n*-type SMOs [27]. In this context, *n*-type SMOs are prospective candidates for developing gas sensors with desired capabilities. Therefore, several approaches have been investigated for the enhancement of gas sensing performances of *n*-type SMOs [6]. The main approaches are through sensitization of the *n*-type SMO material by noble metals [28] and heterojunction formation with another *n*-type SMO or *p*-type SMOs [29]. Furthermore, the gas sensing mechanism occurring at the surface of the *n*-type SMOs can be controlled by tuning the structure and morphology of the oxide [30–32]. This implies that the *n*-type SMOs can easily be manipulated to produce a material functionalized for improved gas sensing performance.

As part of the *n*-type SMOs, gallium oxide (Ga_2O_3), which is an ultrawide band gap material ($\sim 4.7\ eV$), has also been demonstrated to possess unique properties [33] which are useful in various applications such as photodetectors, power-electronics, and gas sensing. This SMO material is known for its existence in six different polymorphs, high chemical stability, and high electrical conductivity [33]. Different phases of Ga_2O_3 which are $\alpha - Ga_2O_3$, $\beta - Ga_2O_3$, $\delta - Ga_2O_3$, $\gamma - Ga_2O_3$, $\varepsilon - Ga_2O_3$, and $\kappa - Ga_2O_3$ [34] have demonstrated excellent gas sensing properties for the detection of different gas analytes such as CO [35], NH_3 [36], H_2S [37], O_2 [38], NO_x [39] and volatile organic compounds (VOCs) like acetone [40] and ethanol [41]. However, the $\beta - Ga_2O_3$ phase is the most studied in terms of gas sensing considering that it presents exceptionally high thermal stability hence can provide microstructural stability that can guarantee the long-term stability of the sensor [23,42]. Due to these properties, Ga_2O_3 materials, especially the $\beta - Ga_2O_3$ phase has been a subject of interest for gas sensing applications even though it is still necessary to enhance its sensitivity and selectivity towards both oxidizing and reducing gases.

To achieve this, manipulation of the microstructural properties of Ga_2O_3 has been explored to tune the sensing properties [23,42]. So far, one-dimensional ($1D$) $\beta - Ga_2O_3$ nanostructures such as nanorods and nanowires present large surface area and excellent electrical conductivity, which are beneficial for the enhancement of the sensor response [36,43]. Moreover, noble metals including Au and Pt, incorporate onto the surface of $1D$ $\beta - Ga_2O_3$ nanostructures to further enhance both the sensor response and selectivity [35,44]. Furthermore, sensitization of the $\beta - Ga_2O_3$ materials through the formation of *n*-*n*-type or *n*-*p*-type of heterojunctions with *n*-type SMOs like WO_3 [45] and SnO_2 [41], or *p*-type SMOs like Al_2O_3 [39] have also been

reported to yield the same effects and achieve improved gas sensor stability and reliability for practical usage.

1.2 Problem statement

According to the 2022 World Health Organization (WHO) report [46], about 6.7 million premature deaths reported annually are associated with combined effects of household and air pollution. The major source of air pollutants includes accidental gas leaks from home appliances, release of gases from industrial processes or emission from cars. Because of this, it is necessary to develop gas sensors that can recognize different gases in indoor and outdoor environments for human safety [4]. Besides, gas sensors receive high demand in the food industry for quality assessment of food quality status control for food safety. For example, gas sensors can be utilized to identify ethanol and propanol in food products such as canned foods, milk, and wines [47,48]. In other scenarios, gas sensors have been applied to monitor analytes like ethylene which directly influence the plant and fruit production and market [49,50]. Furthermore, gas sensors are also beneficial in the health sector for diagnostic purposes. For instance, the detection of certain concentrations of ethylene or acetone from one's breath gives information about their tuberculosis and diabetes condition [51,52]. In this context, novel nanostructured materials that can be used as platforms for the effective detection of various gas analytes are needed for the protection of humans and the environment, and also easing diagnostic ways in the health care system.

The materials that are currently used for the gas sensors available in the market are based on SMOs such as WO_3, ZnO and SnO_2 [53]. These SMO based materials present good sensor response towards both oxidizing and reducing gases; however, they lack selectivity [54] and are

often operated at high temperatures [53]. Therefore, there is great need for the development of low-temperature-operated (energy saving) and reliable materials that can efficiently detect specific gases with less cross sensitivity towards other gases present in the same environment. $1D\ Ga_2O_3$ nanomaterials with tuned properties are promising candidates to address these drawbacks. This is because of their high catalytic behavior, high chemical stability, and excellent electrical conductivity whose applications in catalysis and high-power electronics have been described in the literature [55,56]. Moreover, $1D\ Ga_2O_3$ materials can be prepared via direct synthesis methods and hence are affordable. Although different $1D\ Ga_2O_3$ materials presenting various microstructural features can be utilized for sensitive detection of gases, the application of undoped $1D\ Ga_2O_3$ sensing materials in real-life applications is limited by the material's low selectivity and poor thermal stability as highlighted earlier. Hence, surface modification through incorporation of noble metal nanoparticles or formation of heterostructures $1D\ Ga_2O_3$ have shown further improvement on the gas sensing performances of Ga_2O_3 materials, through the sensitization mechanisms [23,42].

Therefore, this study is focused on synthesis of $1D\ Ga_2O_3$ nanostructured materials followed by systematic investigation of their gas sensing performances. A detailed attention on the optimization of the structural and morphological properties of Ga_2O_3 for enhancement of their gas sensing capabilities has been given. The influences of numerous parameters such as annealing temperature and reaction pH were also evaluated. Furthermore, $1D\ Ga_2O_3$ nanostructures were also modified with Ag and Au nanoparticles for enhanced sensor characteristics. This study demonstrates that surface modification by Ag nanocrystals significantly enhanced the gas sensing performances of Ga_2O_3 nanorods.

1.3 Study aims and objectives

This work is aimed at optimization of Ga_2O_3 nanostructured materials for gas sensing applications through the modification of their microstructural and surface properties as well as electrical property enhancement. The effects of tuning the crystal structure and noble metal (Ag, Au) modification on the structural, morphological, optical, composition, and gas sensing characteristics are investigated. The main objectives of this study are as follows:

i. To synthesize $1D$ Ga_2O_3 nanostructures using the microwave-assisted hydrothermal method followed by heat-treatment and investigate their polymorph transformation temperatures.
ii. To prepare different polymorphs of $1D$ Ga_2O_3 and test their gas sensing capabilities.
iii. To prepare different $1D$-based Ga_2O_3 morphologies of the best performing polymorphs from (ii) and study their gas sensing performances.
iv. Modify the surface of the best $1D$ morphology Ga_2O_3-based sensor from (iii) with Ag and Au, set at different concentrations and study their gas sensing behaviors.

Characterization of all synthesized materials was conducted by thermogravimetric analysis (TGA), X-ray diffraction (XRD), Raman analysis, scanning electron microscope (SEM), transmission electron microscope (TEM), Brunauer-Emmett-Teller (BET), photoluminescence (PL), diffuse reflectance spectroscopy (DRS), and X-ray photoelectron spectroscopy (XPS).

1.4 Thesis chapter outline

Chapter 1 gives a synopsis of this study. **Chapter 2** details the literature survey on the progress made on SMO-based gas sensors, with particular attention given to Ga_2O_3-based gas sensors.

Chapter 3 discusses the sample preparation and characterization methods used in this study. **Chapter 4** discusses the phase transformation properties of the different polymorphs of $1D\ Ga_2O_3$. **Chapter 5** reports the impacts of polymorphism on the gas sensing performances of $1D\ Ga_2O_3$. **Chapter 6** reports the influences of $1D$-based morphologies on the gas detection capabilities of $\beta - Ga_2O_3$. **Chapter 7** details the effect of modifying $\beta - Ga_2O_3$ with Ag and Au nanocrystals on the gas sensing behavior of the material while **Chapter 8** summarizes the conclusions of this study and outlines the future work.

CHAPTER 2

Literature review

2.1 Introduction

Sensors have significantly improved the everyday life of human beings through their applications in many fields such as industrial production, air quality monitoring, medical devices [5]. A sensor is a device that detects and responds to a change in its input from a specific physical environment such as chemical/gas, heat, light, moisture, motion, and pressure environment/source signal and converts the physical phenomena into a measurable digital signal which can be read and processed [5]. Various specialists and researchers classify sensors in different ways. One of the common classifications is based on the kind of source signals including temperature, motion, pressure, and gas sensors [5,57].

2.2 Gas sensors in general

Gas sensors are devices that detect and undergo physical and chemical changes on their surface due to the adsorption of a chemical stimulant. The chemically adsorbed species change the electrical properties of a gas sensor and consequently convert it into a measurable and readable signal output [58]. The produced output signal can either be electrical or non-electrical, and these form a means of classifying gas sensors as electrical and non-electrical sensors [59]. Electrical sensors are electronic devices that detect variations in electrical resistance, conductance, and current upon interaction with target gas molecules. Examples of electrical sensors include electrochemical and chemiresistive gas sensors [59]. The non-electrical sensors present measurable signal outputs such as optical, calorimetric, and acoustic when exposed to target

gases [58]. Among several electrical sensors, electrochemical gas sensors present variations in current and voltage and are known for their high sensitivities. However, they are losing attention due to their limited operation temperature ranges and short lifetimes [17]. In contrast, the chemiresistive type of gas sensors show direct variation in electrical resistances as a result of interacting with the gas molecules. This type of gas sensor has drawn a lot of attention owing to its wide operating temperature range, high stability, a simple circuit which enables miniaturization of the sensor device and low-cost production [53]. In addition, chemiresistive gas sensors are environmentally friendly because they do not produce waste during their operation [17]. Researchers around the world are still trying to explore novel chemiresistive gas sensors with improved sensing performances. For this reason, chemiresistive gas sensors are well known for playing a significant role in terms of monitoring and sensing of harmful gases and VOCs.

2.3 SMO based gas sensors

SMO gas sensors consist of a sensing element with planar arrangement with an active sensitive layer deposited over a substrate containing electrodes for the measurement of electrical properties. The active sensing layer is normally heated by a heater located at the back of the substrate. In addition, SMO based gas sensors also known as chemiresistive gas sensors continue to receive tremendous attention due to direct variation in electrical resistance in response to changes of nearby atmospheric environment. This novel finding on SMO-based gas sensor was first reported by Brattain and Bardeen in 1953 from a germanium material [60]. Then, a further step was taken in early 1960s when Seiyama *et al.* [61] and Taguchi [62] reported the gas detection capabilities of ZnO and SnO_2, respectively. A study by Taguchi led to the first commercialized SnO_2-based sensor [62]. Since that year (i.e., 1962), there has been a growing

interest in exploration of different SMO materials as active sensing layers. Hence, various materials for use as active sensing layers to produce chemiresistive gas sensors were explored including carbon nanotubes [12], conducting polymers [11] and SMOs [63]. Most importantly, part of the research work has been focused on understanding the role of SMO materials to achieve improved gas sensor properties [15,64]. Studies conducted on gas sensing capabilities of SMOs have demonstrated that the gas sensing performance of SMOs for detection of various gases strongly depend on the semi-conductivity nature of the SMO and as well as the type of the target gas that is being detected. In fact, a wide range of SMOs utilized as active sensing layers in the field of gas sensing are characterized as either *n*-type where electrons as the majority charge carriers, and *p*-type with holes being the majority charge carriers. Up to date, the *n*-type SMOs are the most studied materials for gas sensing application due to their higher response towards both oxidizing and reducing gases than *p*-type SMOs. Besides the pioneer SMO gas sensing materials (i.e., SnO_2 and ZnO [53]), other *n*-type SMOs that have been previously investigated for gas sensing applications include TiO_2 [20], WO_3 [21], In_2O_3 [65], Fe_2O_3 [66], and Ga_2O_3 [23]. In the case of *p*-type SMOs, materials like CuO, NiO, and $LaFeO_3$ perovskite material have been extensively studied for gas sensing applications [67]. Among these SMOs, the focus in this study is on Ga_2O_3 as it presents high conductivity, ultrawide band gap, high chemical and thermal stability, which makes it a good material for detecting different gases [42].

2.3.1 Operating gas sensing phenomenon of SMO gas sensors

The gas sensing processes by both *n*- and *p*-type SMO sensing layers involve a reaction between the surface of an active sensing material, the gas molecules and the preadsorbed oxygen, and the conversion of this chemical reaction into a readable electrical signal output. However, the way

these two types of SMOs respond upon interacting with oxidizing or reducing gases is different [68]. When the *n*-type SMO gas sensing materials are exposed to ambient air, molecular oxygen is ionosorbed to form O_2^-, O^-, and O^{2-} reactive species on the surface of the SMO operating at temperatures T < 100 ℃, 100 ℃ ≤ T < 300 ℃, and ≥ 300 ℃, respectively [18]. The molecular oxygen trap electrons from the surfaces of the SMO causing formation of a thick electron depleted layer on the surface of the SMO sensing material as shown in Fig. 2.1(a). This increases the electrical resistance of the SMO. Regarding a *p*-type SMO, the capturing of electrons from the sensing material creates a hole accumulation layer near its surface as depicted in Fig. 2.1(d) thus leading to higher resistance. Furthermore, when the *n*-type SMO sensing material interacts

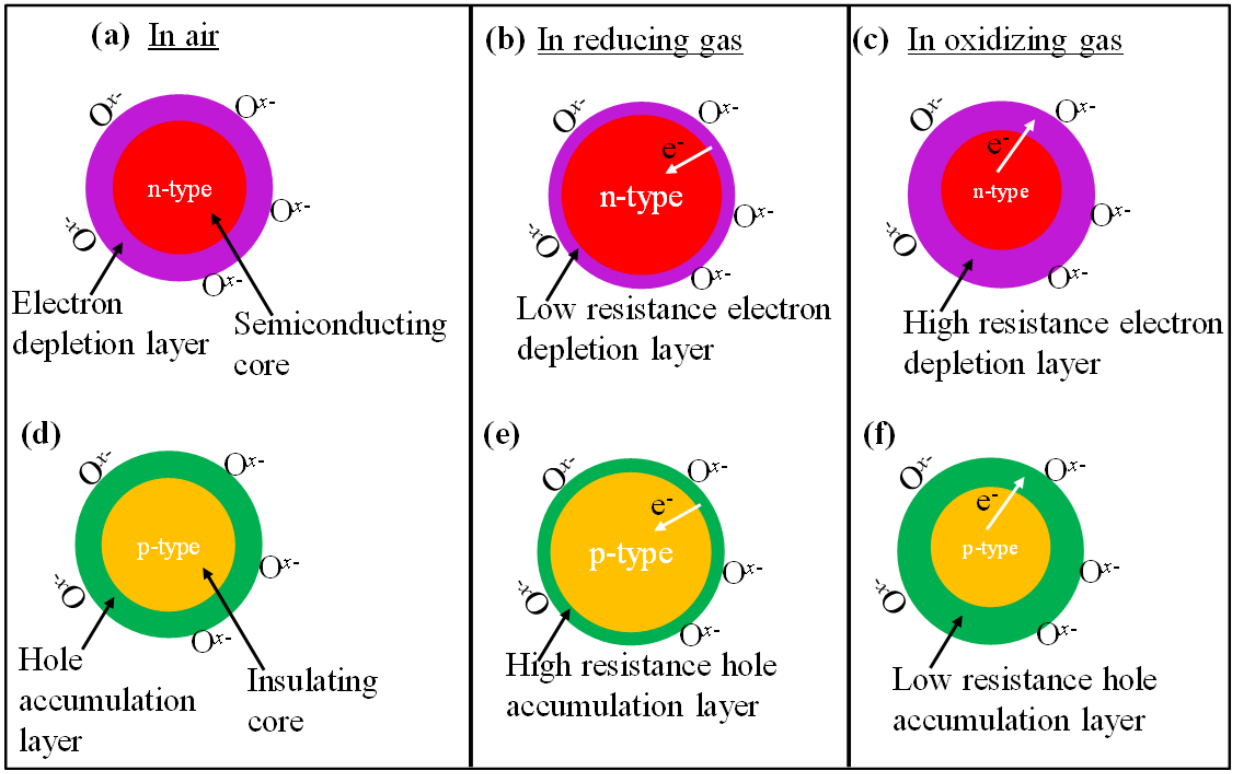


Fig. 2.1. *Sensing mechanism of n- and p-type semiconductor metal oxides in (a, d) air, (b, e) reducing gas and (c, f) oxidizing gas. O^{x-} represents the charged oxygen species (O_2^-, O^-, and O^{2-}) and x is 1 or 2.*

with reducing gases such as carbon monoxide (CO), ethylene (C_2H_4), or ammonia (NH_3), charged oxygen species oxidize the reducing gas and electrons are de-trapped back to the sensing material. This causes narrowing of the depletion layer as shown in Fig. 2.1(b) and hence a reduction in the resistance [15]. However, when the *n*-type SMO sensing layer encounters oxidizing gases like nitrogen dioxide (NO_2) and sulphur dioxide (SO_2), the gas molecules get reduced, and more electrons are captured from the conduction band of the active sensing material. Consequently, the depletion layer widens (Fig. 2.1(c)) and the resistance of the *n*-type SMO sensing layer increases. In contrast, the interaction of a *p*-type SMO material with a reducing gas de-traps electrons back to the sensing material resulting to higher resistance (Fig. 2.1(e)) [69]. Regarding oxidizing gases, the resistance of the *p*-type SMO sensing layer decreases as holes are increased in the hole accumulation layer as shown in Fig. 2.1(f).

2.4 Gas sensor characteristics

In literature, the merits of SMO based gas sensors in certain environments and conditions are evaluated by their: (i) operating temperature, (ii) response, (iii) response/recovery times, (iv) selectivity, (v) limit of detection, (vi) sensitivity, and (vii) stability [14,18].

2.4.1 Gas sensor operating temperature

It is well-known that the operating temperature is a significant parameter in determining the optimal sensing characteristics of a SMO sensor [18]. Often time, most SMOs require exposure to high operating temperatures to achieve enhanced gas sensor performance. Although high operating temperatures allow for desirable fast gas response/recovery times, it has been one of the researchers' aims over a couple of years to design gas sensors that can operate at room

temperature to reduce the gas sensor's power consumption and explosion hazards, improve simplicity in gas sensor-device configurations, eliminate drifts in gas sensor's response, and prolong the lifetime of the sensor [14].

2.4.2 Gas sensor response

Gas sensor response refers to a relative change in a sensing signal upon interaction between the SMO sensing material surface and target gas molecules. Considering the chemi-resistive nature of these sensing materials, the output sensor signal is electrical resistance. Mathematically, the response is calculated as $R = \Delta R/R_g$ upon exposure to a reducing gas and $R = \Delta R/R_a$ for an oxidizing gas, where R_a and R_g represent the resistance of the sensor exposed to air and target gas molecules, respectively, and $\Delta R = (R_a - R_g)$. Alternatively, a gas sensor response can be calculated using the following equations: R_a/R_g upon exposure to a reducing gas and R_g/R_a for an oxidizing gas as well as $R(\%) = (\Delta R/R_g) \times 100\%$ for a reducing gas and $R(\%) = (\Delta R/R_a) \times 100\%$ for an oxidizing gas [16].

2.4.3 Gas sensor response and recovery times

Gas sensor response and recovery times are regarded as the time taken by a gas sensor to reach 90% of its total resistance change when exposed to target gas molecules and ambient air, respectively. An efficient gas sensor is expected to display a rapid response time when detecting target gas molecules which is very important for real-time monitoring in ambient and humid environmental conditions. On the other hand, rapid recovery times enables instant reusability of the sensor [18].

2.4.4 Gas sensor selectivity

Gas sensor selectivity defines the capability of a sensor to respond to only a specific target gas in the presence of other gases. A gas sensor with poor selectivity shows a change in resistance when exposed to target gases of similar properties (i.e., reducing, or oxidizing gases) or any target gas. Experimentally, the gas sensor selectivity is estimated by comparing responses obtained for the same gas sensor exposed to different target gases under similar conditions. SMOs sensing materials usually show poor selectivity since they respond similarly to different target gases with common properties. Thus far, different methods have been proposed and investigated to improve the selectivity of SMO sensing materials including morphology optimization, sensitization by noble metals and by the formation of metal oxide-based heterojunctions [14].

2.4.5 Gas sensor limit of detection (LoD)

Gas sensor LoD describes the lowest concentration of a target gas that the gas sensor can identify with acceptable noise. This value can be extrapolated from the intercept of a linear graph fitted to a log concentration (x-axis) versus log response (y-axis) plot using the linearized power law according to Equation (2.1) [70]. In this equation, R is the sensor response, constant b is the slope of the curve and is related to the sensitivity of the sensor. Constant a relates the y-intercept of the graph and to the LoD. On the other hand, the LoD can also be calculated by using Equation (2.2) as the concentration that a sensor can detect with a 3:1 signal-to-noise ratio. In Equation (2.2), the slope is extracted from the graph of response (y-axis) versus target gas concentration (x-axis). The peak-to-peak noise ($noise_{rms}$) is calculated by Equation (2.3) as the standard deviation in N data points positioned at x_i with average value $\bar{x}$. In this method,

constants a and b are dependent on the gas type detected as well as the sensor operating temperature [71].

$$\log R = b \log C + \log a \tag{2.1}$$

$$LoD = \frac{3\, noise_{rms}}{slope} \tag{2.2}$$

$$noise_{rms} = \sqrt{\sum_{i=0}^{N} \frac{(x_i - \bar{x})^2}{N}} \tag{2.3}$$

2.4.6 Gas sensor sensitivity

Gas sensor sensitivity defines the gas sensor response per unit concentration. The value of this parameter may be extracted from the gradient of a linear fit to the graph of log concentration against log response according to Equation (2.1). The higher the sensitivity value, the more efficient the gas sensor is [14,18].

2.4.7 Gas sensor stability

Gas sensor stability refers to the capability of a gas sensor to produce similar response values when operating under similar sensing test experimental conditions over time. This parameter is often time influenced by the type of sensing material, working temperature and humid environment [14].

2.5 Applications of SMO-based gas sensors

SMO-based gas sensors have many applications such as the detection of harmful gases in mines, environmental and home safety, and healthcare [4,72–74] due to their excellent sensitivity, high stability, rapid response/recovery times, and relatively low power consumption. For example, in

the mining industry, the presence of 10 ppm of H_2S poses a life threat to the mine personnel, hence its rapid detection is key. SMOs are utilized for the fabrication of portable mobile sensing devices that effectively detect this gas compared to the electrochemical sensors that were used in the past [4,75]. In addition, toxic gases such as CO, SO_2, NO_x, and NH_3 cause problems such as sick house syndrome, acid rain, and global warming [72,76]. SMO-based gas sensors help minimize these effects by rapidly detecting the toxic gases and triggers alarm systems when the concentrations of these gases are beyond the exposure limits. In terms of healthcare, SMO-based sensors are highly promising candidates for the rapid, real-time, non-destructive, and economical monitoring and analysis of biological samples. Fields of interest include in endoscopy, tomography, blood analysis, and ultrasonic processes. Particularly, the recognition of VOCs from breath samples making use of SMO sensing material have so far demonstrated capabilities to detect the presence of particular diseases such as heart disease, lung cancer, asthma, diabetes, and kidney failure [76]. For instance, the detection and quantification of ammonia and acetone from human breath can be used to evaluate kidney malfunction and diabetes, respectively [72]. Furthermore, over recent years, SMO-based gas sensors have been applied in food quality control. For example, the quantification of ethanol and propanol has been of importance in determining the quality and predict fermentation rates of wine products [77,78].

2.6 Fundamental properties of gallium oxide (Ga_2O_3)

In the late nineteenth century (1875), Lecoq de Boisbaudran discovered the gallium element and its compounds [79]. This resulted in groundbreaking research on Ga_2O_3 in terms of its properties and applications. Ga_2O_3 possesses several outstanding properties including polymorphisms, transparency in a wide range of wavelengths, vast content of defects, wide band

gap and high electron mobility hence it is considered a potential candidate for applications in gas sensing technology [33]. It is well known that as the material's crystal structure is changed or sizes of the materials are reduced from micro to nano range, some of the physical properties of the materials may change as well. For example, when the crystal structure of Ga_2O_3 changes from rhombohedral to monoclinic, the electrical conductivity of this material changes [33,34]. Also, when Ga_2O_3 materials are synthesized in the nano-range, they exhibit variation in their band gaps and emission properties relative to those of micro-sized materials [33]. It is therefore important to understand the fundamental properties of Ga_2O_3 materials intended for use in gas sensing applications to cater for any changes associated with structure, sizes, and structural defects.

2.6.1 Polymorphism and lattice parameters of Ga_2O_3

Ga_2O_3 is a wide-band gap semiconducting material which crystallizes into six different crystal structures or polymorphs namely $\alpha - Ga_2O_3$ (rhombohedral), $\beta - Ga_2O_3$ (monoclinic), $\gamma - Ga_2O_3$ (cubic), $\delta - Ga_2O_3$ (cubic), $\varepsilon - Ga_2O_3$ (orthorhombic) and $\kappa - Ga_2O_3$ (orthorhombic). The first five polymorphs were first identified by Roy *et al*. in 1952 through phase equilibrium analysis of the $Al_2O_3 - Ga_2O_3 - H_2O$ system [80], and $\kappa - Ga_2O_3$ was later discovered by Playford *et al*. [81]. The different structural properties of these phases are key in this study, hence the unit cells of all six structures are shown in Fig. 2.2. The corresponding lengths of sides *a*, *b*, and *c*, making each unit cell in Fig. 2.2 and their angular separations $\hat{\alpha}$, $\hat{\beta}$, and $\hat{\gamma}$ are shown in Table 2.1. The rhombohedral $\alpha - Ga_2O_3$ structure belongs to the R$\bar{3}$c space group and in the configuration shown in Fig. 2.2(a), the Ga ion is tetrahedrally bonded to oxygen ions and vice versa [82]. As presented in Fig. 2.2(b), the unit cell of monoclinic $\beta - Ga_2O_3$

possesses two non-equivalent Ga-sites and three non-equivalent O-sites as depicted in Fig. 2.2(b). One type of Ga ions ($Ga1$) forms a distorted tetrahedral coordination while the second type ($Ga2$) forms a distorted octahedral coordination [82]. The oxygen ions form a distorted cubic structure with two three-fold coordinated types ($O1$ and $O2$) and one fourfold coordinated type ($O3$). These co-ordinations cause different bonding environments in $\beta - Ga_2O_3$ [82]. The $\beta - Ga_2O_3$ belongs to the $C2/m$ space group. The cubic $\gamma - Ga_2O_3$ structure presented in Fig. 2.2(c) is a member of the $Fd\bar{3}m$ space group and consists of tetrahedrally and octahedrally coordinated Ga with a ratio of 1:2. Fig. 2.2(d) shows the orthorhombic $\varepsilon - Ga_2O_3$ structure

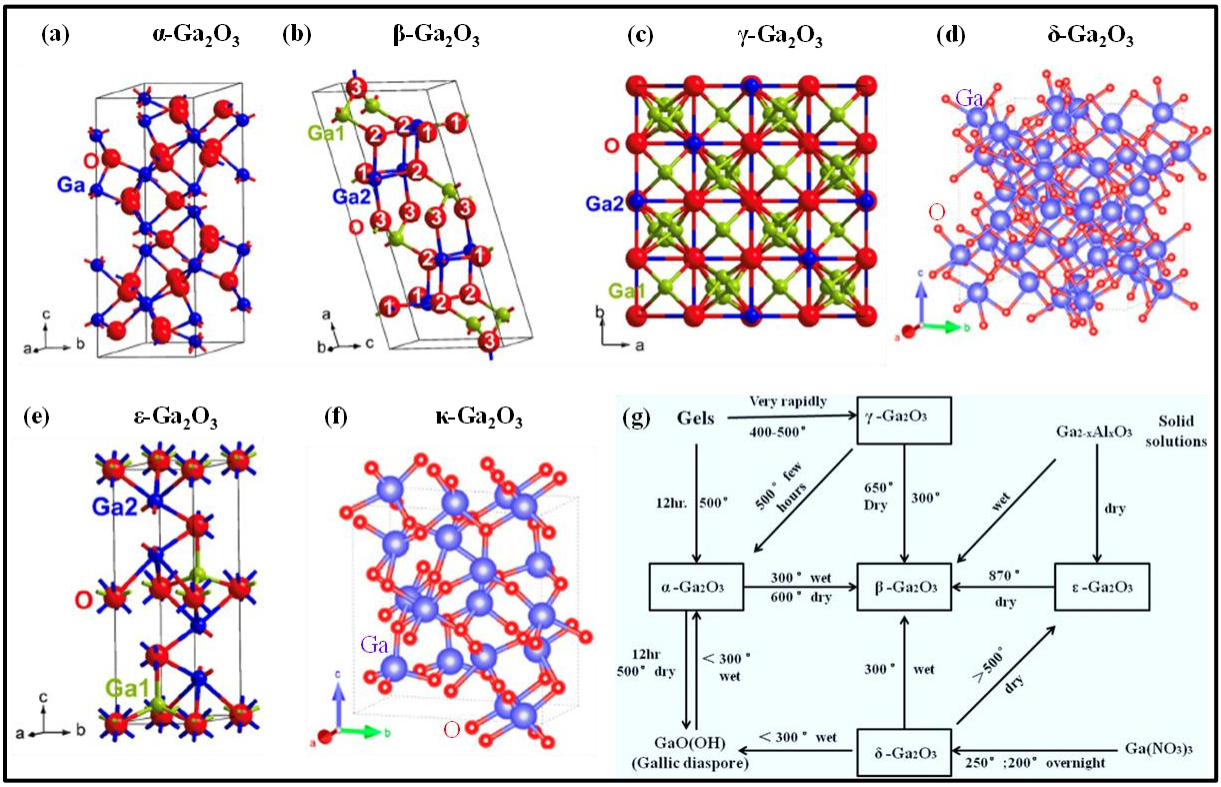


Fig. 2.2. *Schematic representation of (a-f) crystal structures of the six polymorphs of* Ga_2O_3 [23] *and (g) preparation temperatures of the different* Ga_2O_3 *phases* [33,81].

which belongs to the $P63mc$ space group. In its unit cell configuration, Ga ions occupy two positions ($Ga1$, $Ga2$). The $Ga1$-type ions are tetrahedrally bonded to oxygen ions while the $Ga2$-type bonds with six oxygen ions [83]. The κ and δ phases of Ga_2O_3 possess the Ga atoms which are octahedrally coordinated with oxygen atoms.

Table 2.1. *Crystal lattice properties of the six polymorphs of* Ga_2O_3 [83–85].

Structure	Lattice	Space group	Lattice Parameters			
			a (nm)	*b* (nm)	*c* (nm)	angle (°)
$\alpha - Ga_2O_3$	rhombohedral	$R\bar{3}c$	0.498-0.504	0.498-0.504	1.340-1.360	$\alpha = \beta = 90, \gamma = 120$
$\beta - Ga_2O_3$	monoclinic	$C2/m$	1.212-1.234	0.303-0.304	0.580-0.587	$\alpha = \beta = 90, \gamma = 103.8$
$\gamma - Ga_2O_3$	cubic	$Fd\bar{3}m$	0.824-0.830	0.824-0.830	0.824-0.830	$\alpha = \beta = \gamma = 90$
$\delta - Ga_2O_3$	cubic	$Ia3$	0.940-1.010	0.940-1.010	0.942-1.010	$\alpha = \beta = \gamma = 90$
$\varepsilon - Ga_2O_3$	orthorhombic	$P63mc$	0.506-0.512	0.869-0.879	0.926-0.940	$\alpha = \beta = 90, \gamma = 120$
$\kappa - Ga_2O_3$	orthorhombic	$Pna2_1$	0.505	0.869	0.927	$\alpha = \beta = \gamma = 90$

The different coordination of Ga and O ions along the *a*, *b*, and *c* directions of all crystal structures of Ga_2O_3 cause a lack of central symmetry in all structures. This anisotropy causes non-equivalent electrical and sensing properties along different crystal orientations of Ga_2O_3 [23]. The $\beta - Ga_2O_3$ phase is the most thermodynamically stable phase, and all the other phases

are metastable. The other phases transform to $\beta - Ga_2O_3$ at certain temperature and pressure conditions indicated in Fig. 2.2(g). Phase transformation temperatures of Ga_2O_3 are confirmed by thermogravimetric analysis [86].

2.6.2 Preparation of Ga_2O_3

As mentioned earlier, the crystal structure, sizes, and particle shapes of Ga_2O_3 materials directly influence the properties of the material. This implies that manipulation of the shape and size of the Ga_2O_3 materials during their synthesis provides a direct way of controlling resulting electrical, optical, and gas-sensing properties. Different growth preparation approaches including both physical and chemical routes or methods have been used to produce different forms of Ga_2O_3 materials [33,84,87,88]. Physical methods like magnetron sputtering, arc discharge, spray pyrolysis and chemical vapor deposition have been successfully used to prepare high-quality films and crystals of Ga_2O_3 [87,88]. However, the use of these physical deposition methods that have been used to prepare different polymorphs of Ga_2O_3 materials are limited by their high preparation temperatures. For instance, Ga_2O_3 materials produced at temperatures above 700 ℃ crystallize to monoclinic phase only. In addition, these physical deposition methods have high operation costs and produce low-yield and low-purity materials [89]. Based on this, researchers have resorted to exploring low-cost chemical methods to produce high purity Ga_2O_3 materials with different crystal structures. The most preferred chemical methods to achieve high purity Ga_2O_3 materials are sol-gel and hydrothermal synthesis methods. Both synthesis methods have been demonstrated to allow manipulation of the crystal phase, microstructure, shape, and size of the synthesized Ga_2O_3 materials [90,91].

The hydrothermal method is a liquid phase synthesis method widely used to prepare metal oxide powders. This method has developed over the years and now incorporates the use of other force fields to improve efficiency of the synthesis process. The most utilized force field are magnetic (autoclaves composed of non-ferroelectric materials) and microwave fields [90]. The microwave-assisted hydrothermal method generally applied the microwave temperature to compensate for the low reaction temperatures in a hydrothermal reaction. This enables synthesis with low power consumption. In this study, a microwave-aided hydrothermal synthesis approach has been used to produce Ga_2O_3 materials and a description of this process will be provided in Chapter 3.

2.6.3 Reaction involved during synthesis of Ga_2O_3 materials through hydrothermal approaches

The hydrothermal synthesis of Ga_2O_3 involves mixing an aqueous soluble salt with a solvent and reacting to the mixture formed under high pressure and temperature. Often, gallium nitrate hydrate ($Ga(NO_3)_3 \cdot xH_2O$) is used as a precursor while water is used as a solvent and ammonium hydroxide (NH_4OH) is used as a base. During the hydrothermal synthesis, the oxyhydroxide ($GaOOH$) precipitate is produced through reactions in Equations (2.4) to (2.8) when ($Ga(NO_3)_3 \cdot xH_2O$) and NH_4OH are used [92]. Tas *et al.* [92] proposed these reactions on the basis that $AlOOH$ and $GaOOH$ possess similar crystal structures hence they are produced via similar reactions. It is of importance to note that the morphology of the $GaOOH$ precursor depends crucially on the reaction pH, time, and temperature.

$$[Ga(H_2O)_6]^{3+}{}_{(aq)} + 2H_2O_{(l)} \rightarrow [Ga(OH)(H_2O)_6]^{2+}{}_{(aq)} + H_3O^+{}_{(aq)} \quad (2.4)$$

$$[Ga(OH)(H_2O)_6]^{2+}{}_{(aq)} + H_2O_{(l)} \rightarrow [Ga(OH)_2(H_2O)_4]^{+}{}_{(aq)} + H_3O^{+}{}_{(aq)} + H_2O_{(l)} \quad (2.5)$$

$$[Ga(OH)_2(H_2O)_4]^{+}{}_{(aq)} + H_2O_{(l)} \rightarrow Ga(OH)_{3\,(aq)} + H_3O^{+}{}_{(aq)} + 3H_2O_{(l)} \quad (2.6)$$

$$Ga(OH)_{3\,(aq)} \rightarrow GaOOH_{(aq)} + H_2O_{(l)} \quad (2.7)$$

$$2GaOOH_{(aq)} \xrightarrow{\Delta} Ga_2O_{3(s)} + H_2O_{(l)} \quad (2.8)$$

2.6.4 Factors leading to morphological evolution of Ga_2O_3

2.6.4.1 Effects of pH

Generally, when the pH of the reaction solution is maintained at low levels from 1 to 7, very few OH^- species in the solution will be adsorbed in the specific crystal planes of the amorphous $[Ga(OH)(H_2O)_6]^{2+}$ and $[Ga(OH)_2(H_2O)_4]^{+}$ particles formed by hydrolysis of Ga^{3+}. This results in the anisotropic growth of $GaOOH$ nanorod-like materials. The Ga atoms within each crystal structure possess different densities and this causes differences in energies of the crystal planes [33]. The energy of crystal planes from low to high is in the following order: {100} – thickness direction < {010} – width direction < {001} – length direction [93]. The effects of NH_4OH base solution addition on the growth rate of these crystal facets has been previously investigated by Dulda [93]. It was observed that a slow and dropwise addition of the NH_4OH base solution induced the adsorption of OH^- ions and growth along the {001} direction resulting in crystallization of $GaOOH$ nanorod-like morphologies. Furthermore, Pilliadugula and Krishna [36] demonstrated that when the pH condition is varied between alkaline and basic conditions, the excess OH^- species are absorbed on the primary crystal facets, and this hinders the

preferential growth thus favoring selective absorption of the OH^- ions. Under such conditions, the isotropic attachments and growth of $GaOOH$ crystals with low-aspect ratio and hierarchical structures occur. Their findings revealed that pH variation from 7 to 14 resulted in the formation of nanorod-like, cocoon-like, and hierarchical structures.

2.6.4.2 Effects of reaction aging time

Reaction aging time defines the time taken before loading the prepared precursor solution into a reactor for the actual hydrothermal process. This parameter controls the properties of the resulting product. In the case of hydrothermally synthesized Ga_2O_3 nanostructures, variation of the reaction time enabled control of the particle sizes, distribution, and crystallinity of the products. Thus, control of the reaction aging times can provide a method of optimizing the surface area and crystallinity for gas sensing applications. It was demonstrated by Bae *et al.* [94] that aging of the precursor solution for less than $<$ 1 hour was not sufficient to allow for the crystallization of Ga_2O_3 single morphology. Instead, they observed a mixture of nanoflower-like, nanoparticle-like and nanoplate-like morphologies of Ga_2O_3 from a solution aged for 10 minutes. However, upon increasing the reaction aging time to 1 hour, Ga_2O_3 spindle-like nanorods were formed from aggregation of face-to-face stacked anisotropic nanoplatelets. Further increase of reaction aging time to 1.5, 2, 3, and 6 hours resulted in morphological evolution from spindle-like nanorods to prism-like nanorods. On another note, unlike nanorod structures of Ga_2O_3 produced at shorter reaction aging times, the morphologies prepared at longer aging times possessed more defects. These advantageously improved the application of Ga_2O_3 in transistors. Shi and Qiao [95] revealed in their study that changing the reaction aging time from 1 hour to 3 and 10 hours resulted in a change of morphology from scattered particles

to nanorod-like and flower-like structures of Ga_2O_3. In addition, it was discovered that the sizes of the Ga_2O_3 nanorods increased significantly and the crystallinity of the synthesized Ga_2O_3 structures was improved. It was then concluded that these morphological variations caused significant changes on the luminescence properties of the synthesized Ga_2O_3 materials [95].

2.6.4.3 Effects of growth reaction temperature

The growth temperature of a hydrothermal process has a fundamental importance in modulating the chemical reaction because it may increase the number of collisions in the solution. The rate of the hydrothermal reaction will increase at higher growth reaction temperature. In the context of Ga_2O_3 materials, Reddy *et al.* [86] observed that varying the growth temperature from room temperature up to 95 ℃ controlled the shape and size of the synthesized Ga_2O_3 nanostructures. Growth at room temperature resulted in the crystallization of 100 nm cocoon-like nanostructures. The width of these cocoon-like nanostructures was found to be double upon increasing the growth reaction temperature to 50 ℃. However, increasing the growth reaction temperature to 95 ℃ formed nanorod-like structures with a width of approximately 1 μm. Their findings revealed that the growth reaction temperature has a significant impact on the Ostwald ripening process [86]. Ostwald ripening process is a well-known phenomenon which describes the dissolving of highly soluble small crystals and their redeposition on energetically favored larger crystals. The growth of larger crystals is caused by the dependence on the diffusion rate of the smaller crystals as they move to the surfaces of the larger crystals. Since the speed of diffusion is governed by the viscosity of the fluid and kinetics of the smaller crystals which directly depend on temperature, it can be concluded that the Ostwald ripening process depends on the growth reaction temperature. The growth reaction temperature influences the Ostwald

ripening process by directly influencing the interfacial energy, growth rate coefficients, and equilibrium solubility [96]. The use of microwaves in the microwave-assisted hydrothermal method is recommended for lowering the growth reaction temperatures. Microwaves are high energy beams that aid the reaction by supplying the energy to the reacting molecules [90].

2.6.4.4 Effects of thermal-treatment temperature

Thermal treatment (also referred to as heat-treatment, annealing or calcination) defines the use of heat energy on the synthesized products, post preparation. In the context of Ga_2O_3, heat treatment of Ga_2O_3 at different temperatures induces crystallization of different polymorphs of this material [97]. This approach has also been demonstrated to effectively control the crystal structure and crystallinity of hydrothermally synthesized nanomaterials. Pilliadugula and Krishnan [98] synthesized Ga_2O_3 nanorods by using the hydrothermal process followed by calcination at various temperatures ranging between 30 and 1000 ℃, and studied their gas sensing properties. Their study revealed that variation of the calcination temperature from 30 to 1000 ℃ resulted in the formation of $\alpha -$ and $\beta - Ga_2O_3$ polymorphs. Treatment temperatures of 700 ℃ and below led to crystallization of $\alpha - Ga_2O_3$ nanorods while temperatures of 900 and 1000 ℃ prepared $\beta - Ga_2O_3$ nanorods. Gas sensing measurements showed highest sensor response and fast response times towards 1000 ppm of CO_2 from $\beta - Ga_2O_3$. The best performance observed from this gas sensor was attributed to optimized structural, surface area, electrical and morphological properties induced by the heat-treatment temperature.

2.7 Ga_2O_3 as an active sensing material

The first application of Ga_2O_3 in gas sensing was reported in the early 1990s by Fleischer and Meixner [99] whereby $\beta-Ga_2O_3$ films were utilized to detect oxygen gas at 1100 ℃. Thereafter, different Ga_2O_3 polymorphs have been examined for detection of different gases [23,42]. Literature demonstrates that the $\beta-Ga_2O_3$ is the most studied phase of Ga_2O_3 as an active sensing layer owing to its stability at high sensor operating temperatures and the high electrical conductivity associated with the monoclinic crystal structure. This polymorph has shown capabilities of detecting various target gases such as CO [35,44,100–103], O_2 [38,99,104–106], CO_2 [98], NH_3 [36,107], H_2S [37], and VOCs [40,41] at operating temperatures ranging from room temperature to 1000 ℃. However, other polymorphs of Ga_2O_3 have also been studied recently as active sensing layers for the identification of various gases. Vorobyeva *et al*. [108], Almaev *et al.* [109,110] described CO, H_2, NO_2, NH_3, and O_2 gas sensing capabilities of $\alpha-Ga_2O_3$ and $\varepsilon(\kappa)-Ga_2O_3$ phases. The observed high gas sensor response of the $\varepsilon(\kappa)-Ga_2O_3$ polycrystalline films was assigned to high electrical conductivity of the material [109]. Furthermore, a blend of $\alpha-Ga_2O_3$ and $\varepsilon-Ga_2O_3$ prepared by Almaev *et al.* exhibited high sensitivity as well as a lower detection limit towards H_2 gas at 125 ℃ than the single phase $\beta-Ga_2O_3$-gas sensor operated at 200 ℃ [110]. This finding revealed that the mixture of Ga_2O_3 phases can be used to improve the sensitivity, lower the operating temperature, and lower the detection limit of Ga_2O_3 sensors [110]. In addition, the gas sensing capabilities of Ga_2O_3 materials were also studied through theoretical approaches. Zhao *et al.* [111] investigated the adsorptions capabilities of various gas molecules (i.e., O_2, CO_2, CO, SO_2, NO_2, H_2S, NH_3, and H_2O) on a two-dimensional Ga_2O_3 monolayer using first-principles calculations. Their results demonstrated that the Ga_2O_3 monolayer can be a promising candidate for the sensing of NO gas

molecules. Although the *n*-type Ga_2O_3 materials are the most utilized sensing layers, fewer studies reported the *p*-type sensing response from Ga_2O_3 materials. Wang *et al.* [39] reported a promising *p*-type response of 58.2% towards 100 $ppm\ NO_x$ from a *p*-type Ga_2O_3/Al_2O_3 composite. Over the past 30 years, the continuously growing interests in Ga_2O_3-based gas sensors have led to publication of on average, at least five research articles per year as summarized in Fig. 2.3; from both experimental [23,42] and theoretical perspectives [111].

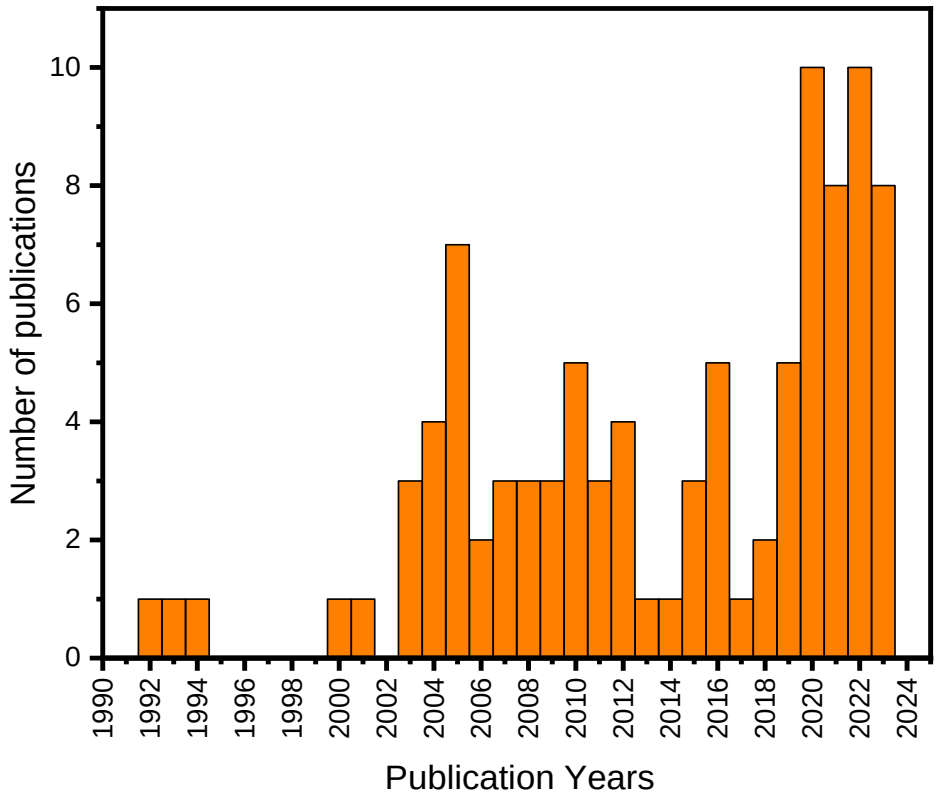


Fig. 2.3. *Number of research articles published between 1992 and 2023 on Ga_2O_3-based gas sensors. Data obtained from the Web of Science with search words "gallium oxide" OR "Ga_2O_3" and filter words "gas sensor".*

2.7.1 Adopted strategies for enhancement of Ga_2O_3 based gas sensor performance

According to literature, various forms of Ga_2O_3 materials have been produced and explored as active sensing layers for gas-sensing applications. Several studies demonstrated utilization of Ga_2O_3 as a sensing layer for sensing of various gases including O_2, NH_3, CO, H_2S, and NO_x [23,33,42] at various temperatures varying from room temperature to 1100 ℃. Despite all the research that has been conducted on Ga_2O_3-based gas sensors, their sensitivity, selectivity, stability as well as operating temperatures still need improvements for real-world applications in the gas sensing field. Therefore, several different strategies have been explored and investigated to date by researchers worldwide to improve the gas sensing capabilities of Ga_2O_3 materials. These strategies include manipulation of microstructure and morphology, structural defects control, surface decoration/modification through noble metal nanoparticle incorporation, and formation of heterostructures.

2.7.1.1 Surface decoration/modification of Ga_2O_3 through addition of noble metal nanoparticles

Evenly distributed or clustered noble metal nanoparticles on the surface of SMO-based sensing layer have been reported to effectively improve the interaction between the target gas molecules and surface of the SMO sensing material [28]. This is one of the adopted strategic methods that are being explored aiming at enhancing the gas sensor performances of SMO based gas sensors through electronic and chemical sensitization effects among other contributing factors [112,113]. In the case of Ga_2O_3, Pt, Au, and Pd are some of the noble metals that have been extensively studied for enhancement of its gas sensing capabilities. For instance, Fleischer *et al.* [114]

investigated H_2 detection capabilities of decorated Ga_2O_3 with Pt nanoparticles whereby the presence of Pt nanoparticles exhibited improved the response towards H_2 gas and reduced the response time. Bausewein *et al.* [115] likewise decorated Pd nanoparticles on the surface of Ga_2O_3 nanowires for CO detection. Their findings demonstrated shorter response times for Pd-decorated Ga_2O_3 nanowires as compared to undecorated ones. In another study, Schwebel *et al.* [116] reported on improved selectivity towards CO gas for Ga_2O_3 decorated with Au nanoparticles [105]. More recently, an inversion to the *p*-type conductivity caused by the loading of Au nanoparticles on the HVPE-prepared *n*-type $\beta - Ga_2O_3$ layer was reported [117]. The Au-modified $\beta - Ga_2O_3$ sensing layer presented high sensitivity towards 16 ppm dimethyl sulfide than to that of the unmodified $\beta - Ga_2O_3$ sensing layer. Furthermore, Kim *et al.* [35] observed enhanced response of 200 to CO at 100 ℃ from Pt surface modified $\beta - Ga_2O_3$ nanowires as compared to the unmodified $\beta - Ga_2O_3$ nanowires. However, the reaction kinetics between CO target gas molecules and the surface of $Pt - \beta - Ga_2O_3$ nanowires were slower than those of the unmodified $\beta - Ga_2O_3$ nanowires. Weng *et al.* [44] compared CO detection capabilities of the undecorated and Au-decorated Ga_2O_3 single nanowires and multiple networked Au-decorated $\beta - Ga_2O_3$ nanowires, and assigned the observed CO gas sensing performance by decorated nanowires to the compound effects from the spillover process, and improved chemisorption and dissociation of CO.

It can be concluded from the cited literature that surface modification of Ga_2O_3 materials through noble metal nanoparticles incorporation plays a significant role in improving gas sensor characteristics. There are two mechanisms that are regarded as main contributing factors towards gas sensor characteristic enhancement, namely, electronic, and chemical sensitization effects

[69,112]. The electronic sensitization mechanism proceeds as follows: when contact is formed between the noble metal and Ga_2O_3, their Fermi energy levels align [35]. Different work functions presented by the noble metal and Ga_2O_3 causes electrons to flow towards the material presenting a lower work function thus resulting in the energy band bending. Hence, a new level of Fermi energy is established [69]. A depletion region and the Schottky barrier are then created at the interface between the noble metal and Ga_2O_3 surface. Consequently, the concentration and mobility of carriers change prompting the modification of the baseline resistance of the sensing material and modulation of a gas sensor response. Furthermore, electronic sensitization by noble metals on the surface of Ga_2O_3 can also occur through the increase of adsorption sites, and rate of gas adsorption-surface interactions [28,118].

The chemical sensitization, also called the spill-over effect, is induced by the catalytic behavior of noble metals [28]. Noble metals are highly effective oxidation catalysts. For this reason, this effect derives from highly effective dissociation catalytic ability of the noble metals. In this case, a noble metal will act as a dissociation site for molecular oxygen while in the process oxygen molecules attach to SMO surface and then diffuse to the noble metal before the desorption process [18]. In addition, chemical sensitization effect can lower the sensor's activation energy as well as operating temperature [28].

2.7.1.2 Ga_2O_3 heterostructure formation

SMO heterostructures present a considerable potential in gas sensors due to their high sensitivity related to high surface-to volume ratio as well as the synergetic effects originating from Schottky junctions [27]. At the interface of two SMOs, Fermi level-dependent charge transfer and bend

bending occur, which often result in higher sensitivity towards gases [27,119,120]. Depending on the type of the participating SMOs, different kinds of heterojunctions can be formed, namely, *n-n* or *p-n* heterojunctions [69,119]. Many heterojunctions have been prepared to improve the gas sensing performance of Ga_2O_3 towards various gases [42]. Ga_2O_3 materials having various morphologies have been used to produce both *n-n* heterostructures with ZnO, SnO_2, WO_3, TiO_2, and *n-p*-type heterostructures with CuO and $LaFeO_3$ perovskite material [23,42]. Mohammadi and Fray [91] investigated gas sensing properties of *n-n* heterostructure based on Ga_2O_3 and TiO_2 thin films and this sensor presented improved responses towards CO and NO_2 gases compared to those presented by unmodified TiO_2. In a different study [41], a gas sensor based on *n-n* heterojunction of Ga_2O_3/SnO_2 core-shell nanowires revealed improved response towards ethanol vapour and was shown to lower the operating temperature from 400 ℃ obtained for the unmodified Ga_2O_3 gas sensor at 200 ℃. Abdullah *et al.* [121] examined the H_2 detection capabilities of a heterostructure based on SnO_2 and Ga_2O_3 and the results demonstrated that the formation of an *n-n* junction facilitated improvement of the sensor response, repeatability, and response/recovery times compared to the performances of the individual oxides. Multiple networked Ga_2O_3/ZnO core–shell nanorod sensors prepared by Jin *et. al*. [122] showed commendable response towards 100 ppm NO_2 at an operating temperature of 300 ℃. The measured response from this heterostructure was higher than that recorded for unmodified Ga_2O_3 and ZnO nanorods-based sensors [122]. Wei *et al.* [123] prepared an *n-n* heterojunction from Ga_2O_3 and WO_3 films and tested their ethylene detection capabilities. They demonstrated that the Ga_2O_3/WO_3 heterostructure operated at 275 ℃ presented 10-times and 4-times higher responses towards ethanol gas than the unmodified Ga_2O_3 and WO_3-film sensors. Moreover, the

heterostructure presented shorter response/recovery times towards ethanol than the unmodified Ga_2O_3 and WO_3 films. On the other hand, Lin *et al.* [100] also discovered that formation of a *p-n* heterojunction between Ga_2O_3 and *p*-type $LaSrFeO_3$ perovskites facilitated fast response times and increased the gas sensor response towards 100 $ppm\ CO$. The gas sensor response of $Ga_2O_3/LaSrFeO_3$ heterostructural nanorod arrays was nearly 10 times the response of Ga_2O_3 nanorods at an operating temperature of 500 ℃. Another *p-n* heterostructure based on Ga_2O_3 and CuO thin films presented 40% faster response times towards acetone than unmodified CuO sensor when operated at 300 ℃ [40].

The sensing mechanism of heterojunctions depends on the formation of the electron depletion layer or hole accumulation layer and the variation of potential height [27,29,119]. Because of the different compositions of the two materials forming a junction, the work functions of the two materials will be different causing the electrons to flow across the junction to balance the Fermi level of the two SMOs in contact [27]. In an *n-n* junction, an accumulation layer is formed and with respect to a *n-p* junction, a depletion layer is formed. Both scenarios lead to changes in the thickness of the depletion or accumulation layers and subsequent changes in the barrier height. Then, this leads to bend bending [29].

2.7.1.3 Modulation of Ga_2O_3 morphology and properties

The gas-sensing mechanism of SMO based gas sensors materials are governed by the interaction between the SMO surface and gas molecules. Therefore, control of properties such as morphology, crystallinity, porosity, and defects when synthesizing the SMO materials significantly influences the resulting gas-sensing performance of the SMO materials [63]. As an

example, depending on the structural nature of the grain boundaries, gas sensor transduction may proceed via grain boundary contact or through sintered necks [63,69]. The shape of the sensing material determines the crystallographic facets that are exposed on the surface of the crystal and the number of active sites available to participate in the target gas-SMO surface interactions [36]. Hence, the morphology parameter also contributes towards enhancement of response and selectivity of the SMO based gas sensors. In addition, the different morphologies vary the active sites available for interaction with the target gas molecules [36]. Furthermore, the even distribution of the nanorods in the hierarchical structure is important to avoid the formation of clusters which hinder the adsorption of gas molecules during the gas-sensing process. For example, the effect of post-deposition annealing conditions on the O_2 detection capabilities of Ga_2O_3 films was investigated by Ogita *et al*. [124]. Their results showed that annealing controlled the film roughness, the content of oxygen vacancies, and the grain sizes. Consequently, the response time was shortened at larger grain size, i.e., at higher annealing temperature. It is also important to mention that the oxygen vacancies are frozen in Ga_2O_3 crystals at low temperatures; however, their presence has been reported for the $\beta - Ga_2O_3$ lattice at high temperatures above 600 ℃ [125–127]. In addition, the density of oxygen vacancies in the lattice maintains a dynamic balance with the concentration of ambient oxygen. For this reason, the changes in oxygen vacancy concentration which is often induced during Ga_2O_3 materials synthesis results changes in the conductivity and gas sensing performances of Ga_2O_3 based-gas sensors [125].

CHAPTER 3

Materials synthesis and characterization

3.1 Introduction

This chapter describes the synthesis method used to prepare Ga_2O_3-based nanostructured materials and techniques used to characterize them. The samples were prepared by using the microwave-assisted hydrothermal synthesis method followed by calcination. The thermal stability, structural, morphology and surface (specific area and porosity) characterizations were conducted using Thermogravimetric analysis (TGA), X-ray diffraction (XRD), Raman spectroscopy, scanning electron microscope (SEM), transmission electron microscope (TEM) and Brunauer-Emmett-Teller analysis. Discussions on these characterization techniques are presented in sections 3.3.1, 3.3.2 and 3.3.3. The chemical composition of the samples was examined by X-ray photoelectron spectroscopy (XPS). Furthermore, the optical and luminescence behavior of the materials were studied by using diffuse reflectance spectroscopy (DRS) and photoluminescence (PL) spectroscopy. The XPS, DRS and PL characterization methods are discussed in sections 3.3.4 and 3.3.5. The gas sensing capabilities of Ga_2O_3-based materials were quantified by a sensing station which allowed for variation of sensor environments (temperature, humidity, and gas concentrations). Details of the gas sensing measurements are given in section 3.3.6.

3.2 Materials synthesis

Materials synthesis methods have always been crucial in the preparation of nanostructured multifunctional materials [7]. It has been a main goal of researchers to use economic,

environmentally friendly, and easy-to-follow synthesis methods that provide high quality materials with high yields. Out of the methods used so far, physical methods such as sputtering present a challenge of poor crystallinity and restricted control on morphology and grain sizes [128]. This limits the tunability of size dependent multifunctional properties of the synthesized materials. In contrast, chemical methods such as sol-gel and hydrothermal processes allow for variation of grain sizes and morphology through control of reagents type, reagents ratio and reaction parameters such as temperature, pH, and reaction time [95,129,130]. However, the chemical methods also present a disadvantage of high operation cost due to high energy consumption [84]. It is for this reason that researchers focus on shortening reaction times and lowering reactions temperatures. One synthesis method that has successfully reduced the reaction times is the hydrothermal method [90].

3.2.1 Hydrothermal synthesis method

In a case where a hydrothermal synthesis method is utilized to produce nanostructured materials, a special closed vessel is used to heat and pressurize an aqueous solution containing precursor material [90]. During the reaction, the high-pressure and high-pressure environment facilitates the dissolution and recrystallization of reactants, which are insoluble or poorly soluble under ambient conditions. A sequence of the hydrothermal synthesis process is depicted in Fig. 3.1(a). The process involves the mixture of reagents with a hydrothermal solvent, which often is water [90,129]. The reagents dissolve in water to form ionic or molecular components. Secondly, due to temperature gradients between different parts of the heated and pressurized solution in the hydrothermal vessel, ions and molecular components are separated and transported to the low-temperature region where seed crystal growth occurs. The ions and molecular groups adsorb on

the seed crystal surfaces in a preferred geometric configuration, followed by nucleation, growth, and crystallization of the materials [90,131].

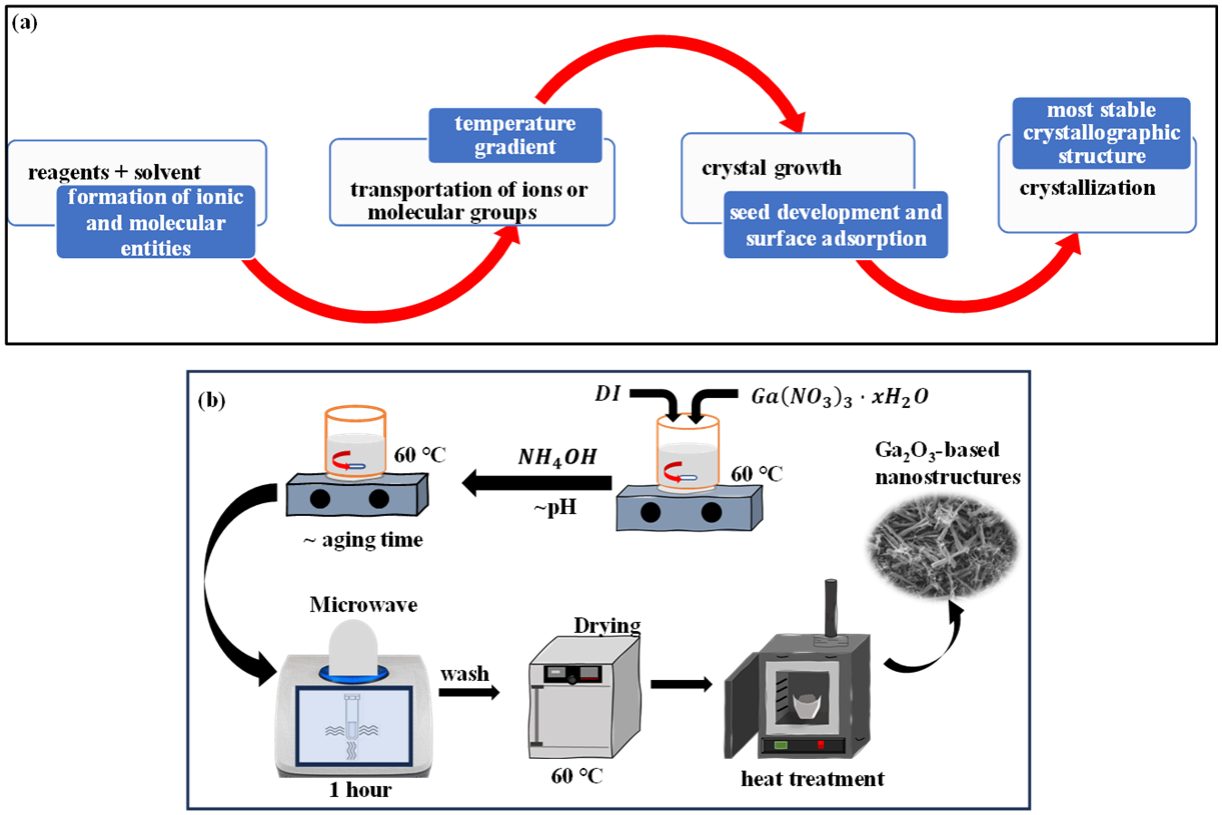


***Fig. 3.1**. Schematic representation of the (a) hydrothermal process and (b) set-up used to synthesize Ga_2O_3-based nanostructures using microwave-assisted hydrothermal method and calcination.*

3.2.2 Microwave-assisted hydrothermal method

High frequency microwaves (0.9 – 300 GHz) can be used to aid the conventional hydrothermal synthesis and in such cases the synthesis process is called "microwave-assisted hydrothermal method" [90]. In this case, microwaves irradiate the surface of the hydrothermal vessel and

penetrate the solution. Part of the radiation is absorbed by the water molecules because of their high dielectric loss factor; leading to high kinetic energy of the molecules. The continuously changing microwave field irradiating the sample facilitates the change in the initial chaotic motion of water molecules into a highly ordered trajectory. This dipole polarization and molecular collisions of the water molecules occurring in the process generate energy which is used for uniform water heating. This heating effect caused by the irradiated microwaves is the most notable difference between the conventional and microwave-assisted hydrothermal methods [90,129]. Due to the heat generated within the synthesis solution itself, the use of microwaves significantly enhances the kinetics of the hydrothermal process. Microwaves induce faster and homogenous heating of the solution resulting in shorter reaction time, making it an economical synthesis method. The microwave-assisted hydrothermal method presents other advantages over the conventional hydrothermal method. These include the ability to produce highly crystalline powders with controllable crystal size, morphology, and distribution (agglomeration).

3.2.2.1 Reagents

To produce Ga_2O_3 nanomaterials using the hydrothermal synthesis method, gallium nitrate is often used as a starting material. While ammonium hydroxide is mostly used in the reaction as a caping agent to achieve different Ga_2O_3 powder samples [33,36]. In this study, the following reagents were used to synthesize Ga_2O_3 nanostructures with different morphologies:

Gallium nitrate hydrate ($Ga(NO_3)_3 \cdot xH_2O$, 99.9%), ammonium hydroxide (NH_4OH, 28%), gold(III) chloride trihydrate ($HAuCl_4 \cdot 3H_2O$, ≥99.9%), and silver chloride ($AgCl$, 99.999%) were commercially acquired from Sigma Aldrich (South Africa) and were used without further purification. De-ionized (DI) water was used as a solvent.

3.2.2.2 Hydrothermal synthesis parameters

The functional properties of nanostructures depend on their crystallographic structure and morphology [129]. In the case of Ga_2O_3, the morphology and polymorphism influence gas sensing, catalytic and luminescence among other material properties [33,36,86,95,97]. Variation of the morphology is possible through control of physical and chemical conditions of the microwave-assisted hydrothermal process. These variable conditions include solution pH [36], reaction temperature [86,132], reaction time [95,130], aging time [94] and post-preparation calcination temperature [33,34,133].

A typical set-up used to synthesize Ga_2O_3-based nanostructures is shown in Fig. 3.1(b). In this study, different morphologies of $GaOOH$ nanostructures were obtained by varying the pH levels of the hydrothermal solution. The hydrothermal solution was prepared by mixing $Ga(NO_3)_3 \cdot xH_2O$ with de-ionized (DI) water. The pH of the solution was set between 7 and 14 by varying the amount of NH_4OH precipitator added to the solution. It is reported in the literature [36] that the variation of the pH level by NH_4OH controls the selective adsorption of mobile ions and molecular components on a preferential facet of the crystal seed. This results in preferential growth of morphology corresponding to different regulated solution pH conditions [36]. Basic conditions (pH >7) are recommended for synthesizing basic shapes as well as the hierarchical-structured ones because of increased chances of ion and molecular adsorption on all facets of the crystal seed [36,131].

Reaction temperature is another important parameter which is tuned to control the morphology of the hydrothermally synthesized final Ga_2O_3 powders. Reaction temperature controls the agglomeration of smaller structures to form different shapes and sizes by facilitating the Ostwald

ripening process [86]. In addition, the reaction temperature directly determines the type and quantity of defects present in the synthesized crystallized $GaOOH$ materials [132].

Besides the reaction temperature, the duration of the reaction plays an important role in controlling the morphology of the crystallized $GaOOH$ products. Variation of the reaction time is reported to cause agglomeration which results in the formation of nanostructures with clearly defined margins and hierarchical structures [95]. This effect could be associated with higher chances of collisions between components in the Ostwald ripening process (smaller and larger crystals) over a long reaction time thus leading to improved grain growth [130]. In addition to the reaction time, the presence of pre-precipitated products during a hydrothermal synthesis is pivotal in the development of the final product. Thus, aging of the hydrothermal solution before the commencement of the actual synthesis is a necessary step [94]. This is because the already available nanostructures become the growth seeds to which the newly forming mobile crystals deposit to. When the attachment is along the preferred growth facets, as a result, morphologically defined shapes are produced. It is also possible to have growth along all facets leading to crystallization of hierarchical structures [36]. The effect of this factor was investigated in this study by varying the aging time between one hour and three hours. Shorter reaction aging times ($<$ 1 hour) were omitted as they are inadequate for crystal development while excessively long aging times ($>$ 3 hours) were excluded from the study to avoid agglomeration of particles and reduction of specific surface areas, which is undesirable in gas sensing applications.

3.2.3 Post-preparation heat-treatment

As shown in Fig. 3.1(b), after the hydrothermal synthesis, precipitates were washed by centrifugation then dried at 60 ℃. The dried crystallized product of the hydrothermal synthesis

was orthorhombic gallium oxyhydroxide ($\alpha - GaOOH$). Therefore, post-preparation heat treatment was necessary to induce phase transformation to form different phases of Ga_2O_3. Calcination at temperatures in the range of 300 – 1000 ℃ in air caused thermal decomposition of $GaOOH$ into single phases of $\alpha - Ga_2O_3$ and $\beta - Ga_2O_3$ and a mixture of the two phases. The heat-treatment temperatures used were chosen based on those reported in the literature for hydrothermally synthesized $GaOOH$ [33]. The ramping rate was maintained at 5 $℃/min$ to allow for homogeneous heating and heat-treatment of the samples. While the dwell time of the heat-treatment process was optimized and set at 2 hours.

According to the literature, surface modification of SMO nanostructures by noble metals have demonstrated capabilities of enhancing gas sensing performances of SMOs. Similarly, the effects of incorporation of Ag and Au nanoparticles on the surface of Ga_2O_3 $1D$ nanostructures on their gas sensing capabilities were investigated. Modified samples were synthesized by following the same microwave-assisted hydrothermal method described for the unmodified samples, but the dopant precursors were mixed with DI and $Ga(NO_3)_3 \cdot xH_2O$. The Ag and Au modifier concentrations were varied between 0.5 and 1.0 $mol\%$. The masses of the modifier precursor used in each synthesis process were calculated by Equation (3.1).

$$Mass\ of\ AgCl\ = \frac{Mr\ (AgCl)}{Mr\ Ga(NO_3)_3.xH_2O} \times \frac{x}{100} \times mass\ of\ Ga(NO_3)_3 \cdot xH_2O\ used\ \times \frac{1}{n} \qquad (3.1)$$

where Mr is the molar mass, *x* is the desired molar percentage of the Ag modifier and n is the number of Ag atoms in the precursor compound. To determine the amount of Au precursor to be used in a reaction, the Mr of $AgCl$ is replaced by the Mr of $HAuCl_4 \cdot 3H_2O$ in Equation (3.1).

3.3 Characterization techniques

Several techniques were used to characterize the thermal stability, crystalline structure, purity, morphology, surface area, porosity, chemical states, and optical properties of the samples. The details of each technique used are discussed in the following sub-sections.

3.3.1 Thermogravimetric Analysis (TGA)

TGA is a method that is applied to evaluate material composition and purity, oxidative and thermal stability, decomposition rates and behavior of materials in reactive atmospheric conditions [134]. These properties are deduced from the weight loss and weight loss rate data recorded over time, a range of temperature and in different reactive sample environments. Fig. 3.2 presents a schematic representation of a TGA analyzer. The system comprises a highly sensitive precision balance with a sample pan attached to it and mounted inside a furnace. When the TGA measurements are conducted, a sample in the oven is exposed to simultaneous flow of air and nitrogen gas and the furnace is continuously heated at a constant rate to facilitate thermal transformations. The temperature in the furnace is monitored by using a thermocouple. The background atmosphere around the sample, in the furnace, can be varied from inert, ambient, reducing, oxidizing and vacuum environments. Similarly, background pressure around the sample can be adjusted from low to high pressure, vacuum, or controlled pressure. Since the mass of a sample changes upon heating, the recorded characteristic thermograph and derivative thermograph profiles can be used to determine the thermal stability, transformation phases, decomposition temperature and compositions of the sample. During the measurement, weight changes are measured by the sensitive balance. Often, weight gain is attributed to oxidation and weight loss is attributed to degradation [134]. In this work, a Perkin Elmer Pyris 1 TGA analyzer

was used. The $GaOOH$ powder sample was cleaned at 25 ℃ with nitrogen gas and then heated to 1000 ℃ at a ramping rate of 10 ℃$/min$.

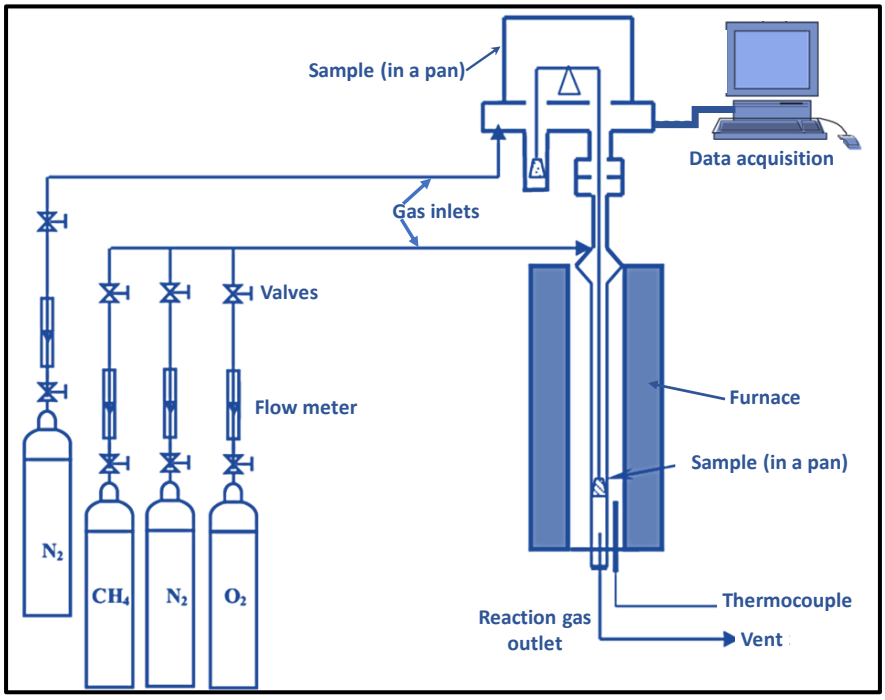


***Fig. 3.2**. Schematic depiction of a thermogravimetric analyser* [135].

3.3.2 X-ray diffraction (XRD)

The XRD technique is a non-destructive method used to study the structural properties such as phase purity and crystallinity of a material [136]. When the material is in a powder form, then the instrument of choice for the task is the powder diffractometer [137]. A powder diffractometer consists of an X-ray source, the sample stage and detector as represented by a schematic in Fig. 3.3(a) [136]. During measurement, powders are subjected to X-ray radiation characterized by a specific wavelength. A copper block is usually used as a source and in that case, source X-ray

wavelength of $Cu\ K\alpha_1$ equals 0.15406 nm. The X-ray beam is projected onto the top surface of the specimen at an incident angle θ, and the scattered beam is detected by a detector always set at 2θ angle from the original X-ray beam path, as presented in Fig. 3.3(a). The detector is motor driven in such a way that it maintains the angle 2θ between its path and the path of the projected X-rays.

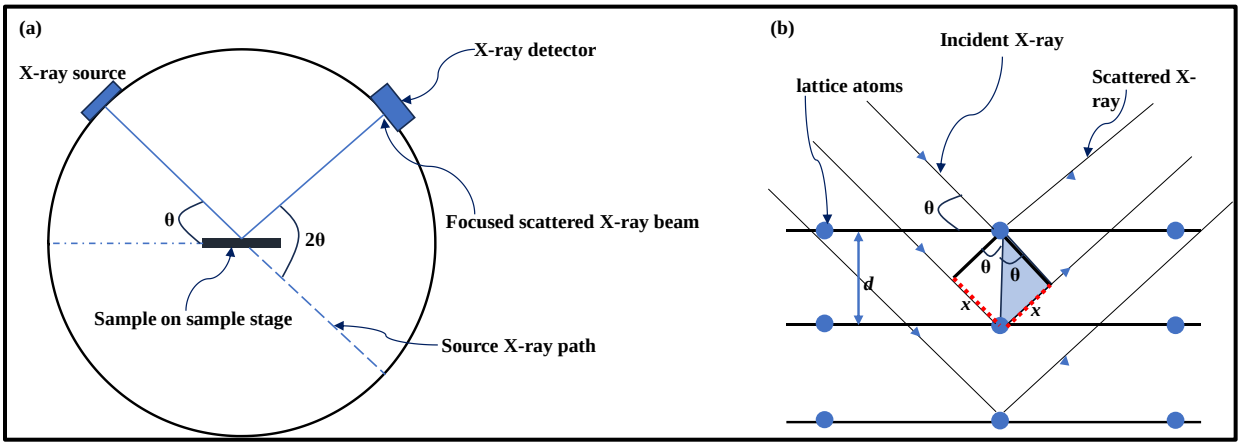


Fig. 3.3*. Schematic diagram of (a) powder X-ray diffractometer with a θ-2θ geometry and (b) X-ray diffraction by a crystalline powder.*

Fig. 3.3(b) illustrates how the X-ray radiation interacts with the powder sample and how the diffraction pattern is generated. This figure demonstrates that a crystal sample is made of regularly spaced atoms which are separated by the interplanar distance *d*. Upon the interaction of the radiation beam with the sample, each atom in the lattice acts as scattering surface for the incident radiation. Part of the radiation is scattered by the top layer of atoms and part of the radiation penetrates the sample. When the penetrated radiation reaches the next layer of atoms, the same partial scattering and penetration processes occur as illustrated in Fig. 3.3(b). The scattered beams are focused and detected by the detector. A path difference between beams

scattered by the topmost layer and the second layer is defined by $2x$ as depicted in Fig. 3.3(b). Using the shaded section in the same figure, the path difference can be determined by Equation (3.2).

$$2d\,sin\,\theta = 2x \tag{3.2}$$

The scattered beams are focused just before being detected and because of the phase relation in Equation (3.2), constructive and destructive interference occurs. In most cases, the interference is destructive and only a few scattering directions results in constructive interference which is recorded as peaks in the diffraction pattern. Constructive interference is observed when the path difference ($2d\,sin\,\theta$), also known as the phase shift, equals integer multiples of the radiation wavelength. This condition only occurs at particular angles and is known as the Bragg condition presented in Equation (3.3).

$$2d\,sin\,\theta = n\lambda \tag{3.3}$$

where d represents the inter-planar spacing, θ represents the Bragg angle, an integer n corresponds to the order of reflection, and λ is the source X-ray radiation wavelength which is of the same order of magnitude as d. The 2θ angle positions and corresponding intensities of the scattered X-rays are measured, and the observed variations are characteristic of the sample. Some of the useful information obtained from analyzing the diffraction patterns include crystallite sizes and micro strain of the sample. These parameters are related to the width of the diffraction peak. Moreover, the diffraction pattern can be used to determine lattice parameters of the crystal structure by performing Rietveld refinement.

In this study, a Bruker D2 Phaser powder X-ray diffractometer using $Cu\,K\alpha_1$ radiation with wavelength 0.15406 nm was used to perform structural characterization of the Ga_2O_3-based powders. Each XRD pattern was recorded with a 0.026 ° scanning step size and a dwell time of 0.01 s at each point. Prior to each measurement, each fine powder sample was gently loaded into a clean sample holder, filling the cavity (in the case of a non-zero background sample holder). Then, the sample was pressed into the cavity or onto the zero-background sample holder and smoothened by using a glass slide, to make a flat surface. Following this, the sample was loaded into the sample chamber for the measurements.

3.3.3 Raman Spectroscopy

Raman spectroscopy is a non-destructive but sensitive technique used to investigate the structural properties of materials through studying the inelastic scattering of monochromatic light (photons) by the phonons of the materials [138]. This characterization technique is based on the Raman effect which stipulates that the frequency of a minute fraction of the scattered radiation differs from the frequency of the monochromatic incident radiation [138]. The frequency of the Raman scattering (ν_s) is related to the vibrational frequency of the phonon of the material (ν_m) and the frequency of the incident photon (ν_0) through Equation (3.4) [138].

$$\nu_s = \nu_m \pm \nu_0 \tag{3.4}$$

In Raman analysis, ν_m is measured as a shift from ν_0. The $\nu_m + \nu_0$ component causes Stokes shift and the $\nu_m - \nu_0$ component causes the anti-Stokes shift in the Raman spectrum [138,139]. A typical schematic representation of a Raman spectrometer is presented in Fig. 3.4. In the set-up, the laser beam is passed through a series of filters and a mirror and directed to the sample.

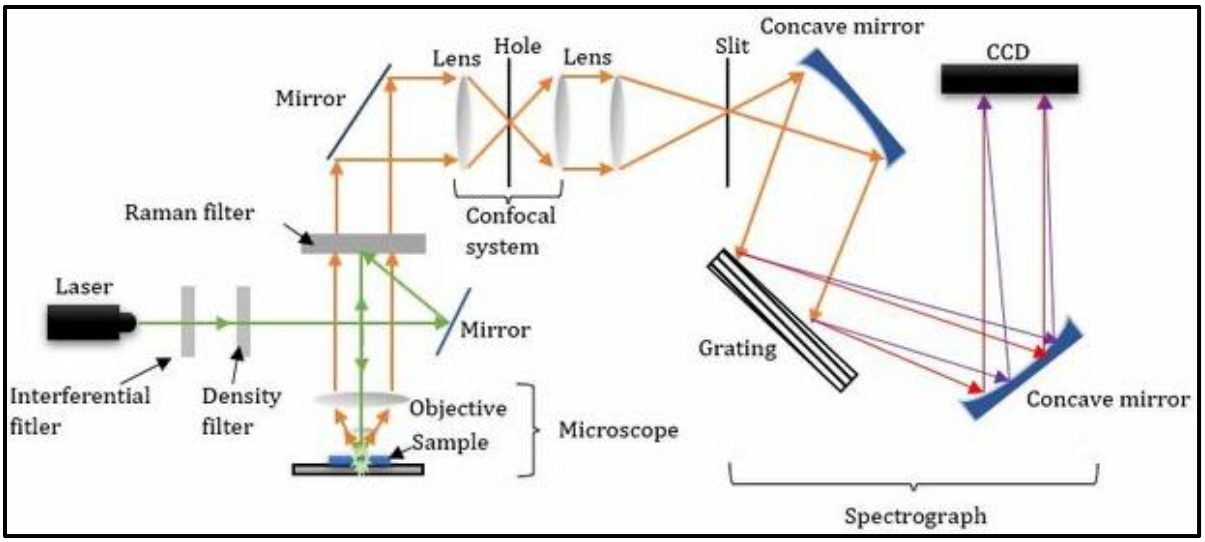


Fig. 3.4. *Schematic diagram of a Raman measurement system* [140].

The scattered beams are passed through an objective to a filter that suppresses the inelastic scattered beams and allows only the Raman signal through. The transmitted Raman light is channeled through a slit to a grating where the signal is dispersed. The dispersed rays are focused by a concave mirror and channeled to a cooled CCD detector. The scattered photons reaching the detector produce photoelectrons which are presented in the form of a spectrum. The spectrum is analyzed and displayed on a computer using Labsec software. The intensity of the spectrum is proportional to the number of photons of certain frequencies reaching the detector. In the Raman spectrum, the signal intensity is plotted against the Raman shift and the signatures observed in the spectrum are characteristic to the sample's composition and structure. For this study, a Horiba LabRAM HR Raman spectrometer with a 514.5 nm argon ion (Ar^{+}) laser source was used for complementary structural analyses. The laser power at the sample was set to $<1\ mW$. To prepare each powder sample for the measurement, a minute quantity of the powder was placed on a glass slide and then another glass slide was used to flatten the top surface of the powder. Following

this, the sample was carefully positioned under the objective, maintaining the same working distance (distance between the objective and the surface).

3.3.4 Scanning electron microscopy (SEM)

SEM is a technique used to characterize the morphology and topography of the surface of materials by raster-scanning them with a high-energy beam of electrons [141]. A typical SEM system is schematically depicted in Fig. 3.5(a). This system comprises two main components, the microscope column, and the control console [142]. The microscope column is made up of an electron gun, a couple of lenses and a detector. The electron gun generates electrons with a thick beam diameter (~10-100 nm) before they can be accelerated by the anode set at ~0.1-50 keV. The condenser lenses are used to de-magnify a large starting electron beam size from the gun into a small and well-focused spot of ~1-10 nm diameter. This focused beam is directed to the sample via an objective lens and interacts with the sample surface through elastic and inelastic processes.

Upon interaction with the sample surface, electrons have a finite depth range varying from 0.01 to 10 μm, based on their energy. Several phenomena occur in this interaction range and these phenomena include formation of secondary electrons and Auger electrons, back scattering of electrons as well as formation of X-rays as presented in Fig. 3.5(b) [141]. Signals generated from these phenomena are detected by different detectors and photomultipliers, and the information is related to the morphology or topography of the sample. The appearance of the recorded $3D$ images displayed on the computer screens, i.e., the magnification, texture, and contrast, depend on the system measurement conditions which are set by using the control console. For this study, a ZEIS-AURIGA field emission-SEM with a 3 kV acceleration voltage was used for morphology

characterization of the Ga_2O_3-based nanostructures. To prepare the samples for SEM measurements, minute fine powders were spread into a carbon tape mounted onto an aluminum holder. The sample was then spray coated with one layer of gold/palladium (Au/Pd) in order to reduce sample charging during SEM measurements.

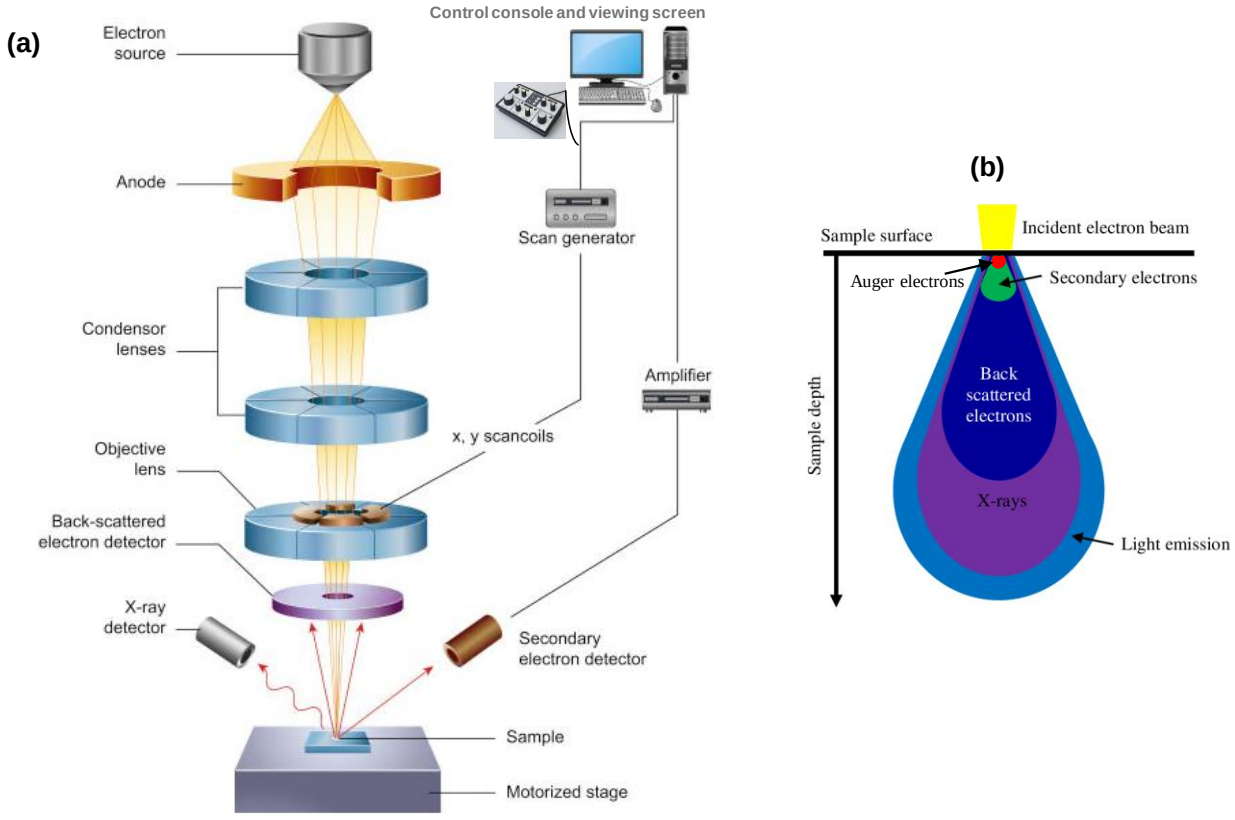


***Fig. 3.5**. Schematic representation of a scanning electron microscope and (b) sample-electron beam interaction* [142].

3.3.5 Transmission electron microscopy (TEM)

TEM is an imaging technique which uses transmitted electrons to create an image. In the process, the electron beam interacts with a thin sample ($<150\ nm$) through elastic and inelastic scattering processes and only electrons transmitted through the sample provide contrast in the

generated $2D$ images [143]. The TEM images are generated with unparalleled high spatial resolution, and they give valuable information on the sample such as the crystal structure, morphology, size, and defects [144]. A typical schematic representation of a transmission electron microscope is shown in Fig. 3.6 and the main components are an electron source, a couple of lenses which are used to control the beam size and trajectory, a sample stage, and a

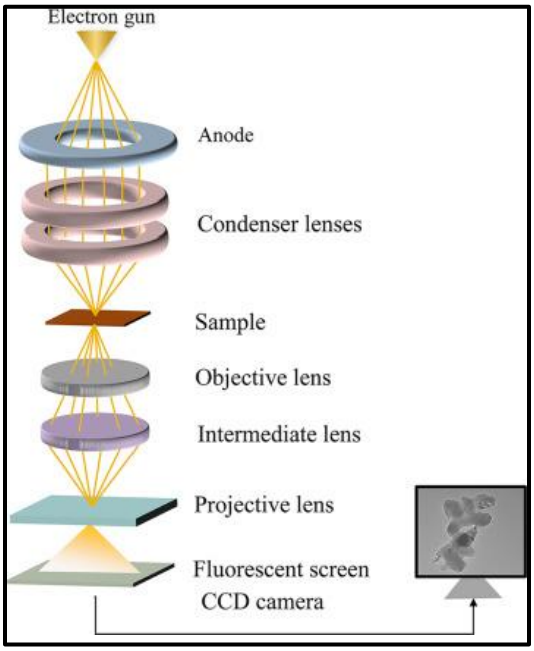


Fig. 3.6*. Schematic diagram of a transmission electron microscope* [143].

fluorescent screen. The images are displayed on the fluorescent screen and on a computer monitor via a charge-coupled device camera. A JOEL TEM-2100 high-resolution microscope with a 200 kV accelerating voltage was used in this study for characterization of sample crystallinity, morphologies, and distribution. To prepare the sample for TEM measurements, minute powder samples were homogeneously dispersed in ethanol through ultrasonication for 30 minutes. The process formed a suspension which was uniformed drop coated onto a copper (Cu) grid to form a thin film of the sample.

3.3.6 Brunauer-Emmet-Teller (BET)

BET is an analytical method applied to quantify specific surface areas and pore size distribution in porous solid materials. This technique is based on the BET theory which is an extension of the Langmuir theory from monolayer adsorption capabilities to multilayer adsorption capabilities [145]. The BET theory is formulated on the following assumptions: (i) gas molecules present an ideal behavior; (ii) molecule adsorption occurs in infinite layers and the BET theory is applicable to each layer, (iii) the adsorption site is homogeneous, and all surface sites present homogenous adsorption energies for the gas molecules, (iv) no molecule-molecule interactions, and (v) all gas molecules are immobile [145].

During the BET characterization, adsorption and desorption isotherms are obtained by measuring respectively, the amount of gas adsorbed and removed, as pressure is increased and decreased, respectively, at a constant temperature. A schematic representation of the BET analyzer is shown in Fig. 3.7. Typically, liquid nitrogen is used as an adsorbate hence the temperature is set at 77 K. Isotherms profiles range from Type I to Type VI. The specific surface area of the material (A_S) may be estimated by Equation (3.5) if the number of N_2 molecules in a densely packed adsorbed monolayer is known [146].

$$A_S = n_{mono} \times N_A \times A = \frac{V_{mono}}{M \cdot V_g} \times N_A \times A \tag{3.5}$$

where n_{mono} is the monolayer capacity (mol), V_{mono} is the monolayer volume (cm^3), M represents the sample mass, V_g represents the molar volume of an idea gas at STP (22 400 cm^3), N_A is the Avogadro constant ($6.023 \times 10^{23}/mol$), and A represents the effective cross-sectional area of adsorbate molecule (m^2). For this study, a Micrometrics TRISTAR 3000 analyzer was

used to analyze powder samples. Prior to every measurement, each powder sample was purified by degassing at 77 K in an inert nitrogen environment for a reasonably adequate period.

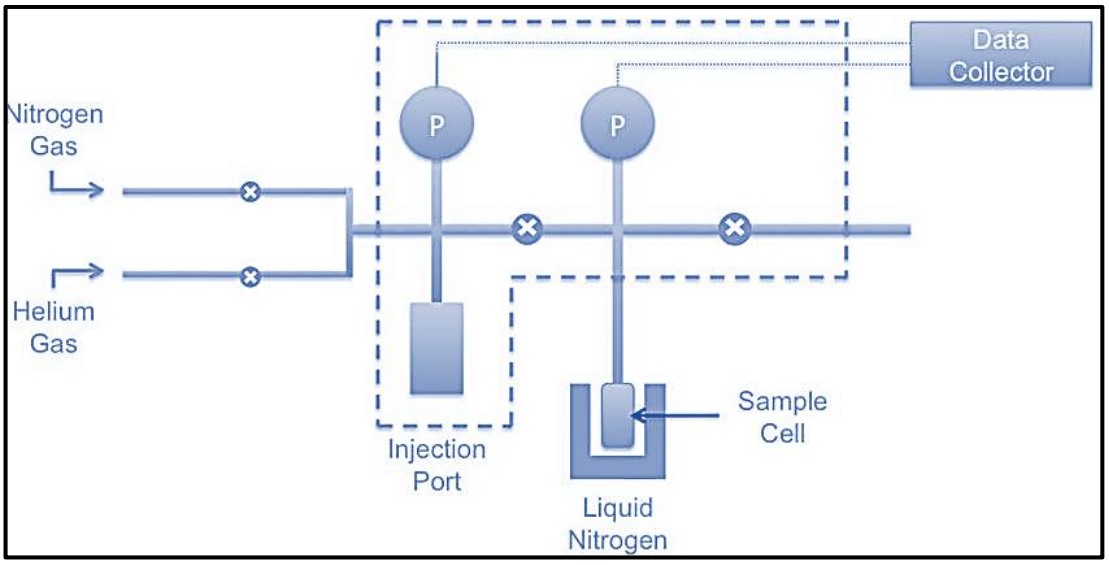


***Fig. 3.7**. Schematic representation of a Brunauer-Emmet-Teller surface analyser* [146].

3.3.7 X-ray Photoelectron Spectroscopy (XPS)

XPS is a non-invasive technique which has for long been used for the study of the material's surface science [147]. This technique depends on the photoelectric effect as illustrated in Fig. 3.8(a). In this process, a beam of X-rays, usually $Al\,K\alpha$ (1486.6 eV) or $Mg\,K\alpha$ (1253.6), interacts with the surface of a material causing excitation and ejection of core electrons of the material. The emitted electrons (photoelectrons) are dispersed into paths governed by their induced kinetic energies (E_K). These different paths are channeled through an energy analyzer then detected by a multi-channel detector and recorded as a photoelectron spectrum.

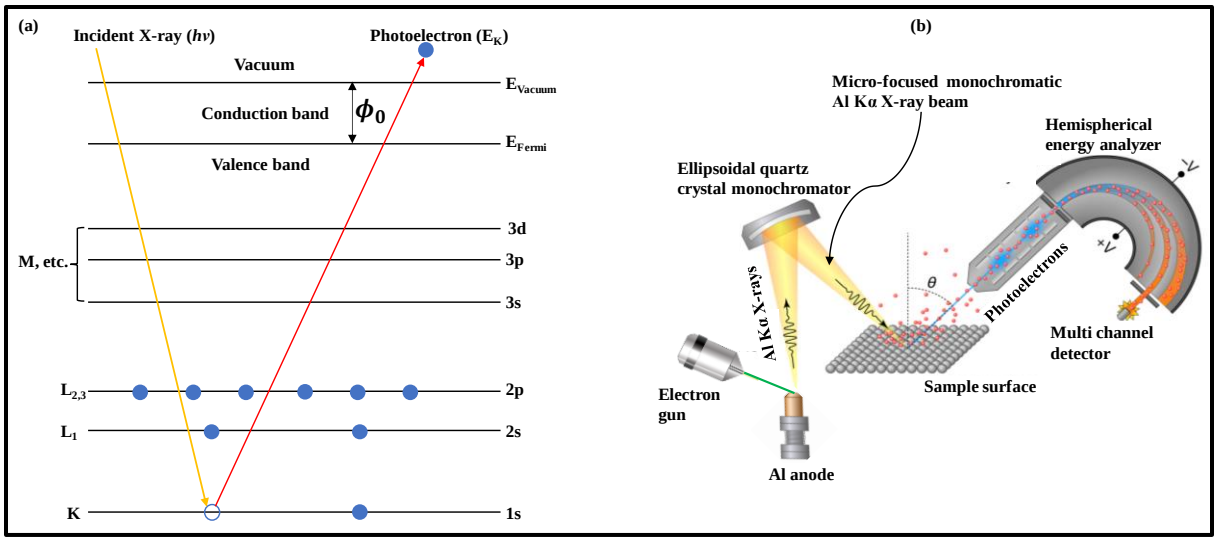


Fig. 3.8*. Schematic depiction of (a) the photoelectric effect and (b) X-ray Photoelectron Spectroscopy analysis system edited from reference* [148].

Using this principle of operation, the XPS instruments have contributed a great deal towards quantitative and qualitative analysis of surface chemical elements detected on the surface of the sample. The detection of peaks at specific energy positions in the photoemission spectrum indicates the presence of specific chemical species in the analyzed sample. This is because each chemical element gives rise to a characteristic set of peaks. Besides the identification of the elements, the peak position data also gives details on the oxidation state of the detected element [149]. This is possible because the XPS instrument is a sensitive instrument and can detect micro shifts in the peak positions. The intensity of the detected peaks produces useful information about the number of electrons with related energy. Thus, the peak intensity quantitatively translates to the concentration of the detected element in the sample.

In this work, powder samples were mounted on carbon tape and their XPS measurements were conducted under an ultrahigh vacuum chamber by using a PHI 5000 Scanning ESCA Microprobe

represented schematically in Fig. 3.8(b). X-rays are generated by the scanning of a focused electron beam (25 W, 15 kV) on an Al anode. An ellipsoidal quartz crystal monochromator is then focused and scanned the generated $Al\ K\alpha_{1,2}$ X-ray beam incident on the sample surface. The paths of photoelectrons are analyzed, and the corresponding electron kinetic energies are detected by a multi-channel detector. The $Al\ K\alpha_{1,2}$ X-ray beam ($h\nu$ = 1486.6 eV) with diameter of 100 μm for measurements in this work presented a linewidth of ~ 0.26 eV. This narrow linewidth enabled the measurement of high-energy resolution spectra characterized by high signal-to-background ratio. A low energy Ar^+ gun and low energy neutralizer gun were used to minimize surface charging of the sample. The binding energy calibration was performed by using the high energy peak of $Cu\ 2p^3$ at 932.62 eV and the low energy peak of $Au\ 4f^7$ at 83.96 eV. The retard linearity is such that the difference between these two peaks is always 848.66 eV. The analyzer resolution of ≤0.5 eV was used to record high-resolution binding energy (BE) spectra. The work function of the spectrometer was set at 3.7 eV in order for the $Ag3d^5$ peak to be at 368.27 eV. The MultiPack version 9 software was utilized to analyse the XPS spectra to identify the chemical compounds and their electronic states using Gaussian–Lorentz fits with Shirley background. Usually, in XPS analysis, a spectrum with binding energies plotted against intensities is used. The BEs are related to kinetic energies through Equation (3.6).

$$BE = h\nu - E_K - \phi_0 \tag{3.6}$$

where $h\nu$ is the photon energy, E_K is the kinetic energy of the photoelectron and ϕ_0 is the work function of the spectrometer.

3.3.8 Diffuse reflectance spectroscopy (DRS)

DRS is a non-invasive technique that can be used to approximate the band gap energies of semiconducting materials. This technique is based on the Schuster-Kubelka-Munk theory [150] which assumes that: (i) light which is incident on the sample undergoes diffusion, (ii) there is no regular reflection of light, (iii) particles forming the sample are randomly distributed, and (iv) the particle sizes are small compared to the sample thickness. Under these conditions, the absorption coefficient (κ) and scattering coefficient (*s*) are key in describing the reflectance of the sample through Equation (3.7) [150] given below.

$$F\ (R)_\infty = \frac{(1-R_\infty)^2}{2R_\infty} = \frac{\kappa}{s} \tag{3.7}$$

where $F\ (R)_\infty$ is a function varying with κ and $(R)_\infty$ is the absolute reflectance measured from the sample. To determine the band gap energy of a material, the measured reflectance data is converted to the Kubelka-Munk function (Equation (3.8)), which was derived from the Tauc function [151].

$$(h\nu\ F\ (R_\infty))^2 = A\ (h\nu - E_g) \tag{3.8}$$

where h represents Plank's constant, ν corresponds to the frequency of vibration, A represents the constant of proportion and E_g stands for the band gap energy value. The $(h\nu\ F\ (R_\infty))^2$ is plotted on the *y*-axis against $h\nu$ on the *x*-axis and a tangent drawn at the point of inflection of the curve gives the band gap energy of the material. The $h\nu$ value at the point of intersection of the tangent line and the horizontal line ($(h\nu\ F\ (R_\infty))^2 = 0$) is the band gap energy.

A schematic diagram of a spectrophotometer is shown in Fig. 3.9. The spectrophotometer consists of a light source, a monochromator, a sample stage, and a photodetector connected to a computer used to monitor the progress of data collection. In a typical DRS measurement, a beam of light is monochromatized and channeled to interact with the sample. A signal from the sample is then detected by a photodetector and converted to a spectrum recorded by a program and monitored on a PC monitor. In this study, a Varian Cary 500 UV-Vis spectrophotometer was used to analyze powder samples. Samples were loaded into a sample holder and the surface was levelled by a glass slide. Scans of each sample were recorded from the visible range to the ultra-violet range, at a scanning rate of 600 nm/min. For reference, a front silver-coated mirror was used as the sample, to get data for the 0% transmittance data. Recorded spectra from all samples were calibrated by the 0% transmittance spectra recorded with reference samples.

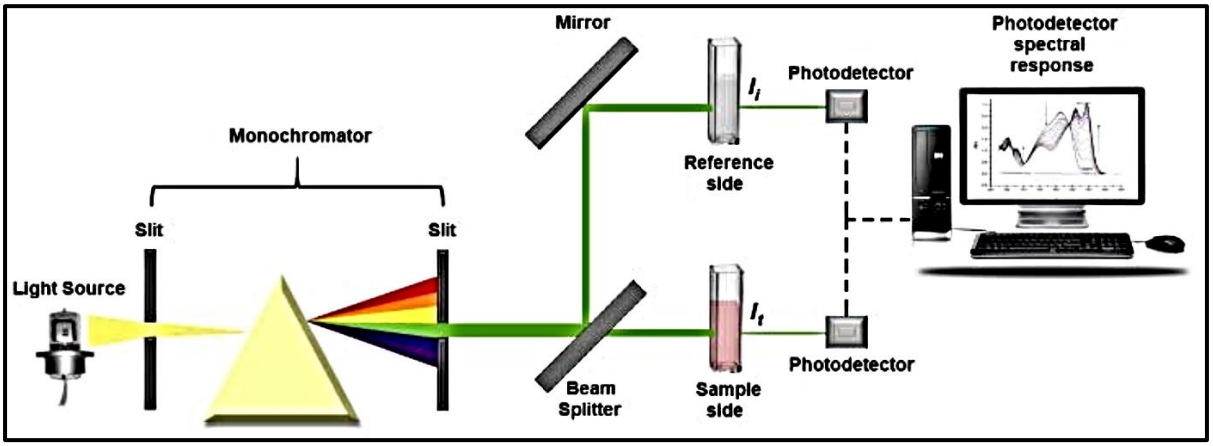


***Fig. 3.9**. A schematic representation of a dual-beam UV-Vis spectrophotometer* [152].

3.3.9 Photoluminescence (PL) spectroscopy

PL spectroscopy is an optical technique used in studying the luminescence behavior of photo-excited materials. Light, which is a beam of photons, is directed onto a sample and the electrons

within the material absorb the photon energy and are excited. Subsequently, the electrons emit energy radiatively or non-radiatively to move back to the ground state [153]. In the radiative emission, light is emitted, and the corresponding spectrum recorded is characteristic of the luminescent material. The spectrum of the emitted light can be measured and analyzed temporally, spectrally, or spatially [153]. Furthermore, the intensity and features of the spectrum have a direct link with the composition of the sample. During a PL experiment, excitation photoenergy is provided by a laser or a lamp. The excitation energy preferred is usually higher than the band gap energy for band edge emission or lower than the band gap energy if emission is through the defects positioned within the band gap of the material. Light from the source is channeled to a monochromator (excitation monochromator) which selects a specific excitation wavelength (energy) to be channeled to the sensor. The chromatized light interacts with the sample and the emitted beams are detected at a single wavelength, as guided by the emission monochromator, and processed into an emission spectrum [154]. Thus, to record an emission spectrum, the excitation monochromator is set to one wavelength and the emission monochromator is scanned. Likewise, to measure an excitation spectrum, the emission monochromator is set to one emission wavelength, preferably the sample's highest emission peak position, intensity, and the excitation source is scanned. A diagram of a PL setup is shown in Fig. 3.10 and major components of the setup are: the light source, monochromators, sample stage/holder, a couple of mirrors and lenses, and a detector. For this study, a Horiba QuantaMaster QM8000 spectrofluorometer was used with a Xe lamp light source.

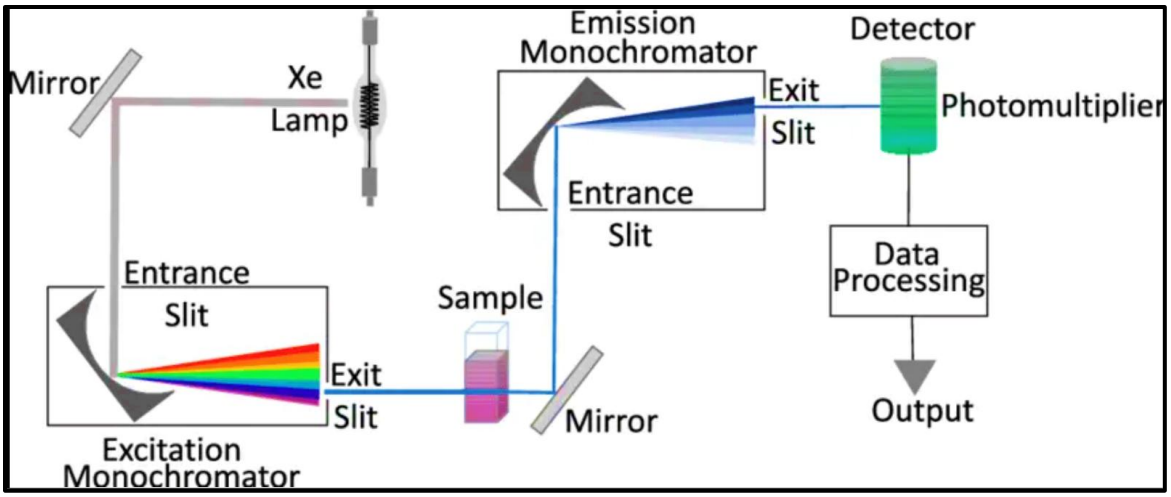


Fig. 3.10*. Schematic representation of a photoluminescence measurement set up* [154].

3.3.10 Gas sensor preparation and characterization

Ga_2O_3-based gas sensors were fabricated by drop coating the sensing material onto Pt electrodes which are interdigitated on alumina substates. Produced sensing films were annealed overnight in a furnace to improve bonding between the sensing material and the electrodes, before mounting them onto the sensor holder in a chamber.

The gas sensing capabilities of the samples were tested using a commercial KENOSISTEC UHV gas sensing station. A schematic diagram of this sensing station is depicted in Fig. 3.11. The main components of this station were: inlets for dry air and test gases, mass flow controllers (MFCs), thermostatic baths, a gas mixer, a sensing chamber, and sensor holder. MFCs controlled the amount of gas supplied to the sensing chamber through the inlets gas lines. The thermostatic baths channeled wet air to a gas mixer which generated humid environments. The sensor holder contained sensor ports each with four probe points, two of which were for the heater electrodes

and the other two for the sensing electrodes. Sensors mounted on the holder were heated by the voltage supplied to the heater electrodes (Fig. 3.11). To drive a current through the sensor a voltage was supplied and the currents flowing through the materials under different gas environments were measured by a KEITHLEY picoammeter. Sensor resistances in air (R_a) and in target gas (R_g) were calculated from the voltage-current data. Sensor responses were calculated using the resistance changes between R_a and R_g. Sensor operating temperatures were varied by controlling the voltage supplied to the heater electrodes printed on the bottom side of the alumina substrate.

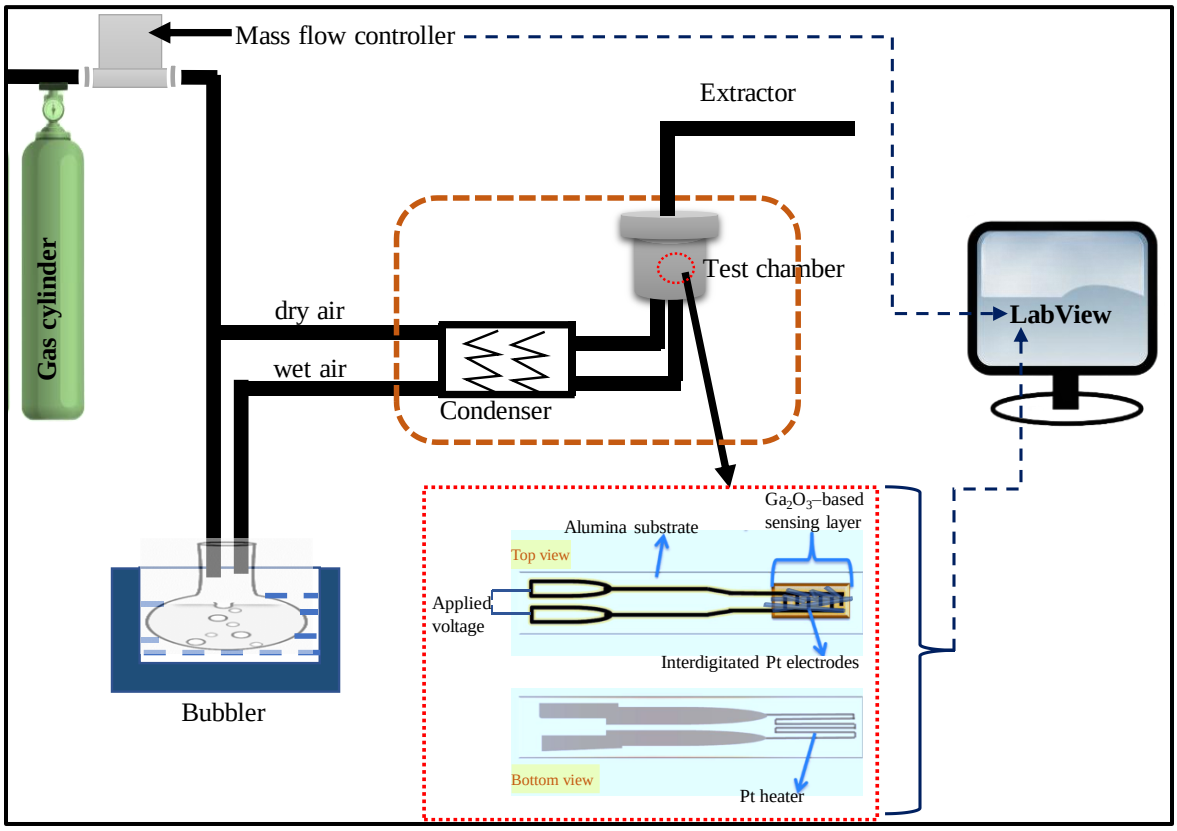


Fig. 3.11. *Schematic view of the gas sensing system.*

CHAPTER 4

Hierarchically ordered nanorods of Ga_2O_3 derived from microwave-assisted hydrothermal approach: investigation of calcination-induced structural evolution and optical behavior

4.1 Introduction

Gallium oxide (Ga_2O_3) exists in different crystal structures, namely corundum ($\alpha - Ga_2O_3$), monoclinic ($\beta - Ga_2O_3$), defective spinel (γ-Ga_2O_3) and orthorhombic (ε-Ga_2O_3 and δ-Ga_2O_3) [33,34,82,87,155]. Among these, the metastable $\alpha - Ga_2O_3$ and stable $\beta - Ga_2O_3$ phases are the most commonly studied for potential use in applications such as power electronic devices [156,157], solar-blind photodetectors [158,159], photocatalysis [160–162], gas sensing [36,39,98] and light emitting devices [163–165]. These two phases may exist in the form of films obtainable using deposition techniques while monitoring specific deposition parameters [166–170]. Physical deposition methods, however, are restricted to some degree as they do not always offer options for controlling particle morphologies and the structural phases of the materials. On the contrary, wet chemistry synthesis methods such as hydrothermal methods provide means of tuning particle morphologies. Furthermore, the material phase can be transformed into other desired phases by post-preparation heat treatment. According to the literature, the $\alpha -$ and $\beta - Ga_2O_3$ phases can be obtained from $\alpha - GaOOH$ through heat treatment under controlled temperature and time [33,34]. Reported morphologies of $\alpha - Ga_2O_3$ and $\beta - Ga_2O_3$ include rods [36,39,98,160–163,171] and spheres [165]. Rods and related hierarchical flower-like and urchin-like morphologies are usually synthesized by the traditional hydrothermal method using autoclaves [36,39,98,160,162,163,172]. The autoclave method gives a high yield from the

chemical reaction, which is one of its advantages over other methods. Nevertheless, the autoclave still consumes high energy and takes much longer time. The microwave-assisted hydrothermal method, therefore, becomes useful in addressing this challenge by offering a faster, cleaner, cost-effective, and rapid way of preparing very fine nanopowders with controlled morphologies and less agglomeration [36,90]. The synthesis environment (solution pH) is one of the key parameters that helps in controlling particle morphologies in microwave-assisted hydrothermal synthesis. Making use of the microwave-assisted hydrothermal method, we synthesized unique bunched-twisted rod-like morphologies of the $\alpha - Ga_2O_3$ and $\beta - Ga_2O_3$, most probably for the first time. This study makes a significant contribution to the preferred parameters required for the synthesis of hierarchically ordered (bunched-twisted) nanorod morphology via the microwave-assisted hydrothermal method. A combination of using microwaves and a basic solution environment were necessary to obtain this unique morphology, and the nucleation and growth mechanism is proposed. Furthermore, the structural and optical properties of the hierarchical Ga_2O_3 nanorods were analyzed in detail to understand the properties of these interlinked nanorods. Structural, optical and photoluminescence properties of different morphologies of Ga_2O_3 phases have been reported before in the literature except for hierarchically ordered (bunched-twisted) nanorods. Therefore, the overriding purpose of this study was to crystallize this unique morphology and evaluate their properties for possible applications in lighting and gas sensing. In particular, these bunched-twisted rods hold a promise in gas sensing as it is known that the material's response depends on the surface area offered for gas adsorption, which is morphology-dependent. Furthermore, the materials can be used in different types of light-emitting devices. Please note that the gas sensing and lighting applications of these materials are not discussed in this paper.

4.2 Materials and methods

4.2.1 Materials

Research-grade $Ga(NO_3)_3 \cdot xH_2O$ (99.9%) and NH_4OH (28–30%) obtained from Sigma-Aldrich were used as obtained, without further purification.

4.2.2 Samples preparation

2.56 g of $Ga(NO_3)_3 \cdot xH_2O$ was dissolved in 100 ml deionized water at room temperature in a beaker, under vigorous magnetic stirring, resulting in a clear solution. The solution was heated to a temperature of 60 ℃ on a hot plate with vigorous stirring followed by dropwise addition of NH_4OH until a pH of 11 was obtained. The resulting white mixture was aged for 3 hours at a constant temperature of 60 ℃, while stirring vigorously, and was microwaved at 150 ℃, 100 W, for 20 minutes using the Discover 2.0 microwave synthesizer. The resulting white precipitate was washed with deionized water and ethanol, three times each and was dried in an oven at 60 ℃. The as-synthesized dry powders were then calcined, in air, using a ramping rate of 10 ℃/min, in the temperature range of 400–750 ℃ for 2 hours to form the corundum $\alpha - Ga_2O_3$ and monoclinic $\beta - Ga_2O_3$ structures. The resulting powder products were labeled R-Uncal for the uncalcined and R-406, R-597, and R-750 for powders calcined at 406 ℃, 597 ℃, and 750 ℃, respectively.

4.2.3 Samples characterization

Thermogravimetric analysis (TGA) and derivative weight analysis (DTGA) of the uncalcined dried powders were carried out in a nitrogen atmosphere at a heating rate of 10 ℃/min from room temperature to 880 ℃ using a TGA Q500 instrument. The crystal structure and crystallinity

of the powders were characterized using a Bruker D2 Phaser desktop powder X-ray diffractometer with $Cu\,K\alpha_1$ radiation, λ = 0.15406 nm. Raman spectroscopy measured by the Horiba UV-Vis Raman spectrometer equipped with a 514.5 nm laser source was used to corroborate the structure of the as-synthesized nanorods and investigate the structural effects induced by calcining at chosen temperatures. The morphologies of the synthesized powder products were characterized using a Zeiss Gemini SEM system operated at 15 kV. UV-Vis diffuse reflectance characterization was carried out using a Varian Cary 500 UV-Vis NIR spectrophotometer equipped with a Praying Mantis Diffuse Reflectance Accessory from Harrick Scientific Products. The steady-state room-temperature PL emission and lifetime measurements of the powders were carried out using Horiba QuantaMaster QM8000 spectrofluorometer with a Xe source and a 250 nm fast pulsed laser source respectively. Analysis of the oxide surface defects was carried out by using X-ray photoelectron spectroscopy (XPS) using AXIS Ultra DLD supplied by Kratos Analytical with a monochromatic Al anode equipped with a charge neutralizer.

4.3 Results and discussion

4.3.1 Thermal stability and structural behavior analysis

Since the targeted future application of the synthesized hierarchical structures is gas sensing, it was important to study the properties of the metastable $\alpha - Ga_2O_3$ and stable $\beta - Ga_2O_3$ phases only. To determine the calcination temperature at which these two phases are formed, a thermal stability study of the as-synthesized (uncalcined) powders was conducted, and the results are presented in Fig. 4.1. Firstly, the successful synthesis of $GaOOH$ was confirmed by the weight

loss observed when the powder was heated from room temperature to 237 ℃, and this was attributed to the removal of the -OH components from water molecules adsorbed on the surface of the R-Uncal powder [98]. Secondly, through the hydroxylation process, $\alpha - GaOOH$ transformed into the metastable $\alpha - Ga_2O_3$ phase at 406 ℃ with a corresponding cumulative 8.5% weight loss. Thirdly, maximum cumulative weight loss (10.4%) was observed at 597 ℃, a temperature at which the most stable $\beta - Ga_2O_3$ starts to form [98]. A minor weight gain observed at temperatures beyond 597 ℃ is attributed to the formation of $\beta - Ga_2O_3$ through further oxidation [98].

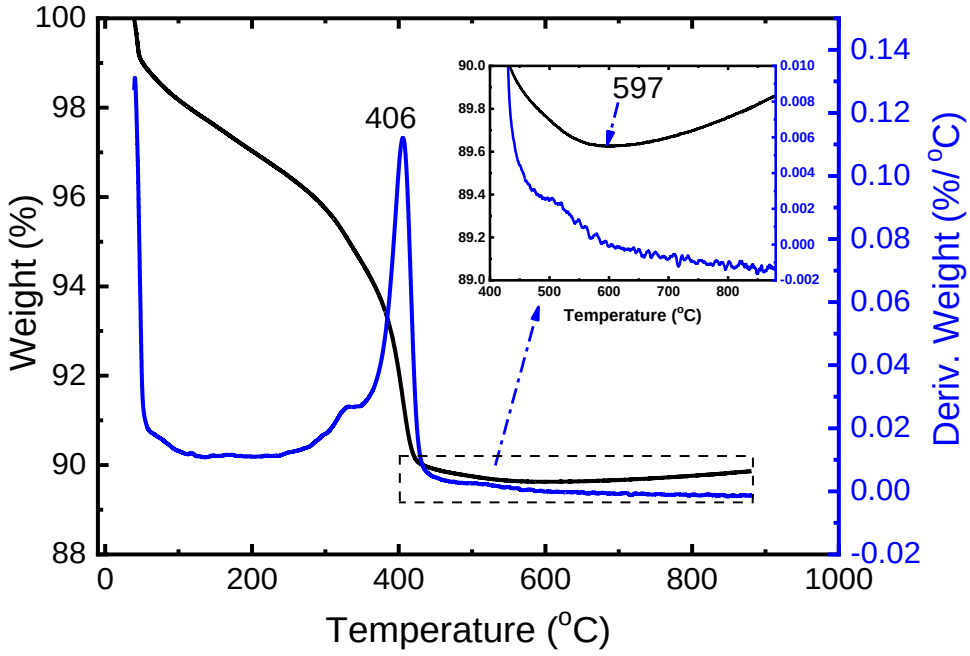


Fig. 4.1. *Thermogravimetric analysis and derivative thermogravimetric analysis curves obtained by heating the uncalcined sample from room temperature to 880* ℃.

Calcination temperatures of 406 and 597 ℃ were chosen to prepare $\alpha - Ga_2O_3$ and $\beta - Ga_2O_3$ phases respectively. The XRD patterns obtained from the calcined products are shown in Fig.

4.2. Included in the same figure are the patterns of the uncalcined powders as well as those calcined at 750 ℃. The powders calcined at higher temperatures are included to evaluate the effects of high-temperature calcination on the structural properties of $\beta - Ga_2O_3$. The patterns of R-Uncal powders were indexed to the orthorhombic structure of $GaOOH$ (PDF: 01–071–2778) with preferential orientation in the (110) plane. Upon increasing the calcination temperature to 406 ℃, the XRD patterns confirm the transformation of the structure to single phase rhombohedral $\alpha - Ga_2O_3$ (PDF: 00–006–0503) phase with most intense peaks from the (104) and (110) planes. Higher temperature calcination (597 ℃) points to the formation of a monoclinic $\beta - Ga_2O_3$ structure (PDF: 00–076–0573) with preferential orientation in the (111) plane. No further structural transformation was observed when the calcination temperature was increased to 750 ℃. However, there was an improvement in the intensity of the $(002)/(\bar{2}02)$ diffraction peaks as shown by the decrease in the line width (see inset). Also, the observed peaks shifted to lower diffraction angles in the pattern of 750 ℃-calcined powders, which is attributed to lattice expansion caused by thermal strains resulting from an increase in calcination temperature [173]. For more information on thermal expansion and thermal strains, the reader is referred to the literature cited [173]. Generally, the sharp peaks in all the spectra of Fig. 4.2(a) indicate the high crystallinity of the synthesized powders. The crystallite size, D, of the powders was estimated using the Scherrer equation $D = K\lambda/\beta Cos\,\theta$, where K (= 0.85) is the average crystallite shape factor for cubic nanocrystals [174,175], λ is the X-ray wavelength, β is the peak width at half maximum, and θ is the diffraction angle of the peak [176]. The diffraction peaks at 21.4, 33.6, 35.2, and 35.1 ° in the patterns listed in the order of increasing calcination temperature were used in the calculations of the average crystallite sizes. The crystallite sizes

obtained were 23.4, 15.4, 16.2 and 20.6 nm, all with error bars of ±0.1 nm, for the R-Uncal, R-406, R-597 and R-750 powders, respectively. A sharp decrease in the crystallite size when the phase transformed into the $\alpha - Ga_2O_3$ indicates that the thermal energy supplied during calcination was used more in the phase transformation than the crystal agglomeration. On the contrary, calcination caused crystal growth in the $\beta - Ga_2O_3$ structures resulting in the increase of crystallite size from 16 to 20 nm and the thermal strain-induced lattice expansion mentioned above. A similar effect of heat treatment on lattice expansion was reported in the literature for $\beta - Ga_2O_3$ [173].

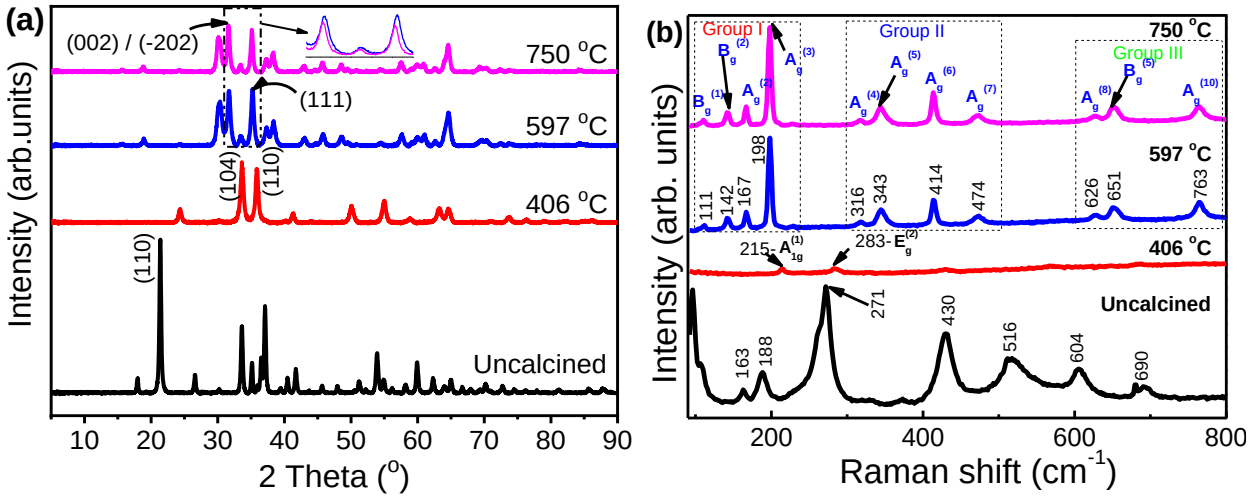


Fig. 4.2. *(a) X-ray diffraction patterns and (b) Raman spectra show structural evolution as functions of calcination temperature of Ga_2O_3 powders.*

Fig. 4.2(b) shows Raman spectra of the calcined samples to investigate further the effects of calcination temperature on the chemical and intramolecular bonds in the different lattices. The Raman modes observed from the uncalcined powders confirmed crystallization of the $\alpha - GaOOH$ structure and the results agree with the only reference available in the literature

[177]. Two weak Raman peaks were observed from the $\alpha - Ga_2O_3$ plane [178,179] and the disappearance of the peaks in the $\alpha - GaOOH$ structure upon transformation to the $\alpha - Ga_2O_3$ structure is most likely due to changes in the arrangement of atoms in $3D$ associated with the phase change. Furthermore, the weak modes from the R-406 samples confirm that there are small crystallite sizes in the sample [180] as discussed in the XRD results. Clearly identifiable characteristic peaks of the $\beta - Ga_2O_3$ were observed from powders calcined at 597 ℃ with four more satellite peaks appearing at 105, 353, 471 and 659 cm^{-1}, and these findings together with the assigned symmetry are consistent with the literature [181,182]. With peak shifts within 2 cm^{-1}, peak intensity ratios were maintained in the powders calcined at 750 ℃ indicating that the induced increase in the calcination temperature did not significantly affect the bond strength although there was lattice expansion as observed from the XRD data.

4.3.2 Particle morphology

Fig. 4.3(a) shows the SEM micrographs obtained from the uncalcined powders and the same morphology was retained after calcining at different temperatures (Fig. 4.3(d-f)). The micrograph shows that the powders crystallized in unique hierarchically ordered bunched-twisted nanorod structures (Fig. 4.3(b)) with some of the bunched rods agglomerating homo-centrally to form 'pom-pom'-like structures as depicted in Fig. 4.3(c). A closer look at the individual rods in Fig. 4.3(b) shows that the nanorods have uniform widths, indicating that the agglomerated crystallites have homogeneous size distribution. Since this morphology is already present in the uncalcined powders and is retained at all calcination temperatures, it is logical to suggest that the formation of this unique morphology depends on the synthesis parameters and was not influenced by post-preparation heat treatment. It is reported in the literature that the morphology of any crystallized

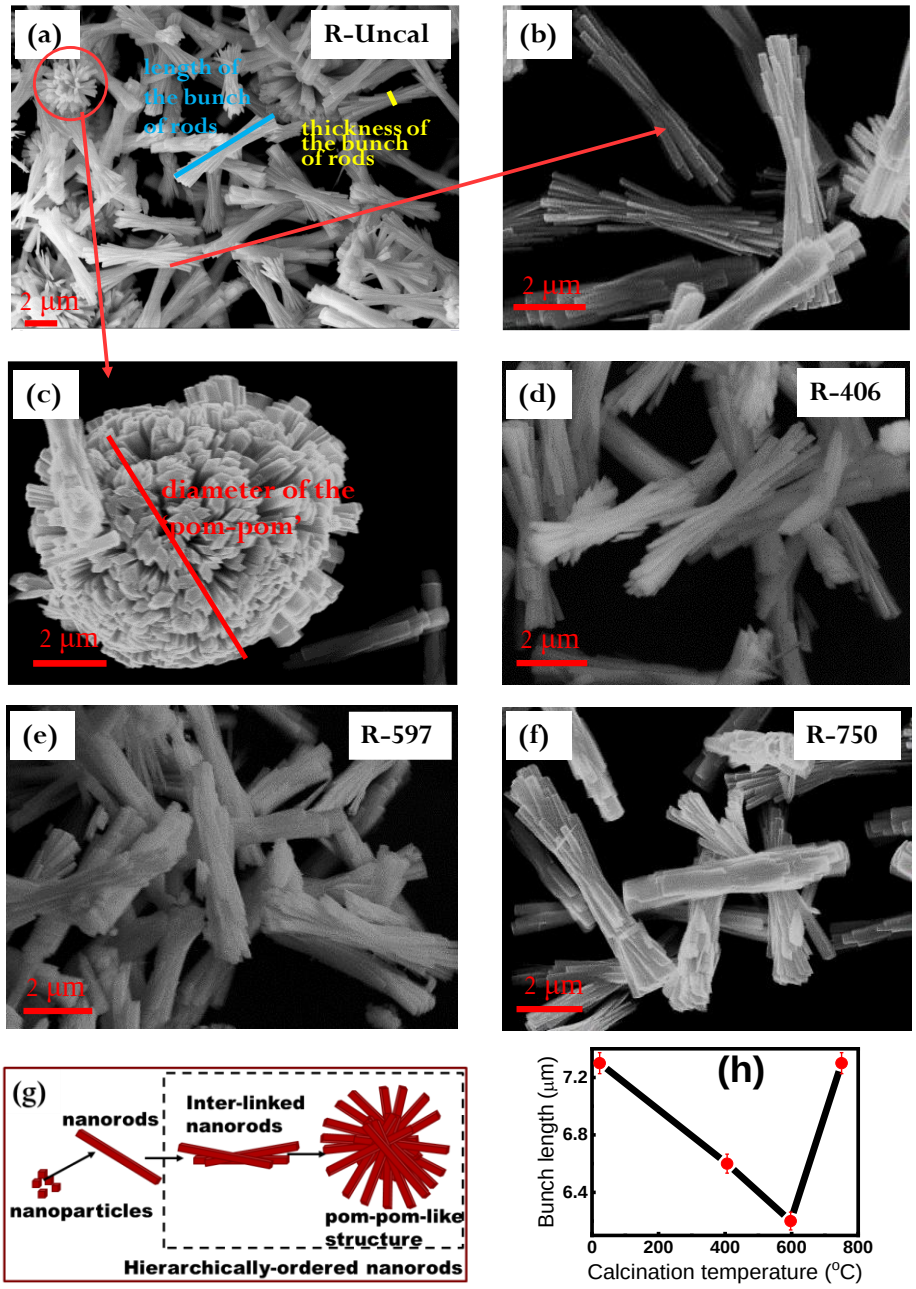


Fig. 4.3. *(a) Scanning electron microscopy micrographs of the as-synthesized $GaOOH$ powder products, (b, c) high-resolution images to show the rod arrangement and appearance in the bunches and urchin-like hierarchical structures present in the $GaOOH$ powders. (d-f) micrographs from powders calcined at 406 ℃ (R-406), 597 ℃ (R-597), and 750 ℃ (R-750). (g) proposed rod-formation mechanism for the hydrothermally synthesized nanostructures. (h) average length of each bunch of rods versus calcination temperature in the various Ga_2O_3 powders in (a-f).*

material fairly depends on the hydrothermal growth conditions [90]. It is paramount to understand how the chosen microwave-assisted hydrothermal method and the solution pH = 11 could have influenced the formation of this unique morphology to predict or suggest the crystal growth mechanism involved.

4.3.2.1 Microwave-assisted hydrothermal method

The use of microwave in assisting the synthesis is applicable in cases like this where the reaction solution contains polarized molecules from water and the ammonium base. The assisted method utilizes both the microwaves and the water heating process from the hydrothermal reaction. Microwave irradiation offers improved reaction speeds, and uniform heating rates, while water heating reduces the viscosity and surface tension of the reaction solution. Thus, a combinatorial effect of microwave and hydrothermal synthesis significantly increases the mobility of the ions or molecular species and consequently increases the rate of crystal growth and controls particle morphology.

4.3.2.2 Solution pH (=11)

The reaction kinetics and growth mechanism during the hydrothermal synthesis method involves dissolving the reactants in a hydrothermal environment to form ions or molecular groups. Since these ionic and molecular species are mobile, they shift to low-temperature region where seed crystals grow from a supersaturated solution. This is followed by adsorption, decomposition and desorption of the ions or molecules at the growth interface and then dissolved species crystallize. These processes control the evolution of the resulting morphology [36,90] and the generation of specific morphology depends on the mobility of ions or molecular groups on the growth interface

as well as the presence of unsaturated bonds in the solution. It is therefore important to use a solution condition that allows for more unsaturated bonds - that is a basic solution. At the chosen pH of 11, the solution is basic and NH_4OH acts as a capping agent with high activity regulating the morphology by allowing for $-OH$ adsorption in a preferred direction resulting in self-agglomeration of crystallites forming rod-like morphology. Further, adjacent agglomerated entities rearrange themselves to a side-by-side attachment configuration which favors lower surface energy in the alkaline solution and thus results in the formation of bunched rods [183,184]. However, since the nanocrystal surfaces are not atomically flat and there will always be other particles in the locality of attaching rods, misorientations of rods will always occur and the bunched rods may appear as bunched-twisted rods. This proposed growth mechanism in a solution of pH = 11 is presented in Fig. 4.3(g) and related formations are known as 'imperfect oriented attachment' [183]. The hierarchically ordered bundles further agglomerate homo-centrically forming a 'perfect' hierarchical structure shaped like a 'pom-pom' as shown in Fig. 4.3(g) and the alkaline condition of the solution facilitates such oriented attachments [36]. Although phase transition did not have a significant effect on the morphology of Ga_2O_3, the average lengths of the rod bundles were considerably affected. The average length value of each bunch of the rods in the different powders measured using ImageJ software is presented in Fig. 4.3(h) and the average thicknesses of these bunches were measured to be ~0.8 μm. The decrease in the bunch lengths at 406 and 597 ℃ suggests that the heat energy supplied to the sample during calcination was utilized in phase transformation rather than in rod growth or agglomeration. On the contrary, increased bunch length was observed for the R-750 powders, and these indicate crystallite and rod growth lengthwise. This finding is consistent with the lattice expansion reported from the XRD data. Individual rod widths were about 200 nm in all

samples and rods have diamond-shaped faces as depicted in a cross-sectional image of the urchin-like hierarchical structure in Fig. 4.3(c).

4.3.3 Optical absorption and emission properties

For more insight into the band structure and origin of defects of the synthesized powder products induced by calcination at different temperatures, detailed UV-Vis diffuse reflectance spectra (DRS) and PL spectroscopic analysis were conducted. The UV-Vis DRS results presented in Fig. 4.4(a) show that all synthesized powders, before and after calcination, strongly absorb light in the 200–300 nm UV range and only ~30% of the incident light was reflected in the visible region. Absorption is through the excitation of electrons from the valence band to the conduction band. The inset of Fig. 4.4(a) shows the Kubelka-Munk plot from which the direct band gap energy values were determined for the synthesized powders. The optical band gap energies decrease with increasing calcination temperature, and this confirms changes in the lattice structures as it is well-known that there is a direct link between the lattice structures of metal oxides and their electronic band structure. Decreasing band gaps with increasing calcination temperature are attributed to an increase in thermally induced localized states in the energy gap. The energy values (inset of Fig. 4.4(a)) are in good agreement with previous reports of hydrothermally synthesized $\alpha - GaOOH$, $\alpha - Ga_2O_3$ and $\beta - Ga_2O_3$ rods [36,98,162,163]. Minor variations in the band gap energies reported here and those reported in the literature may be ascribed to the difference in the synthesis parameters such as pH, reaction time and temperature. PL is a non-destructive technique used to determine the emission properties and positions of defects within the band gap of semiconducting materials. The room-temperature PL spectra of $\alpha - GaOOH$, $\alpha - Ga_2O_3$ and $\beta - Ga_2O_3$ rods at an excitation wavelength of 250 nm

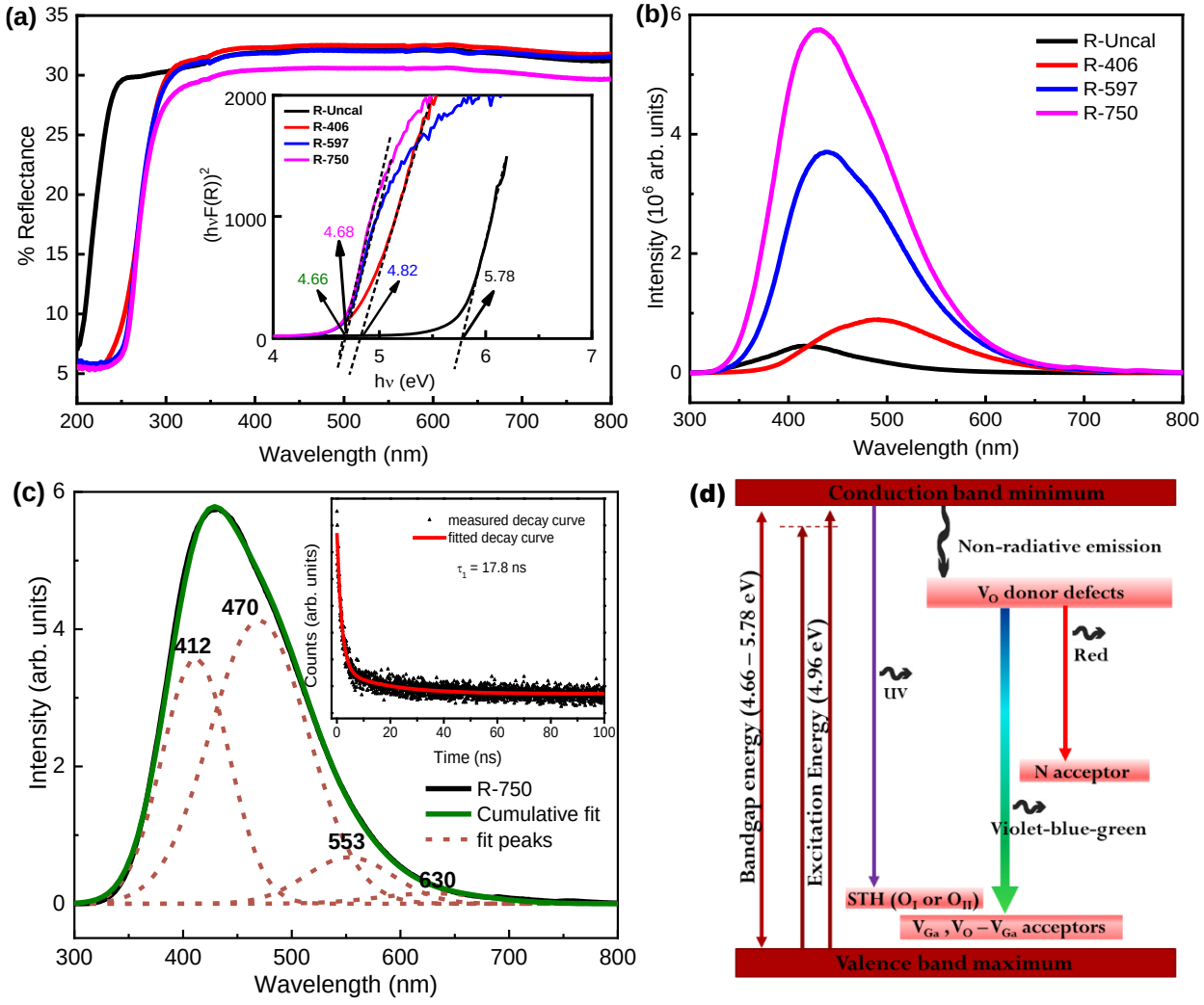


Fig. 4.4. *(a) UV-Vis diffusive reflectance spectra of the synthesized powder products. The inset shows the Kubelka-Munk plots with determined band energy values, (b) room-temperature photoluminescence of the synthesized powder products, (c) the deconvoluted emission from R-750 powder and the inset shows the blue-emission decay curve. (d) proposed PL mechanism involved in the observed emission. R-Uncal, R-406, R-597, and R-750 represent uncalcined $GaOOH$ powders and Ga_2O_3 powders calcined at 406, 597 and 750* ℃*, respectively.*

are shown in Fig. 4.4(b). All the powders displayed a broad emission band in the 300 – 650 nm wavelength range regardless of the calcination temperature, hence it is reasonable to conclude

that similar electronic transitions were involved in their radiative emissions [185]. Fig. 4.4(c) shows the deconvoluted most intense spectrum and the violet (412 nm), blue (470 nm) and green (553 nm) emissions are attributed to donor-acceptor-pair recombination involving an electron trapped in an oxygen vacancy (V_O) donor and a hole that is trapped in a gallium vacancy (V_{Ga}) or gallium–oxygen vacancy (V_O–V_{Ga}) acceptor pair [165,168–170,185,186]. The positions of the deep-level defects (donors and acceptors) and self-trapped holes used to deduce the transitions in the proposed PL mechanism in Fig. 4.4(d) were obtained from the reported experimental work in the literature cited [39,168,170,187]. The decay curve of the blue emission in the inset of Fig. 4.4(c) shows a decay time of 17.8 ns. This value, together with the strong blue emission, indicates that the synthesized structures can be used in optical lasing or as blue phosphors in light-emitting devices. A weak bump in the R-uncal spectrum at ~350 nm is attributed to the recombination involving free electrons and self-trapped holes (STH) at the $O1$ or $O2$ site [187] while weak red emission centered at ~630 nm is assigned to the donor-acceptor pair recombination involving electrons trapped in the V_O donor states and a hole trapped in a nitrogen (N) acceptor [165]. Nitrogen impurity is most likely coming from $Ga(NO_3)_3 \cdot xH_2O$ starting material. Generally, the intensity of the blue emission increases with increasing calcination temperature as more surface oxygen defects (V_O) are created from oxygen atoms escaping the lattice at higher calcination temperatures. This broad and intense room-temperature blue emission from these hierarchically ordered nanorods may have potential applications as light-emitting materials in optoelectronic devices. The presence of surface V_O defects (as confirmed from XPS analysis in Section 4.3.4 below) in these hierarchical structures of gallium oxide may indicate the useful application of these powders in gas sensing applications.

4.3.4 Compositional analysis

X-ray photoelectron spectroscopy (XPS) was used to investigate the composition of the surface of the synthesized $\beta - Ga_2O_3$ R-750 powder. Fig. 4.5(a) shows the survey full range (0 – 1200 eV) XPS spectrum of $\beta - Ga_2O_3$ showing the core-level of $Ga\ 2p$, $Ga\ 3d$, $O\ 1s$ photoelectron peaks, the $Ga\ LLM$, $O\ KLL$ Auger electron peaks and the carbon peak ($C\ 1s$) from atmospheric hydrocarbons. The deconvoluted high-resolution XPS spectra of $Ga\ 3d$, $O\ 1s$ and $Ga\ 2p$ are presented in parts (b)-(e) of Fig. 4.5. All the spectra were calibrated with the main peak of carbon at 284.8 eV (Fig. 4.5(b)) as reference [167,188] to compensate for the surface charge effects and background subtraction and peak deconvolution was conducted with Origin software. The four fitted Gaussian curves in the $C\ 1s$ core level spectrum in Fig. 4.5(b) correspond to the sp^2-, sp^3-carbon bonding, $C - O$ bonding and $C = O$ bonding [189]. Further, the high-resolution spectrum of the $Ga\ 3d$ peak presented in Fig. 4.5(c) was deconvoluted into two overlapping peaks at 20.2 and 21.1 eV attributed to the Ga-O bond [190]. Fig. 4.5(d) shows the $O\ 1s$ peak deconvoluted in two peaks, 530.8 eV from the lattice oxygen of Ga_2O_3 and 531.6 eV from surface adsorbed water molecules [191]. These peaks are attributed to the O^{2-} ions of the $Ga - O$ bond and the presence of adventitious hydroxyl of water on the surface of the oxide [166,191]. The presence of the $Ga\ 2p$ peaks at binding energy positions shown in Fig. 4.5(e) represent the typical $Ga - O$ bond in Ga_2O_3. The binding energies located at 1117.7 and 1144.5 eV are ascribed to $Ga\ 2p_{3/2}$ and $Ga\ 2p_{1/2}$ electrons, respectively, resulting from the crystal field splitting of the $Ga\ 2p$ energy level. Doublets observed in the $Ga\ 2p$ peaks indicate the presence of Ga in both elemental and oxide compound form. As shown in Fig. 4.5, the Ga and O elements were detected on the surface, with their corresponding binding energies, confirming that the powder calcined at

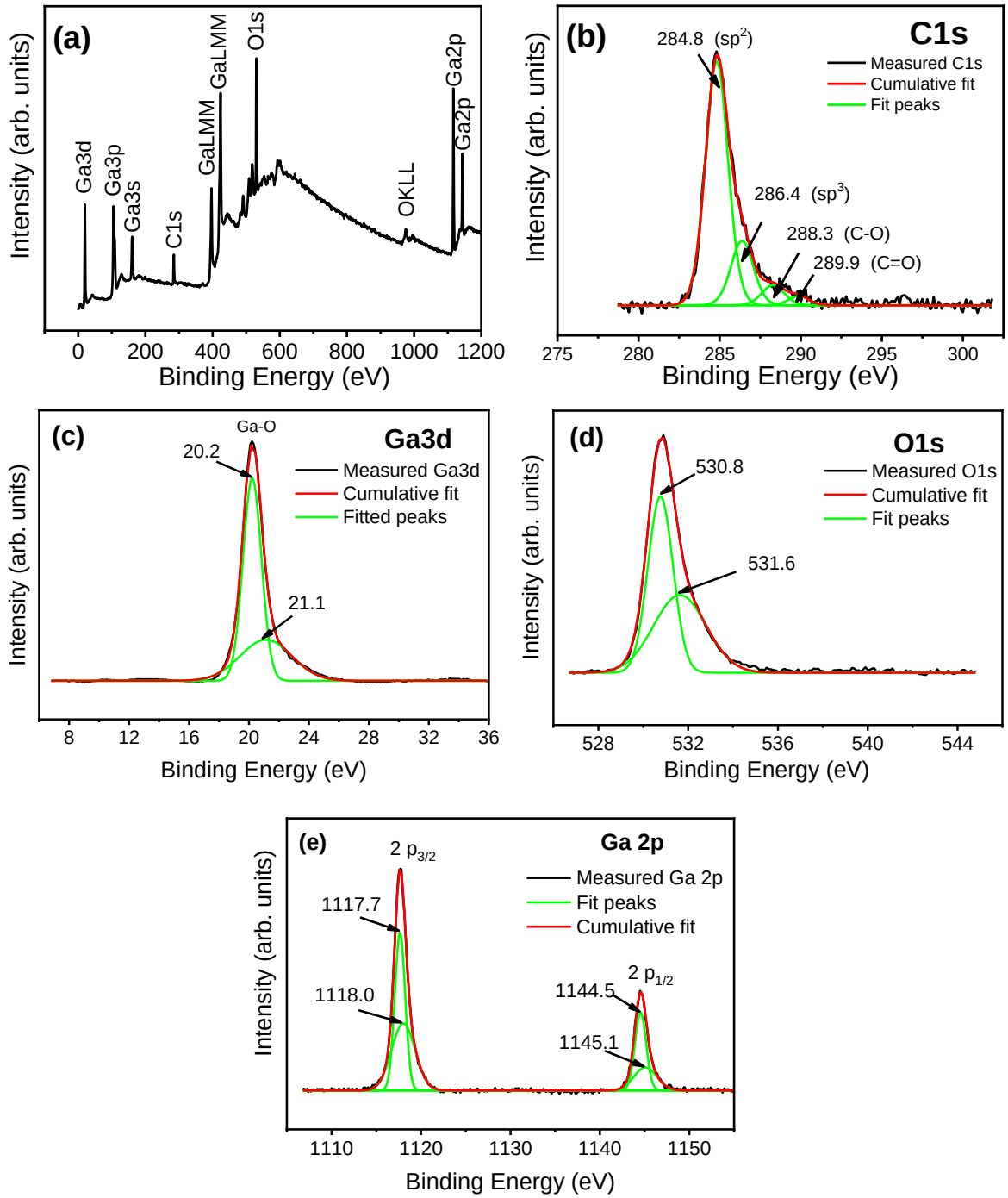


Fig. 4.5. *X-ray photoelectron (a) survey and ((b)-(e)) high-resolution spectra measured from* Ga_2O_3 *powders calcined at 750* ℃.

750 ℃ successfully crystallized in the Ga_2O_3. This structure has Ga and O atoms in a 2:3 stochiometric ratio calculated by the area ratios of the $Ga\ 2p$ and $O\ 1s$ peaks, and these findings corroborate the XRD results and are consistent with the literature cited [82,192].

4.4 Conclusion

A direct microwave-assisted hydrothermal method coupled with calcination was used to prepare hierarchically ordered nanorods of the $\alpha - Ga_2O_3$ and $\beta - Ga_2O_3$ phases. A combination of microwaves and solution pH was the determinant in the resulting morphology. Structural, morphological, and optical properties of these unique morphologies of $\alpha - Ga_2O_3$ and $\beta - Ga_2O_3$ were explained. In addition, the growth mechanism was proposed to account for particle morphology. Since morphologies are known to influence the surface area available for target gas-oxide surface interactions in gas sensing, these synthesized metastable and stable phases of Ga_2O_3 in the unique morphology could be useful in gas sensing. The strong blue photoluminescence with fast decay time indicates that this material can be used as a source of blue light in optoelectronic devices.

CHAPTER 5

Synthesis, characterization, and gas-sensing performance of rhombohedral (α) and monoclinic (β)-Ga_2O_3 nanorods/nanowires

5.1 Introduction

Over the years, there has been a rapid increase in industrial activities both in the mining and energy sectors that release various toxic gases such as carbon monoxide (CO), ammonia (NH_3), sulphur dioxide (SO_2), and nitrogen dioxide (NO_2) posing a hazard to human health and the surrounding environment [193]. Effects of these toxic gases may vary from respiratory and central nervous system diseases, death, and acid rain [194,195]. Therefore, to protect human health and ecological environment, it is important to develop gas sensors for accurate and real-time monitoring of these gases.

Of particular interest, semiconductor metal oxides (SMOs) present reversible gas interaction with pre-adsorbed ambient oxygen which induces direct change in their electrical resistance measured as an output signal. Due to this simplicity in operation, SMOs based-gas sensors have generated interest. Thus far, numerous nanostructured SMO materials such as ZnO, SnO_2, TiO_2, and Ga_2O_3 [10,23,196,197] have been comprehensively studied and applied in gas sensors because of their simple and low-cost synthesis, high sensitivity, and tunable properties [8]. One dimensional ($1D$) SMOs with morphologies such as wires and rods, offer large active surface area which leads to improved surface interaction with gas molecules due to stimulation of target gas molecules adsorption and circulation [155]. Among the aforementioned SMO materials, $1D$ Ga_2O_3 nanostructures such as nanorods and nanowires demonstrated efficient detection of

various toxic gases and vapors [23,42]. The interest in Ga_2O_3 is inspired by its wide band gap, moderate free carrier concentration, excellent chemical resistance, and structural stability under harsh environments. However, among the different polymorphs of Ga_2O_3, namely $\alpha -$, $\delta -$, $\gamma -$, $\varepsilon(\kappa) -$ and $\beta - Ga_2O_3$ [34], the most stable monoclinic $\beta - Ga_2O_3$ is the most researched for gas sensing applications [23]. Although there have been excellent sensing performances observed for $\beta - Ga_2O_3$-based sensors at high operating temperatures of 300 ℃ and above, the high-power consumption hinders them from practical application. Hence, the need to explore other phases of Ga_2O_3, i.e., the metastable and pseudo $\alpha -$, $\delta -$, $\gamma -$ and $\varepsilon(\kappa) - Ga_2O_3$ phases, for the recognition of various gases at relatively low temperatures. Recently, Vorobyeva *et al*. [108] and Almaev *et al*. [109,110] investigated gas sensing capabilities of $\alpha - Ga_2O_3$ and $\varepsilon(\kappa) - Ga_2O_3$ films. The $\varepsilon(\kappa) - Ga_2O_3$ films demonstrated the highest responses towards NO_2, (H_2 and CO) and O_2 at 550, 500 and 450 ℃ operating temperatures, respectively. In another study, a blend of $\alpha - Ga_2O_3$ and $\varepsilon - Ga_2O_3$, i.e., α/ε-Ga_2O_3 films, presented the highest response and a low detection limit towards H_2 at 125 ℃ compared to the $\beta - Ga_2O_3$ films [110]. This demonstrated that the mixture of Ga_2O_3 phases can be used to improve the sensitivity, lower the operating temperature, and lower the detection limit of the Ga_2O_3 sensors [110,162]. However, the high ohmic resistances of the $\alpha - Ga_2O_3$ phase limits its incorporation in phase mixtures for improved Ga_2O_3 sensing performances [108,110].

In this context, a study on the sensing performance of the $\alpha - Ga_2O_3$ and a blend of $\alpha - Ga_2O_3$ and $\beta - Ga_2O_3$ (i.e., $\alpha/\beta - Ga_2O_3$) may give insight of the combination of the two phases on the sensing characteristics. The ohmic resistance (R) of SMOs, in this case $\alpha - Ga_2O_3$, defined by $R = \rho\frac{L}{A}$ where ρ is the electrical resistivity, L is the length and A is the cross-sectional area

can be reduced by preparing nanostructures with high surface area and short lengths. The dimensions and surface areas of Ga_2O_3 nanostructures can be controlled during synthesis and in post-synthesis heat treatments. Furthermore, the electrical resistance of Ga_2O_3 can be changed by controlling the background impurities of chromium ions (Cr^{3+}) contained in the material through variation of calcination environments and temperature [97,198,199].

In this study, a mixture of non-uniform $GaOOH$ nanorods and nanowires were synthesized using microwave-assisted hydrothermal method. The $\alpha - Ga_2O_3$, $\beta - Ga_2O_3$, and ($\alpha/\beta - Ga_2O_3$) polymorphs were produced by calcination in air at different temperatures ranging from 550 ℃ – 950 ℃. The effects of fundamental properties, large surface area and background Cr^{3+} impurities on the gas sensing performances of Ga_2O_3 have been investigated. The gas sensing mechanism for Ga_2O_3 nanorods/nanowires-based sensors is discussed.

5.2 Materials and methods

5.2.1 Preparation of Ga_2O_3

Analytical-grade chemicals from Sigma Aldrich were used without additional purification. 0.2557 (± 0.0001) g of $Ga(NO_3)_3.xH_2O$ (99.9%) was dissolved in 10 ml of deionized water under vigorous stirring at 60 ℃ resulting in a 0.1M Ga^{3+}solution as illustrated in Fig. 5.1(a). NH_4OH(28%) was added dropwise until the solution pH was 12. After aging for one hour at 60 ℃, the solution was loaded into a vial and then to a microwave chamber of the Discover 2.0 microwave synthesizer for a reaction at 150 ℃ and 100 W for 1 hour. The precipitate obtained was washed several times with water and ethanol through centrifugation and a paste was obtained. The paste was dried at 60 ℃, before separating it into smaller portions. The portions

were heat-treated separately at 550, 650, 750, 850, and 950 ℃ in air for 2 hours at a rate of 5 $℃/min$. Accordingly, the heat-treated samples were labelled S550, S650, S750, S850, and S950.

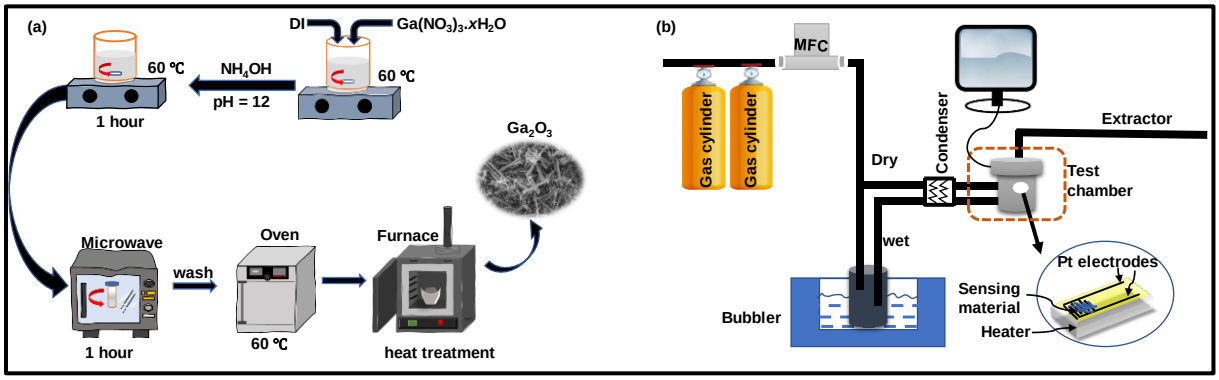


Fig. 5.1*. Schematic diagrams showing (a) Ga_2O_3 synthesis process and (b) gas sensor characterization system.*

5.2.2 Characterization

The crystallinity and phase purity of Ga_2O_3 powders were examined by an X-ray diffractometer (Bruker D2 Phaser, ($\lambda_{Cu\,K\alpha1}$ = 0.15406 nm). Morphology of the powders were analysed by a JEOL JSM-7500F field-emission scanning electron microscope. The surface area and porosity were quantified by the Micromeritics TriStar 3000 surface-area analyzer. A PHI 5000 Scanning ESCA Microprobe X-ray photoelectron spectroscope with $Al - K\alpha$ beam ($hv = 1486.6\ eV$) was used to analyse the chemical composition and electronic states of the samples. Photoluminescence spectra were measured using Horiba QuantaMaster QM8000 spectrofluorometer equipped with a xenon lamp source.

5.2.3 Ga_2O_3 based-gas sensors fabrication and testing

Ga_2O_3-based sensors were prepared by dispersing the samples in ethanol, followed by ultrasonication into a slurry suspension. The suspension was coated uniformly onto the upper

side of an alumina substrate with previously interdigitated platinum (Pt) electrodes (Fig. 5.1(b)). All sensors were annealed at 300 ℃ in a muffle furnace overnight to enhance adhesion of the paste to the substrates. Gas sensing properties were evaluated using a KSGAS6S (KANOSISTEC, Italy) -sensing station, and all target gases (CO_2, CH_4, NH_3, NO_2, and SO_2) tested were commercially acquired. The sensor operating temperature was varied from room temperature to 180 ℃. Each sensor was connected to a 2 V current-driving voltage and the electrical resistance modulations were measured using a Keithley 6487 Picoammeter/voltage source meter. Humid atmospheric conditions were achieved by evaporating water in a bubbler (Fig. 5.1(b)) at 50 ℃. The sensor response was determined by $\left|((R_a - R_g)/R_g)\right|$ for reducing target gas and $\left|((R_g - R_a)/R_a)\right|$ for oxidizing gas, where R_a and R_g are sensor resistances in air and gas, respectively. The response and recovery times were determined from the time taken to reach 90% of the total change in sensor resistance upon gas adsorption and desorption, respectively.

5.3 Results and discussion

5.3.1 Crystal structure

The XRD patterns of heat-treated Ga_2O_3 powders are presented in Fig. 5.2. The patterns of S550 were indexed to rhombohedral $\alpha - Ga_2O_3$ phase (PDF:006-0503). Since no secondary phases were detected, this implies that high purity rhombohedral $\alpha - Ga_2O_3$ phase was crystallized. All the diffraction peaks in the patterns of S750, S850, and S950 samples were indexed to monoclinic $\beta - Ga_2O_3$ (PDF:076-0573). In the case of S650, the patterns contained diffraction

peaks from both $\alpha - Ga_2O_3$ and $\beta - Ga_2O_3$ polymorphs, pointing to the formation of a blend of $\alpha/\beta - Ga_2O_3$ polymorph.

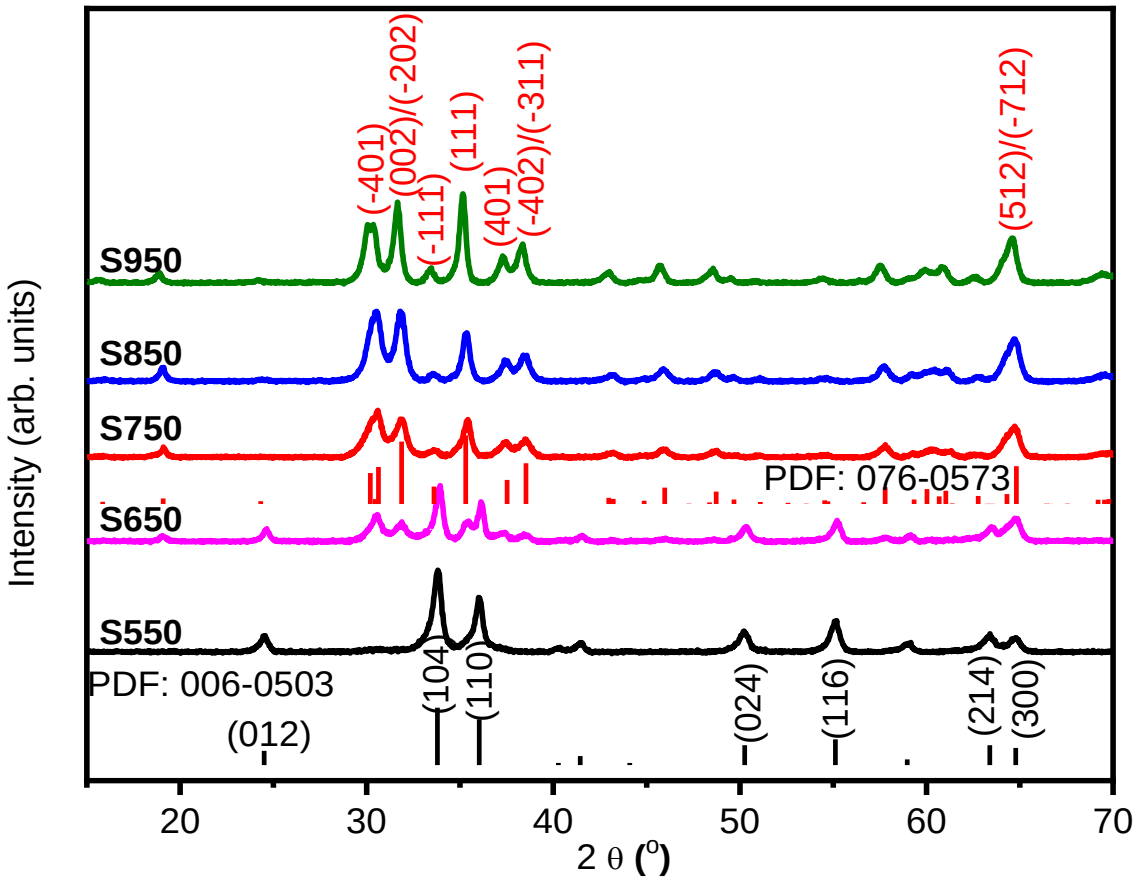


Fig. 5.2*. X-ray diffraction patterns of hydrothermally synthesized Ga_2O_3 powders. S550, S650, S750, S850, and S950 represent Ga_2O_3 powders heat treated at 550, 650, 750, 850, and 950 ℃, respectively.*

5.3.2 Morphology and texture analysis

Fig. 5.3 (a-e) show the SEM micrographs from the samples revealing that the synthesized nanopowders were composed of non-uniform nanorods and nanowires. Furthermore, Fig. 5.3(f) demonstrates that the average diameters of the nanorods were found to be in the range of ~ 110 – 255 nm and the nanowires were characterized by diameters of ~ 90 nm. The S750 sample

predominately contained nanowires compared to its counterparts. This suggests that the heat-treatment thermal energy supplied to this sample favored phase transformation from $\alpha - Ga_2O_3$ to $\beta - Ga_2O_3$ rather than nanorod growth. The Brunnauer-Emmett-Teller specific surface area

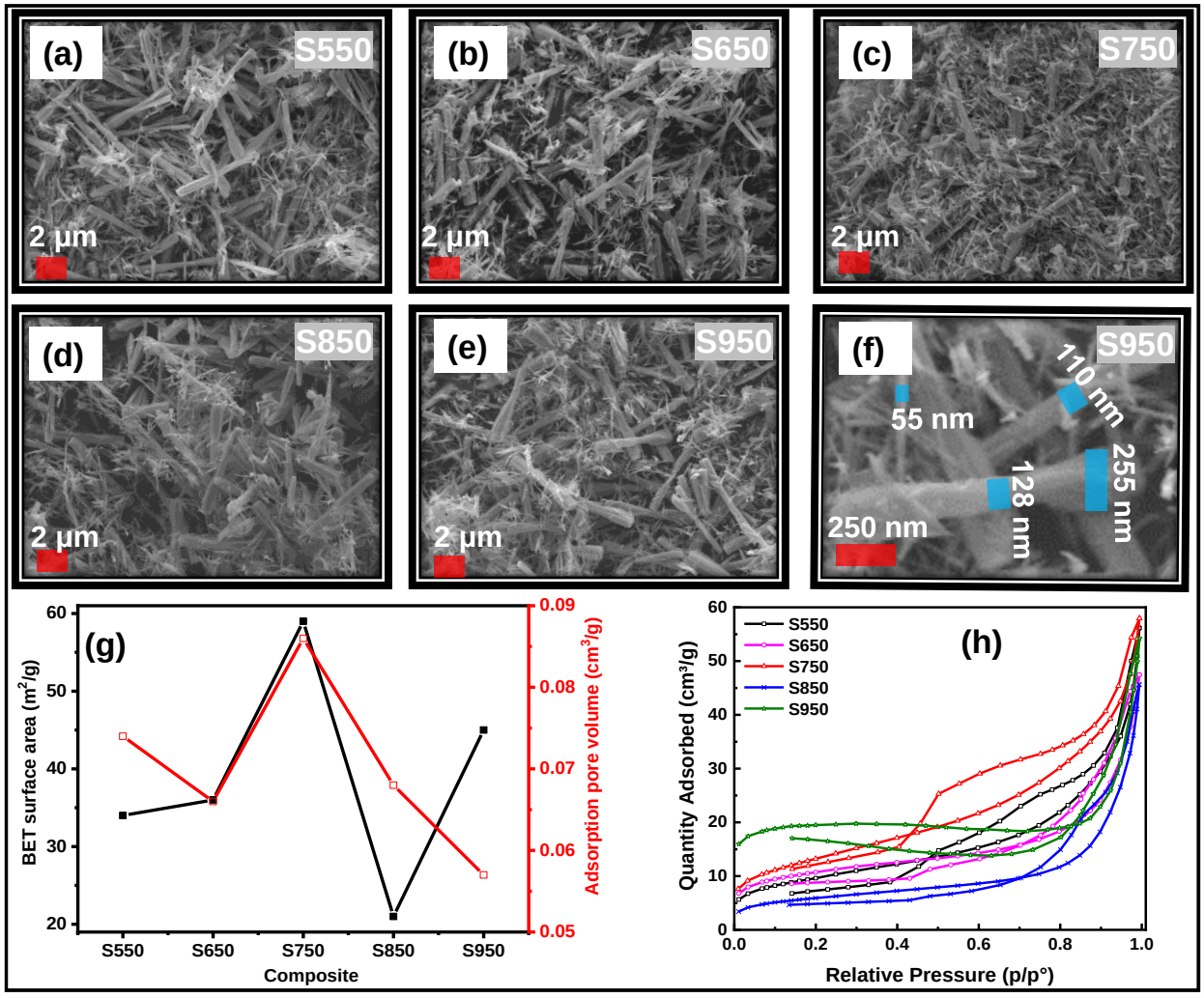


Fig. 5.3*. (a-f) Scanning electron microscopy images, (g) Brunauer-Emmett-Teller surface area and Barrett-Joyner-Halenda pore volume, and (h) Nitrogen adsorption-desorption isotherms measured at 77 K of heat treated Ga_2O_3 powders. S550, S650, S750, S850, and S950 represent Ga_2O_3 powders heat treated at 550, 650, 750, 850, and 950 ℃, respectively.*

results presented in Fig. 5.3(g) demonstrates the larger surface area from the S750 sample which can be attributed to the presence of more nanowires in the sample. The (N_2) adsorption-desorption isotherms presented in Fig. 5.3(h) revealed that all the samples presented Type-IV isotherms with Type-H3 hysteresis loops suggesting mesoporosity with non-uniform pore sizes and shapes [145]. A relatively high Barrett-Joyner-Halenda (BJH) pore volume recorded from the S750 powder (Fig. 5.3(g)) can be associated with the low sintering effects achieved at 750 ℃.

5.3.3 Surface chemistry of Ga_2O_3 nanorods/nanowires

Fig. 5.4 presents the XPS results of the heat treated Ga_2O_3 nanorods/nanowires. All the data were calibrated by using a carbon (C) peak at 284.8 eV and analyzed with the MultiPak software using the Shirley background. The survey scans in Fig. 5.4(a) confirmed the existence of Ga and O species in all samples and chromium (Cr) impurities. The high-resolution XPS spectra of the $Ga\ 2p$ electronic states in Fig. 5.4(b) revealed a spin-orbit splitting energy of $26.9 \pm 0.1\ eV$ in all the spectra. This confirmed the successful crystallization of Ga_2O_3 in all samples [190]. Structurally, the $\alpha - Ga_2O_3$ and $\beta - Ga_2O_3$ present specific arrangement of oxygen atoms around gallium atoms [33] leading to variations in $Ga - O$ bond lengths. These variations impact the core-level binding energies and consequently, the XPS line widths. This may be the reason for the observed variations in line widths of the $Ga2p$ peaks in the $\alpha - Ga_2O_3$-dominated (S550, S650) and $\beta - Ga_2O_3$ samples (S750, S850, S950).

Furthermore, the oxygen species on the surface of the annealed oxides presented broad and asymmetric $O\ 1s$ core-level spectra as shown in Fig. 5.4(c). These spectra were each fitted with peaks representing lattice oxygen (O_L) and adsorbed molecular water[191,200]. The most intense

peaks located at 531.1, 530.9, 531.2, 530.9, and 531.0 eV correspond to O_L in the S550, S650, S750, S850, and S950 samples, respectively. Meanwhile, the peaks centered at 532.9, 532.9, 533.2, 532.4, and 532.4 eV are ascribed to water molecules adsorbed on to the surface of the

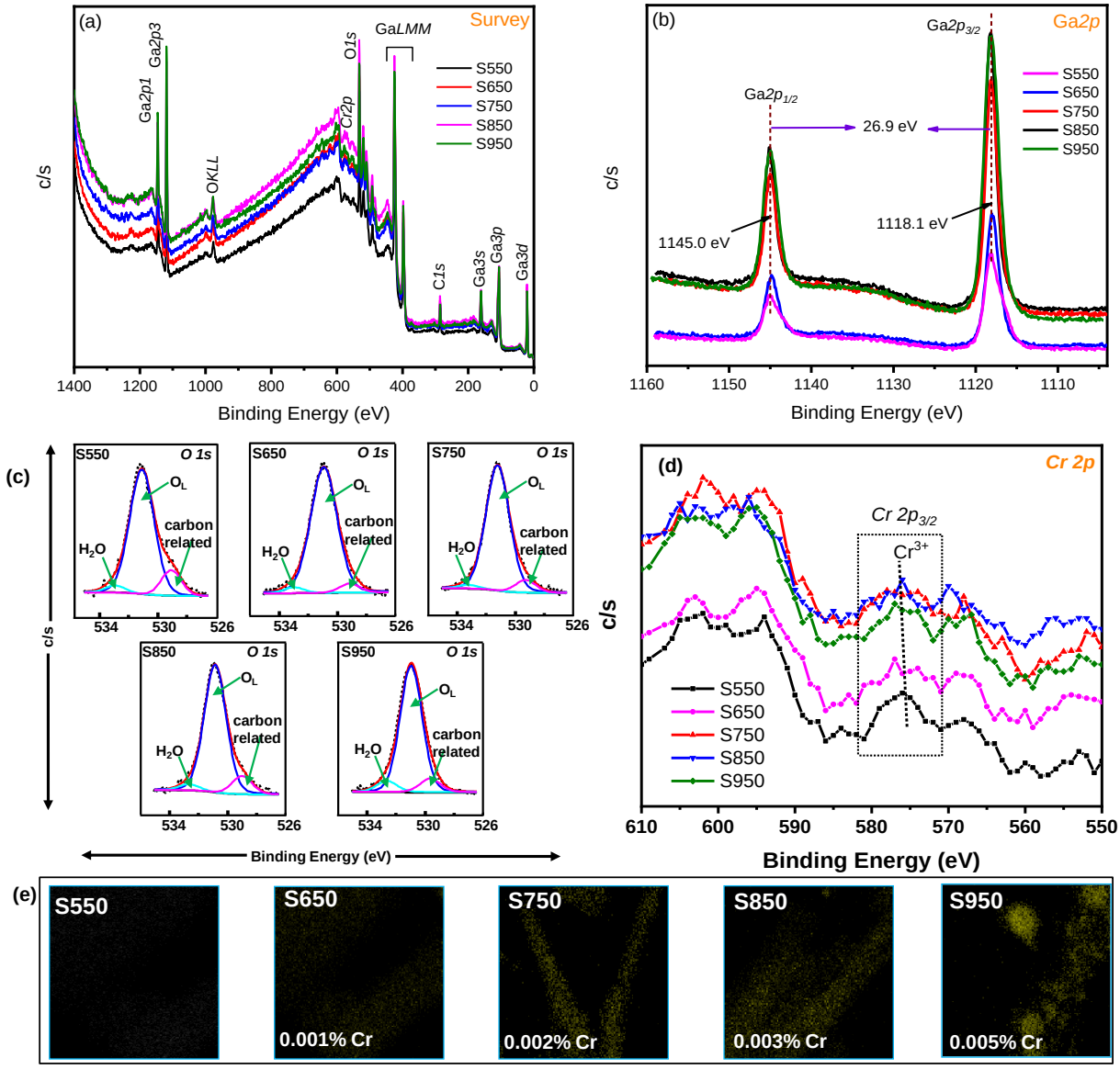


Fig. 5.4. *(a) X-ray photoelectron spectroscopy survey spectra and (b-d) high resolution spectra of Ga 2p, O 1s, and Cr 2p core-levels of heat-treated Ga_2O_3 nanorods/nanowires. (e) STEM images of the Ga_2O_3 samples heat treated as indicated. S550, S650, S750, S850, and S950 represent Ga_2O_3 powders heat treated at 550, 650, 750, 850, and 950 ℃, respectively.*

S550, S650, S750, S850, and S950 samples, respectively. These positions fairly agree with those reported in the literature for Ga_2O_3 and other various metal oxides [191,201]. However, for better fitting of the measured data, another peak was fitted at 529.3 ± 0.4 eV, in all the samples. The same peak was recently observed by Chowdhury [201] from annealed Ga_2O_3 films and was attributed to the presence of carbon. In the cited study, the peak disappeared after sputtering the sample by Ar^+ ion. In this study, the same attribution to carbon was adopted and carbon was from the carbon tape on which the sample was mounted for the XPS measurements. However, the peak did not completely disappear after Ar^+ sputtering because of more carbon tape exposed due to small amount of the sample deposited on the carbon tape. Furthermore, by first excluding the carbon-related peak, the area contributions of the O_L and O_C defects to the overall $O\ 1s$ peak were calculated. The results revealed that all the samples composed of 96 ± 2% of lattice oxygen and 4 ± 1% of adsorbed water molecules, demonstrating less significant effect of varying the heat treatment temperature.

Furthermore, the properties of Cr defects, which are a common impurity in hydrothermally synthesized Ga_2O_3 materials were studied, and the related peaks are shown in Fig. 4(d). Although the peak presented low signal to noise ratio, a peak centred at 575.6 ± 0.4 eV was identified in all the samples and attributed to the Cr^{3+} state of the $Cr\ 2p_{3/2}$ component belonging to the $Cr\ 2p$ spin-orbit doublets [202]. Identification of other oxidation states of Cr was impossible because of the low signal to noise ratio. This low signal from Cr indicates that the impurities are present at very low concentrations. To further confirm the existence of Cr defects on the surface of Ga_2O_3 samples, chemical mappings were recorded by surface scanning TEM (STEM), and the images are shown in Fig. 4(e). The results demonstrate that the Cr^{3+}

impurities in synthesized Ga_2O_3 nanorods/nanowires were present at less than 0.01%. As reported in the literature [97,203], these background Cr impurities are inherent in the high purity (99.9%) $Ga(NO_3)_3.xH_2O$ precursor used to synthesize Ga_2O_3. According to the supplier, this precursor contains Cr impurities at a level of $\leq$ 0.1%. Furthermore, the STEM results demonstrate an increase in Cr concentration at the surface of Ga_2O_3 samples with an increase in the heat treatment temperature. The same effect was recently observed from Ga_2O_3 calcined at ~1000 ℃ and it has been reported that the concentration increases due to promoted out-diffusion of the Cr towards the surface of Ga_2O_3 [204]. Based on the cited discussion, out diffusion of Cr could be the reason for its varying concentration on the surfaces of the heat-treated Ga_2O_3 nanowire/nanorod samples.

To complement the surface composition of the samples with bulk-defect characteristics, room temperature PL measurements were taken under unchanged conditions for all samples. As revealed in Fig. 5.5(a), all the samples emitted in the 350-800 nm wavelength regions of the electromagnetic spectrum. The emission spectra were each fitted with Gaussian peak components attributed to UV (~ 2.9 eV), blue/green (~ 2.3 – 2.5 eV), and red (~1.6 eV) emission. The UV emission arose from the recombination of free electrons with self-trapped holes positioned at the lattice oxygen sites [187], while the blue/green peaks originated from the recombination involving donor states at the V_O site and acceptor states created by the gallium vacancy (V_{Ga}) or gallium-oxygen vacancy pairs (V_{Ga}-V_O) [205]. The red emission was attributed to the electronic transitions between the energy levels of the Cr^{3+} ions background impurities present in the Ga_2O_3 powders [97,198]. The red emission particularly arises from the electron transitions from the $^4T_2$ and ^2E states to the $^4A_2$ levels of the Cr^{3+} impurities [203]. The

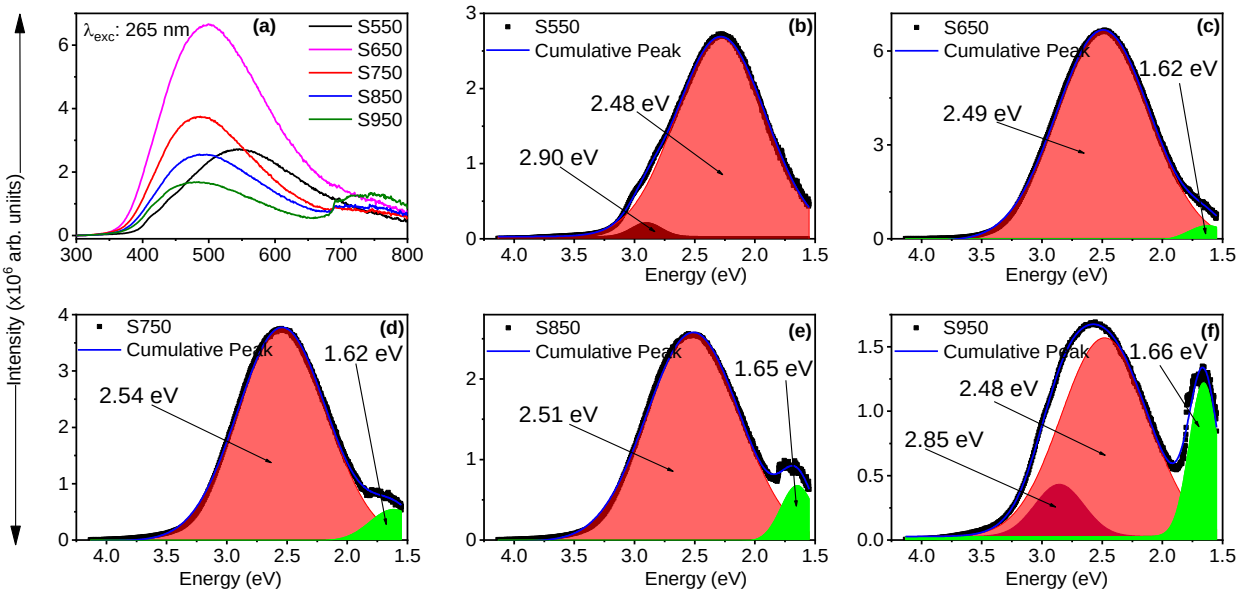


Fig. 5.5*. (a) As-measured and (b-f) deconvoluted room-temperature photoluminescence emission spectra of heat treated Ga_2O_3 nanorods/nanowires. S550, S650, S750, S850, and S950 represent Ga_2O_3 powders heat treated at 550, 650, 750, 850, and 950* ℃*, respectively.*

responsible excitation of Cr^{3+} defects is through sensitization by the intrinsic defects present in the band gap of Ga_2O_3 [204]. Also noteworthy the split of the ^4T and ^4A energy levels is significantly influenced by the crystal field of the Ga_2O_3 lattice [198], and hence the intensity variation in the Cr^{3+} luminescence observed from $\alpha - Ga_2O_3$, $\alpha/\beta - Ga_2O_3$, and $\beta - Ga_2O_3$ crystal structures shown in Fig. 5(b-f). In particular, the intensity of this peak increased with increasing heat-treatment temperature and this effect is attributed to diffusion of Cr impurities from the bulk to the surface of Ga_2O_3, observed from STEM (Fig. 4(e)). Similar diffusion of Cr in annealed Ga_2O_3 was observed by Wu *et al*. [204] through secondary-ion mass spectrometry (SIMS) measurements, and it was further linked to an increase in the carrier mobility and carrier density in the samples through performed Hall measurements. Although we did not perform measurements to determine the density and mobility of carriers in our samples, we will base our

discussion on the fact that the cited literature observed similar trends in their PL results. Therefore, we will assume that our samples will also demonstrate variations in conductivity (and response to the presence of gases) due to the presence of background Cr impurities which out-diffused to the surface of the sample at different concentrations due to different annealing temperatures.

5.3.4 Gas-sensing characteristics of Ga_2O_3 nanorod/nanowire-based gas sensors

Fig. 5.6(a) presents the electrical resistances of all the Ga_2O_3-based sensors in air and 90 ppm CO in the range of 100 to 180 ℃. The decrease in both R_a and R_g observed with increasing temperature is ascribed to the increased mobility of thermally generated electrons, and the trend observed for the sensors in CO confirms the *n*-type behavior of all the sensors. Optimization of the gas sensor operating temperature is necessary for regulation of the sensing process and sensor operating costs [14]. Therefore, the relationship between the response of Ga_2O_3 sensors in 90 ppm CO and their operating temperature was further studied, and the outcomes are shown in Fig. 5.6(b). All sensors presented low response signal-to-noise-ratio at room temperature, 40, 60 and 80 ℃, therefore those data points are not included in Fig. 5.6(b). The recorded responses of all sensors revealed an increase with increasing operating temperature until they reached the optimum response at 165 ℃ then decreased at 180 ℃. This observed trend indicates the effects of slow kinetics at lower temperatures and gas desorption at high temperatures [18]. Therefore, 165 ℃ was adopted for further gas sensing analyses.

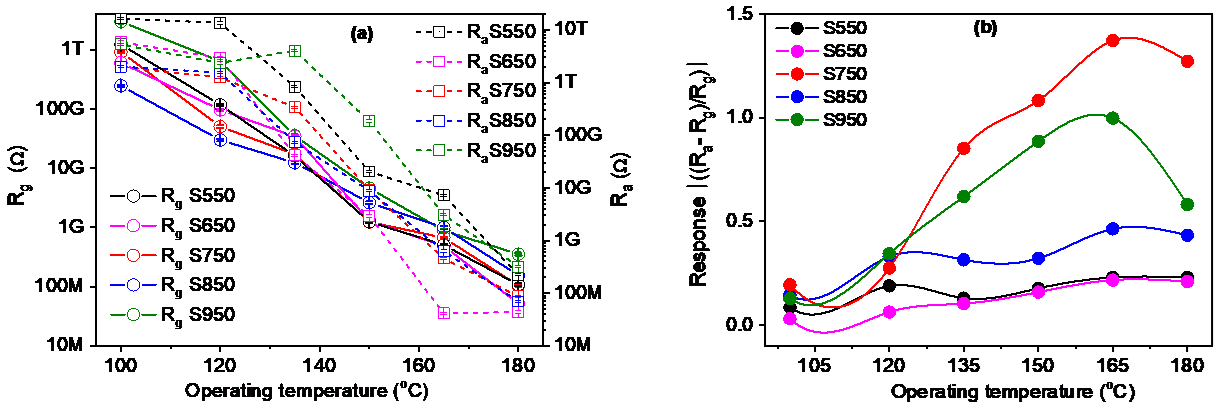


Fig. 5.6*. (a) Electrical resistance in air (R_a) and 90 ppm CO (R_g) versus operating temperature of the Ga_2O_3 sensors. (b) Sensor response towards 90 ppm CO at the various operating temperatures. S550, S650, S750, S850, and S950 represent Ga_2O_3 powders heat treated at 550, 650, 750, 850, and 950* ℃*, respectively.*

To determine the sensing capabilities of all Ga_2O_3-based sensors in a wide detecting concentration range, the dynamic resistance-transient curves towards different CO concentrations from 10 to 90 ppm were measured at 165 ℃ as illustrated in Fig. 5.7(a). The resistances of all sensors rapidly decreased when exposed to each concentration of CO and reached a saturation point during CO adsorption and then increased instantly back to the baseline resistance during desorption when CO was removed from the system. The S750, S850, and S950 $\beta - Ga_2O_3$-based sensors showed higher resistance modulation than the $\alpha - Ga_2O_3$-based sensors. Furthermore, the resistance modulation increased continuously upon increasing CO concentration as shown in Fig. 5.7(b). This is attributed to increased number of CO molecules available to interact with the Ga_2O_3 gas sensing layers. Fig. 5.7(c) demonstrates the relationship between CO concentration and the responses of all sensors plotted on a log-scale as guided by the linear calibration model of SMO-based gas sensors [70]. All sensors presented good linearity between the concentration of the gas and the sensor response. The limit of detection (LoD)

values of 3.6, 5.1, 2.3, 4.5, and 2.3 ppm were obtained as the lowest concentration that a sensor was capable of detecting with a 3:1 signal-to-noise ratio for S550, S650, S750, S850, and S950 sensors, respectively. According to Occupational Safety and Health Administration (OSHA),

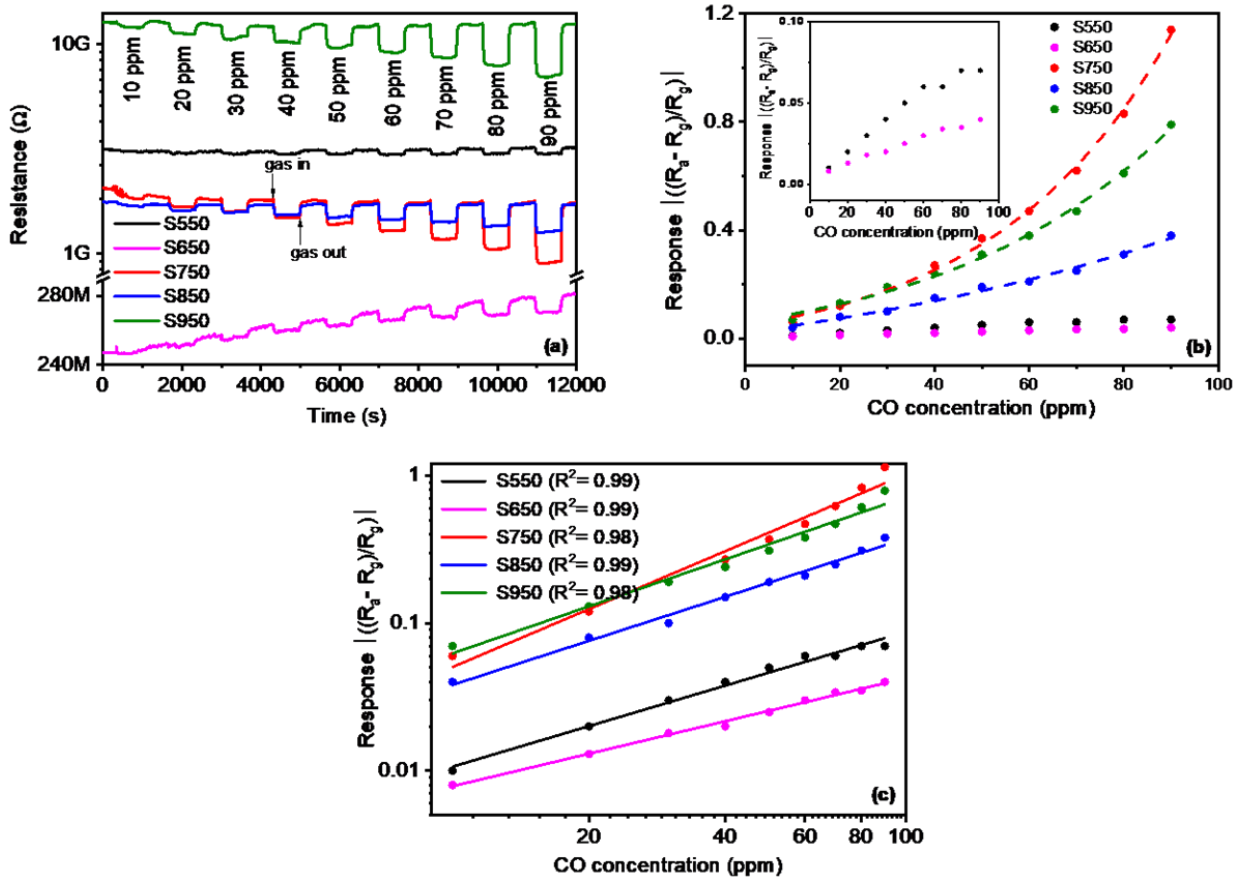


Fig. 5.7. *(a) Dynamic resistance transient curves and (b, c) response against CO concentrations at 165* ℃ *of Ga_2O_3 nanorods/nanowires heat treated at 550* ℃ *(S550), 650* ℃ *(S650), 750* ℃ *(S750), 850* ℃ *(S850), and 950* ℃ *(S950).*

human exposure to 87.1 ppm CO for 15 minutes may increase carboxyhemoglobin level to above 2.5% causing neurological disorders, cardiovascular diseases and possibly fatalities [194]. Therefore, the Ga_2O_3-based sensors could be useful for the sensing of low CO concentrations to prevent inhalation for the purpose of air quality monitoring and control. Furthermore, the

sensitivity of each sensor which is the sensor response per analyte gas concentration was also extracted from slope of the calibration line based on Equation 2.1. Sensitivity values of 0.91, 0.73, 1.30, 0.99, and 1.06 ppm^{-1}, were obtained for S550, S650, S750, S850, and S950 sensors, respectively.

The lower limit of detection and higher sensitivities displayed by the $\beta - Ga_2O_3$ based sensors towards CO may suggest higher surface reactivity of $\beta - Ga_2O_3$ compared to that of $\alpha - Ga_2O_3$-containing sensors nanorods/nanowires caused by the presence of Cr^{3+} impurities [38,206]. Additionally, larger surface areas of S750 and S950 sensors also offer more active space for interactions with CO molecules which improves the sensor sensitivity to CO. On the other hand, the $\alpha - Ga_2O_3$ and $\alpha/\beta - Ga_2O_3$-based sensors showed low Cr^{3+} densities and still presented measurable responses and comparable sensitivities and LoDs. This can be ascribed to their measurable sensitivities which allow the interaction between the CO gas molecules and the surface of the sensors.

The selectivity of all the sensors was studied when all sensors at 165℃ were exposed to 90 ppm of CH_4, C_2H_4, NH_3, NO_2, and SO_2 gases and the results are presented in Fig. 5.8(a). The $\beta - Ga_2O_3$-based sensors (S750, S850, S950) showed high response toward CO with S750 presenting a highest response of 1.18. The $\alpha - Ga_2O_3$ phase (S550) responded better to SO_2 and the $\alpha/\beta - Ga_2O_3$ co-phase (S650) displayed high response towards CH_4 and NH_3 gases.

To further evaluate performance of the $\alpha - Ga_2O_3$ and $\alpha/\beta - Ga_2O_3$-based sensors, their response to selected target gases (SO_2, NH_3 and CH_4), for which they demonstrated high

responses, were measured at 135, 150 and 180 ℃. This characterization enabled the optimization of sensor operating temperatures for these two phases. Fig. 5.8(b) shows that the $\alpha - Ga_2O_3$ and $\alpha/\beta - Ga_2O_3$ sensors recorded the highest responses toward SO_2 and NH_3, respectively, at 180 ℃. Therefore, an operating temperature of 180 ℃ was adopted for further characterizations of the S550 and S650 sensors.

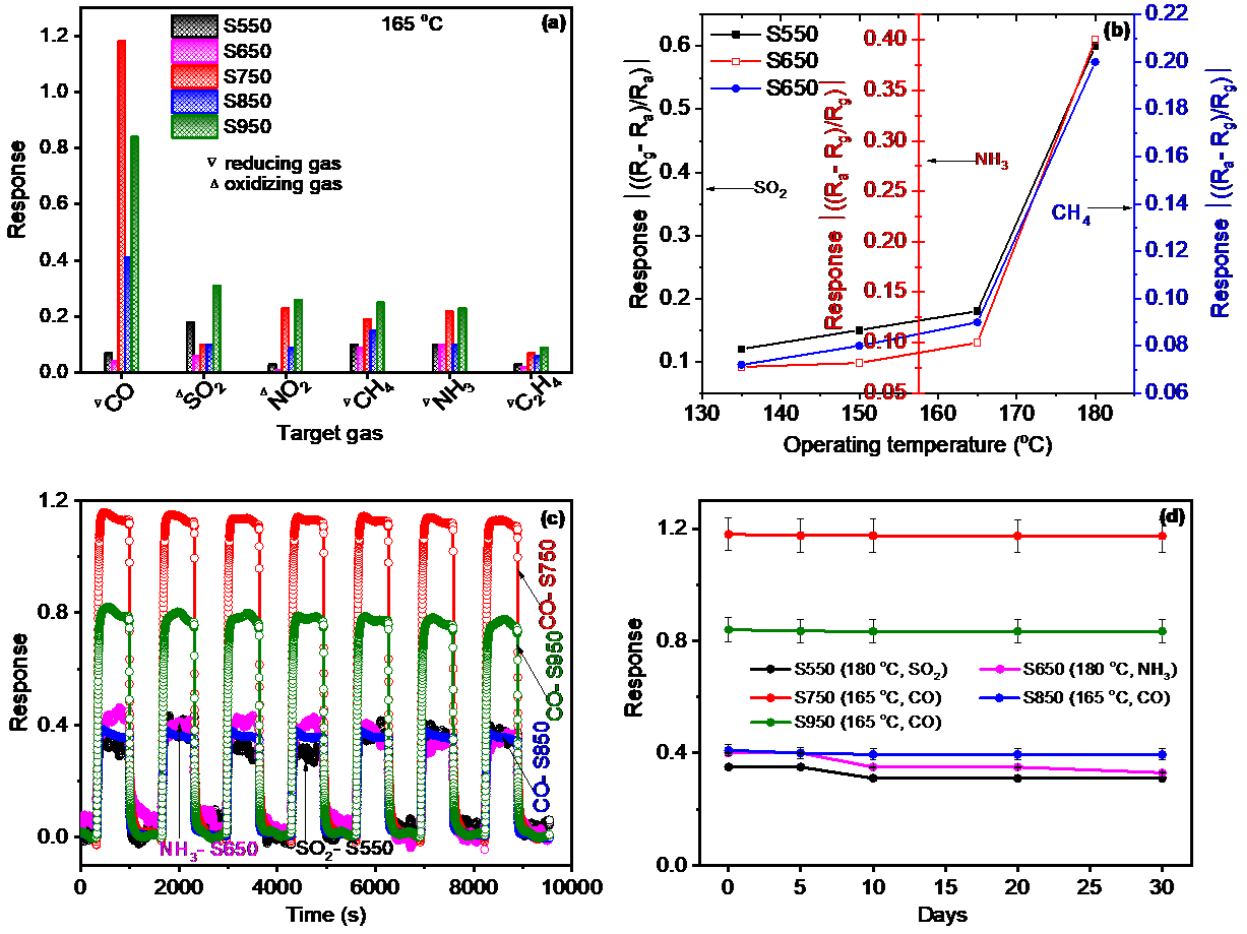


Fig. 5.8. *(a) Responses of Ga_2O_3 sensors at 165 ℃ towards 90 ppm of different gases. (b) responses of S550 and S650 sensors towards 90 ppm of SO_2, CH_4 and NH_3 gases at various operating temperatures. (c) reproducibility and (d) stability curves of the sensors. S550, S650, S750, S850, and S950 represent Ga_2O_3 powders heat treated at 550, 650, 750, 850, and 950 ℃, respectively.*

The ability of each sensor to produce repeatable sensor response signal was evaluated and the results are presented in Fig. 5.8(c). The repeatability curves demonstrate constant sensor responses with negligible variations over seven cycles of target gases, which indicated good reproducibility from all the sensors. Furthermore, the long-term stability of the sensors was studied over 30 days period with the sensors under the same conditions. The stability curves shown in Fig. 5.8(d) demonstrate good long-term sensor stability within experimental error towards the detected gases.

Environmental humidity affects the frequency of gas adsorption and sensitivity of the sensing material, and this complicates the realization of sufficiently sensitive gas sensor for real-world application. To evaluate the analytical impacts of humidity on the sensing properties of Ga_2O_3-based sensors, all the sensors were tested in 90 ppm of the selected gases under 0%, 60% and 90% relative humidity (RH), and the results are presented in Fig. 5.9(a-c). The responses of all sensors decreased, and the sensor response/recovery times were prolonged in humidity. The decrease in the sensor responses can be attributed to reduced active sites available for the adsorption of oxygen species and gas-oxide surface interactions [18] as a result of pre-adsorption of water vapor molecules. Hence, the response times (t_{res}) and recovery times (t_{rec}) of all the sensors in 0%RH were studied, and the outcomes are presented in Fig. 5.9(d). All $\beta - Ga_2O_3$-based sensors (i.e., S750, S850, S950) presented sub-minutes response/recovery times with the S850 sensor showing the shortest sub-minute response/recovery times of 29/24 seconds toward CO. On the other hand, the $\alpha - Ga_2O_3$ and $\alpha/\beta - Ga_2O_3$ based sensors showed longer response/recovery times ascribed to low surface activity of the sensors. The sub-minute

response/recovery times presented by all the Ga_2O_3 sensors enable rapid detection of CO, SO_2, and NH_3 gases and reusability of the sensors.

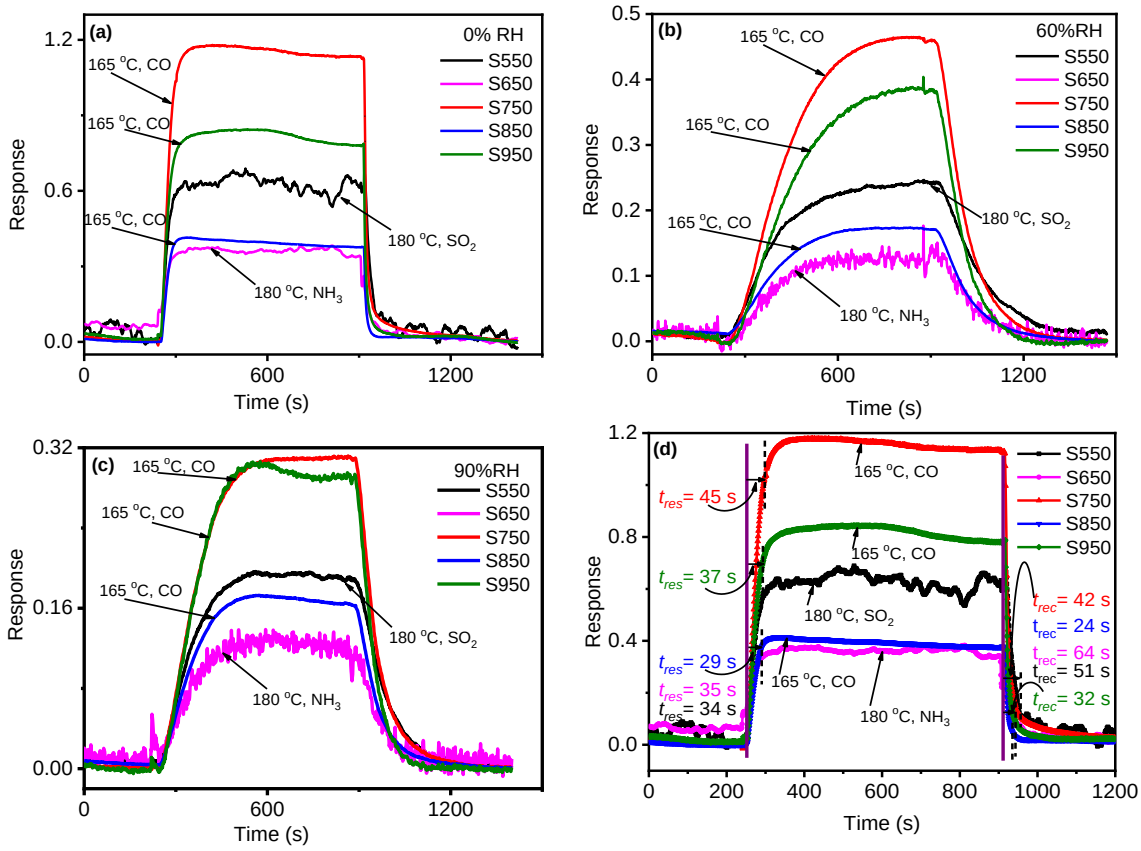


Fig. 5.9. *Response of the Ga_2O_3 nanorod/nanowire-based sensors under (a) dry (0%RH), (b) 60%RH, and (c) 90%RH. (d) response/recovery curves of the sensors. S550, S650, S750, S850, and S950 represent Ga_2O_3 powders heat treated at 550, 650, 750, 850, and 950 ℃, respectively.*

The performances of all the Ga_2O_3 sensors characterized in this study were compared in Table 5.1 with those of most previously reported Ga_2O_3-based sensors and other $1D$ and nanostructured SMO-based sensors reported in the literature over the past five years (2018-2023). It can be inferred from this comparison that the $\beta - Ga_2O_3$ sensors-based on the nanorod/nanowire morphology present highly selective, sensitive and rapid detection of low

concentrations of CO at relatively lower sensor operating temperatures compared to pristine or modified ZnO and Ga_2O_3 nanorods [35,44,100,108,207]. It is worth noting that the gas sensing performance of our $\beta - Ga_2O_3$ nanorod/nanowires was similar to that of CuO nanotubes operated at 175 ℃ [208]. Improved sensor performance of the Ga_2O_3 nanorod/nanowire-based sensors implies that interaction between nanorods and nanowires contribute significantly to the electron transport behavior and sensitivity of the material. The performances of $\alpha - Ga_2O_3$ and $\alpha/\beta - Ga_2O_3$ were in general poorer than those cited in Table 5.1. Nevertheless, these two phases hold a promise to serve as future candidates for the detection of toxic gases. Therefore, sensing mechanisms for the detection of CO, NH_3 and SO_2 by the *n*-type $\alpha - Ga_2O_3$, $\alpha/\beta - Ga_2O_3$ and $\beta - Ga_2O_3$ nanorods/nanowires are proposed in this study.

Table 5.1. Summary of CO, SO_2 and NH_3 gas sensing performance of different $1D$ SMO-based sensing materials. (Key: NTs- nanotubes, NRs- nanorods, NPs- nanoparticles, CNT- carbon nanotubes. Res.- response, Ref.- reference, ± - a percentage fraction of ambient air, T – operating temperature, + - LoD). Responses were calculated using the following formulas: $*(R_a - R_g)/R_g$, $**((R_a - R_g)/R_g) \times 100\%$, $§(R_g - R_a)/R_a$, $§§((R_g - R_a)/R_a) \times 100\%$, $\&R_a/R_g$, $\&\&R_g/R_a$, $\$(R_a/R_g) \times 100\%$, and $\$\$(G_g - G_a)/G_a)$ where G is the electrical conductance.

Gas	Material	Conc. (ppm)	T (℃)	t_{res} (s)	t_{rec} (s)	Res.	Ref.
CO	CuO NTs	100 ($^{+}$0.6)	175	24	29	$^{\&\&}$1.55	[208]
	$PbS - ZnO$ NRs	300	300	119.6	223.8	§§122%	[207]
	$PbS - CrZnO$ NRs	300	300	117.0	237.7	§§195.2%	[207]
	$\beta - Ga_2O_3$(Sn) NRs– 750	115	500	-	-	$^{\$\$}$1.02	[108]
	$\varepsilon - Ga_2O_3$	$^{±}$1.5%	500	-	-	**25%	[109]
	$\beta - Ga_2O_3/LSFO$ NRs	100	500	~200	~500	*~70	[100]
	$\beta - Ga_2O_3$ NWs	200	200	-	-	§3.95	[104]
	$\beta - Ga_2O_3$ NWs	100	100	440	300	**6.61%	[35]
	$Pt/\beta - Ga_2O_3$ NWs	100	100	650	750	**111.65%	[35]
	$Au/\beta - Ga_2O_3$ NWs	100	RT	21.14	21.34	**~4.8%	[44]
	$\beta - Ga_2O_3$(Sn) - 950	120	500	-	-	$^{\$\$}$1.3	[108]
	$\beta - Ga_2O_3$ -750 NRs/NWs	90 ($^{+}$2.3)	165	45	42	*1.18	This work
	$\beta - Ga_2O_3$ -850 NRs/NWs	90 ($^{+}$4.5)	165	29	24	*0.41	This work
	$\beta - Ga_2O_3$ -950 NRs/NWs	90 ($^{+}$2.3)	165	37	32	*0.84	This work
SO_2	$Pt - WO_3$ NPs	8 ($^{+}$0.1)	160	150	200	$^{\&}$17.07	[209]
	$Al - WO_3$ NPs	8 ($^{+}$0.1)	290	10	20	$^{\&}$2.6	[209]
	$\alpha - Ga_2O_3$ NRs/NWs	90	165	34	51	§0.6	This work
NH_3	$Sn - TiO_2@rGO/CNT$	250	RT	99	66	**85.9%	[210]
	$\beta - Ga_2O_3$ NRs	160	RT	-	-	§§~185%	[36]
	$\beta - Ga_2O_3$ (Sn) NRs -1000	115	500	-	-	$^{\$\$}$1.1	[34]
	$\beta - Ga_2O_3$ NWs	200	150			$^{\$}$~119%	[102]
	$\alpha/\beta - Ga_2O_3$ -650 NRs/NWs	90	165	36	64	*0.4	This work

5.3.5 Gas sensing mechanism of Ga_2O_3 nanorods/nanowires-based sensors

The gas sensing mechanism of gas sensors based on SMOs such as Ga_2O_3 is attributable to the chemisorption of oxygen on the SMO surface along with the subsequent reaction between adsorbed oxygen species and tested gas resulting in electrical resistance change [10,63]. The similar gas sensing principle has been adopted to describe the CO, NH_3, and SO_2 sensing properties of *n*-type Ga_2O_3 nanorods/nanowires in this study. In air, molecular oxygen (O_2) adsorbs on the surface of Ga_2O_3 nanorods/nanowires and attracts electrons to form O^{2-}, O^-, and O_2^- species through temperature-dependent reactions [18]. At 165 and 180 ℃, the O^- species are formed by the reaction presented in Equation (5.1) [18]. As a result, a thick electron depletion layer is formed near the surface of Ga_2O_3 nanorods/nanowires as presented in Fig. 5.10(b) and the electrical resistance increases. When the Ga_2O_3 nanorods/nanowires-based sensor is exposed to CO, NH_3 reducing gases, the surface pre-adsorbed O^- species react with the target gas molecules according to Equations (5.2) and (5.3) and the previously captured electrons are released back to the conduction band of the nanowires/nanorods. The electron concentration increases as shown in Fig. 5.10(c) and the resistance of the Ga_2O_3 nanorods/nanowires decreases. However, exposure of the Ga_2O_3 nanorods/nanowires-based sensor to SO_2, which is an oxidizing gas, the pre-adsorbed O^- oxidizes the target gas molecules according to Equation (5.4) and more electrons are drawn from the surface of Ga_2O_3 nanorods/nanowires. This leads to the widening of the electron depleted layer and a higher electrical resistance as illustrated in Fig. 5.10(e) [43].

$$O_{2(ads)}^- + e^- \rightarrow 2O_{(ads)}^- \qquad (100 < T_{oper} < 300\ ℃) \tag{5.1}$$

$$2CO_{gas} + 2O_{(ads)}^- \rightarrow 2CO_{2(gas)} + 2e^- \tag{5.2}$$

$$2NH_{3(gas)} + 3O^-_{(ads)} \rightarrow N_{2(gas)} + 3H_2O + 3e^- \quad (5.3)$$

$$SO_{2(gas)} + O^-_{(ads)} \rightarrow SO^-_{3(ads)} \quad (5.4)$$

The high gas sensing performances observed from the $\beta - Ga_2O_3$-based sensors originated from a combination of the large specific surface area and high porosity. The large surface area offered plenty of adsorption sites and porosity allowed diffusion of the gas analytes into the grains and improved the oxide-gas interactions. Furthermore, the presence of Cr impurities contributed towards high sensor conductivity while the oxygen vacancies created more adsorption sites for oxygen species leading to improved surface interactions between a target gas and $\beta - Ga_2O_3$ nanorods/nanowires.

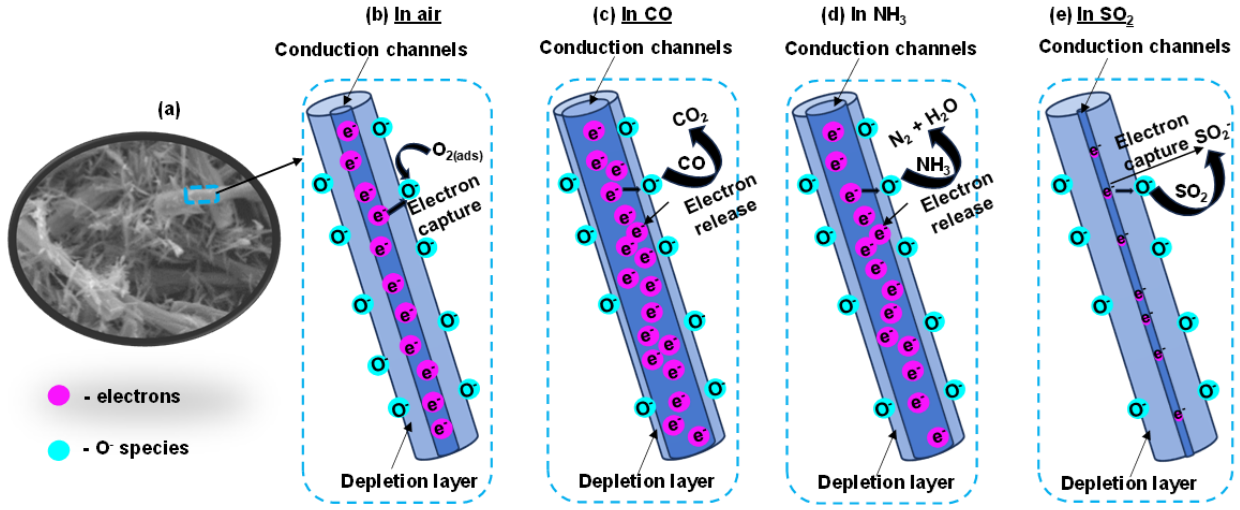


Fig. 5.10. *(a) Scanning electron microscopy image of the synthesized Ga_2O_3 nanorods/nanowires; the gas sensing mechanism of n-type Ga_2O_3 nanorods/nanowires in (b) air and toward (c) CO, (d) NH_3 and (e) SO_2 gases.*

5.4 Conclusion

Ga_2O_3 nanorods/nanowires were synthesized using the microwave-assisted hydrothermal method. $\alpha - Ga_2O_3$, $\beta - Ga_2O_3$, and $\alpha/\beta - Ga_2O_3$ polymorphs were obtained after calcining at different temperatures and the formation of these phases was confirmed by the XRD and XPS techniques. Furthermore, the XPS data and PL data demonstrated changes in defect densities present in the samples induced by variation of the heat treatment temperature. Incidental Cr impurity was detected in the samples by PL spectroscopy and XPS. The gas sensing results demonstrated higher gas sensing performances of $\beta - Ga_2O_3$ than the $\alpha - Ga_2O_3$ and $\alpha/\beta - Ga_2O_3$ sensors, ascribed to the high catalytic activity, larger surface area and high porosity and the presence of incidental Cr impurity. The $\beta - Ga_2O_3$-based sensors showed the highest response towards CO at 165 ℃ while the $\alpha - \mathrm{Ga_2O_3}$ and $\alpha/\beta - Ga_2O_3$-based sensors showed the highest response towards SO_2 and NH_3, respectively, at 180 ℃.

CHAPTER 6

Effects of reaction pH control on regular nanorods and hierarchically structured $\beta - Ga_2O_3$ and their isopropanol sensing capabilities

6.1 Introduction

Volatile organic compounds (VOCs) such as toluene, ethanol, benzene, acetone, and isopropanol are commonly found in commercial products including perfumes, cosmetics, and glues [211]. However, their substantial release to indoor environments may result in short and long-term detrimental consequences on human health. The short-term impacts vary from irritation of the respiratory tract and eyes while the long-term effects may include cancer and renal failure [211,212]. In the case of isopropanol, continuous exposure, and inhalation of 400 ppm may lead to mild and severe skin irritation and dizziness [213]. Therefore, real-time identification of isopropanol is vital for indoor environmental monitoring and control.

Spectroscopic techniques, such as chromatography, are currently utilized for the accurate detection of VOCs. However, these methods often require skilled personnel and expensive instruments, making chromatography challenging for real-time monitoring of the VOCs. Therefore, other portable, low-cost, and reliable methods for the detection of VOCs are being investigated. Different sensing materials have been studied for accurate detection of the VOCs. Among these materials, the chemiresistive semiconductor metal oxides (SMOs) gas sensors have gained special attention because of their simple circuit design, easy and inexpensive fabrication process, long-term stability, and high sensitivity.

Among SMOs that have been previously explored for the detection of VOCs is gallium oxide (Ga_2O_3). Ga_2O_3 can crystallize in five polymorphic forms, namely $\alpha - Ga_2O_3$, $\beta - Ga_2O_3$, $\gamma - Ga_2O_3$, $\delta - Ga_2O_3$, and $\varepsilon(\kappa) - Ga_2O_3$. Among these polymorphs, the $\beta - Ga_2O_3$ is the most thermally stable hence mostly studied for gas sensing applications. In addition, $\beta - Ga_2O_3$, usually *n*-type, has a band gap of ~ 4.9 eV, high free electron concentration (10^{16} – 10^{20} cm^{-3}), and electron mobility (200 $cm^2V^{-1}s^{-1}$), making it an appropriate candidate for application in gas sensing. Nanostructured $1D$ $\beta - Ga_2O_3$ materials have been extensively explored for sensing of various gases such as NH_3, O_2, CO at different operating temperatures [42]. However, challenges related to selectivity and high operating temperatures still hinder practical usage of $\beta - Ga_2O_3$ for gas sensing. Therefore, different morphological features from $1D$ to $3D$ exhibiting improved sensitivity are regarded as alternatives to overcome this challenge. For instance, one-dimensional ($1D$) SMO nanostructures such as nanowires, nanorods, nanobelts, have been found to exhibit excellent VOCs sensing capabilities owing to their high aspect ratio which offer fast electron transfer and more gas sensing activity sites. In addition, nanostructured $1D$ SMOs present unique physical and chemical properties. On the other hand, $3D$ hierarchical structures assembled from nanostructured $1D$ features have recently been generating interest as potential sensing materials for the recognition of VOCs. This is because they provide large surface area and particle-to-particle interaction which facilitates fast interfacial interaction and charge transport for enhanced sensor performances [32].

In the case of Ga_2O_3 materials, previous findings have revealed that their morphological behavior strongly depends on control of various parameters such as reaction pH, among other things, during the synthesis process. For instance, Pilliadugula and Krishna [36] reported that

when the pH condition is varied between alkaline and basic, the excess OH^- species are absorbed on the primary crystal facets, and this hinders the preferential growth thus favoring selective absorption of the OH^- ions. Under such conditions, the isotropic attachments and growth of $GaOOH$ crystals with low-aspect ratio and hierarchical structures occur. The findings of Pilliadugula and Krishna revealed that pH variation from 7 to 14 resulted in the formation of nanorod-like, cocoon-like, and hierarchical structures. Besides, studies conducted on the utilization of undoped $\beta - Ga_2O_3$ as sensing materials for VOCs detection are still rare. Park *et al.* [45] produced $\beta - Ga_2O_3 - WO_3$ heterostructures and observed remarkably improved sensor response and the response/recovery times towards 200 ppm ethanol at 200 ℃ compared to the ethanol sensing performances of undoped $\beta - Ga_2O_3$ nanostructures. The observed improved ethanol sensing capability was ascribed to synergistic effects of electron depletion and potential barrier-dependent carrier transport. Jang *et al.* [41] prepared $\beta - Ga_2O_3/SnO_2$ core-shell nanowires and demonstrated a high response of ~ 100 towards 1000 ppm of ethanol gas at a sensor operating temperature of 600 ℃. Jin *et al.* [122] studied the effects of encapsulating $\beta - Ga_2O_3$ nanorods with ZnO on the NO_2 sensing capabilities of the material. The results revealed that the encapsulated nanorods presented an improved response towards 100 ppm than that was presented by $\beta - Ga_2O_3$ nanorods [122]. Based on these previous reports on $\beta - Ga_2O_3$ as VOCs detection platform, the operating temperatures are still high, and sensitivity and selectivity require improvement.

This work focused on the preparation of surface engineered 1D nanorods and 3D hierarchical $\beta - Ga_2O_3$ structures composed of nanorod features derived from a microwave-assisted hydrothermal method achieved through variation of the pH of reaction solution. The study was

aimed at lowering the operating temperatures and improving sensitivity and selectivity of $\beta - Ga_2O_3$ structures towards isopropanol. The structural, morphological, and chemical properties of the synthesized $\beta - Ga_2O_3$ nanostructures were investigated and correlated with their gas sensing behavior recorded towards various gas analytes. The study developed $\beta - Ga_2O_3$-based gas sensors operated at low sensor operating temperature. A sensing mechanism involved in the observed gas sensing performance of $\beta - Ga_2O_3$ is proposed.

6.2 Experimental section

6.2.1 Preparation of $\beta - Ga_2O_3$ nanorod-based nanostructures

Gallium oxide hydroxide ($GaOOH$) powders were synthesized by microwave-assisted hydrothermal method prior to their conversion into $\beta - Ga_2O_3$ powders. To prepare undoped $GaOOH$ powders, three portions of 0.26 g of $Ga(NO_3)_3 \cdot xH_2O$ (acquired from Sigma Aldrich) were each dissolved in 10 ml of DI water, separately to obtain 0.1 M Ga^{3+} concentrated solutions. While vigorously stirring these solutions on a magnetic stirrer, all three solutions were heated to a constant temperature of 60 ℃. Drops of NH_4OH solution were added to the solutions to achieve different pH levels of 7, 11, and 14. The pH value of each solution was measured prior to aging the solution for 1 hour. The three solutions were transferred to the microwave vessels and microwaved for 1 hour by using a Discover 2.0 microwave synthesizer set at 100 W and 150 ℃. The obtained cloudy white precipitates were washed with distilled water and ethanol, then dried in an oven set at 60 ℃ to form $GaOOH$ powders. The as prepared $GaOOH$ powders were heat treated in air in a muffle furnace maintained at 750 ℃, for 2 hours, at a ramping rate of

5 ℃$/min$ to produce $\beta - Ga_2O_3$ powders. The powders were labelled pH7, pH11 and pH14 in line with the pH of each.

6.3 Sample characterization

The crystal structure and morphology of the powders were characterized by a Bruker D2 Phaser X-ray diffractometer with $\lambda_{Cu\,K\alpha 1} = 0.15406\ nm$ radiation source and ZEIS-AURIGA field emission scanning electron microscope, respectively. The specific surface area and porosity of the powder samples were analyzed by a Micromeritics TriStar 300 analyzer. Chemical composition and defects were studied by X-ray photoelectron spectroscopy (XPS) using a PHI 5000 Versaprobe-Scanning ESCA Microprobe with monochromatic $Al\text{-}K\alpha$ radiation ($h\nu$ = 1486.6 eV).

6.4 Fabrication and testing of $\beta - Ga_2O_3$ nanorods-, nanobundles- and nanodandelions-based gas sensor films

To fabricate $\beta - Ga_2O_3$-based gas sensing films, 10 mg of each powder was ultrasonicated in 0.05 ml of ethanol to form a suspension which was drop-coated onto platinum electrodes interdigitated on an alumina substrate. All deposited films were annealed overnight at 300 ℃ for evaporation of ethanol and improved film-substrate adhesion. The gas sensing measurements were performed using a commercial KSGAS6S (KANOSISTEC, Italy) gas sensing station under both dry and humid atmospheric environments at different operating temperatures ranging from room temperature to 165 ℃ with a 2 V applied voltage across the sensors. Desired concentrations of the different gas analytes, in parts per million (ppm) were obtained as the ratios of synthetic air and compressed target gas. The target gases were commercially acquired in gas cylinders and

the flow rates were controlled by a mass flow controller. The variations in electrical resistances across each sensor were acquired by a KEITHLEY 6487 picoammeter/voltage source meter in air (R_a) and gas (R_g). Sensor response towards reducing and oxidizing gases was calculated from $\frac{R_a}{R_g}$ and $\frac{R_g}{R_a}$, respectively. The response time was measured as the duration taken to reach 90% of saturation resistance value and 10% above the base resistance upon injecting the target gas into the test chamber and stopping the target gas flow, respectively.

6.5 Results and discussion

6.5.1 Crystal structure analysis of $\beta - Ga_2O_3$ powders

After the successful synthesis of $\beta - Ga_2O_3$ powders, their crystal structures were verified by XRD analysis. Diffraction patterns in Fig. 6.1(a) reveal that all the powder samples were readily indexed to the monoclinic phase of Ga_2O_3, i.e., $\beta - Ga_2O_3$ (Entry no. 96-200-4988). Moreover, Fig. 6.1(b) revealed that increasing the pH value resulted in higher diffraction intensities and a shift of the diffraction peaks to lower 2θ angles coupled with decreasing values of the full width at half maximum (FWHM) for the (111) crystallographic plane. The FWHM values were 0.53, 0.51 and 0.48 ° for the pH7, pH11 and pH14 powders, respectively. This observation suggests higher degree of crystallinity and larger crystallite sizes present in pH11 and pH14 powder samples. The average crystallite sizes for all samples were calculated from the most intense $\beta - Ga_2O_3$ diffraction peak corresponding to (111) using a Debye-Scherrer formula [174]. The crystallite sizes were found to be 16, 17, and 18 nm, all with an error bar of ± 1 nm for pH7, pH11, and pH14 powder samples, respectively. The observed gradual increase in the crystallite sizes upon increasing the reaction pH value can be explained in terms of the increased rate of

nucleation resulting from lowered degree of supersaturation of the [Ga^{3+}] precursor solution [214]. At higher pH values, the surface of the adsorbent is negatively charged which increases the attraction of Ga^{3+} and crystal growth.

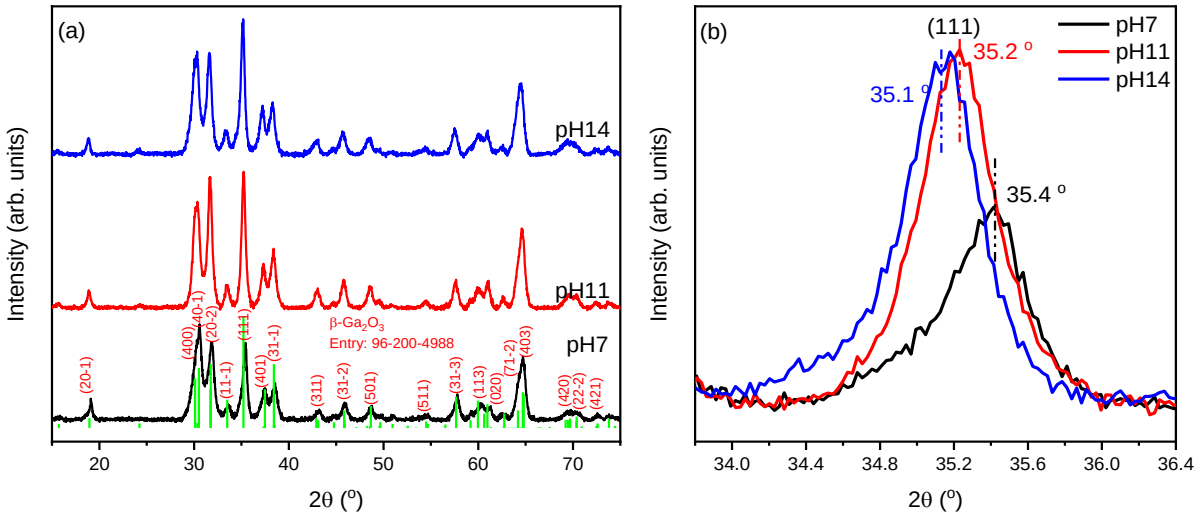


Fig. 6.1. *(a) Full-range X-ray diffraction patterns of $\beta - Ga_2O_3$ powders prepared using a microwave-assisted hydrothermal method at different reaction pH levels. (b) plot of the (111) X-ray diffraction peaks from the samples.*

6.5.2 Morphology characterization of $\beta - Ga_2O_3$ nanostructures

The effects of varying reaction pH on the morphological behavior of $\beta - Ga_2O_3$ powders were further investigated by FESEM, and the results are presented in Fig. 6.2. Microstructures with different shapes, produced by agglomeration of the nanorods were observed from FESEM micrographs as shown in Fig. 6.2(a-c). A pH value of 7 induced the formation of randomly oriented regular nanorods with uneven edges resulting from random attachment of nanoplatelet-like structures. Increasing the reaction to pH levels of 11 and 14 resulted in attachment of regular nanorods forming $3D$ bundle-like and dandelion-like hierarchical structures, respectively. These

results indicate the importance of the hydroxide ligand (OH^-) in the precipitation of the $GaOOH$ precursor. According to Cüneyt *et al*. [92], when NH_4OH is added to the reaction, it decomposes to produce OH^- and NH_4^+ ions. Then, the OH^- ligand forms a complex with Ga^{3+} ions in the solution according to Equation (6.1). Pilliadugula and Krishna [36] further stipulated that, generally, the OH^- ions preferentially adsorb along the *c*-crystallographic axis where there is low

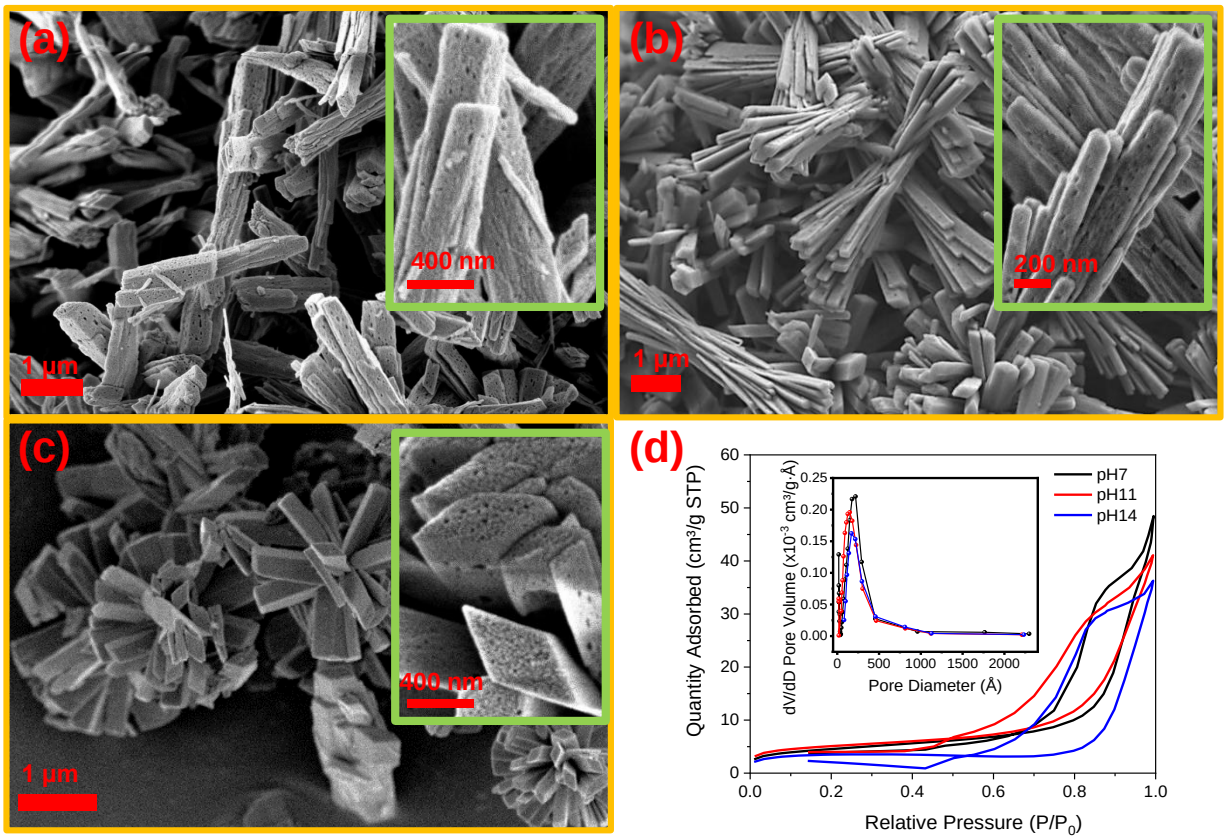


Fig. 6.2. *Field emission scanning electron microscopy images of* $\beta - Ga_2O_3$ *(a) nanorods, (b) nanobundles, and (c) nanodandelions prepared at the pH levels of 7, 11, and 14, respectively. (d)* N_2 *adsorption-desorption isotherms and pore size distribution of the nanorods, nanobundles and dandelions.*

density of unsaturated bonds, leading to the formation of nanorod-like units in most hydrothermally synthesized $GaOOH$ precursors. However, an increase in the pH value implies

increased concentration of OH^- ions and a subsequent formation of new complex $[Ga(OH)_6]^{3-}$ according to Equation (6.2) [36]. This acts as a new growth precursor to the $GaOOH$ seed obtained from Equation (6.1). This results in the oriented attachments as observed from the pH11 and pH14 samples [214]. Yue *et al*. [183] also suggested that the addition of NH_4OH alters the surface energy of nanorods such that the nanorods self-assemble into an oriented format.

$$Ga^{3+} + 3OH^- \leftrightarrow Ga(OH)_3 \leftrightarrow GaOOH + H_2O \quad (6.1)$$

$$Ga(OH)_3 + 3OH^- \leftrightarrow [Ga(OH)_6]^{3-} \quad (6.2)$$

Hereafter, the nanostructures prepared at pH values of 7, 11 and 14 are referred to as nanorods, nanobundles and nanodandelions, respectively.

6.5.3 Texture analysis of $\beta - Ga_2O_3$ nanorods, nanobundles and nanodandelions

Porous nanorod-based $3D$ structures are considered beneficial for gas sensing applications since they provide adequate space for gas diffusion into the sensing material, which results in fast response/recovery times [215]. For this reason, BET measurements were carried out and the nitrogen (N_2) adsorption-desorption isotherms of the $\beta - Ga_2O_3$ nanorods, nanobundles and nanodandelions are shown in Fig. 6.2(d). All $\beta - Ga_2O_3$ nanorod-based morphologies presented Type IV(a) isotherms with H3 hysteresis loops with capillary condensation in the relative pressure range of $0.5 < P/P_0 < 1.0$ indicating that all samples were mesoporous [145]. The inset of Fig. 6.2(d) further revealed that the $\beta - Ga_2O_3$ nanorods, nanobundles and nanodandelions presented average Barrett-Joyner-Halenda (BJH) pore diameters of 22.1, 11.3, and 13.8 nm, respectively. In addition, specific surface areas of 15.8, 17.1, and 10.8 m^2/g were measured for

these $\beta - Ga_2O_3$ nanorods, nanobundles and nanodandelions, respectively. These textural properties show that control of the pH induced variation in the porosity of hydrothermally synthesized $\beta - Ga_2O_3$ nanorod-based morphologies.

6.5.4 Chemical composition of $\beta - Ga_2O_3$ nanorods, nanobundles and nanodandelions

The material's capacity to adsorb charged oxygen species significantly influences its gas sensing performance [216]. However, this adsorption relies on the chemical state and composition of the sensing material. Therefore, to gain insights about the chemical composition of $\beta - Ga_2O_3$ nanorods, nanobundles and nanodandelions, XPS analysis was conducted, and the results are presented in Fig. 6.3. All data was calibrated by the carbon peak at 284.8 eV. Firstly, Fig. 6.3(a) shows the high-resolution $Ga2p_{3/2}$ and $Ga2p_{1/2}$ spin-orbit doublet of the $Ga2p$ core-level separated by 26.9 eV; confirming the $Ga - O$ bonding in all samples [97]. Secondly, the quantity of oxygen species available at the surface of $\beta - Ga_2O_3$ nanorods, nanobundles and nanodandelions was determined by the analysis of the high-resolution $O\ 1s$ core-level XPS spectra presented in Fig. 6.3(b-d). The broad and asymmetric $O\ 1s$ components from all samples fitted with Gaussian peaks can be associated with lattice oxygen (O_L) and adsorbed molecular water [191,200], and their area contributions are indicated in Fig. 6.3(b-d). The content of water adsorbed on the surfaces of the samples increased in $\beta - Ga_2O_3$ nanobundles and nanodandelions and this could probably be due to favorable surface properties. A peak at 530.8 eV is attributed to the presence of carbon, possibly form carbon tape on which the sample was mounted for the XPS measurements. A similar peak was observed by from XPS of annealed Ga_2O_3 and its intensity decreases after sputtering the sample by Ar^+ ion [201].

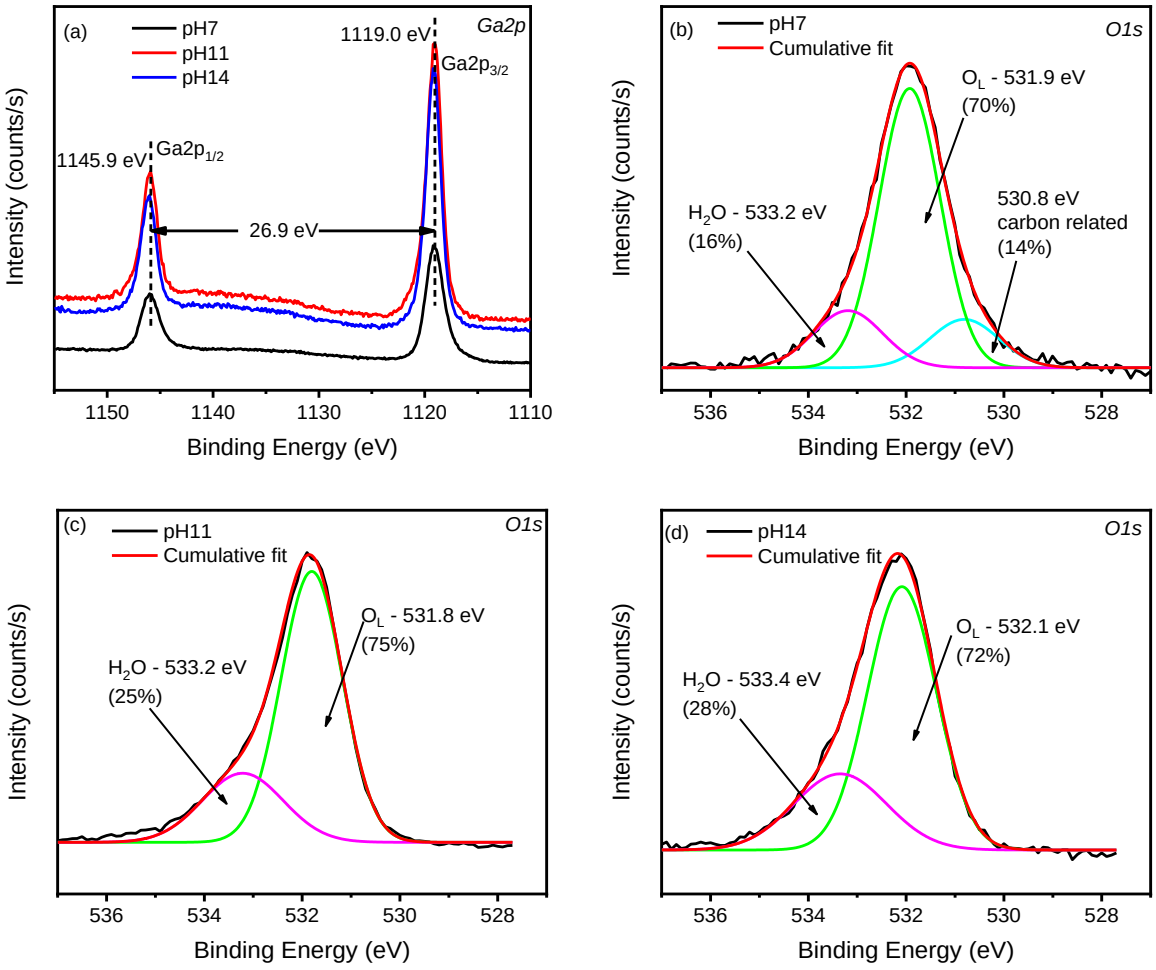


Fig. 6.3. *High-resolution X-ray photoelectron spectroscopy of the (a) Ga 2p and (b-d) O 1s core-levels for* $\beta - Ga_2O_3$ *nanorods, nanobundles and nanodandelions prepared under reaction pH levels of 7, 11 and 14, respectively.*

6.5.5 Gas sensor performances of $\beta - Ga_2O_3$ nanorods-, nanobundles- and nanodandelions-based gas sensors

The operating temperature of an SMO-based gas sensor significantly influences its gas sensing response by controlling the adsorption-desorption equilibrium of the target gas at the surface of the sensing oxide [18]. Hence, the impacts of the sensor operating temperature on the gas sensing capability of $\beta - Ga_2O_3$-based sensors produced at 7, 11, and 14 pH levels were studied to

determine their optimal operating temperatures. All sensors were exposed to 90 ppm isopropanol at operating temperatures from 25 to 165 ℃ and the responses are presented in Fig. 6.4(a). Values obtained at 25, 40, and 60 ℃ are not included in the figure because of low response signal to noise ratio. The recorded response curves revealed that initially all sensing signals improved with increasing operating temperature before reaching their optimum operating temperatures at 150 ℃. This improvement could be attributed to the sufficient energy possessed by the isopropanol gas molecules participating in the reaction with the surface-adsorbed oxygen species. Furthermore, the generation of a high number of thermally excited electrons which subsequently facilitates interaction between the isopropanol molecules and $\beta - Ga_2O_3$ nanorods-based sensing material may also account for the improvement in the response. However, a decrease in responses of all sensors was recorded upon further increasing the operating temperature to 165 ℃ and this may be due to reduced number of active sites available for the adsorption of isopropanol gas molecules resulting from increased oxygen dissociation and adsorption on the active sites of $\beta - Ga_2O_3$ [14]. In addition, the rate of desorption of isopropanol gas molecules from the $\beta - Ga_2O_3$ surface is likely to be higher at high operating temperatures, hence the observed reduction in sensor responses.

To explore the gas sensing behavior of these $\beta - Ga_2O_3$ sensors exposed to various isopropanol concentrations, transient response curves were recorded with all sensors exposed to 5 – 90 ppm isopropanol at the optimum operating temperature of 150 ℃. All sensor responses presented in Fig. 6.4(b) increased stepwise upon the sensors' interaction with isopropanol and decreased back to baseline upon the removal of isopropanol from the sensing chamber, confirming the typical *n*-

type behavior of SMOs. Furthermore, the sensor responses displayed a gradual increase with increasing isopropanol concentration in the $5-90\ ppm$, and this can be associated with the

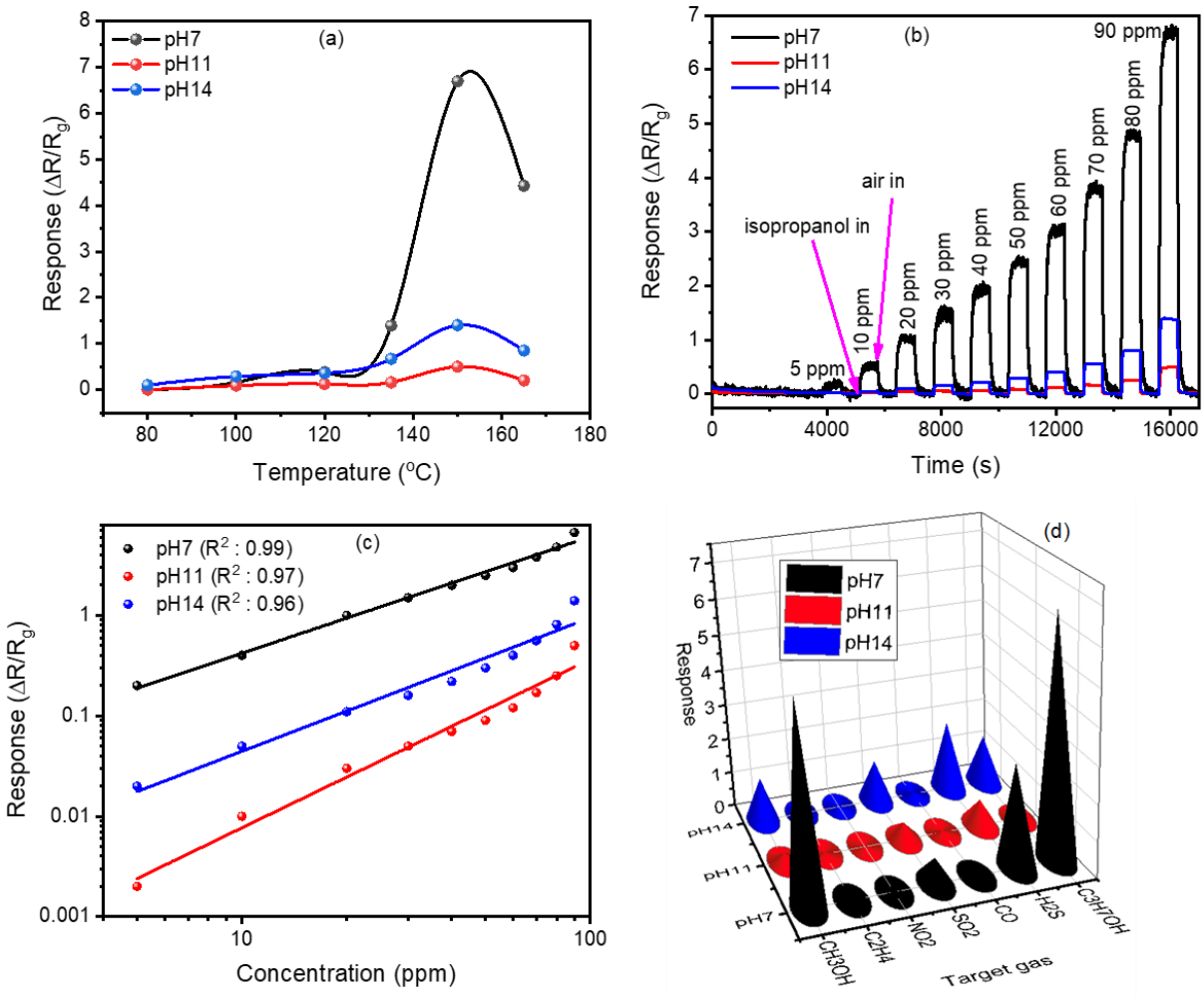


Fig. 6.4. *Responses of $\beta - Ga_2O_3$ based sensors to 90 ppm isopropanol at different operating temperatures. (b) transient response curves and (c) corresponding double-log plots of $\beta - Ga_2O_3$ sensors exposed to 5 to 90 ppm isopropanol at 150 ℃. (d) Sensor response towards 90 ppm of various gas analytes tested with sensors operating at 150 ℃. pH7, pH11, and pH14 indicate pH conditions at which the samples where synthesized.*

increased number of isopropanol molecules participating in the surface reaction. The $\beta - Ga_2O_3$ sensor produced at a pH level of 7 showed the highest response of 6.7 towards 90 ppm

isopropanol compared to those produced at pH levels of 11 and 14 with responses of 0.5 and 1.4, respectively. Besides high response, it is also important for a sensor to exhibit a linear calibration between its response and concentration of the detected gas. To evaluate this relationship, the concentration-response data was plotted on a double-log scale for all $\beta - Ga_2O_3$ based sensors and the results are presented in Fig. 6.4(c). All sensors showed good linear dependence ($R^2 \geq$0.96) of the responses from 5 to 90 ppm of isopropanol. Furthermore, the sensitivities of 1.2, 1.7 and 1.3 ppm^{-1} for $\beta - Ga_2O_3$ sensors produced at pH levels of 7, 11, and 14, respectively, were extrapolated from the slopes of the linear curves fitted in Fig. 6.4(c) by using the linearized empirical power law of SMO-based gas sensors [217]. The limits of detection of 3.2, 4.4 and 3.3 ppm were estimated as the lowest concentration of isopropanol that a sensor is capable of detecting with a 3:1 signal-to-noise ratio for the $\beta - Ga_2O_3$ sensors produced at pH level of 7, 11, and 14, respectively [71]. Another key feature of a gas sensor is its capability to selectively detect the gas of interest. To assess this capability, the responses of all $\beta - Ga_2O_3$ sensors towards 90 ppm of different VOCs and gases was measured. The results presented in Fig. 6.4(d) registered higher responses to VOCs (i.e., isopropanol-C_3H_7OH and methanol-CH_3OH) than ethylene- C_2H_4, hydrogen sulphide- H_2S, carbon monoxide- CO, sulphur dioxide (SO_2) and nitrogen dioxide (NO_2). The high response towards VOCs may be associated with the relatively low bond energy of isopropanol and methanol ($C - C$, 345 kJ/mol) compared to the bonds in ethylene ($C - H$, 415 kJ/mol), nitrogen dioxide ($N - O$, 469 kJ/mol), sulphur dioxide ($S - O$, 522 kJ/mol), carbon monoxide ($C - O$, 1072 kJ/mol), and hydrogen sulphide ($H - S$, 376 kJ/mol).

The response/recovery times of the best performing sensor (i.e., $\beta - Ga_2O_3$ produced at a pH level of 7) were further measured and the steady-state curve obtained is presented in Fig. 6.5(a). It is demonstrated that the variation in morphology of $\beta - Ga_2O_3$ induced changes in the rate of reaction between the isopropanol gas molecules and the surface of the sensing material. In the

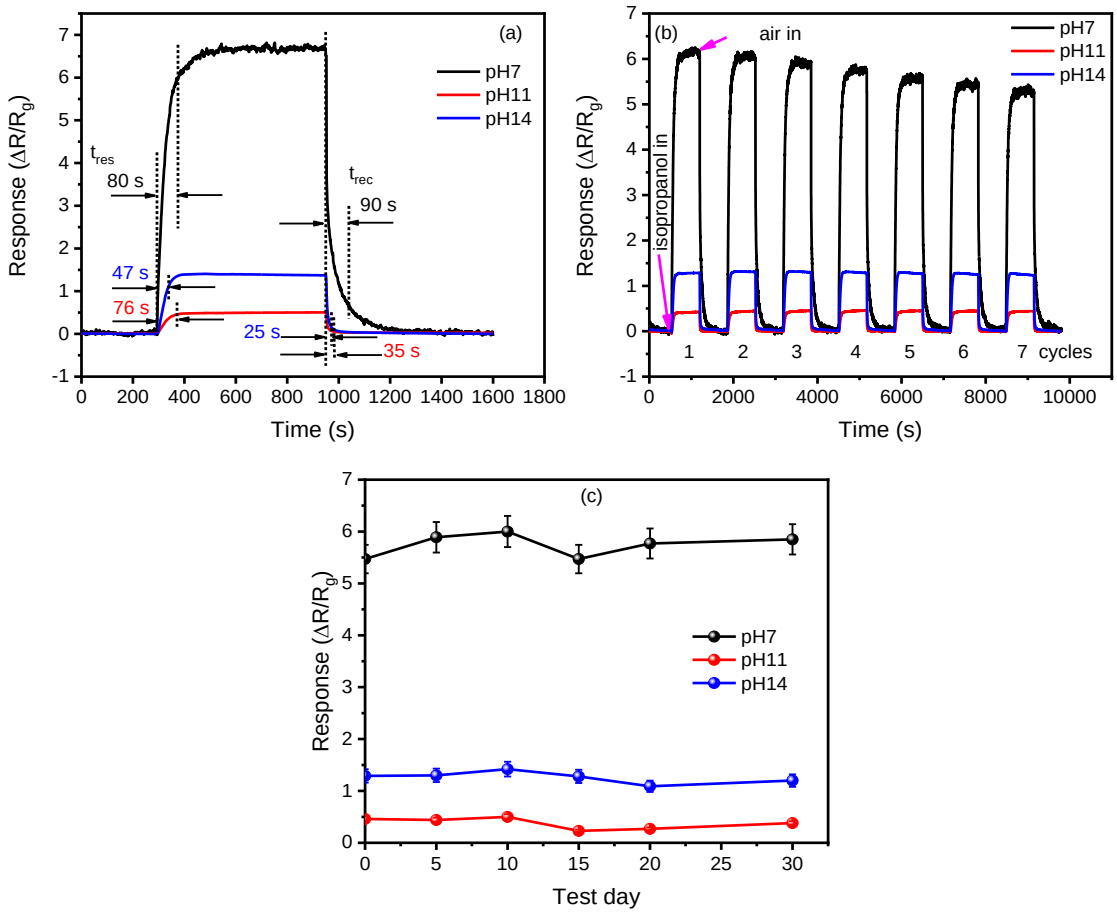


Fig. 6.5. *(a) Response times (t_{res}) and recovery times (t_{rec}) of the $\beta - Ga_2O_3$ sensors, (b) response reproducibility, and (c) response stability curves of the $\beta - Ga_2O_3$ sensors at 150 ℃ exposed to 90 ppm isopropanol. pH7, pH11, and pH14 indicate pH conditions at which the samples where synthesized.*

present study, the dandelion-like structures ($\beta - Ga_2O_3$ sensor produced at a pH level of 14) presented the shortest response/recovery times and this may be attributed to the high number of

contact points available promoting charge flow. In addition, the presence of more adsorbed oxygen species facilitates the fast interaction and electron transfer between the gas molecules and sensing material. The shorter recovery time recorded for the hierarchical structures ($\beta - Ga_2O_3$ sensor produced at pH levels of 11 and 14), compared to the regular nanorods ($\beta - Ga_2O_3$ sensor produced at a pH level of 7), may be caused by the fast desorption rate of isopropanol at these surfaces.

The practicality of a gas sensor is governed by its ability to reproduce the sensing signal. The reproducibility of the $\beta - Ga_2O_3$ nanorods-based sensor was measured by exposing the sensor to consecutive cycles of 90 ppm isopropanol at 150 ℃ and the transient curves obtained are presented in Fig. 6.5(b). All sensors exhibited good short-term stability with minor variations in the response values. Furthermore, the long-term sensor stability was also evaluated under the same conditions over a 30-day test period. The results presented in Fig. 6.5(c) revealed that all $\beta - Ga_2O_3$ sensors presented good long-term stability with the sensors presenting less than 10% fluctuations from test day 20.

Table 6.1 shows a comparison of VOCs gas sensors based on $\beta - Ga_2O_3$. As revealed in Table 6.1, the $\beta - Ga_2O_3$ nanorod-, nanobundle- and nanodandelion-based sensors obtained in this study produced commendable gas sensing performances towards isopropanol. High response, fast response/recovery times were recorded at a lower operating temperature.

Table 6.1. *Isopropanol detection capabilities of various Ga_2O_3-based gas sensors.*

Sensing material	Gas	T (℃)	Conce. (ppm)	Response	t_{resp}/t_{reco} (s)	Ref.
Ga_2O_3/SnO_2 core-shell NWs	Ethanol	400	1000	60 $\left(\frac{R_a}{R_g}\right)$	---/--	[41]
Ga_2O_3-core/WO_3 shell NWs	Ethanol	200	200	~540 $\left(\frac{R_a}{R_g} \times 100\%\right)$	~20/~130	[45]
Ga_2O_3 nanowires	Ethanol	200	200	~210 $\left(\frac{R_a}{R_g} \times 100\%\right)$	~20/~185	[45]
$CuO: Ga_2O_3$ films	Acetone	300	0.25	~1.1 $\left(\frac{R_g}{R_a}\right)$	394/563	[40]
$\beta - Ga_2O_3$ nanorods	Isopropanol	150	90	6.7 $\left(\frac{R_a}{R_g} - 1\right)$	80/90	This work
$\beta - Ga_2O_3$ nanobundles	Isopropanol	150	90	0.5 $\left(\frac{R_a}{R_g} - 1\right)$	76/35	This work
$\beta - Ga_2O_3$ nanodandelions	Isopropanol	150	90	1.4 $\left(\frac{R_a}{R_g} - 1\right)$	47/25	This work

6.5.6 Gas sensing mechanism of $\beta - Ga_2O_3$ sensors produced at pH levels of 7, 11, 14

The gas sensing performance of the SMO-based gas sensors depends on the change in sensor electrical resistance resulting from the sensing materials surface interaction with the target gas molecules [43]. Generally, when $\beta - Ga_2O_3$ nanorods (pH7), nanobundles (pH11) and nanodandelions (pH14) are exposed to air, oxygen molecules adsorb onto the surfaces of each nanostructure and get ionized to O_2^-, O^-, or O^{2-} species by trapping of conduction electrons

[18]. Consequently, the energy bands of these $\beta - Ga_2O_3$ nanostructures bend up creating an electron depleted layer near surface of $\beta - Ga_2O_3$ nanostructures as presented Fig. 6.6(a, c, e). As a result, the electrical resistance of the $\beta - Ga_2O_3$ nanostructures (nanorods, nanobundles and nanodandelions) increases. The O^- type of oxygen species is adsorbed on the surface of these $\beta - Ga_2O_3$ since their optimal operating temperature was found to be 150 ℃ [43]. Upon exposure of the $\beta - Ga_2O_3$ nanostructures to a reducing gas (i.e., isopropanol), the gas gets oxidized by the chemisorbed O^- to form CO_2 and H_2O as shown by Equation (6.3). As a result, electrons are released back to the conduction band of the $\beta - Ga_2O_3$ nanorods (pH7), nanobundles (pH11) and nanodandelions (pH14) and their electrical resistances are lowered as demonstrated in Fig. 6.6(b, d, f).

$$C_3H_7OH_{(g)} + 9O^-_{(ads)} \rightarrow 3CO_{2\,(g)} + 4H_2O_{\,(g)} + 9e^- \qquad (6.3)$$

The high response recorded form the $\beta - Ga_2O_3$ sensor produced at a level pH7 maybe attributed to the high porosity of the morphology compared to those produced at pH levels of 11 and 14 as observed from BET analysis. In addition, the high content of the adsorbed water molecules observed from XPS results might also have contributed towards low sensor response of the nanobundles (pH11) and the nanodandelions (pH14) by reducing the active sites available for the adsorption of charged oxygen species and isopropanol gas molecules. In addition, although the limited accessibility to the individual nanorod surfaces in the nanobundles and nanodandelions by the isopropanol molecules may have contributed towards the observed low responses, the high contact networks in these hierarchical morphological features could be responsible for their high sensitivities and fast response kinetics (i.e., response/recovery times).

The contact networks increase the number of charge transport channels. Furthermore, the nanobundles (pH11) and nanodandelions (pH14) presented the low limits of detection towards isopropanol, and this could be attributed to the preference of isopropanol molecules to attach to crevices sites present on the nanobundles and nanodandelions. This result indicated that the nanorod-based hierarchical morphological features may be ideal candidates for sensing of low concentrations of isopropanol.

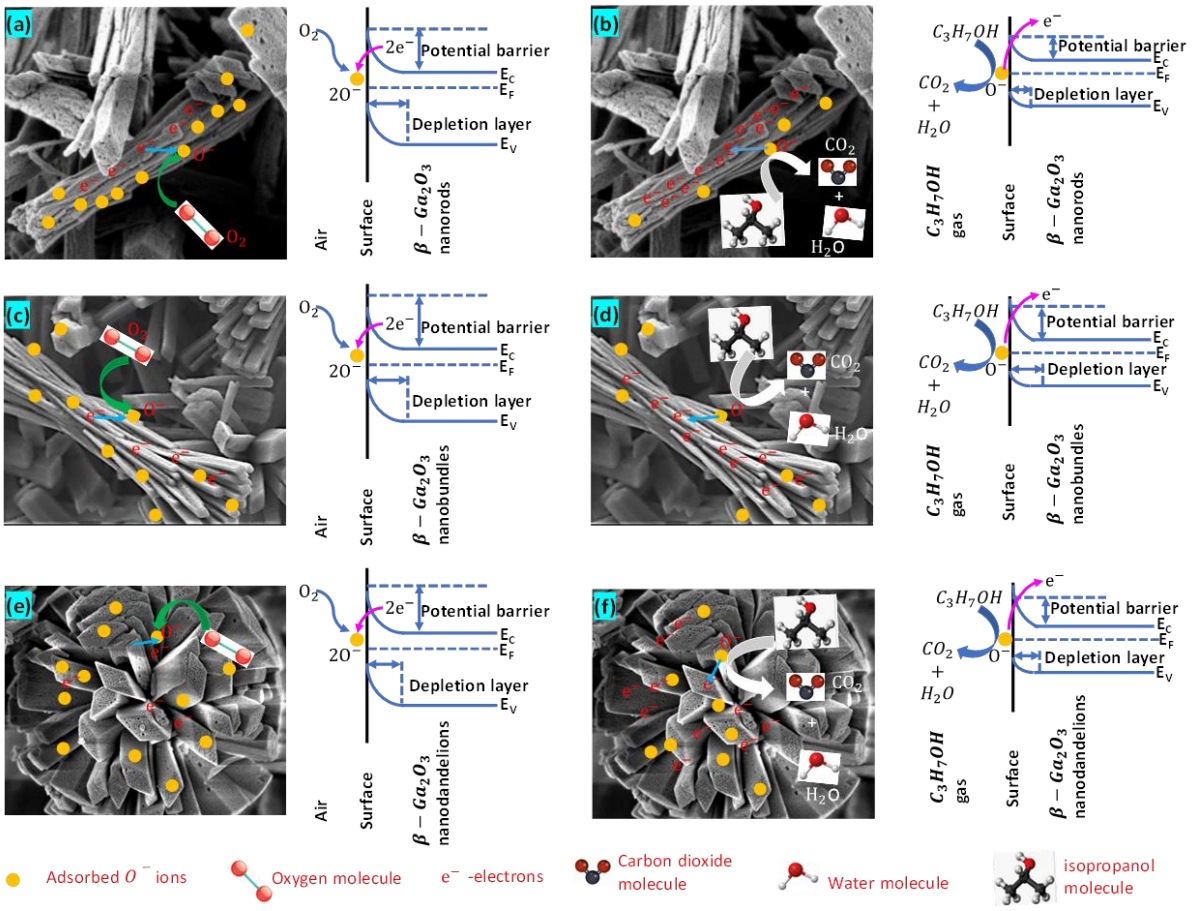


Fig. 6.6. *Schematic representations and band diagrams of $\beta - Ga_2O_3$ (a, b) nanorods (pH7), (c, d) nanobundles (pH11) and (e, f) nanodandelions (pH14)-based gas sensors in air and towards isopropanol vapour.*

6.6 Conclusion

In this study, we described the preparation of regular and hierarchical $\beta - Ga_2O_3$ nanorod-based nanostructures derived from the microwave-assisted hydrothermal method by variation of reaction pH conditions. Furthermore, structural, morphological, and compositional analysis of the nanostructures were conducted, and were correlated with the gas sensing performances of the nanostructures. The XRD results confirmed the synthesis of highly crystalline $\beta - Ga_2O_3$ powders while the FESEM micrographs revealed the crystallization of nanorod-like, nanobundle-like, and nanodandelion-like morphologies at pH levels of 7, 11 and 14, respectively with varying specific surface area and porosity demonstrated by the BET results. Furthermore, the XPS results revealed that the three different morphologies of $\beta - Ga_2O_3$ possessed different content of lattice oxygen and adsorbed water molecules species. Gas sensing measurements were performed, and the results revealed that the $\beta - Ga_2O_3$ nanorods presented a higher response towards isopropanol than the nanobundles and nanodandelions. The highest response of 6.7 was recorded towards 90 ppm propanol from the $\beta - Ga_2O_3$ nanorods at 150 ℃. The high response from this morphology was explained in terms of the large specific surface area and the type of defects present on the surface of the sensing material. In addition, it was also observed that the nanobundles and nanodandelions morphologies of $\beta - Ga_2O_3$ presented fast response kinetics and high sensitivities, and this was attributed to the high contact networks in these morphologies which provide large number of charge transport channels. According to these results, it can be concluded that controlling the nanorod-based morphology of $\beta - Ga_2O_3$ could provide methods of tuning the gas sensing properties (i.e. sensor response, response/recovery times and sensitivity) of this material which may be useful in the reliable real-time detection of isopropanol for indoor environments.

CHAPTER 7

A highly ethylene responsive $\beta - Ga_2O_3$ nanorods chemiresistive sensor: effects of electronic and chemical sensitization induced by incorporation of noble metal nanocrystals

7.1 Introduction

Atmospheric condition monitoring and control of perishable food products such as climacteric fruits during transportation and storage are very crucial in the food supply chain to maintain their freshness and quality status. Apart from O_2 and CO_2, ethylene is another key gas which requires monitoring and control in the fruit supply chain [51]. Most climacteric fruits ripen at ethylene concentration levels between 0.1 and 1 parts per million (ppm) [49], while flowers often start to blossom below 0.1 ppm [50]. Besides in fruit supply chains, previous reports have revealed that 7 ppm of ethylene effectively promotes suppression of sprout elongation and root development of onion bulbs, and this remarkably prolongs the storage life and quality of onions by 7 months [218]. Conventional methods such as gas chromatographic techniques, although robust and sensitive, fail to address the need for quick and simple ethylene detection on-field [50,219]. Therefore, it is important to design highly selective, sensitive, and stable gas sensors that can identify low concentration levels (ppm or ppb) of ethylene.

Semiconductor metal oxide (SMO)-based gas sensors have gained widespread attention for efficient detection of several gases owing to their simplicity, easiness of fabrication, miniaturization, high thermal and chemical stability, rapid response, low cost, and high

sensitivity [51]. Among SMO materials used in gas sensing, gallium oxide (Ga_2O_3) has received tremendous attention, in particular $\beta - Ga_2O_3$ polymorph, due to its high conductivity attributed to its high free electron concentration (10^{16} – 10^{20} cm^{-3}) and electron mobility (200 $cm^2V^{-1}s^{-1}$) [87,220,221] associated with the double chains of GaO_6 octahedra arranged along the *b*-axis direction [23]. Moreover, interconnected one-dimensional ($1D$) $\beta - Ga_2O_3$ nanostructures such as nanorods and nanowires [36,42,103] have demonstrated efficient sensing capabilities to detect low concentrations of various gas analytes owing to their continuous charge transport properties, high surface to volume ratio, and excellent thermal and chemical stabilities [23,42]. However, undoped $\beta - Ga_2O_3$ $1D$ nanostructures are still far from fulfilling requirements for practical application due to their poor specificity and high operating temperature causing high energy consumption [42]. To address these drawbacks, different strategies have been adopted, including morphology optimization [36], the use of ultraviolet (UV) illumination [103], elemental/ionic doping [108], heterojunction construction [121,123] and surface modification [35,44]. Among these approaches, surface modification of $\beta - Ga_2O_3$ by noble metal nanoparticles such as Au and Pt has proven to significantly improve the detection capabilities of $\beta - Ga_2O_3$ towards various gases and volatile organic compounds (VOCs) [35,44,222]. For instance, Kim *et al*. reported Pt-functionalized $\beta - Ga_2O_3$ multiple networked nanowires and their responses were approximately 17-, 22-, 26- and 28-fold to 100, 50, 25, and 10 ppm of CO, respectively at 100 ℃ compared to the non-functionalized $\beta - Ga_2O_3$ multiple networked nanowires [35]. In another study, Au-modified $\beta - Ga_2O_3$ nanowires presented high sensitivity (4.8%) towards 100 ppm CO gas at room temperature compared to unmodified $\beta - Ga_2O_3$ nanowires [44]. Both studies attributed the enhancement of gas sensor

performance of modified $\beta - Ga_2O_3$ nanowires to synergistic electronic and chemical sensitization effects from the catalytic activity of noble metal nanoparticles [35,44].

Within this context, we prepared unmodified and 0.5 and 1.0 $mol\%$, Ag and Au surface modified $\beta - Ga_2O_3$ nanorods using microwave-assisted hydrothermal synthesis followed by annealing at 750 ℃ and evaluated their gas sensing performance. The gas sensing behavior was explained from the viewpoint of detailed and systematic investigation of crystal structural, surface morphology and defects of $\beta - Ga_2O_3$ nanorods. The proposed gas sensing mechanism for the Ag-modified $\beta - Ga_2O_3$ nanorod-based ethylene sensors, which exhibited comparatively excellent sensing performance is discussed.

7.2 Experimental Section

7.2.1 Materials

Gallium nitrate hydrate ($Ga(NO_3)_3.xH_2O$, 99.9%), ammonium hydroxide (NH_4OH, 28%), gold(III) chloride trihydrate ($HAuCl_4.3H_2O$, ≥99.9%), and silver chloride ($AgCl$, 99.999%) were commercially acquired from Sigma Aldrich and were used without additional purification.

7.2.2 Preparation of unmodified $\beta - Ga_2O_3$ nanorods

$\beta - Ga_2O_3$ nanorods were synthesized using microwave-assisted hydrothermal method followed by heat treatment. A 0.1 M Ga^{3+} solution was prepared by mixing 0.26 g of $Ga(NO_3)_3.xH_2O$ and 10 ml of deionized (DI) water. The solution was heated to 60 ℃ while stirring continuously and vigorously. A few drops of NH_4OH solution were added at 5 second interval until the pH of the solution reached 7. The resulting milky solution was aged for 1 hour at 60 ℃ then

microwaved for 1 hour by using a Discover 2.0 microwave synthesizer set at 100 W and 150 ℃. The obtained white precipitate was centrifuged with *DI* water and ethanol, then dried at 60 ℃ forming a white powder. The powders were heat-treated in air in a muffle furnace maintained at 750 ℃, for 2 hours, at a ramping rate of 5 ℃/min. The unmodified $\beta - Ga_2O_3$ powders obtained were labelled 0%.

7.2.3 Preparation of Ag- or Au-modified $\beta - Ga_2O_3$ nanorods

0.72 and 1.43 mg of $AgCl$ were added to 10 ml of 0.1 M Ga^{3+} solution in separate beakers to produce $GaOOH$ nanorods modified with 0.5 and 1.0 $mol\%\, Ag$, respectively. Likewise, 1.97 and 3.94 mg of $HAuCl_4.3H_2O$ precursors were added separately to 10 ml of 0.1 M Ga^{3+} solution to prepare $GaOOH$ nanostructures modified with 0.5 and 1.0 $mol\%\, Au$. The solutions in the four beakers were heated to 60 ℃ and a few drops of NH_4OH were added at 5 second intervals until the pH of each solution was 7. The aging, microwaving, washing, drying, and heat-treatment were conducted in a similar manner described above for the 0% sample. The compounds obtained were labelled 0.5%Ag, 1.0%Ag, 0.5%Au, and 1.0%Au corresponding to $\beta - Ga_2O_3$ containing 0.5 $mol\%\, Ag$, 1.0 $mol\%\, Ag$, 0.5 $mol\%\, Au$, and 1.0 $mol\%\, Au$, respectively.

7.2.4 Sample characterization

The crystal structure of the 0%, 0.5%Ag, 1.0%Ag, 0.5%Au, and 1.0%Au samples was determined by the Bruker D2 Phaser powder X-ray diffractometer using $Cu\ K\alpha_1$ radiation source (λ = 0.15406 nm). Morphological analysis was conducted using JEOL TEM-2100 transmission electron microscope. The composition, electronic states and surface defects were examined by an

X-ray photoelectron spectroscope (PHI 5000 Scanning ESCA Microprobe) equipped with a monochromatic $Al\text{-}K\alpha$ beam.

7.2.5 Fabrication and gas sensor testing of unmodified and Ag- and Au- modified $\beta - Ga_2O_3$ nanorods

To fabricate unmodified and Ag- and Au- modified $\beta - Ga_2O_3$ nanorod-based gas sensors, 10 mg of each powder sample was added to 0.05 ml of ethanol to produce a monodispersed solution. This solution was then evenly drop-coated to make a film onto an alumina substrate consisting of interdigitated Pt electrodes and a Pt heater at the back side, as shown in Fig. 7.1. All the films were annealed overnight at 300 ℃ to remove organic solvents and improve adhesion. The gas sensor testing was performed using a KSGAS6S (KANOSISTEC, Italy) sensing station, with the films kept in both dry air and humid environments at different operating temperatures from room temperature to 180 ℃. A source voltage of $2V$ was applied across the sensors as illustrated schematically in Fig. 7.1. The desired concentrations of the tested gases, in parts per million (ppm), were obtained by varying the flow rate ratios of synthetic air and compressed target gas using a mass flow controller. The variations in sensor electrical resistances in air (R_a) and in the vicinity of the target gas (R_g) were acquired by a Keithley 6487 picoammeter/voltage source meter. The gas sensor responses, *R*, to the test gases were calculated as electrical resistance changes upon sensor-gas interaction, i.e., $\Delta R/R_g$ for reducing gases where $\Delta R = R_a - R_g$. The sensor response and recovery times were determined as the duration taken by a sensor to reach 90% of the total change in resistance upon target gas injection into the sensing chamber and its removal, respectively.

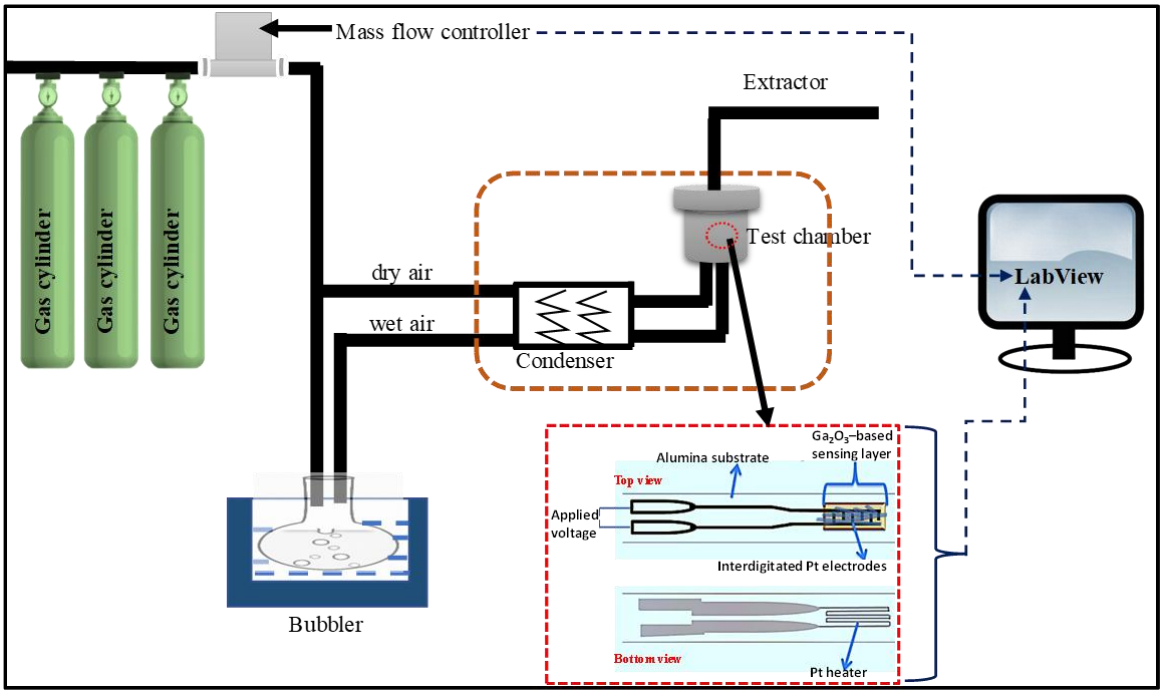


***Fig. 7.1**. Schematic presentation of the gas sensing station and process.*

7.3 Results and discussion

7.3.1 Crystal structure of unmodified and Ag- and Au-modified $\beta - Ga_2O_3$ nanorods

Fig. 7.2 shows the XRD results of the samples and the XRD pattern for the unmodified sample was readily indexed to the monoclinic phase of Ga_2O_3, i.e., $\beta - Ga_2O_3$ (Entry no. 96-200-4988). Upon the incorporation of 0.5 and 1.0 $mol\%$ Ag, the relative intensities of the $\beta - Ga_2O_3$ diffraction peaks from the $(11\bar{1})$, $(40\bar{1})$, (401), $(31\bar{1})$, $(60\bar{1})$, (113), $(71\bar{2})$, $(\bar{1}14)$, (421), and (603) crystallographic planes increased. This suggests an overlap with the diffraction peaks from cubic Ag crystal structure (Entry no. 96-150-1947) and hexagonal Ag_2O crystal structure

(Entry no. 96-150-9685). The diffraction peaks arising from cubic Ag were detected at 38.39, 44.62, 64.95, 78.04, and 82.23 ° and are associated with (111), (200), (202), (311), and (222) crystallographic planes, respectively. For the hexagonal Ag_2O phase, diffraction peaks positioned at 33.66, 38.40, 60.20, 72.39, and 73.70 ° correspond to (100), (101), (110), (112), and (201) planes, respectively. Furthermore, Fig. 7.2 revealed that the addition of 0.5 and 1.0 $mol\%\ Au$ resulted in the detection of other diffraction peaks at 38.19, 44.39, 64.58, 77.56, and 81.73 ° arising from the (111), (200), (202), (311), and (222) planes of cubic Au crystal structure (Entry no. 96-900-8464), respectively.

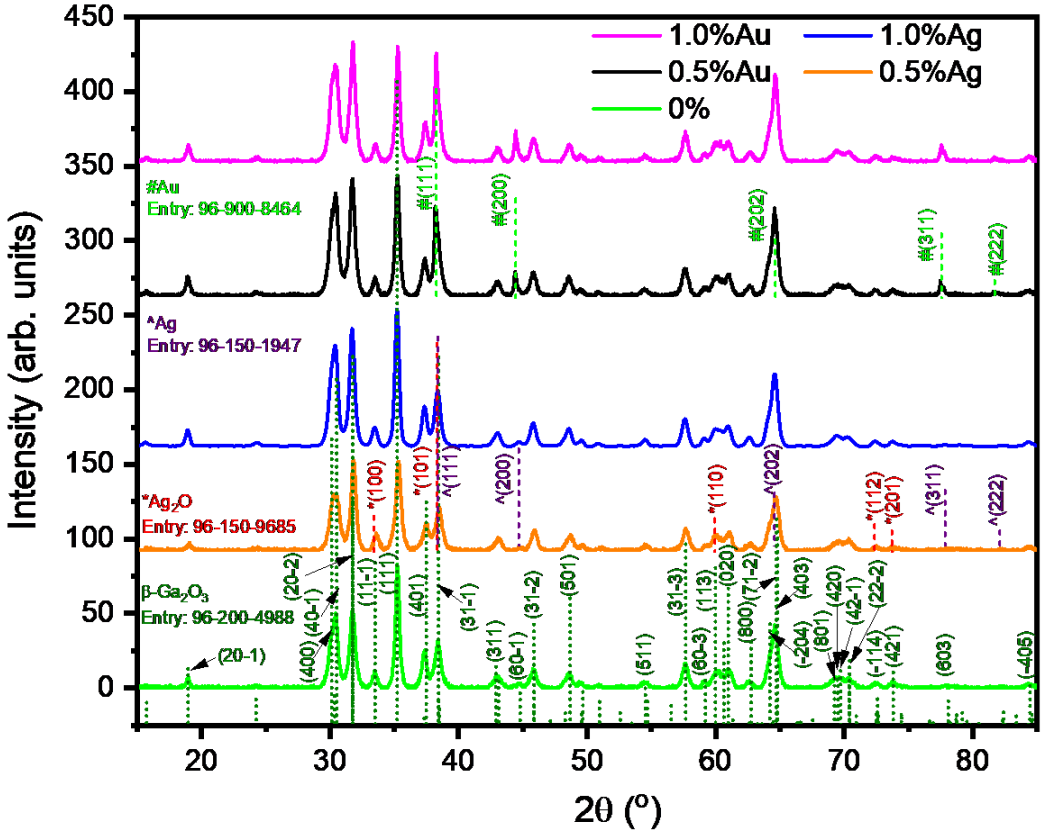


Fig. 7.2. *X-ray diffraction patterns of the samples. 0%, 0.5%Ag, 1.0%Ag, 0.5%Au, and 1.0%Au represent* $\beta - Ga_2O_3$ *nanorods unmodified and modified with indicated concentration of Ag and Au.*

The crystallite sizes of the unmodified and Ag- and Au-modified $\beta - Ga_2O_3$ nanorods were determined using the Debye-Scherrer formula [174] and the details of the most intense (111) diffraction peak of $\beta - Ga_2O_3$. The crystallite sizes of 22.2, 17.5, 21.4, 21.2, and 22.0 nm, all with an error bar of ± 0.3, were estimated for the 0%, 0.5%Ag, 1.0%Ag, 0.5%Au, and 1.0%Au-containing samples, respectively. The decrease in average crystallite sizes with addition of noble metals can be attributed to constrained rate of nucleation and growth of $GaOOH$ during the hydrothermal process caused by the ionic radii mismatch between the ions of Ga, Ag, and Au.

7.3.2 Morphological and structural analysis

Low-resolution and high-resolution TEM images of the samples are presented in Fig. 7.3. The 1.0%Ag and 1.0%Au samples were selected for the analysis of the surface modified samples. Fig. 7.3(a, c, e) reveal that the unmodified and 1.0%Ag and 1.0%Au modified samples contained nanorod-like features. In addition, Fig. 7.3(c, e) show the presence of randomly distributed nano-sized crystallites on the surface of the nanorods in the modified samples, attributed to Ag and Au nanocrystals. Both Ag and Au nanocrystals presented hexagonal shapes (Fig. 7.3, insets) with the Ag nanocrystals (~ 10-16 nm) more densely populated than the larger Au nanocrystals (~61 nm). The HRTEM micrographs in Fig. 7.3(b, d, f) show the lattice fringes detected in all the samples. Fringes with inter-planar spacings (*d-spacings*) of 0.467, 0.294 and 0.289 nm match the $(20\bar{1})$, $(40\bar{1})$, and (002) planes of the monoclinic $\beta - Ga_2O_3$ (Fig. 7.3(b)). In the 1.0%Ag sample shown in (Fig. 7.3(d)), *d*-spacings of 0.262 nm and 0.469 nm arouse from the (100) and $(20\bar{1})$ planes of Ag_2O and $\beta - Ga_2O_3$, respectively [223] while for the 1.0%Au sample (Fig. 7.3(f)), the *d*-spacing values of 0.375 nm and 0.239 nm arouse from the monoclinic $\beta - Ga_2O_3$ (201) and cubic Au (111) planes, respectively. The selected area electron diffraction (SAED)

patterns presented as insets of Fig. 7.3(b, d, f) revealed that all samples are polycrystalline, and this agrees with the XRD results.

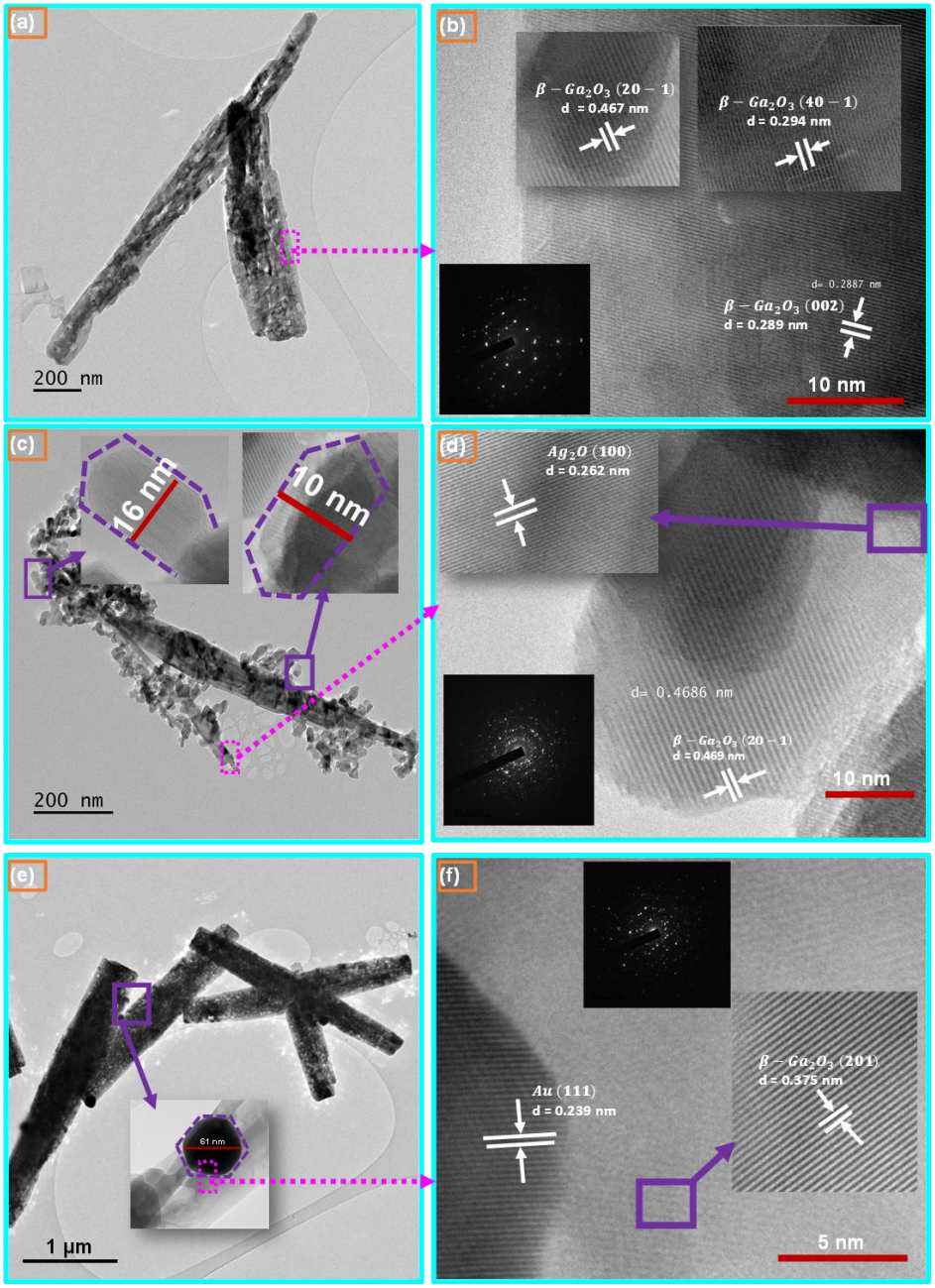


Fig. 7.3. *Low-resolution transmission electron microscopy images (a, c, e) and high-resolution transmission electron microscopy images and selected area electron diffraction patterns (b, d, f) of unmodified and 1.0mol%Ag- and 1.0mol%Au-modified* $\beta - Ga_2O_3$ *nanorods.*

7.3.3 Chemical state analysis

Fig. 7.4 displays the X-ray photoelectron spectroscopy (XPS) results of all samples, calibrated by the carbon peak at 284.8 eV and analyzed with a PHI Multipak software using the Shirley background. Firstly, the $Ga2p$ core-levels shown in Fig. 7.4(a) comprises of the $Ga2p_{3/2}$ and $Ga2p_{5/2}$ spin-orbit doublets separated by 26.9 eV which confirm $Ga-O$ bonding in all the samples. The peak $FWHM$ of these doublet components increased in the modified samples, suggesting chemical interaction between the $\beta-Ga_2O_3$ surface and the incorporated noble metal nanocrystals. Fig. 7.4(a) further reveal apparent asymmetric behavior and shifting of the $Ga\ 2p$ doublet component peaks in the modified samples. The asymmetry may be caused by the surface plasmonic resonances of the noble metal nanocrystals [224] while a shift to lower binding energies could probably be due to increased electron density around $\beta-Ga_2O_3$. The 1.0%Ag sample recorded the highest shift of 1.1 $eV$and the largest peak broadening from 1.7 eV to 2.3 eV which could suggest stronger interactions and high electron transfer in this sample.

To ascertain the electron transfer, the $Ag\ 3d$ and $Au\ 4f$ core-levels were analyzed, and the results are shown in Fig. 7.4(c-f). Fig. 7.4(c, d) reveals that the $Ag\ 3d_{5/2}$ and $Ag\ 3d_{3/2}$ spin-orbit doublets were separated by ~6 eV [225] and exhibited an apparent asymmetry, which suggested a contribution from more than one chemical state of Ag. Therefore, the doublet-components were fitted with multiple Gaussian functions. The peaks at 368.4 and 374.6 eV for the 0.5%Ag sample and 368.0 and 373.9 eV for the 1.0%Ag sample correspond to metallic Ag (i.e., Ag^0) while peaks at 367.5 and 373.4 eV for 0.5%Ag and 367.2 and 373.2 eV in 1.0%Ag can be associated with the Ag_2O (i.e., Ag^+) present on the surface of $\beta-Ga_2O_3$ nanorods [225].

The area contributions of the two Ag states in the Ag-modified samples are listed in Table 7.1, and both samples show a higher Ag^{+} content than Ag^{0}.

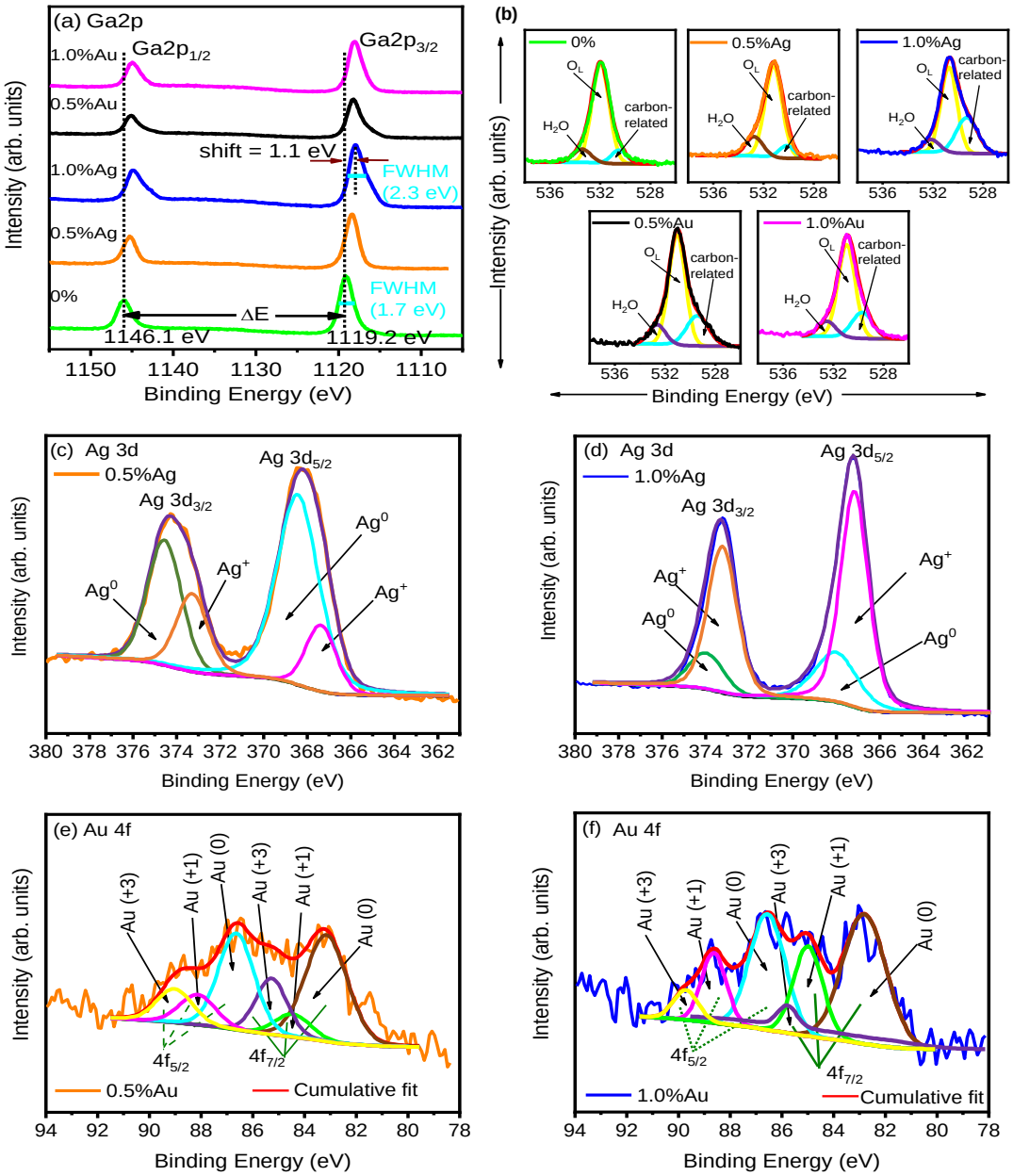


Fig. 7.4. *High-resolution X-ray photoelectron spectroscopy core-level spectra of (a) Ga 2p, (b) O 1s, (c, d) Ag 3d, and (e, f) Au 4f of the samples. 0%, 0.5%Ag, 1.0%Ag, 0.5%Au, and 1.0%Au represent* $\beta - Ga_2O_3$ *nanorods unmodified and modified with indicated concentration of Ag and Au.*

In the case of the $Au\ 4f$ core-levels, spectra from the 0.5%Au and 1.0%Au samples were fitted with components of the $Au\ 4f_{7/2}$ and $Au\ 4f_{5/2}$ doublets as presented in Fig. 7.4(e, f). The peaks at 83.1 and 86.8 eV for the 0.5%Au sample together with those at 82.8 and 86.7 eV for the 1.0%Au sample arose from the Au^0 (i.e., Au metal) electronic state [226]. The peaks detected at 84.5 and 88.3 eV in the 0.5%Au and 85.0 and 88.7 eV in the 1.0%Au sample are probably due to Au^+ electronic state in the nanocrystals. Lastly, the peaks at 85.3 and 89.3 eV and 85.7 and 89.8 eV for the 0.5%Au sample and 1.0%Au sample, respectively, are ascribed to Au^{3+}. The area contributions of these chemical states of Au are summarized in Table 7.1. The values presented in Table 7.1 show a higher content of metallic Au^0 state than the charged states present on the $\beta - Ga_2O_3$ nanorods surfaces. According to these XPS results, the transfer of electrons from Ag and Au nanocrystals to $\beta - Ga_2O_3$ nanorods was most likely facilitated by the high electronegativity of O (3.44) compared to those of Ag and Au in different valence states (i.e., 0, $+1$, $+3$) ranging from 1.10 to 1.95 [227,228].

Table 7.1. *The area contributions of various charge states and oxygen species in the samples, obtained from XPS spectra. x represents valence state of 1 or 3. 0%, 0.5%Ag, 1.0%Ag, 0.5%Au, and 1.0%Au represent $\beta - Ga_2O_3$ nanorods unmodified and modified with indicated concentration of Ag and Au.*

Sample	Ag^0 or Au^0 area	Ag^x or Au^x area	O_L		adsorbed H_2O	
			B.E. (eV) (±0.1)	Area (%) (±1)	B.E. (eV) (±0.1)	Area (%) (±1)
0%	--	--	531.9	79	533.4	11
0.5%Ag	26	74	531.2	75	532.7	16
1.0%Ag	24	76	530.8	59	532.2	9
0.5%Au	62	38	531.0	65	532.6	12
1.0%Au	64	36	531.0	66	532.5	11

Fig. 7.4(b) shows the broad and asymmetric $O\ 1s$ spectra of all the samples fitted with peaks corresponding to lattice oxygen (O_L) and adsorbed molecular water components [191,200], and their area contributions are provided in Table 7.1. Another peak at the lower energy positions arises from carbon from the carbon tape used to mount the samples for XPS measurements [201]. The content of O_L decreased in the modified samples which indicates incorporation of Ag and Au in the oxides [229]. Minor changes were recorded for the quantity of the peak ascribed to O_C and/or adsorbed water molecules, after the addition of Ag and Au nanocrystals. Besides the variation in the quantity of the oxygen species, Table 7.1 shows inherent $O\ 1s$ peak shifts to lower binding energies which further confirm electron transfer to $\beta - Ga_2O_3$ nanorods.

7.3.4 Gas sensing

All the sensors were exposed to 90 ppm ethylene for operating temperatures ranging from 20 to 180 ℃ and the results are presented in Fig. 7.5(a). Initially the sensing signal of all sensors increased with increasing temperature before reaching optimum values. The optimum operating temperature of unmodified $\beta - Ga_2O_3$ (i.e., 0%) was 165 ℃ while that of the modified $\beta - Ga_2O_3$ sensors was 140 ℃. However, a significant decrease in response of all the sensors was observed upon increasing the operating temperature to 180 ℃. These sensor response variations can be explained by the adsorption-desorption kinetics of the analyte gas molecules on the sensor surface. At low sensor operating temperatures, the response signal was limited by the slow rate of the chemical reaction caused by low thermal energy of the ethylene gas molecules [14]. On the other hand, elevated temperatures increased number of thermally generated electrons which facilitated the target gas-sensing layer interaction thereby enhancing the sensor response signal. At higher temperatures, low sensor response is most likely due to the high rate of diffusion of

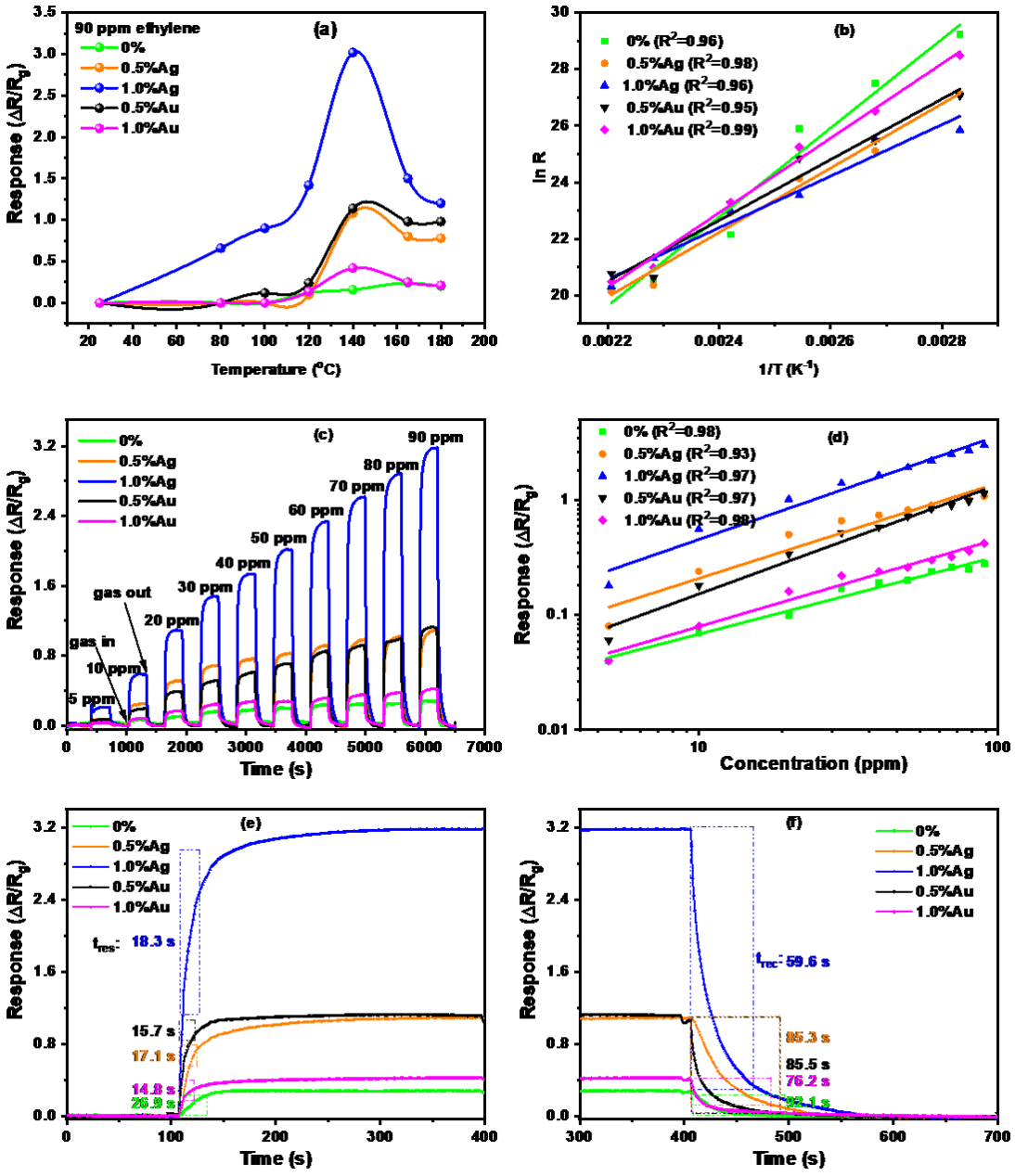


Fig. 7.5. *(a) Responses of the sensors towards 90 ppm ethylene at various operating temperatures. (b) dependence of* R_a *on the sensor operating temperature. (c) transient response curves and (d) corresponding double-log plots sensors exposed to various ethylene concentrations at 165 ℃ for the unmodified sample and at 140 ℃ for the modified samples. (e) response times (*t_{res}*) and (f) recovery times (*t_{rec}*) of the unmodified and modified sensors operating at 140 ℃ and 165 ℃, respectively, subjected to 90 ppm ethylene. 0%, 0.5%Ag, 1.0%Ag, 0.5%Au, and 1.0%Au represent* $\beta - Ga_2O_3$ *nanorods unmodified and modified with indicated concentration of Ag and Au.*

target ethylene gas molecules which reduces the target gas-sensing layer interaction. Based on this result, all sensors were operated at their optimum temperatures. To explain the significant reduction in sensor operating temperatures of the modified samples, the sensor activation energies were determined by the Arrhenius equation. Fig. 7.5(b) shows the temperature dependence of the sensor resistance in air (R_a) and the activation energies of 1.36, 0.98, 0.79, 0.93 and 1.214 eV for the 0%, 0.5%Ag, 1.0%Ag, 0.5%Au, and 1.0%Au sensors, respectively, were estimated from the slopes of the fitted curves. The lower activation energies presented by the modified sensors than that of the unmodified sample could be the reason for the lower optimal operating temperature obtained for the modified sensors.

Fig. 7.5(c) presents the responses of all the sensors to different ethylene concentrations in the 5 – 90 ppm range. As expected for *n*-type $\beta - Ga_2O_3$-based materials, all sensors showed a rapid increase in the response and reached saturation values following the injection of ethylene gas into the gas chamber followed by a sharp decrease in sensor response upon the removal of ethylene from the test chamber. Moreover, the responses of all the sensors increased with increasing ethylene concentrations and this may be due to the enhanced surface coverage by the ethylene gas molecules, which in turn enhanced the surface reaction. This good linear dependence is demonstrated in Fig. 7.5(d) and agrees with the response of $\beta - Ga_2O_3$ gas sensors exposed to various gas analytes [42]. The gas sensor sensitivity values of 0.68, 0.83, 0.90, 0.95 and 0.76 ppm^{-1} in the 0%, 0.5%Ag, 1.0%Ag, 0.5%Au, and 1.0%Au sensors, respectively, were obtained from gradients of curves fitted in Fig. 7.5(d). The improvements in the sensitivities recorded from the modified samples were most likely caused by the catalytic effects of the noble metal nanocrystals on $\beta - Ga_2O_3$ surfaces. Furthermore, the limit of

detection values of 9.3, 3.4, 1.3, 3.7, and 4.1 ppm for the 0%, 0.5%Ag, 1.0%Ag, 0.5%Au, and 1.0%Au-containg sensors, respectively, were extrapolated from the *y*-intercepts of the linear regression fittings in Fig. 7.5(d). Although all sensors demonstrated excellent detection of ethylene over a wide range of concentrations, the 1.0 $mol\%\ Ag$ modified $\beta - Ga_2O_3$ exhibited the highest response of 3.18.

Furthermore, Fig. 7.5(e-f) demonstrates significant reduction of the response/recovery times after $\beta - Ga_2O_3$ nanorods surface modification with Ag and Au nanocrystals. Fast response could be attributed to the promotion of the adsorption-desorption of the ethylene gas molecules and increased number of adsorbed oxygen species induced by these noble metal nanocrystals. On the other hand, high catalytic activities of the Ag and Au nanocrystals promote rapid desorption of ethylene molecules from the sensing active layer, resulting in fast recovery times [28]. The 1.0%Ag sensor presented the quickest response/recovery times of 18/60 s than the rest of the sensors.

Selectivity of our unmodified and modified $\beta - Ga_2O_3$ nanorod-based sensors was measured when the sensors were exposed to 90 ppm of different gases (i.e., methane (CH_4), methanol (CH_3OH), ammonia (NH_3), propanol (C_3H_7OH), carbon dioxide (CO_2) and carbon monoxide (CO)) and the results are shown in a column chart in Fig. 7.6(a). The 1.0 $mol\%\ Ag$ displayed a highly selective response towards ethylene gas, indicating that it is a potential gas sensing material for the detection of ethylene.

To further assess the potential of the 1.0%Ag sensor to detect ethylene gas, the reproducibility of the sensor was evaluated by consecutively subjecting it to 90 ppm ethylene under similar conditions. The transient response-recovery curve recorded (Fig. 7.6(b)) demonstrates a good

short-term stability of the sensor with slight fluctuation (<6%) in the initial sensor response. Furthermore, the long-term stability of the sensor was examined at unchanged conditions over a 30-days test period and Fig. 7.6(c) reveals good long-term sensor stability.

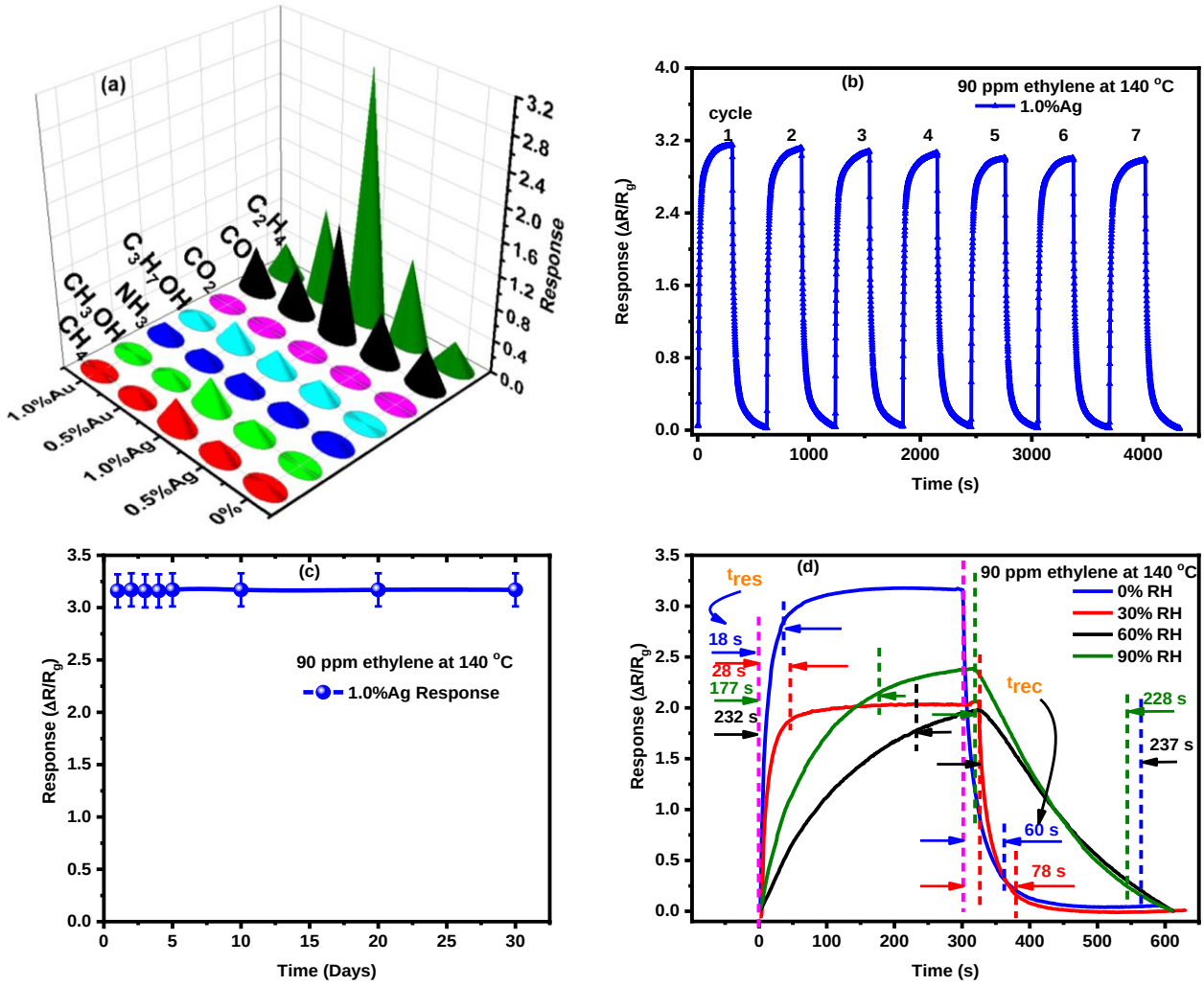


Fig. 7.6. *Sensor performances measured at operating temperatures of 165 ℃ and 140 ℃ for the unmodified and surface modified* $\beta - Ga_2O_3$ *nanorod-based sensors, respectively. (a) Sensor response towards 90 ppm of various gas analytes. (b) response reproducibility curve, (c) response stability curves, and (d) response* (t_{res})*-recovery* (t_{rec}) *curves towards 90 ppm ethylene of the 1.0%Ag sensor at 0%RH, 30%RH, 60%RH, and 90%RH. 0%, 0.5%Ag, 1.0%Ag, 0.5%Au, and 1.0%Au represent* $\beta - Ga_2O_3$ *nanorods unmodified and modified with indicated concentration of Ag and Au.*

During practical application of gas sensors, atmospheric moisture may be a concern to normal operation of the sensors. Therefore, the responses of the 1.0%Ag sensor under dry as well as 30, 60 and 90% relative humidity (RH) atmospheric conditions were examined, and the results are shown in Fig. 7.6(d). The sensor response decreased by 35%, 38% and 25% when exposed to 30%RH, 60%RH and 90%RH, respectively. This result is commendable in comparison to the Pd- and Au-loaded-SnO_2 nanocrystals-based sensors operated at 450 ℃ whose responses decreased by 70 and 74% at 30%RH, respectively [230]. Lower responses recorded under humid sensor environments may be associated with competition for the surface reactive sites by the water vapour molecules and the ethylene molecules [18]. Besides lowering the sensor response, 30%RH, 60%RH, and 90%RH prolonged the response times of the 1.0%Ag sensor by ~ 2-, 13-, and 10-times as shown by Fig. 7.6(d). This indicates slow adsorption of ethylene on the sensor surface possibly because constrained accessibility of the sensing surface due to the presence of pre-adsorbed water vapour molecules.

Table 7.2 compares performances of sensors produced in the present study and those of various noble metal-modified SMO-based ethylene sensors reported in the literature. The Ag- and Au-modified $\beta - Ga_2O_3$ nanorods sensors from this study that were operated at 140 ℃ presented comparable sensor performances to those sensors from the cited literature that were operated at higher temperatures.

*Table 7.2. Ethylene detection performances of various noble-metal modified SMO-based sensors. NPs represents nanoparticles, NFs stands for nanoflowers, † imply sensor tested in humidity, * represent $\frac{R_a}{R_g}$, and -- indicate data not reported.*

Material	Temp (℃)	C_2H_4 (ppm)	Response	t_{res}/t_{rec} (s)	Ref.
$Pd-SnO_2$ NPs	250	100	11.1*	1/--	[231]
$Pd/rGO-\alpha-Fe_2O_3$ NFs	250	1000	150*	18/50	[232]
SnO_2+ $1\%Pd$ NPs	450	100	4.53*	--	[230]
SnO_2+ $1\%Au$ NPs	450	100	5.33*	--	[230]
SnO_2+ $1\%Pd$ NPs	450 (30%RH)†	100	1.37*	--	[230]
SnO_2+ $1\%Au$ NPs	450 (30%RH)†	100	1.36*	--	[230]
SnO_2+ $1\%Pt$	350	20	8.13*	--	[233]
$\beta-Ga_2O_3$ NRs	165	90	0.3	27/93	This
$\beta-Ga_2O_3$: $0.5\%Ag$ NRs	140	90	1.1	17/85	work
$\beta-Ga_2O_3$: $1.0\%Ag$ NRs	140	90	3.1	18/60	↓
	140 (30%RH)†	90	2.0	28/78	
	140 (60%RH)†	90	1.9	232/237	
	140 (90%RH)†	90	2.4	177/228	
$\beta-Ga_2O_3$: $0.5\%Au$ NRs	140	90	1.2	16/86	
$\beta-Ga_2O_3$: $1.0\%Au$ NRs	140	90	0.4	15/76	

7.3.5 Gas sensing mechanism of unmodified and 1.0mol% Ag-modified $\beta-Ga_2O_3$ nanorods

The gas sensing performance of the $\beta-Ga_2O_3$ NRs-based sensor depends on the change in sensor electrical resistance which is caused by the adsorption and desorption of the target gas molecules at the surface of the nanorods [43]. In principle, upon exposure of unmodified $\beta-Ga_2O_3$ nanorods to air, oxygen molecules adsorb onto the surface of the nanorods and subsequently act as trapping centers of electrons from the conduction band of the nanorods and

become ionized to O_2^-, O^-, or O^{2-} species, depending on the sensor operating temperature [18]. As a result, the energy band of $\beta - Ga_2O_3$ nanorods bends up and a highly resistive electron depleted layer is formed close to $\beta - Ga_2O_3$ nanorods surfaces as depicted in Fig. 7.7(a). In this study, ethylene was detected at 165 and 140 ℃ for the unmodified, and modified sensors, respectively, hence the stabilization and chemisorption of O^- species onto the sensor active layer occurs according to Equation (7.1) [43].

$$O_{2\,(ads)}^- + e_{(surface)}^- \leftrightarrow 2O_{(ads)}^- \quad (100 - 300\ ℃) \qquad (7.1)$$

However, upon exposure of the unmodified $\beta - Ga_2O_3$ nanorods to ethylene, which is a reducing gas, the ethylene gas molecules interact with the pre-adsorbed O^- species to form CO_2 and H_2O according to reaction (7.2) and electrons are de-trapped from the oxygen species and released back to the $\beta - Ga_2O_3$ nanorods. Hence, the electrical resistance of the nanorods decreases as depicted in Fig. 7.7(b).

$$C_2H_{4\,(g)} + 6O_{(ads)}^- \rightarrow 2CO_{2\,(g)} + 2H_2O_{\,(g)} + 6e_{(conduction)}^- \qquad (7.2)$$

In the case of Ag-modified $\beta - Ga_2O_3$ nanorods-based sensor, the enhanced response towards ethylene can be explained based on the contribution of the electronic and chemical sensitization by the Ag nanocrystals. The XPS results demonstrated existence of Ag in both the elemental and oxide forms. Therefore, in the case of electronic sensitization, the contact between $\beta - Ga_2O_3$ nanorods and the Ag/Ag_2O nanocrystal possessing work function values of 4.11 and ~ 4.26/4.72 eV,

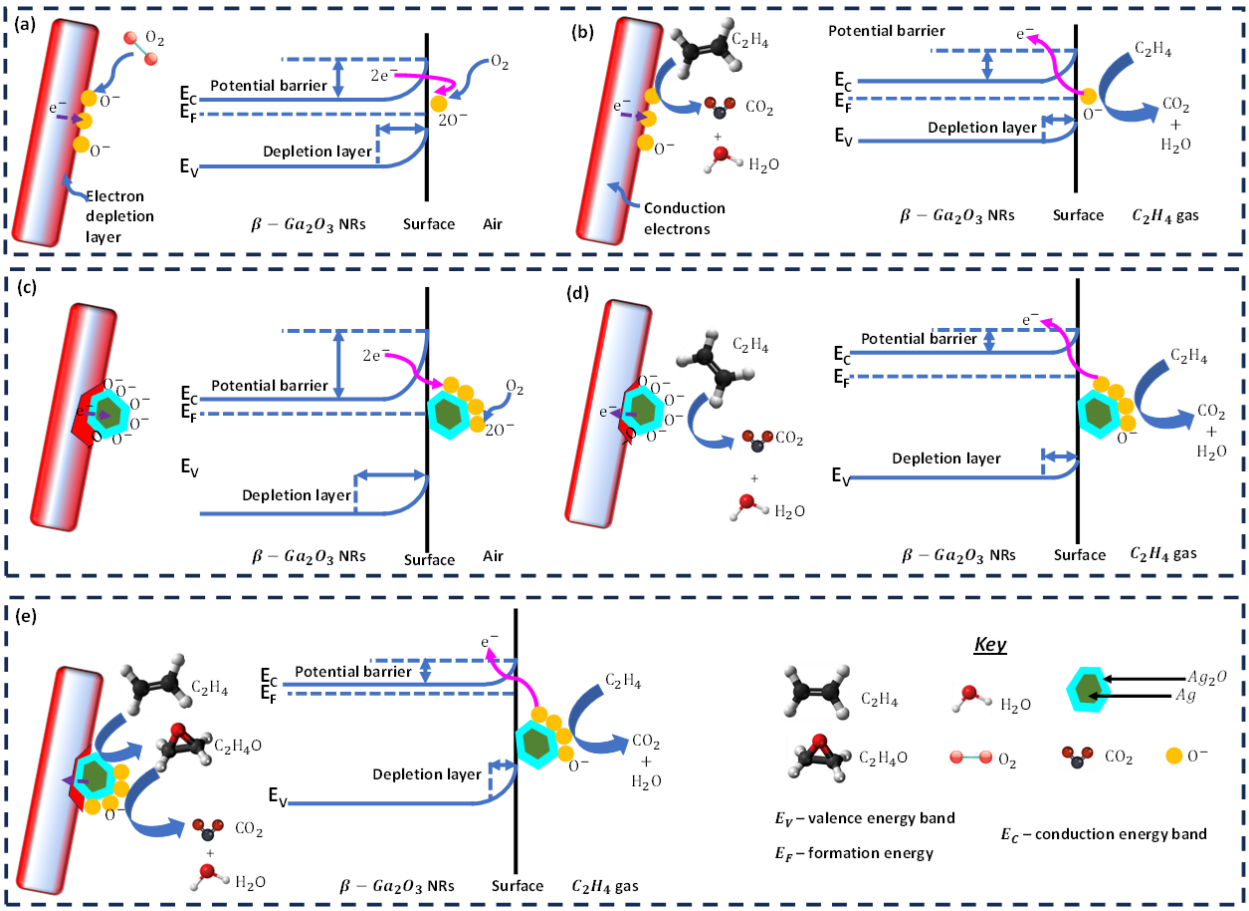


Fig. 7.7. *Schematic representations and band diagrams of (a, b) unmodified and (c-e) Ag-modified* $\beta - Ga_2O_3$ *nanorod-based sensors in air and in ethylene gas. (c, d) Electronic sensitization and (e) chemical sensitization of* $\beta - Ga_2O_3$ *nanorods by the* Ag/Ag_2O *nanocrystals.*

respectively, created a Schottky junction at the interface [234]. Ag_2O is a narrow band gap (1.0 – 1.5 eV) *p*-type semiconductor hence the junction formed is a *p-n* type [235] and electrons flow from the $\beta - Ga_2O_3$ nanorod to the Ag/Ag_2O nanocrystal. This widens the electron depletion layer and increases the base resistance of the modified $\beta - Ga_2O_3$ nanorods [236], as shown in Fig. 7.7(c). Consequently, when the Ag-modified $\beta - Ga_2O_3$ nanorods-based sensor is exposed to ethylene, it exhibits higher resistance change than the unmodified sensor (Fig. 7.7(d)).

Regarding the chemical sensitization process, the high catalytic activity of the Ag/Ag_2O nanocrystal facilitates the dissociation of ethylene molecules. The ethylene gas molecules are oxidized to C_2H_4O according to Equation (7.3) before spilling-over to the surface of $\beta - Ga_2O_3$ nanorods where they are oxidized further by the pre-adsorbed O^- species to form CO_2 and H_2O according to Equation (7.4). As a result, additional oxygen species are created to react with the ethylene gas molecules as illustrated in Fig. 7.7(e).

$$Ag_2O_{(s)} + C_2H_{4\,(g)} \rightarrow 2Ag_{(s)} + C_2H_4O_{(g)} \quad (7.3)$$

$$C_2H_4O_{(g)} + 5O^-_{(ads)} \rightarrow 2CO_{2(g)} + 2H_2O_{(g)} + 5e^-_{(conduction)} \quad (7.4)$$

In addition, since ethylene detection by Ag-modified $\beta - Ga_2O_3$ nanorods is a surface reaction process, the response of the modified sensor can also be influenced by the density of intrinsic defects present on the surface of the modified nanorods. The XPS results demonstrated that the 1.0%Ag sensor presented highest lattice oxygen. Therefore, it is apparent that the sensing response of the $\beta - Ga_2O_3$ nanorods modified with 1.0 $mol\%\ Ag$ is enhanced by the presence of lattice oxygen at the surface of the sensing material.

7.4 Conclusion

We successfully prepared unmodified and Ag- and Au-modified $\beta - Ga_2O_3$ nanorods using a microwave-assisted hydrothermal method and evaluated their ethylene detection abilities in both dry and humid atmospheric conditions. Characterization of $\beta - Ga_2O_3$ nanorods, before and after modification with 0.5 $mol\%\ Ag$, 1.0 $mol\%\ Ag$, 0.5 $mol\%\ Au$ and 1.0 $mol\%\ Au$ were performed and the XRD, TEM, and XPS results revealed the presence of randomly distributed Ag and Au nanocrystals on the surface of $\beta - Ga_2O_3$ nanorods in the modified samples.

Furthermore, the XPS results demonstrated that the Au and Ag nanocrystals possess more than one electronic state. The gas sensing measurements results showed that all Ag- and Au-modified $\beta - Ga_2O_3$ nanorods-based gas sensors presented high, selective, and rapid response to ethylene at a lower operating temperature, compared to the unmodified $\beta - Ga_2O_3$ nanorods-based sensor. The 1.0 $mol\%$ Ag-modified $\beta - Ga_2O_3$ nanorods displayed the highest response of 3.18, towards 90 ppm ethylene, with limit of detection of 1.3 ppm, when operated at 140 ℃ in $0\%RH$, and this was explained with reference to the electronic and chemical sensitization effects induced by the Ag/Ag_2O nanocrystals and the high density of lattice oxygen defects in the sensing material. In addition, the $\beta - Ga_2O_3$ nanorods modified with 1.0 $mol\%Ag$ still presented commendable responses under humid atmospheric environments. Based on these results, the 1.0 $mol\%Ag$-modified $\beta - Ga_2O_3$ nanorods could be applied in the precise and economical detection of ethylene around plants and fruits.

CHAPTER 8

Conclusion and future prospects

8.1 Conclusion

This study described the synthesis and characterization of Ga_2O_3 nanostructures, and their investigation as sensing layers for detection of carbon monoxide, ethylene, and isopropanol. The synthesized materials were characterized by several analysis techniques namely, thermogravimetric analysis (TGA), X-ray diffraction (XRD), Raman analysis, scanning electron microscope (SEM), transmission electron microscope (TEM), Brunauer-Emmett-Teller (BET), photoluminescence (PL), diffuse reflectance spectroscopy (DRS), and X-ray photoelectron spectroscopy (XPS). The systemic gas sensing measurements were conducted on Ga_2O_3-based sensors and the results obtained were correlated to crystallinity, microstructural, defects density, surface area, porosity, and morphology of the synthesized materials.

In summary, unmodified and noble metal modified $1D$ Ga_2O_3 nanostructures were prepared by microwave-assisted hydrothermal method followed by heat-treatment. The systematic heat-treatment study revealed that control of the treatment temperature can significantly influence the crystal, fundamental properties, and gas sensing characteristics of Ga_2O_3 materials. Post preparation heat-treatment had direct influence on the crystallinity, defects (type and density), surface area and porosity of the Ga_2O_3 nanorods/nanowires, which demonstrated higher capabilities of carbon monoxide capabilities. Further, on a separate study of the different morphologies of $\beta - Ga_2O_3$, we observed that the regular and hierarchical nanorod-based gas sensing materials presented different isopropanol gas sensing performances. This is because the

preferred orientation of nanorod attachments in bundle-like and dandelion-like nanostructures influenced the materials porosity, surface area and density of defects available on the surfaces for interaction with the isopropanol gas molecules. The randomly oriented nanorods presented the highest response towards isopropanol than the nanobundles and nanodandelions structures, which was attributed to high porosity and large surface area. However, the nanobundles showed the fastest response/recovery times than its counterparts and this was attributed to the high number of surface contact channels available for enhanced charge transport. This study demonstrated possibilities of tuning the gas sensing properties of $\beta - Ga_2O_3$ nanorods by controlling the synthesis parameters. From a study that focused on the effects of surface modification by Ag and Au noble metal nanoparticles, the $\beta - Ga_2O_3$ nanorods modified with 1.0 $mol\%$ Ag presented highest response towards ethylene. The observed enhanced sensor performance was ascribed to the electronic and chemical sensitization effects of the Ag nanocrystals. In addition, the presence of Ag nanocrystals controlled the oxygen defects distribution in the sensing material, which had a direct influence on the material's ethylene detection capabilities.

This study demonstrated that the fundamental properties and gas sensing performance of Ga_2O_3 nanostructures can be optimized by controlling synthesis parameters and post-preparation heat-treatment temperature. It is therefore safe to conclude that the response and selectivity towards gases like carbon monoxide and isopropanol were enhanced dramatically by controlling the synthesis parameters and heat treatment temperature to tailor particle morphology, improve crystallinity and stability, increase porosity and the surface area of Ga_2O_3 nanostructures. Finally, dramatic improvement of response and selectivity towards ethylene at lower working

temperature was observed from the Ga_2O_3 nanostructures decorated with controlled concentration of noble Ag metal nanoparticles.

8.2 Prospects

This work has demonstrated the potential of unmodified and noble metal modified Ga_2O_3 material as platforms for effective detection of carbon monoxide, propanol, and ethylene. However, further steps still need to be implemented to fully optimize this material for commercial use. Firstly, Ag-modified $\beta - Ga_2O_3$ can be used in the formation of ternary oxides or heterostructures with other metal oxides for improved gas sensor response, selectivity, and stability. However, the different models used to interpret the sensing performances of ternary oxides and heterostructures need to be understood through sets of experiments aimed at following trends on the formation of the ternary oxides or heterostructures on fundamental properties of $\beta - Ga_2O_3$.

Another perspective is to apply a different method for fabricating the test sensor and film. This will aim at providing a film deposition method that will completely eliminate interaction between the sensing material and the Pt electrodes and heater used in the current method. This will significantly reduce effects from the interfering sensing materials on the sensor signal and temperature calibrations. Furthermore, in the film deposition method, controlled measures are necessary for the deposition of films with similar thicknesses for fair comparison of the sensor signals.

In view of this evaluation, the present work can inspire more research towards the hydrothermally synthesized unmodified and Ag-modified nanorod-based Ga_2O_3 materials for

the application in gas sensors as their flexibility enables tuning of properties. In addition, their sensitivity towards carbon monoxide, isopropanol, and ethylene within the tested concentration ranges can generate interest towards their application in indoor air quality monitoring and food safety control. Therefore, the unmodified and Ag-modified $\beta - Ga_2O_3$ nanomaterials present the capacity to be used in real time detection of gases.

8.3 Further applications of Ga_2O_3 materials

The Ga_2O_3 powders synthesized in this study demonstrated unique gas sensing properties. However, the characterization results for structural, chemical, and optical properties further demonstrate unique inherent properties which include high thermal stability, chemical inertness, wide band gap, optical transparency, and electrical conductivity. This suggests that the studied materials can also be applied in other technological domains such as power electronics, high-energy devices, photocatalysis, biomedicine, high-temperature sensors, photonics and optoelectronic devices, and ultraviolet detectors.

Solar-blind photodetectors: The hydrothermally-synthesized Ga_2O_3 materials present an ultra-wide band gap of 4.6-4.8 eV. According to the literature [158,159,171,237,238], this property makes the materials promising candidates for solar-blind photodetectors. This large band gap of Ga_2O_3 directly corresponds to the solar-blind ultraviolet detection band with wavelength below 280 nm. Recent studies demonstrated solar-blind photodetection using $\beta(Al) - Ga_2O_3$ crystal [239], $\beta - Ga_2O_3$ nanorod arrays [240], and $\alpha/\beta - Ga_2O_3$ [241] and it concluded that theGa_2O_3 materials exhibit excellent UV photodetection than most doped materials such as $MgZnO$ and $AlGaN$. This insight reveals that the synthesized Ga_2O_3 can be utilized in various

applications including in flame detection, UV dosimetry, missile tracking, ozone holes monitoring, and so on.

Transparent conductive oxides: Ga_2O_3 material is a promising candidate for transparent conductive oxide electrodes. Its application in this area is supported by its ultra-wide band gap, excellent chemical and thermal stability, and high transmittance to visible light. Furthermore, the carrier concentration of Ga_2O_3 materials can be tuned from low ($10^{17}\ cm^{-3}$) up to $10^{20}\ cm^{-3}$ by doping with metals such as Si, Ge, or Sn [242,243] and this improved the conductivity of the material, making it easily applicable as transparent conductive electrodes. Ga_2O_3 materials have so far demonstrated excellent properties as an electrode than most commercial electrodes such as indium tin oxide, fluorine-doped tin oxide and aluminum-doped zinc oxide [244].

Phosphors: The hydrothermally-synthesized Ga_2O_3 materials have demonstrated excellent optical properties and by taking advantage of its high transparency, Ga_2O_3 can be tuned into a multicolor-emitting phosphor. This is through doping it with rare-earths or other elements which exhibits strong luminescence emissions at various wavelengths [164]. In addition to this, Ga_2O_3 present good thermal and chemical stability which makes Ga_2O_3-based materials suitable for making devices such as high-brightness light emitting displays. Besides, as undoped, the blue and red emission shown by Ga_2O_3 materials may be useful in the production of white light.

High-temperature sensing and photocatalysis: Due to their high thermal stability, Ga_2O_3 can also be applied in gas sensing applications under high temperature conditions such as in exhaust pipes of automobiles, incinerators, and refinery plants [23,42]. On the other hand, in photocatalysis, Ga_2O_3 presents good photocatalytic behavior especially towards the

defluorination of fluorinated substances [161,190,245–247]. This material presents higher redox potential and a wider band gap compared to TiO_2, enabling it to efficiently degrade organic substances attached to the catalyst surface than TiO_2.

High-power devices: Ga_2O_3 materials possess fundamental electronic properties such as high thermal stability, wide band gap, high breakdown field, high electron mobility that make them ideal candidates for high-power devices [87,88]. For example, $\beta - Ga_2O_3$ presents a high breakdown field (~10 MV/cm) that is higher than the breakdown field of GaN (3.3 MV/cm) and SiC (2.5 MV/cm). This high breakdown field enables Ga_2O_3-based devices to be biased at a high drain voltage ($V_{\text{break-down}} \gg 100\ V$) while maintaining a large dynamic range [157,248–250]. Furthermore, the wide band gap of Ga_2O_3 allows device operation at elevated temperature (>300 °C) without degradation. In addition, Ga_2O_3 has a high saturation electron velocity ($v_{\text{sat}} = 2 \times 10^7\ cm/s$), which is partially accountable for the high current density. Thus, $\beta - Ga_2O_3$ materials synthesized in this study may find application in power electronic devices operating in high-temperature environments, such as automotive, aerospace, and industrial applications.

Multifunction drug carrier: Besides application of $\beta - Ga_2O_3$ in optoelectronic devices due to the excellent optical properties, this material also presents good potential in bio-imaging. A recent study of the multifunctional drug carriers of porous $\beta - Ga_2O_3{:}\,Cr^{3+}$ nanoparticles demonstrated effective drug delivery to tumor cells [251]. Nanoparticles loaded with doxorubicin hydrochloride and coated by hyaluronic acid demonstrated drug release behavior that is associated with rapid internalization of the nanoparticles into tumor cells. A similar application

for gallium oxyhydroxide nanomaterials has been reported in literature [252]. This insight demonstrates that the $GaOOH$ and Ga_2O_3 material prepared in this study, which presented emission from background chromium impurities, can be studied further for potential application in drug delivery.

These applications highlight the versatility of Ga_2O_3 in advanced technology fields, contributing to its growing popularity in research and industrial use.

REFERENCES

[1] Nasiri, N. and Clarke, C. Nanostructured gas sensors for medical and health applications: Low to high dimensional materials. *Biosensors*. 2019; 9(1):43. doi. 10.3390/bios9010043.

[2] Chavali, M.S. and Nikolova, M.P. Metal oxide nanoparticles and their applications in nanotechnology. *SN Applied Science*. 2019; 1(6):607. doi: 10.1007/s42452-019-0592-3.

[3] Vargas-Bernal, R., and Herrera-Pérez, G. Importance of the nanostructured ceramic materials on gas sensing, *Nanotechnology for optics and sensors, Aliofkhazraei, M. (Ed.) Ed. One Central Press*, Cheshire, UK. 2014:1–34.

[4] Fine, G.F., et al. Metal oxide semi-conductor gas sensors in environmental monitoring. *Sensors*. 2010; 10(6):5469. doi: 10.3390/s100605469.

[5] Javaid, M., et al. Sensors for daily life: A review. *Sensors International*. 2021; 2:100121. doi: 10.1016/j.sintl.2021.100121.

[6] Xue, S., et al. Improving gas-sensing performance based on MOS nanomaterials: A review. *Materials*. 2021; 14(15):4263. doi: 10.3390/ma14154263.

[7] Baig, N., Kammakakam, I., and Falath, W. Nanomaterials: A review of synthesis methods, properties, recent progress, and challenges. *Materials Advances*. 2021; 2(6):1821. doi: 10.1039/d0ma00807a.

[8] Krishna, K.G., et al. Nanostructured metal oxide semiconductor-based gas sensors: A comprehensive review. *Sensors and Actuators A: Physical*. 2022; 341:113578. doi: 10.1016/j.sna.2022.113578.

[9] Xu, J., et al. Synthesis and optimization strategies of nanostructured metal oxides for chemiresistive methanol sensors. *Ceramics International*. 2023; 49(13):21113. doi: 10.1016/j.ceramint.2023.03.274.

[10] Arafat, M.M., et al. Gas sensors based on one dimensional nanostructured metal-oxides: A review. *Sensors*. 2012; 12(6):7207. doi. 10.3390/s120607207.

[11] Bai, H. and Shi, G. Gas Sensors Based on Conducting Polymers. *Sensors*. 2007; 7(3):267. doi: 10.3390/s7030267.

[12] Wang, Y. and Yeow, J.T.W. A review of carbon nanotubes-based gas sensors. *Journal of Sensors*. 2009; 2009:493904. doi: 10.1155/2009/493904.

[13] Goel, N., et al. Metal oxide semiconductors for gas sensing. *Engineering Reports*. 2023; 5(6):e12604. doi:10.1002/eng2.12604.

[14] Bochenkov, V. E., and G. B. Sergeev. "Sensitivity, selectivity, and stability of gas-sensitive metal-oxide nanostructures." *Metal oxide nanostructures and their applications* 3 (2010): 31-52.

[15] Gardon, M. and Guilemany, J.M. A review on fabrication, sensing mechanisms and performance of metal oxide gas sensors. *Journal of Materials Science: Materials in Electronics*. 2013; 24(5):1410. doi: 10.1007/s10854-012-0974-4.

[16] Saruhan, B., Fomekong, R.L., and Nahirniak, S. Review: Influences of semiconductor metal oxide properties on gas sensing characteristics. *Frontiers in Sensors*. 2021; 2:657931. doi: 10.3389/fsens.2021.657931.

[17] Lahade, S.V. and Pardhi, P.D. Gas sensing technologies: Review, scope and challenges. *International Journal of Recent Trends in Engineering and Research*. 2018; 4:108. doi: 10.23883/ijrter.2018.4073.m2xns.

[18] Wang, C., et al. Metal oxide gas sensors: Sensitivity and influencing factors. *Sensors*. 2010; 10(3):2088. doi: 10.3390/s100302088.

[19] Franco, M.A., et al. A review on chemiresistive ZnO gas sensors. *Sensors and Actuators Reports*. 2022; 4:100100. doi: 10.1016/j.snr.2022.100100.

[20] Tian, X., et al. Gas sensors based on TiO_2 nanostructured materials for the detection of hazardous gases: A review. *Nano Materials Science*. 2021; 3(4):390. doi: 10.1016/j.nanoms.2021.05.011.

[21] Dong, C., et al. A review on WO_3 based gas sensors: Morphology control and enhanced sensing properties. *Journal of Alloys Compounds*. 2020; 820:153194. doi: 10.1016/j.jallcom.2019.153194.

[22] Masuda, Y. Recent advances in SnO_2 nanostructure based gas sensors. *Sensors and Actuators B: Chemical*. 2022; 364:131876. doi: 10.1016/j.snb.2022.131876.

[23] Zhu, J., et al. Gallium oxide for gas sensor applications: A comprehensive review. *Materials*. 2022; 15(20):7339. doi: 10.3390/ma15207339.

[24] Mokoena, T.P., Swart, H.C., and Motaung, D.E. A review on recent progress of p-type nickel oxide based gas sensors: Future perspectives. *Journal of Alloys Compounds*. 2019; 805:267. doi: 10.1016/j.jallcom.2019.06.329.

[25] Steinhauer S. Gas sensors based on copper oxide nanomaterials: A review. *Chemosensors*. 2021; 9(3):51. doi: 10.3390/chemosensors9030051.

[26] Toan, N.N., Saukko, S., and Lantto, V. Gas sensing with semiconducting perovskite oxide $LaFeO_3$. *Physica B: Condensed Matter.* 2003; 327(2-4); 279. doi: 10.1016/S0921-4526(02)01764-7.

[27] Meng, F-J., Xin, R-F., and Li, S-X. Metal oxide heterostructures for improving gas sensing properties: A review. *Materials*. 2023; 16(1):263. doi; 10.3390/ma16010263.

[28] Zhu, LY., et al. Advances in noble metal-decorated metal oxide nanomaterials for chemiresistive gas sensors: Overview. *Nano-Micro Letters*. 2023; 15:89. doi: 10.1007/s40820-023-01047-z.

[29] Zappa, D., et al. Metal oxide-based heterostructures for gas sensors- A review. *Analytic Chimica Acta*. 2018; 1039:1. doi: 10.1016/j.aca.2018.09.020.

[30] Sun, Y-F., et al. Metal oxide nanostructures and their gas sensing properties: A review. *Sensors*. 2012; 12(3):2610. doi: 10.3390/s120302610.

[31] Mirzaei, A., et al. Metal oxide semiconductor nanostructure gas sensors with different morphologies. *Chemosensors*. 2022; 10(7):289. doi: 10.3390/chemosensors10070289.

[32] Lin, T., et al. The morphologies of the semiconductor oxides and their gas-sensing properties. *Sensors*. 2017; 17(12):2779. doi: 10.3390/s17122779

[33] Shi, F., and Qiao, H. Preparations, properties and applications of gallium oxide nanomaterials – A review. *Nano Select*. 2022; 3(2):348. doi: 10.1002/nano.202100149.

[34] Sharma, A., et al. Nano-structured phases of gallium oxide (GaOOH, α-Ga_2O_3, β-Ga_2O_3, γ-Ga_2O_3, δ-Ga_2O_3, and ε-Ga_2O_3): fabrication, structural, and electronic structure investigations. *International Nano Letters*. 2020; 10:71. doi: 10.1007/s40089-020-00295-w.

[35] Kim, H., et al. Fabrication and CO gas-sensing properties of Pt-functionalized Ga_2O_3 nanowires. *Ceramics International*. 2012; 38(5):3563. doi: 10.1016/j.ceramint.2011.12.072.

[36] Pilliadugula, R., and Krishnan N.G. Effect of pH dependent morphology on room temperature NH_3 sensing performances of β-Ga_2O_3. *Materials Science Semiconductor Processing*. 2020; 112:105007. doi: 10.1016/j.mssp.2020.105007.

[37] Balasubramani, V., et al. Highly sensitive and selective H_2S gas sensor fabricated with β-Ga_2O_3/rGO. *ECS Journal of Solid State Science and Technology*. 2020; 9(5):055009. doi: 10.1149/2162-8777/ab9a18.

[38] Almaev, A.V., et al. Oxygen sensors based on gallium oxide thin films with addition of chromium. *Superlattices and Microstructure*. 2020; 139:106392. doi: 10.1016/j.spmi.2020.106392.

[39] Wang J, Jiang S, Liu H, et al. P-type gas-sensing behavior of Ga_2O_3/Al_2O_3 nanocomposite with high sensitivity to NO_x at room temperature. *Journal of Alloys and Compounds*. 2020; 814:152284. doi: 10.1016/j.jallcom.2019.152284.

[40] Dyndal, K., et al. CuO-Ga_2O_3 thin films as a gas-sensitive material for acetone detection. *Sensors*. 2020; 20(11):3142. doi: 10.3390/s20113142.

[41] Jang Y-G., et al. Fabrication of Ga_2O_3/SnO_2 core–shell nanowires and their ethanol gas sensing properties. *Journal of Materials Research*. 2011; 26(17):2322. doi: 10.1557/jmr.2011.189.

[42] Zhai, H., Wu, Z., and Fang Z. Recent progress of Ga_2O_3-based gas sensors. *Ceramics International*. 2022; 48(17):24213. doi: 10.1016/j.ceramint.2022.06.066.

[43] Afzal A. β-Ga_2O_3 nanowires and thin films for metal oxide semiconductor gas sensors: Sensing mechanisms and performance enhancement strategies. *Journal of Materiomics*. 2019; 5(4):542. doi: 10.1016/j.jmat.2019.08.003.

[44] Weng, T.F., et al. VLS growth of pure and Au decorated β-Ga_2O_3 nanowires for room temperature CO gas sensor and resistive memory applications. *Applied Surface Science*. 2020; 533:147476. doi: 10.1016/j.apsusc.2020.147476.

[45] Park, S., et al. Synthesis, structure and ethanol sensing properties of Ga_2O_3-core/WO_3-shell nanostructures. *Thin Solid Films*. 2015; 314(Part B):341. doi. 10.1016/j.tsf.2015.04.045.

[46] World Health Organization, Household air pollution, (2023). https://www.who.int/news-room/fact-sheets/detail/household-air-pollution-and-health. Last updated 15 December 2023. (accessed 3 June 2024).

[47] Galstyan, V., et al. Metal oxide nanostructures in food applications: Quality control and packaging. Chemosensors. 2018; 6(2):16. doi: 10.3390/chemosensors6020016.

[48] Van Duy, L., et al. Room temperature ammonia gas sensor based on p-type-like V_2O_5 nanosheets towards food spoilage monitoring. *Nanomaterials*. 2023; 13(1):146. doi: 10.3390/nano13010146.

[49] Janssen, S., et al. Ethylene detection in fruit supply chains. *Philosophical Transactions of the Royal Society A*. 2014; 372:20130311. doi: 10.1098/rsta.2013.0311.

[50] Cristescu, S.M., et al, Current methods for detecting ethylene in plants, *Annals of Botany*. 2013; 111(3):347. doi: 10.1093/aob/mcs259.

[51] Chen, X., Wreyford, R., and Nasiri, N. Recent advances in ethylene gas detection. *Materials*. 2022; 15(17):5813. doi: 10.3390/ma15175813.

[52] Xing, R., et al. Preparation and gas sensing properties of In_2O_3/Au nanorods for detection of volatile organic compounds in exhaled breath. *Scientific Reports*. 2015; 5:10717 doi: 10.1038/srep10717.

[53] Neri G. First fifty years of chemoresistive gas sensors. *Chemosensors*. 2015; 3(1):1. doi: 10.3390/chemosensors3010001.

[54] Ponzoni, A., et al. Metal oxide gas sensors, a survey of selectivity issues addressed at the SENSOR Lab, Brescia (Italy). *Sensors*. 2017; 17(4):714. doi: 10.3390/s17040714.

[55] Liang, C.H., et al. Catalytic synthesis and photoluminescence of β-Ga_2O_3 nanowires. *Applied Physics Letters*. 2001; 78(21):3202. doi: 10.1063/1.1374498.

[56] Swallow, J.E.N., et al. Influence of polymorphism on the electronic Structure of Ga_2O_3. *Chemistry of materials*. 2020; 32(19):8460. doi: 10.1021/acs.chemmater.0c02465.

[57] Vetelino, J., and Reghu, A. *Introduction to Sensors*. (1st ed.). CRC Press. 2017. doi: 10.1201/9781315218274CRC.

[58] Liu, X., et al. A survey on gas sensing technology. *Sensors*. 2012; 12(7):9635. doi: 10.3390/s120709635.

[59] Yunusa, Z., et al. Gas sensors: A review. *Sensors and Transducers*. 2014; 168(4):61.

[60] Brattain, W.H., and Bardeen, J. Surface properties of germanium. *Bell System Technical Journal*. 1953; 32(1):1. doi: 10.1002/j.1538-7305.1953.tb01420.x.

[61] Seiyama, T., et al. A new detector for gaseous components using semiconductive thin films. *Analytical Chemistry*. 1962; 34(11):1502. doi:10.1021/ac60191a001.

[62] Taguchi, N., et al. Gas detecting device. Japan, 1972: patent number 3695848. 1972.

[63] Dey A. Semiconductor metal oxide gas sensors: A review. *Materials Science and Engineering: B*. 2018; 229:206. doi: 10.1016/j.mseb.2017.12.036.

[64] Shankar, P., and Rayappan J.B.B. Gas sensing mechanism of metal oxides: The role of ambient atmosphere, type of semiconductor and gases- A review. *Science Letters Journal*. 2015; 4:126.

[65] Xu, X., et al. Porous hierarchical In_2O_3 nanostructures: Hydrothermal preparation and gas sensing properties. *Sensors and Actuators B: Chemical*. 2012; 171-172:1066. doi: 10.1016/j.snb.2012.06.035.

[66] Lee, Y.C., et al. p-type α-Fe2O3 nanowires and their n-type transition in a reductive ambient. Small. 2007; 3(8):1356. doi: 10.1002/smll.200700004.

[67] Ahmed, S., and Sinha S.K. Studies on nanomaterial-based p-type semiconductor gas sensors. Environmental Science and Pollution Research. 2023; 30(10):24975. doi:10.1007/s11356-022-21218-6.

[68] Ji H, Zeng W, Li Y. Gas sensing mechanisms of metal oxide semiconductors: A focus review. *Nanoscale*. 2019; 11(47):22664. doi:10.1039/c9nr07699a.

[69] Deng Y. *Sensing mechanism and evaluation criteria of semiconducting metal oxides gas sensors, Semiconducting metal oxides for gas sensing*. Springer Singapore; Singapore. 2019:23-51. doi: 10.1007/978-981-13-5853-1.

[70] Burgués J., Jiménez-Soto, J.M., and Marco S. Estimation of the limit of detection in semiconductor gas sensors through linearized calibration models. *Analytica Chimica Acta*. 2018; 1013:13. doi: 10.1016/j.aca.2018.01.062.

[71] Honeycutt, W.T., Ley, M.T., and Materer, N.F. Precision and limits of detection for selected commercially available, low-cost carbon dioxide and methane gas sensors. *Sensors*. 2019; 19(14):3157. doi: 10.3390/s19143157.

[72] Chen, X., et al. Nanostructured gas sensors: From air quality and environmental monitoring to healthcare and medical applications. *Nanomaterials*. 2021; 11(8):1927. doi: 10.3390/nano11081927.

[73] Dhall, S., et al. A review on environmental gas sensors: Materials and technologies. *Sensors International*. 2021; 2:100116. doi: 10.1016/j.sintl.2021.100116.

[74] Basu, S., and Basu, P.K. Nanocrystalline metal oxides for methane sensors: Role of noble metals. *Journal of Sensors*. 2009; 2009:861968. doi:10.1155/2009/861968.

[75] Khan, M.A.H., Rao, M.V., and Li, Q. Recent advances in electrochemical sensors for detecting toxic gases: NO_2, SO_2 and H_2S. *Sensors*. 2019; 19(4):905. doi:10.3390/s19040905.

[76] Kaushik, A., et al. Nanostructured gas sensors for health care: An overview. *Journal of Personalized Nanomedicine*. 2015; 1(1):10.

[77] Cordente, A.G., et al. Aromatic higher alcohols in wine: Implication on aroma and palate attributes during chardonnay aging. *Molecules*. 2021; 26(16):4979. doi:10.3390/molecules26164979.

[78] Wei, Q., et al. Identification of characteristic volatile compounds and prediction of fermentation degree of pomelo wine using partial least squares regression. *Lebensmittel-Wissenschaft and Technologie*. 2022; 154. doi: 10.1016/j.lwt.2021.112830.

[79] de Boisbaudran L. On the chemical and spectroscopic characters of a new metal (gallium). *The London, Edinburgh, and Dublin Philosophical Magazine and Journal of Science*. 1875; 50(332):414. doi: 10.1080/14786447508641312.

[80] Roy, R., Hill, V.G., and Osborn, E.F. Polymorphism of Ga_2O_3 and the system Ga_2O_3-H_2O. *Journal of the American Chemical Society*. 1952; 74(3):719.

[81] Playford, H.Y., et al. Structures of uncharacterised polymorphs of gallium oxide from total neutron diffraction. *Chemistry - A European Journal*. 2013; 19(8):2803. doi:10.1002/chem.201203359.

[82] Zhang, J., et al. Recent progress on the electronic structure, defect, and doping properties of Ga_2O_3. *APL Materials*. 2020; 8(2):020906. doi: 10.1063/1.5142999.

[83] Playford, H.Y., Hannon, A.C., Tucker, M.G., et al. Characterization of structural disorder in γ-Ga_2O_3. *Journal of Physical Chemistry C*. 2014; 118(29):16188. doi: 10.1021/jp5033806.

[84] Chiang, J.L., et al. A Review on gallium oxide materials from solution processes. *Nanomaterials*. 2022; 12(20):3601. doi: 10.3390/nano12203601.

[85] Nishinaka, H., et al. Single-domain and atomically flat surface of κ-Ga_2O_3 thin films on FZ-grown ϵ-$GaFeO_3$ substrates via step-flow growth mode. *ACS Omega*. 2020; 5(45):29585. doi: 10.1021/acsomega.0c04634.

[86] Reddy, L.S., Ko, Y.H., and Yu, J.S. Hydrothermal synthesis and photocatalytic property of β-Ga_2O_3 nanorods. *Nanoscale Research Letters*. 2015; 10(364):1. doi: 10.1186/s11671-015-1070-5.

[87] Pearton, S.J., et al. A review of Ga_2O_3 materials, processing, and devices. *Applied Physics Review*. 2018; 5(1):011301. doi: 10.1063/1.5006941.

[88] Higashiwaki, M. β-Ga_2O_3 material properties, growth technologies, and devices: A review. *AAPPS Bulletin*. 2022; 32:3. doi: 10.1007/s43673-021-00033-0.

[89] Alhalaili, B., Mao, H., Islam, S. *Ga_2O_3 nanowire synthesis and device applications, Novel nanomaterials—Synthesis and applications*. George, Z.K., Athanasios, C.M., Eds. IntechOpen: London, UK, 2017.

[90] Yang, G., and Park, S.J. Conventional and microwave hydrothermal synthesis and application of functional materials: A review. *Materials*. 2019; 12(7):1177. doi: 10.3390/ma12071177.

[91] Mohammadi, M.R., and Fray, D.J. Semiconductor TiO_2-Ga_2O_3 thin film gas sensors derived from particulate sol-gel route. *Acta Materialia*. 2007; 55(13):4455. doi: 10.1016/j.actamat.2007.04.011

[92] Taş, A.C., Majewski, P.J., and Aldinger, F. Synthesis of gallium oxide hydroxide crystals in aqueous solutions with or without urea and their calcination behavior. *Journal of the American Ceramic Society*. 2002; 85(6):1421. doi:10.1111/j.1151-2916.2002.tb00291.x.

[93] Dulda, A. Morphology controlled synthesis of α-GaO(OH) nanoparticles: Thermal conversion to Ga_2O_3 and photocatalytic properties. *Advances in Materials Science and Engineering*. 2016; 2016: 3905625. doi:10.1155/2016/3905625.

[94] Bae, H.J., et al. High-aspect ratio β-Ga_2O_3 nanorods via hydrothermal synthesis. *Nanomaterials*. 2018; 8(8):594. doi:10.3390/nano8080594.

[95] Shi, F., and Qiao, H. Influence of hydrothermal reaction time on crystal qualities and photoluminescence properties of β-Ga_2O_3 nanorods. *Journal of Materials Science: Materials in Electronics*. 2020; 31(22):20223. doi:10.1007/s10854-020-04542-w.

[96] Madras, G., and McCoy, B.J. Temperature Effects during Ostwald Ripening. *Journal of Chemical Physics*. 2003; 119(3):1683. doi: 10.1063/1.1578617.

[97] Gatsi, N.C., et al. Hierarchically-ordered nanorods of Ga_2O_3 derived from microwave-assisted hydrothermal approach: Investigation of calcination-induced structural evolution and optical behavior. *Materials Today Communications*. 2022; 33:104808 doi:10.1016/j.mtcomm.2022.104808.

[98] Pilliadugula, R., and Krishnan, N.G. Gas sensing performance of GaOOH and β-Ga_2O_3 synthesized by hydrothermal method: A comparison. *Materials Research Express*. 2019; 6(2):025027. doi:10.1088/2053-1591/aaede8.

[99] Fleischer, M., and Meixner, H. Oxygen sensing with long-term stable Ga_2O_3 thin films. *Sesnors and Actuators B: Chemical*. 1991; 5(1-4):115. doi: 10.1016/0925-4005(91)80230-H.

[100] Lin, H-J., et al. Perovskite nanoparticle-sensitized Ga_2O_3 nanorod arrays for CO detection at high temperature. *ACS Applied Materials and Interfaces*. 2016; 8(14):8880. doi: 10.1021/acsami.6b01709.

[101] Yan., S, et al. Synthesis of a mesoporous single crystal Ga_2O_3 nanoplate with improved photoluminescence and high sensitivity in detecting CO. *Chemical Communications*. 2010; 46(34):6388. doi: 10.1039/c0cc01579b.

[102] Park, S.H., et al. Synthesis and CO gas sensing properties of surface-nitridated Ga_2O_3 nanowires. *RSC Advances*. 2014; 4(108):63402. doi: 10.1039/c4ra09538c.

[103] Lin, H-J., Gao, H., and Gao, P-X. UV-enhanced CO sensing using Ga_2O_3-based nanorod arrays at elevated temperature. *Applied Physics Letters*. 2017; 110(4):043101. doi: 10.1063/1.4974213.

[104] Liu, Z., et al. O_2 and CO sensing of Ga_2O_3 multiple nanowire gas sensors. *Sensors and Actuators B: Chemical*. 2008; 129(2008):666. doi: 10.1016/j.snb.2007.09.055.

[105] Schwebel, T., Fleischer, M., and Meixner, H. A selective, temperature compensated O_2 sensor based on Ga_2O_3 thin films. *Sensors and Actuators B: Chemical*. 2000; 65(1-3):176. doi: 10.1016/S0925-4005(99)00326-3.

[106] Baban, C., Toyoda, Y., and Ogita, M. Oxygen sensing at high temperatures using Ga_2O_3 films. *Thin Solid Films*. 2005; 484(1-2):369. doi: 10.1016/j.tsf.2005.03.001.

[107] Pandeeswari, R., and Jeyaprakash, B.G. High sensing response of β-Ga_2O_3 thin film towards ammonia vapours: Influencing factors at room temperature. *Sensors and Actuators B: Chemical*. 2014; 195:206. doi: 10.1016/j.snb.2014.01.025.

[108] Vorobyeva, N., et al. Ga_2O_3(Sn) oxides for high-temperature gas sensors. *Nanomaterials*. 2021; 11(11):2938. doi: 10.3390/nano11112938.

[109] Almaev, A., et al. Gas sensors based on pseudohexagonal phase of gallium oxide. *Physica Status Solidi B*. 2022; 259(2):2100306. doi: 10.1002/pssb.202100306.

[110] Almaev, A.V., et al. Hydrogen influence on electrical properties of Pt-contacted α-Ga_2O_3/ϵ-Ga_2O_3 structures grown on patterned sapphire substrates. *Journal of Physics D: Applied Physics*. 2020; 53(41):414004. doi: 10.1088/1361-6463/ab9c69.

[111] Zhao, J., et al. Two-dimensional gallium oxide monolayer for gas-sensing application. *Journal of Physical Chemistry Letters*. 2021; 12(24):5813. doi:10.1021/acs.jpclett.1c01393.

[112] Liu, C., et al. The effect of noble metal (Au, Pd and Pt) nanoparticles on the gas sensing performance of SnO_2-based sensors: a case study on the {221} high-index faceted SnO_2 octahedra. *CrystEngComm*. 2015; 17(33):6308. doi:10.1039/c5ce01162k.

[113] Huang, K., et al. Au- or Ag-decorated ZnO-rod/rGO nanocomposite with enhanced room-temperature NO_2-sensing performance. *Nanomaterials*. 2023; 13(16):2370. doi:10.3390/nano13162370.

[114] Fleischer, M., Hollbauer, L., and Meixner, H. Effect of the sensor structure on the stability of Ga_2O_3 sensors for reducing gases. *Sensors and Actuators B: Chemical*. 1994; 18(1-3):119. doi: 10.1016/0925-4005(94)87069-1.

[115] Bausewein, A., et al. Effects of palladium dispersions on gas-sensitive conductivity of semiconducting Ga_2O_3 thin-film ceramics. *Journal of the American Ceramic Society*. 1997; 80(2):317. doi: 10.1111/j.1151-2916.1997.tb02832.x.

[116] Schwebel, T., et al. CO-sensor for domestic use based on high temperature stable Ga_2O_3 thin films. *Sensors and Actuators B: Chemical*. 1998; 49(1-2):46. doi: 10.1016/S0925-4005(97)00334-1.

[117] Krawczyk, M., et al. P-type inversion at the surface of β-Ga_2O_3 epitaxial layer modified with Au nanoparticles. *Sensors*. 2022; 22(3):932. doi:10.3390/s22030932.

[118] Ren, Y., et al. Noble metal nanoparticles decorated metal oxide semiconducting nanowire arrays interwoven into 3D mesoporous superstructures for low-temperature gas sensing. *ACS Central Science*. 2021; 7(11):1885. doi: 10.1021/acscentsci.1c00912.

[119] Yang, S., et al. Metal oxide based heterojunctions for gas sensors: A review. *Nanomaterials*. 2021; 11(4):1026. doi: 10.3390/nano11041026

[120] Walker, J.M., Akbar, S.A., and Morris, P.A. Synergistic effects in gas sensing semiconducting oxide nano-heterostructures: A review. *Sensors and Actuators B: Chemical*. 2019; 286:624. doi: 10.1016/j.snb.2019.01.049.

[121] Abdullah, Q.N., et al. Novel SnO_2-coated β-Ga_2O_3 nanostructures for room temperature hydrogen gas sensor. *International Journal of Hydrogen Energy*. 2021; 46(9):7000. doi: 10.1016/j.ijhydene.2020.11.109.

[122] Jin, C., et al. Ultrasensitive multiple networked Ga_2O_3-core/ZnO-shell nanorod gas sensors. *Sensors and Actuators B: Chemical*. 2012; 161(1):223. doi: 10.1016/j.snb.2011.10.023.

[123] Wei, Z., et al. Ultra-thin sub-10 nm Ga_2O_3-WO_3 heterostructures developed by atomic layer deposition for sensitive and selective C_2H_5OH detection on ppm level. *Sensors and Actuators B: Chemical*. 2019; 287:147. doi: 10.1016/j.snb.2019.02.046.

[124] Ogita, M., et al. Ga_2O_3 thin films for high-temperature gas sensors. *Applied Surface Science*. 1999; 142(1-4):188. doi: 10.1016/S0169-4332(98)00714-4.

[125] Usseinov, A., et al. Pair vacancy defects in β-Ga_2O_3 crystal: Ab initio study. *Optical Materials: X*. 2022; 16:100200 doi: 10.1016/j.omx.2022.100200.

[126] Usseinov A., et al. Ab-initio calculations of oxygen vacancy in Ga_2O_3 crystals. *Latvian Journal of Physics and Technical Sciences*. 2021; 58(2):3. doi: 10.2478/lpts-2021-0007.

[127] Usseinov, A., et al. Vacancy defects in Ga_2O_3: First-principles calculations of electronic structure. *Materials*. 2021; 14(23):7384. doi: 10.3390/ma14237384.

[128] Tulinski, M. and Jurczyk, M. *Nanomaterials synthesis methods*; Metrology and standardization of nanotechnology. Mansfield, E., and Kaiser, D.L., E., Fujita, D., and Van de Voorde, M.; Eds. 2017; doi. 10.1002/9783527800308.ch4.

[129] Meng, L.Y., et al. The progress of microwave-assisted hydrothermal method in the synthesis of functional nanomaterials. *Materials Today Chemistry*. 2016; 1-2:63. doi: 10.1016/j.mtchem.2016.11.003.

[130] Tehrani, F.S., Ahmadian, H., Aliannezhadi, M. Hydrothermal synthesis and characterization of WO_3 nanostructures: Effect of reaction time. *Materials Research Express*. 2020; 7(1):015911. doi: 10.1088/2053-1591/ab66fc.

[131] Zhang, A., et al. Effects of pH on hydrothermal synthesis and characterization of visible-light-driven $BiVO_4$ photocatalyst. *Journal of Molecular Catalysis A: Chemical*. 2009; 304(1-2):28. doi: 10.1016/j.molcata.2009.01.019.

[132] Shi F, Qiao H. Effects of hydrothermal temperatures on crystalline quality and photoluminescence properties of β-Ga_2O_3 microspheres using ammonia as a precipitator. *CrystEngComm*. 2021; 23(2):492. doi: 10.1039/D0CE01471K.

[133] Makinudin, A.H.A., et al. Gallium oxide nanospheres: Effect of the post-annealing treatment. *Materials Letters*. 2017; 194:53. doi: 10.1016/j.matlet.2017.02.021.

[134] Zainal, N.F.A., et al. Thermal analysis: basic concept of differential scanning calorimetry and thermogravimetry for beginners. *Chemistry Teacher International*. 2021; 3(2):59. doi: 10.1515/cti-2020-0010.

[135] Roux, S., Bensakhria, A., and Antonini, G. Study and improvement of the regeneration of metallic oxides used as oxygen carriers for a new combustion process. *International Journal of Chemical Reactor Engineering.* 2006; 4(1). doi: 10.2202/1542-6580.1300.

[136] Suryanarayana, C., and Norton. M.G. *X-rays and diffraction, X-ray diffraction: A Practical Approach*. Springer US; 1998:3-19. doi:10.1007/978-1-4899-0148-4_1.

[137] Holder, C.F., and Schaak, R.E. Tutorial on powder X-ray diffraction for characterizing nanoscale materials. *ACS Nano*. 2019; 13(7):7359. doi: 10.1021/acsnano.9b05157.

[138] K Ferraro, J.R., Nakamoto, K., and Brown, C.W. *Introductory Raman spectroscopy*. San Diego: Academic Press, Inc. 2003:1-61.

[139] Kapesi, L. *Promoting carbon nanotube interlinking using ion implantation and high pressures in a diamond anvil cell*. Master's dissertation, University of Johannesburg (South Africa); 2018.

[140] Fakih, A. *Current controlled negative differential resistance in niobium dioxide*. Doctoral dissertation, Sorbonne Université), 2019. doi: 10.13140/RG.2.2.14609.17765.

[141] Reimer, L. Scanning electron microscopy: Physics of image formation and microanalysis; Springer: Berlin/Heidelberg, Germany, 1985; ISBN 3540135308.

[142] Massabuau, F.C-P., et al, *Microscopy of defects in semiconductors, Characterisation and control of defects in semiconductors, Materials, circuits and devices*. Institution of Engineering and Technology, 2019:2077761, doi: 10.1049/PBCS045E_ch8.

[143] Zhao, J., Liu, X.. Electron microscopic methods (TEM, SEM and energy dispersal spectroscopy). In: Goss MJ, Oliver M, eds. *Encyclopedia of Soils in the Environment (Second Edition)*. Academic Press; 2023:575. doi: 10.1016/B978-0-12-822974-3.00013-6.

[144] Zuo, J.M., and Spence, J.C.H. *Advanced transmission electron microscopy: Imaging and diffraction in nanoscience*. Springer New York, NY.; 2017. doi: 10.1007/978-1-4939-6607-3.

[145] Thommes, M., et al. Physisorption of gases, with special reference to the evaluation of surface area and pore size distribution (IUPAC Technical Report). *Pure and Applied Chemistry*. 2015; 87(9-10):1051. doi: 10.1515/pac-2014-1117.

[146] Hwang, N., and Barron, A.R. BET surface area analysis of nanoparticles. *The Connexions project*. 2011:1.

[147] Moulder, J.F., et al. Handbook of X-ray photoelectron spectroscopy. Chastain, J. (Ed.). Perkin-Elmer Corporation: Physical Electronics Division. 1992:34-180.

[148] Krishna, D.N.G., and Philip, J. Review on surface-characterization applications of X-ray photoelectron spectroscopy (XPS): Recent developments and challenges. *Applied Surface Science Advances*. 2022; 12:100332. doi: 10.1016/j.apsadv.2022.100332.

[149] Carl, A.D., et al. Synthesis and characterization of alkylamine-functionalized Si(111) for perovskite adhesion with minimal interfacial oxidation or electronic defects. *ACS Applied Materials and Interfaces*. 2017; 9(39):34377.

[150] Landi, S., et al. Use and misuse of the Kubelka-Munk function to obtain the band gap energy from diffuse reflectance measurements. *Solid State Communications*. 2022; 341:114573. doi: 10.1016/j.ssc.2021.114573.

[151] Nowak, M., Kauch, B., and Szperlich, P. Determination of energy band gap of nanocrystalline SbSI using diffuse reflectance spectroscopy. *Review of Scientific Instruments*. 2009; 80(4):046107. doi. 10.1063/1.3103603.

[152] Braga, M.S., et al. Multispectral colorimetric portable system for detecting metal ions in liquid media. *2019 4th International Symposium on Instrumentation Systems, Circuits and Transducers (INSCIT)*, 2019: 1-6. doi: 10.1109/INSCIT.2019.8868861.

[153] Gilliland, G.D. Photoluminescence spectroscopy of crystalline semiconductors. *Materials Science and Engineering: R: Reports*. 1997; 18(3-6):99. doi: 10.1016/S0927-796X(97)80003-4.

[154] Gomes, A.J., et al. Experimental methods in chemical engineering: Fluorescence emission spectroscopy. *Canadian Journal of Chemical Engineering*. 2019; 97(8):2168. doi: org/10.1002/cjce.23506.

[155] Penner, S., et al. Physico-chemical properties of unusual Ga_2O_3 polymorphs. *Monatshefte für Chemie- Chemical Monthly*. 2016; 147(2):289. doi: 10.1007/s00706-015-1628-z.

[156] Ahmadi, E., and Oshima, Y. Materials issues and devices of α- and β-Ga_2O_3. *Journal of Applied Physics*. 2019; 126(16):160901. doi:10.1063/1.5123213.

[157] Xue, H.W., et al. An overview of the ultrawide bandgap Ga_2O_3 semiconductor-based Schottky barrier diode for power electronics application. *Nanoscale Research Letters*. 2018; 13:290. doi: 10.1186/s11671-018-2712-1.

[158] Kaur, D., and Kumar, M. A strategic review on gallium oxide based deep-ultraviolet photodetectors: Recent progress and future prospects. *Advanced Optical Materials*. 2021; 9(9):2002160. doi: 10.1002/adom.202002160.

[159] Chen, X., et al. Review of gallium-oxide-based solar-blind ultraviolet photodetectors. *Photonics Research*. 2019; 7(4):381. doi: 10.1364/prj.7.000381.

[160] Sun, H., et al. Phase junction enhanced photocatalytic activity of Ga_2O_3 nanorod arrays on flexible glass fiber fabric. *RSC Advances*. 2020; 10(19):11499. doi: 10.1039/d0ra01461c.

[161] Das, B., et al. Tailored mesoporous nanocrystalline Ga_2O_3 for dye-selective photocatalytic degradation. *Microporous and Mesoporous Materials*. 2019; 288:109600. doi: 10.1016/j.micromeso.2019.109600.

[162] Li, D., et al. Ionic liquid-assisted synthesis of mesoporous α-Ga_2O_3 hierarchical structures with enhanced photocatalytic activity. *Journal of Materials Chemistry A*. 2013; 1(40):12417. doi: 10.1039/c3ta12619f.

[163] Hong, S., Rhee, C.K., and Sohn, Y. Photoluminescence, electro- and thermal catalytic properties of bare and Eu(III)-doped GaOOH, α- and β-Ga_2O_3 nanorods. *Journal of Alloys and Compounds*. 2019; 774:11-17. doi: 10.1016/j.jallcom.2018.09.381.

[164] Sinha, G., and Patra, A. Generation of green, red and white light from rare-earth doped Ga_2O_3 nanoparticles. *Chemical Physics Letters*. 2009; 473(1-3):151. doi: 10.1016/j.cplett.2009.03.074.

[165] Zhang, T., et al. Single-crystalline spherical β-Ga_2O_3 particles: Synthesis, N-doping and photoluminescence properties. *Journal of Luminescence*. 2013; 140:30. doi: 10.1016/j.jlumin.2013.02.031.

[166] Jiao, S., et al. The structural and photoelectrical properties of gallium oxide thin film grown by radio frequency magnetron sputtering. *ECS Journal of Solid State Science and Technology*. 2019; 8(7):Q3086. doi: 10.1149/2.0161907jss.

[167] An, Y., et al. Epitaxial growth of β-Ga_2O_3 thin films on Ga_2O_3 and Al_2O_3 substrates by using pulsed laser deposition. *Journal of Advanced Dielectrics*. 2019; 9(4):1950032. doi: 10.1142/S2010135X19500322.

[168] Ho, C-H., Tseng, C-Y., Tien, L-C. Thermoreflectance characterization of β-Ga_2O_3 thin-film nanostrips. *Optic Express*. 2010; 18(16):16360. doi: 10.1364/OE.18.016360.

[169] Ghadbeigi, L., et al. Optical characterization of gallium oxide α and β polymorph thin-films grown on c-plane sapphire. *Journal of Electronic Materials*. 2021; 50(6):2990. doi: 10.1007/s11664-021-08809-8.

[170] Mi, W., et al. Ultraviolet-green photoluminescence of β-Ga_2O_3 films deposited on $MgAl_6O_{10}$ (100) substrate. *Optical Materials*. 2013; 35(12):2624. doi: 10.1016/j.optmat.2013.07.030.

[171] Huang, L., et al. Self-powered solar-blind ultraviolet photodetector based on α-Ga_2O_3 nanorod arrays fabricated by the water bath method. *Optical Materials Express*. 2021; 11(7):2089. doi: 10.1364/ome.431377.

[172] Prakasam A.B., et al. Synthesis of self-assembled α-GaOOH microrods and 3D hierarchical architectures with flower like morphology and their conversion to α-Ga_2O_3. *Materials Letters*. 2015; 158:370. doi: 10.1016/j.matlet.2015.05.044.

[173] Liao, M.E., et al. Coefficients of thermal expansion of single crystalline β-Ga_2O_3 and in-plane thermal strain calculations of various materials combinations with β-Ga_2O_3. *APL Materials*. 2019; 7(2):022517. doi: 10.1063/1.5054327.

[174] Langford J.I., and Wilson, A.J.C. Scherrer after sixty years: A survey and some new results in the determination of crystallite size. *Journal of Applied Crystallography*. 1978; 11:102. doi. 10.1107/S0021889878012844.

[175] Liu, H., et al. A simple polyacrylamide gel route for the synthesis of $MgAl_2O_4$ nanoparticles with different metal sources as an efficient adsorbent: Neural network algorithm simulation, equilibrium, kinetics and thermodynamic studies. *Separation and Purification Technology*. 2022; 281:119855. doi: 10.1016/j.seppur.2021.119855.

[176] Suryanarayana, C., and Norton, M.G. Determination of crystallite size and lattice strain. C. Suryanarayana, M.G. Norton (Eds.), X-ray Diffraction: A practical approach, Springer US, Boston, MA (1998), pp. 207-221. doi: 10.1007/978-1-4899-0148-4_9.

[177] Zhao, Y., and Frost, R.L. Raman spectroscopy and characterisation of α-gallium oxyhydroxide and β-gallium oxide nanorods. *Journal of Raman Spectroscopy*. 2008; 39(10):1494. doi: 10.1002/jrs.2028.

[178] Machon, D., et al. High-pressure study of the β-to-α transition in Ga_2O_3. *Physical Review B*. 2006; 73(9):094125. doi: 10.1103/PhysRevB.73.094125.

[179] Wang, X., et al. Study of the phase transformation of single particles of Ga_2O_3 by UV-Raman spectroscopy and high-resolution TEM. *Chemistry- An Asian Journal*. 2013; 8(9):2189. doi: 10.1002/asia.201300433.

[180] Zuo, J., et al. Crystallite size effects on the Raman spectra of Mn_3O_4. *Nanostructured Materials*. 1998; 10(8):1331. doi: 10.1016/S0965-9773(99)00002-1.

[181] Dohy, D., Lucazeau, G., and Revcolevschi, A. Raman spectra and valence force field of single-crystalline β-Ga_2O_3. *Journal of Solid State Chemistry*. 1982; 45(2):180. doi: 10.1016/0022-4596(82)90274-2.

[182] Rao, R., et al. Blueshifted Raman scattering and its correlation with the [110] growth direction in gallium oxide nanowires. *Journal of Applied Physics*. 2005; 98(9):094312. doi: 10.1063/1.2128044.

[183] Yue, D., et al. A facile synthesis and optical properties of bundle-shaped $TbPO_4 \cdot H_2O$ nanorods. *Advances in Condensed Matter Physics*. 2013; 2013:673945. doi: 10.1155/2013/673945.

[184] Lu, Q., et al. Design of Sb_2S_3 nanorod-bundles: Imperfect oriented attachment. *Nanotechnology*. 2006; 17(9):2098. doi: 10.1088/0957-4484/17/9/004.

[185] Huang, C.C., Yeh, C.S. GaOOH, and β- and γ-Ga_2O_3 nanowires: Preparation and photoluminescence. *New Journal of Chemistry*. 2010; 34(1):103. doi: 10.1039/b9nj00392d.

[186] Quan, Y., et al. Synthesis and characterization of gallium oxide nanowires via a hydrothermal method. *Materials Chemistry and Physics*. 2010; 121(1-2):142. doi: 10.1016/j.matchemphys.2010.01.009.

[187] Liu, H., et al. Characterization of defect levels in β-Ga_2O_3 single crystals doped with tantalum. *CrystEngComm*. 2021; 23(15):2835. doi: 10.1039/d0ce01639j.

[188] Tak, B.R., et al. Point defects induced work function modulation of β-Ga_2O_3. *Applied Surface Science*. 2019; 465:973. doi: 10.1016/j.apsusc.2018.09.236.

[189] Dwivedi, N., et al. Understanding the role of nitrogen in plasma-assisted surface modification of magnetic recording media with and without ultrathin carbon overcoats. *Scientific Reports*. 2015; 5:7772. doi: 10.1038/srep07772.

[190] Rodríguez, C.I.M., et al. α-Ga_2O_3 as a photocatalyst in the degradation of malachite green. *ECS Journal of Solid State Science and Technology*. 2019; 8(7):Q3180. doi: 10.1149/2.0351907jss.

[191] Idriss, H. On the wrong assignment of the XPS O1s signal at 531–532 eV attributed to oxygen vacancies in photo- and electro-catalysts for water splitting and other materials applications. *Surface Science*. 2021; 712:121894. doi: 10.1016/j.susc.2021.121894.

[192] Girija, K., et al. Photocatalytic degradation of organic pollutants by shape selective synthesis of β-Ga_2O_3 microspheres constituted by nanospheres for environmental remediation. *Journal of Materials Chemistry A.* 2015; 3(6):2617. doi: 10.1039/c4ta05295a.

[193] Lancet, T. WHO's global air-quality guidelines. *Lancet*. 2006; 368:1302.

[194] Townsend, C.L., and Maynard, R.L. Effects on health of prolonged exposure to low concentrations of carbon monoxide. *Occupational and Environmental Medicine*. 2002; 59(10):708. doi: 10.1136/oem.59.10.708.

[195] Al-Ghussain, L. Global warming: review on driving forces and mitigation. *Environmental Progress and Sustainability Energy*. 2019; 38(1):13. doi:10.1002/ep.13041.

[196] Mhlongo, G.H., et al. A highly responsive NH_3 sensor based on Pd-loaded ZnO nanoparticles prepared via a chemical precipitation approach. *Scientific Reports*. 2019; 9(1):9881. doi: 10.1038/s41598-019-46247-z.

[197] Patil, V.L., et al. Low temperature chemiresistive gas sensing performance towards oxidising gas based on chemically prepared Ga doped ZnO nanorods. *Inorganic Chemistry Communications*. 2023; 152:110691. doi: 10.1016/j.inoche.2023.110691.

[198] Naresh-Kumar, G., et al. Origin of red emission in β-Ga_2O_3 analyzed by cathodoluminescence and photoluminescence spectroscopy. *Phys Status Solidi B*. 2021; 258(2):2000465. doi: 10.1002/pssb.202000465.

[199] Vasyltsiv, V., et al. Correlation between electrical conductivity and luminescence properties in β-Ga_2O_3:Cr^{3+} and β-Ga_2O_3:Cr,Mg single crystals . *Journal of Vacuum Science & Technology A*. 2021; 39(3):033201. doi: 10.1116/6.0000859.

[200] Dupin, J.C., et al. Systematic XPS studies of metal oxides, hydroxides and peroxides. *Physical Chemistry Chemical Physics*. 2000; 2(6):1319. doi: 10.1039/a908800h.

[201] Chowdhury, T.A. XPS Depth profile study of sprayed Ga_2O_3 thin films. *Engineering*. 2023; 15(8):459. doi: 10.4236/eng.2023.158035.

[202] Kgomo, M.B., et al. Evolution of In_2O_3 morphology from belt to fibrous-like structure for ethanol detection at low working temperature induced by Cr-addition. *Applied Surface Science*. 2023; 639:158210. doi: /10.1016/j.apsusc.2023.158210.

[203] Luchechko, A., et al. The effect of Cr^{3+} and Mg^{2+} impurities on thermoluminescence and deep traps in β-Ga_2O_3 crystals. *ECS Journal of Solid State Science and Technology*. 2020; 9(4):045008. doi: 10.1149/2162-8777/ab8b4d.

[204] Wu S, et al. Effects of annealing on surface residual impurities and intrinsic defects of β-Ga_2O_3. *Crystals*. 2023; 13(7):1045. doi: 10.3390/cryst13071045.

[205] Zhu, X., et al. Defect energy levels in monoclinic β-Ga_2O_3. *Journal of Luminescence*. 2022; 246:118801. doi: 10.1016/j.jlumin.2022.118801.

[206] Habib, I.Y., et al. Enhanced carbon monoxide-sensing properties of chromium-doped ZnO nanostructures. *Scientific Reports*. 2019; 9(1):9207. doi: 10.1038/s41598-019-45313-w.

[207] Brahim, N.S., et al. Enhanced CO gas sensing with DFT Optimized PbS loading on ZnO and CrZnO nanocomposites. *Sustainability*. 2022; 14(21):13978. doi: 10.3390/su142113978.

[208] Hou, L., et al. CO gas sensors based on p-type CuO nanotubes and CuO nanocubes: Morphology and surface structure effects on the sensing performance. *Talanta*. 2018; 188:41. doi: 10.1016/j.talanta.2018.05.059.

[209] Liu, H., et al. High-sensitivity SO_2 gas sensor based on noble metal doped WO_3 nanomaterials. *International Journal of Electrochemical Science*. 2021; 16(12):211240. doi: 10.20964/2021.12.39.

[210] Seekaew, Y., Pon-On, W., and Wongchoosuk, C. Ultrahigh selective room-temperature ammonia gas sensor based on tin-titanium dioxide/reduced graphene/carbon nanotube nanocomposites by the solvothermal method. *ACS Omega*. 2019; 4(16):16916. doi: 10.1021/acsomega.9b02185.

[211] Zhou, X., et al. Environmental and human health impacts of volatile organic compounds: A perspective review. *Chemosphere*. 2023; 313:137489. doi: 10.1016/j.chemosphere.2022.137489.

[212] Manisalidis, I., et al. Environmental and health impacts of air pollution: A review. *Frontiers in Public Health*. 2020; 8(14). doi: 10.3389/fpubh.2020.00014.

[213] United Nations Environment Programme, World Health Organization, & International Labour Organisation (1990). *2-Propanol - Environmental Health Criteria 103*. https://wedocs.unep.org/20.500.11822/29415. Accessed 3 June 2024.

[214] Amin, G., et al. Influence of pH, precursor concentration, growth time, and temperature on the morphology of ZnO nanostructures grown by the hydrothermal method. *Journal of Nanomaterials*. 2011; 2011:269692. doi: 10.1155/2011/269692.

[215] Li, T., and Zeng, W. New insight into the gas sensing performance of SnO_2 nanorod-assembled urchins based on their assembly density. *Ceramics International*. 2017; 43(1, Part A):728. doi: 10.1016/j.ceramint.2016.10.001.

[216] Ciftyurek, E., Li. Z., and Schierbaum, K. Adsorbed oxygen ions and oxygen vacancies: their concentration and distribution in metal oxide chemical sensors and influencing role in sensitivity and sensing mechanisms. *Sensors*. 2023; 23(1):29. doi: 10.3390/s23010029.

[217] Nemufulwi, M.I., Swart, H.C., and Mhlongo, G.H. Enhanced propanol response behavior of $ZnFe_2O_4$ NP-based active sensing layer induced by film thickness optimization. *Processes*. 2021; 9(10):1791. doi: 10.3390/pr9101791.

[218] Forney, C.F., Cue, K., and Fillmore, S. Ethylene inhibits sprouting of onion bulbs during long-term storage. *Horticulture Science*. 2022; 57(6):686. doi: 10.21273/HORTSCI16547-22.

[219] Caprioli, F., and Quercia, L. Ethylene detection methods in post-harvest technology: A review. *Sensors and Actuators B: Chemical*. 2014; 203:187. doi: 10.1016/j.snb.2014.06.109.

[220] Zhang, Y., et al. Tight-binding band structure of β- and α-phase Ga_2O_3 and Al_2O_3. *Journal of Applied Physics*. 2022; 131(17):175702. doi: 10.1063/5.0074598.

[221] Akaiwa, K., et al. Conductivity control of Sn-doped α-Ga_2O_3 thin films grown on sapphire substrates. *Japanese Journal of Applied Physics*. 2016; 55:1202BA. doi: 10.7567/JJAP.55.1202BA.

[222] Stegmeier, S., Fleischer, M., and Hauptmann, P. Influence of the morphology of platinum combined with β-Ga_2O_3 on the VOC response of work function type sensors. *Sensors and Actuators B: Chemical*. 2010; 148(2):439. doi: 10.1016/j.snb.2010.05.030.

[223] Albiter, E., et al. Photocatalytic deposition of Ag nanoparticles on TiO_2: Metal precursor effect on the structural and photoactivity properties. *Journal of Saudi Chemical Society*. 2015; 19(5):563. doi: 10.1016/j.jscs.2015.05.009.

[224] Zhang, J., Kolhatkar, G., and Ruediger, A. Localized surface plasmon resonance shift and its application in scanning near-field optical microscopy. *Journal of Materials Chemistry C*. 2021; 9(22):6960. doi: 10.1039/d1tc00877c.

[225] Hoflund, G.B., Hazos, Z.F., and Salaita, G.N. Surface characterization study of Ag, AgO, and Ag_2O using X-ray photoelectron spectroscopy and electron energy-loss spectroscopy. *Physical Review B*. 2000; 62(16):11126. doi: 10.1103/PhysRevB.62.11126.

[226] Sylvestre, J.P., et al. Surface chemistry of gold nanoparticles produced by laser ablation in aqueous media. *Journal of Physical Chemistry B*. 2004; 108(43):16864. doi: 10.1021/jp047134.

[227] Emsley, J. *Nature's Building Blocks: An AZ guide to the elements*; Oxford University Press: Oxford, UK, 2011.

[228] Li, K., and Xue, D. Estimation of electronegativity values of elements in different valence states. *Journal of Physical Chemistry A*. 2006; 110(39):11332. doi: 10.1021/jp062886k.

[229] Liu, S., et al. Atomically embedded Ag on transition metal hydroxides triggers the lattice oxygen towards sustained seawater electrolysis. *Nano Energy*. 2022; 98:107212. doi: 10.1016/j.nanoen.2022.107212.

[230] Ivanov, P., et al. Towards a micro-system for monitoring ethylene in warehouses. *Sensors and Actuators, B: Chemical*. 2005; 111-112:63. doi: 10.1016/j.snb.2005.06.064.

[231] Zhao, Q., et al. High performance ethylene sensor based on palladium-loaded tin oxide: Application in fruit quality detection. *Chinese Chemical Letters*. 2020; 31(8):2045. doi: 10.1016/j.cclet.2020.04.032.

[232] Li, B., et al. Highly sensitive ethylene sensors using Pd nanoparticles and rGO modified flower-like hierarchical porous α-Fe_2O_3. *Sensors and Actuators B: Chemical*. 2019; 290:396. doi: 10.1016/j.snb.2019.04.002.

[233] Espinosa, E., et al. Drop-coated sensing layers on ultra low power hotplates for an RFID flexible tag microlab. *Sensors and Actuators B: Chemical*. 2010; 144(2):462. doi: 10.1016/j.snb.2009.07.005.

[234] Alhalaili, B., Vidu, R., and Islam, M.S. The growth of Ga_2O_3 nanowires on silicon for ultraviolet photodetector. *Sensors.* 2019; 19(23):5301. doi: 10.3390/s19235301.

[235] Wang, T., et al. Ag_2O/TiO_2 hollow microsphere heterostructures with exposed high-energy {001} crystal facets and high photocatalytic activities. *Journal of Materials Science: Materials in Electronics*. 2020; 31(14):11496. doi: 10.1007/s10854-020-03697-w.

[236] Navale, S., et al. Effect of Ag addition on the gas-sensing properties of nanostructured resistive-based gas sensors: An overview. *Sensors*. 2021; 21(19):6454. doi: 10.3390/s21196454.

[237] Wang, S., et al. In situ synthesis of monoclinic β-Ga_2O_3 nanowires on flexible substrate and solar-blind photodetector. *Journal of Alloys and Compounds.* 2019; 787:133. doi: 10.1016/j.jallcom.2019.02.031.

[238] Xu, Y, et al. Solar blind deep ultraviolet β-Ga_2O_3 photodetectors grown on sapphire by the Mist-CVD method. *Optical Materials Express*. 2018; 8(9):2941. doi: 10.1364/ome.8.002941.

[239] Arrateig, X., et al. Development and simulated environment testing of β-(Al)Ga_2O_3-based photodetectors for space-based observation of the Herzberg continuum. In: *Proceeding.SPIE*. 2021; 11858:1185813. doi: 10.1117/12.2603565.

[240] Wang, S., et al. β-Ga_2O_3 nanorod arrays with high light-to-electron conversion for solar-blind deep ultraviolet photodetection. *RSC Advances*. 2019; 9(11):6064. doi: 10.1039/C8RA10371B.

[241] Hu, H., et al. α/β phase junction Ga_2O_3 based high-performance self-powered deep ultraviolet photodetectors with Ti_3C_2/Ag nanowire hybrid conductive electrode. *Journal of Alloys and Compounds*. 2023; 945:169307. doi: 10.1016/j.jallcom.2023.169307.

[242] Guo, D., et al. Review of Ga_2O_3-based optoelectronic devices. *Materials Today Physics*. 2019; 11:100157. doi. 10.1016/j.mtphys.2019.100157.

[243] Upadhyay, D., Joshi, N., and Jha P.K. Two dimensional hexagonal GaOOH: A promising ultrawide bandgap semiconductor for smart optoelectronic applications. *Chemical Physics Letters*. 2021; 765:138310. doi: 10.1016/j.cplett.2020.138310.

[244] Ginley, D.S., and Bright, C. Transparent conducting oxides. *MRS Bulletin*. 2000; 25(8):15. doi: 10.1557/mrs2000.256.

[245] Kawaguchi, Y., et al. Preparation of gallium oxide photocatalysts and their silver loading effects on the carbon dioxide reduction with water. *Journal of Photochemistry and Photobiology A: Chemistry*. 2018; 358:459. doi: 10.1016/j.jphotochem.2017.11.010.

[246] Jędrzejczyk, M., et al. Wide band gap Ga_2O_3 as efficient UV-C photocatalyst for gas-phase degradation applications. *Environmental Science and Pollution Research*. 2017; 24(34):26792. doi: 10.1007/s11356-017-0253-2.

[247] Zhang, X., et al. Phase transition of two-dimensional β-Ga_2O_3 nanosheets from ultrathin γ-Ga_2O_3 nanosheets and their photocatalytic hydrogen evolution activities. *ACS Omega*. 2018; 3(10):14469. doi: 10.1021/acsomega.8b01964.

[248] Chikoidze, E., et al. P-type β-gallium oxide: A new perspective for power and optoelectronic devices. *Materials Today Physics*. 2017; 3:118. doi: 10.1016/j.mtphys.2017.10.002.

[249] Higashiwaki, M., et al. State-of-the-art technologies of gallium oxide power devices. *Journal of Physics D: Applied Physics*. 2017; 50(33):333002. doi: 10.1088/1361-6463/aa7aff.

[250] Green, A.J., et al. β-Gallium oxide power electronics. *APL Materials*. 2022; 10(2):029201. doi: 10.1063/5.0060327.

[251] Wang, X.S., et al. β-Ga_2O_3:Cr^{3+} nanoparticle: A new platform with near infrared photoluminescence for drug targeting delivery and bio-imaging simultaneously. *Acta Biomaterialia*. 2015; 22:164. doi. 10.1016/j.actbio.2015.04.010.

[252] Pilliadugula, R., et al. Effect of morphology and (Sn, Cr) doping on in vitro antiproliferation properties of hydrothermally synthesized 1D GaOOH nanostructures. *Journal of Science: Advanced Materials and Devices*. 2021; 6(3):351. doi: 10.1016/j.jsamd.2021.03.003.